

Final Report

The Reduction of Advanced Military Aircraft Noise

SERDP Project WP-1583

December 2011

Philip J. Morris
Penn State University

This document has been cleared for public release



This report was prepared under contract to the Department of Defense Strategic Environmental Research and Development Program (SERDP). The publication of this report does not indicate endorsement by the Department of Defense, nor should the contents be construed as reflecting the official policy or position of the Department of Defense. Reference herein to any specific commercial product, process, or service by trade name, trademark, manufacturer, or otherwise, does not necessarily constitute or imply its endorsement, recommendation, or favoring by the Department of Defense.

REPORT DOCUMENTATION PAGE				Form Approved OMB No. 0704-0188	
The public reporting burden for this collection of information is estimated to average 1 hour per response, including the time for reviewing instructions, searching existing data sources, gathering and maintaining the data needed, and completing and reviewing the collection of information. Send comments regarding this burden estimate or any other aspect of this collection of information, including suggestions for reducing the burden, to the Department of Defense, Executive Services and Communications Directorate (0704-0188). Respondents should be aware that notwithstanding any other provision of law, no person shall be subject to any penalty for failing to comply with a collection of information if it does not display a currently valid OMB control number.					
PLEASE DO NOT RETURN YOUR FORM TO THE ABOVE ORGANIZATION.					
1. REPORT DATE (DD-MM-YYYY) 12/01/2011		2. REPORT TYPE FINAL		3. DATES COVERED (From - To) 05/08/2007-10/31/2011	
4. TITLE AND SUBTITLE The Reduction of Advanced Military Aircraft Noise				5a. CONTRACT NUMBER W912HQ-07-C-0031	
				5b. GRANT NUMBER	
				5c. PROGRAM ELEMENT NUMBER	
6. AUTHOR(S) Philip Morris, Dennis McLaughlin, Victor Sparrow, James Bridges, Brenda Henderson, Kenneth Plotkin, Steve Martens, Richard McKinley.				5d. PROJECT NUMBER WP-1583	
				5e. TASK NUMBER	
				5f. WORK UNIT NUMBER	
7. PERFORMING ORGANIZATION NAME(S) AND ADDRESS(ES) Penn State University, 110 Technology Center, University Park, PA, 16802 General Electric, One Research Circle, Niskayuna, NY, 12309 Wyle Laboratories, 241 18th Street S, Suite 701, Arlington, VA, 22202				8. PERFORMING ORGANIZATION REPORT NUMBER	
9. SPONSORING/MONITORING AGENCY NAME(S) AND ADDRESS(ES) Strategic Environmental Research and Development Program 901 N Stuart Street, Suite 303 Arlington VA 22203				10. SPONSOR/MONITOR'S ACRONYM(S) SERDP	
				11. SPONSOR/MONITOR'S REPORT NUMBER(S)	
12. DISTRIBUTION/AVAILABILITY STATEMENT The document is approved for public release; distribution unlimited					
13. SUPPLEMENTARY NOTES					
14. ABSTRACT This report describes a combined experimental and computational study of the generation and radiation of jet noise from high performance military fighter aircraft. An emphasis is on the methodology for scaling measurements at small and moderate scale to full scale aircraft engines. Promising concepts for jet noise reduction are explored at small and moderate scale. Numerical simulations are performed to support the experiments and provide additional insight into the noise generation and radiation process. Noise and flow measurements are performed in the Anechoic Jet Noise Research Facility at Penn State and the Aero-Acoustic Propulsion Laboratory at the NASA Glenn Research Center. Designs for the baseline nozzles are developed by General Electric Aviation. A computational study of the effect of chevrons on the jet flow is conducted by General Electric and used to design chevron nozzles that are then studied experimentally by NASA and Penn State. The results were transferred for use in the Advanced Acoustic Model, which is used to assess the impact of aircraft operations on communities surrounding military bases.					
15. SUBJECT TERMS Adjoint design, Aeroacoustics, Jet noise, Mach wave radiation, Military aircraft, Noise reduction, Shock-associated noise, Turbulence					
16. SECURITY CLASSIFICATION OF:			17. LIMITATION OF ABSTRACT		18. NUMBER OF PAGES
a. REPORT	b. ABSTRACT	c. THIS PAGE			19a. NAME OF RESPONSIBLE PERSON Philip J. Morris
					19b. TELEPHONE NUMBER (Include area code) 814-863-0157

Reset

1. Table of Contents

2.	List of tables _____	3
3.	List of figures _____	4
4.	List of acronyms _____	12
5.	Keywords _____	14
6.	Acknowledgements _____	15
7.	Abstract _____	16
8.	Objective _____	17
9.	Background _____	18
10.	Tasks and results _____	20
10.1.	Task 1: nozzle design and configuration control _____	20
10.2.	Task 2. Small scale experiments _____	31
10.3.	Task 3: moderate scale noise experiments _____	71
10.4.	Task 4. Numerical simulations of jet noise _____	77
10.5.	Task 5. Integration of program elements _____	132
10.6.	Task 6. Assessment of scaling methodology _____	141
11.	Summary and Conclusions _____	178
12.	References _____	181

2. List of Tables

Table 1. Chevron CFD DOE parameters	21
Table 2. Testing nozzles and measured distances of acoustic measurements from each facility.	39
Table 3. Jet operating conditions for measurements conducted with CD nozzle ($M_d = 1.5$).	41
Table 4. Nozzle parameters and jet conditions for all experiments run for this task.....	64
Table 5. Experimental cycle points.....	74
Table 6. Chevron parameters	74
Table 7. Operating conditions.....	79
Table 8. Predicted integral scales of the turbulent structures for all jets. Calculated at $x / D = 4.0$ along the lip line based on the second-order cross correlation of the axial velocity fluctuations.....	97
Table 9. Operating conditions of measurement	132
Table 10. Chevron CFD Design of Experiments (DOE) parameters.....	133
Table 11. Chevron parameters used in moderate scale experiments	134
Table 12. File format of chevron correction file.....	135
Table 13. Input parameters for SAE ARP 876 code based on F/A-18E/F profile points.	136
Table 14. Contour areas, square miles, for each of the sources run in AAM.	139
Table 15. Nozzle parameters and jet operation conditions for data shown in figures.	164

3. List of Figures

Figure 1 Assembly drawing containing nozzle drawings provided to SERDP team.	20
Figure 2. Description of geometric parameters.....	21
Figure 3 Total Temperature CFD results on a plane through the tip of the chevron.	22
Figure 4 TKE CFD results through the tip of the chevron.	23
Figure 5 Total temperature contours through the cross-section of the plume at $x/D=0.5$	24
Figure 6 TKE contours through a cross-section of the plume for two chevron configurations, at three axial locations.	25
Figure 7. Scale Model Data Comparison, OASPL.	26
Figure 8. Scale Model Data Comparison, SPL at 60 deg.	26
Figure 9 Scale Model Data Comparison, SPL at 100 deg.	27
Figure 10 Scale Model Data Comparison, SPL at 150 deg.	27
Figure 11 Comparison of engine and scale model data, SPL at 60 deg.....	28
Figure 12. Comparison of engine and scale model data, SPL at 90 deg.....	29
Figure 13. Comparison of engine and model scale data, SPL at 130 deg.....	29
Figure 14. Comparison of engine and model scale data, SPL at 150 deg.....	30
Figure 15. The Pennsylvania State University high speed jet noise facility.....	31
Figure 16. The Pennsylvania State University high speed jet noise facility.....	32
Figure 17. Schematic of non-dimensional measured locations of microphones.	33
Figure 18. Flow chart of the data acquisition process.	33
Figure 19. Lossless spectra comparison of unheated jets from PSU and NASA Glenn Research Center both issuing from $M_d = 1.65$ GE nozzle operated at $M_j = 1.56$, and scaled to $R/D = 100$	35
Figure 20. Acoustic measurements from Penn State, NASA Langley Research Center (LaRC), and NASA Glenn Research Center (GRC) conducted with CD nozzle ($M_d = 1.5$, $D = 0.5$) accordingly operated at $M_j = 1.5$, $TTR = 2.2$, and scaled to $R/D = 100$	36
Figure 21. Spectra comparison of heat simulated jets issuing from $M_d = 1.5$ ($AR = 1.18$) CD Nozzle with 0.5" and 1" in diameter operated at $M_j = 1.5$, $TTR = 3.2$, and scaled to $R/D = 100$	37
Figure 22. Spectral comparison of experiments measured at various locations from NASA Glenn Research Center (NGRC) issuing from $M_d = 1.5$ ($AR = 1.18$) CD Nozzle operated at $M_j = 1.5$, $TTR_{core} = 2.6$, $TTR_{mix} = 2.2$, scaled to $R/D = 100$	38
Figure 23. Estimated peak noise emission location as a function of Strouhal number for cold and heated jets operated at $M_j = 1.$, Green, Cold Jets ^{17,18} ; Yellow, Heated Jets ²¹ ; Magenta, Tester et al ²²	40
Figure 24. Estimated peak noise emission location as a function of Strouhal number for cold and heated supersonic jets. Red ²¹ , Blue ⁹ , Purple ²²	40
Figure 25. Schematic of the data processing procedure based on the noise source distribution locations for the acoustic measurements conducted at various radial distances.....	43

Figure 26. Acoustic measurements from PSU conducted with CD nozzle ($M_d = 1.5$, $D = 0.5$) operated at $M_j = 1.5$, $TTR = 2.2$, and $TTR = 1$, as measured at $R/D = 140$.	44
Figure 27. Sound intensity contour plot in for specific frequencies from jets operating at various conditions (a) $M_j = 1.5$, $TTR = 1$, (b) $M_j = 1.5$, $TTR = 2.2$.	45
Figure 28. Optical Deflectometer measurements performed with CD nozzle ($M_d = 1.5$, $D = 0.5$) operated at $M_j = 1.5$, $TTR = 1$ measured along nozzle lip line accordingly from $x/D = 4$ to 9. Convection velocity as a function of St .	46
Figure 29. Optical Deflectometer measurements conducted with CD nozzle ($M_d = 1.5$, $D = 0.5$) operated at $M_j = 1.5$, $TTR = 1$ measured along nozzle lip line accordingly from $x/D = 4$ to 9. Density fluctuation level as a function of St .	47
Figure 30. OASPL plot measured at $R/D = 35$, 70 , and 140 for jets operated at	47
Figure 31. Acoustic measurements conducted with CD nozzle ($M_d = 1.5$, $D = 0.5$) as measured at $R/D = 35$, 70 , 140 , 280 , (a) operated at $M_j = 1.5$, $TTR = 1$, (b) operated at $M_j = 1.5$, $TTR = 2.2$.	48
Figure 32. Acoustic measurements conducted with CD nozzle ($M_d = 1.5$, $D = 0.5$) operated at $M_j = 1.5$, $TTR = 1$ for left column and $M_j = 1.5$, $TTR = 2.2$ for right column and corrected with noise source distribution. (a) and (b) spectra from $R/D = 70$ synthesized to $R/D = 140$.	49
Figure 33. Acoustic measurements conducted with CD nozzle ($M_d = 1.5$, $D = 0.5$) operated at $M_j = 1.5$, $TTR = 1$ for left column and $M_j = 1.5$, $TTR = 2.2$ for right column and corrected with noise source distribution. (a) and (b), spectra from $R/D = 35$ synthesized to $R/D = 140$, (c) and (d), spectra from $R/D = 140$ synthesized to $R/D = 35$.	50
Figure 34. Acoustic measurements conducted with CD nozzle ($M_d = 1.5$, $D = 0.5$) operated at $M_j = 1.5$, $TTR = 2.2$, as measured at $R/D = 35$, 70 , 140 , 280 for $\theta = 40^\circ$, and 70° and corresponding values of the Morfey-Howell indicator of nonlinearity.	52
Figure 35. Normalized pressure time histories from acoustic measurements conducted with CD nozzle ($M_d = 1.5$, $D = 0.5$) operated at $M_j = 1.5$, $TTR = 2.2$, $\theta = 40^\circ$, at $R/D = 35$, 70 , 140 , and 280 .	53
Figure 36. Acoustic measurements conducted with CD nozzle ($M_d = 1.5$, $D = 0.5$) operated at $M_j = 1.5$, $TTR = 2.2$, as measured $R/D = 280$. Synthesized spectra were reconstructed respectively from $R/D = 35$, 70 , and 140 and scaled $R/D = 280$.	54
Figure 37 a) 1/48 scale aircraft model end view with model rotating azimuthal angle, ϕ , where red line represents the measured plane of microphone array. b) Spectra comparison from measurements conducted with GE $M_d 1.5$ baseline nozzle operated at $M_j = 1.36$, cold accompanied with empennage set at $\phi = 0^\circ$, 45° , and 90° respectively.	56
Figure 38. The Beveled Nozzles – Left: 2-D Cross-Sectional Drawing; Right: Image of Rapid Prototyped Nozzles.	59
Figure 39. Schematic Showing the Convention for the Azimuthal Angle (ϕ).	60
Figure 40. Shadowgraph Images – Top Row: $M_j = 1.4$; Center Row: $M_j = 1.6$; Bottom Row: $M_j = 1.9$. Left: Baseline Nozzle; Middle Bevel24 Nozzle, Right: Bevel35 Nozzle	61

Figure 41. Top – Schlieren Imagery of the Bevel24 Nozzle with M_j (from Left to Right) = 1.47, 1.64, 1.77. Bottom – Comparison of the Flow Exit Angles at M_j = 1.47, 1.64, 1.77.....	62
Figure 42. Overlay of the Pressure Distribution inside the Nozzle at the Short Lip Side, Midpoint, and Long Lip Side.....	63
Figure 43. Spectra and OASPL Comparison of Heated jets, measured at $\phi = 0^\circ$ (Long Lip Side), issuing from GE C-D $M_d = 1.65$ Beveled Nozzle, with $M_j = 1.47$, TTR = 3, $D_{noz} = 0.708''$, $f_c = 42693$ Hz, Scaled $R/D_j = 100$	65
Figure 44. Spectra and OASPL Comparison of Heated jets, measured at $\phi = 180^\circ$ (Short Lip Side), issuing from GE C-D $M_d = 1.65$ Beveled Nozzle, with $M_j = 1.47$, TTR = 3, $D_{noz} = 0.708''$, $f_c = 42693$ Hz, Scaled $R/D_j = 100$	65
Figure 45. Spectra and OASPL Comparison of Heated jets, measured at $\phi = 0^\circ$ (Long Lip Side), issuing from GE C-D $M_d = 1.65$ Beveled Nozzle, with $M_j = 1.64$, TTR = 3, $D_{noz} = 0.708''$, $f_c = 43644$ Hz, Scaled $R/D_j = 100$	68
Figure 46. Spectra and OASPL Comparison of Heated jets, measured at $\phi = 180^\circ$ (Short Lip Side), issuing from GE C-D $M_d = 1.65$ Beveled Nozzle, with $M_j = 1.64$, TTR = 3, $D_{noz} = 0.708''$, $f_c = 43644$ Hz, Scaled $R/D_j = 100$	68
Figure 47. Spectra and OASPL Comparison of heated jets issuing from GE C-D $M_d = 1.65$ Beveled Nozzle, with $M_j = 1.47$, TTR = 3, $D_{noz} = 0.708''$, $f_c = 42693$ Hz, Scaled $R/D_j = 100$. The beveled nozzle jet data are shown for various azimuthal angles.	69
Figure 48. Spectra and OASPL Comparison of heated jets issuing from GE C-D $M_d = 1.65$ Beveled Nozzle, with $M_j = 1.64$, TTR = 3, $D_{noz} = 0.708''$, $f_c = 43644$ Hz, Scaled $R/D_j = 100$, again at various azimuthal angles.	69
Figure 49. Spectra and OASPL Comparison of Heated Baseline jet with and without Forward Flight, issuing from GE C-D $M_d = 1.65$ Beveled Nozzle, with $M_j = 1.47$, TTR = 3, $D_{noz} = 0.708''$, $f_c = 42693$ Hz, Scaled $R/D_j = 100$. The forward flight data have been corrected for outer stream shear layer refraction.....	70
Figure 50. Spectra and OASPL Comparison of Heated jets issuing from GE C-D $M_d = 1.65$ Beveled Nozzle, with Forward Flight of $M_f = 0.17$, with $M_j = 1.47$, TTR = 3, $D_{noz} = 0.708''$, $f_c = 42693$ Hz, Scaled $R/D_j = 100$	70
Figure 51. A photograph of the Aero-Acoustic Propulsion Laboratory (AAPL) showing the Nozzle Acoustic Test Rig (NATR).....	71
Figure 52. The $M_d = 1.65$ nozzle mounted on the fan stream of the HFJER.....	72
Figure 53. Acoustic data acquired at a 90° observation angle for $NPR_c = 2.5$ and $NTR_c = 3.0$. ..	72
Figure 54. Photographs of fluorescent oil applied to the nozzle trailing edge. The photographs were taken before and after testing at representative takeoff conditions.....	73
Figure 55. The nozzles used in the chevron experiments.	74
Figure 56. The chevron design space used in the MDOE study.....	75
Figure 57. One-third octave band modeled and measured spectra for the P03L08W06 chevrons and the average baseline spectra at setpoint 44543 and observation angles equal to (a) 80° and (b) 160°	76

Figure 58. One-third octave band modeled and measured spectra for the P06L18W10 chevrons and the average baseline spectra at setpoint 44543 and observation angles equal to (a) 80° and (b) 160°	76
Figure 59. The military-style nozzle with chevrons and three geometric parameters. (Only 4 out of 12 chevrons are shown for clarity)	79
Figure 60. Sketch of the immersed boundary method	80
Figure 61. Computational mesh for the chevron nozzle simulations. The grids around the chevrons are refined significantly to improve the IBM representation of chevrons. No local grid refinement is used in the baseline nozzle simulations. (a) Full computational domain and the FWH integration surface (pink lines). (b) A symmetric plane through one chevron tip. (c) An axial station at about 50% of the chevron length. (d) Grid details around point A.	82
Figure 62. The IBM representation of the chevron geometries. The region with red color shows the immersed grid points. (a) A symmetric plane through one chevron tip. (b) An axial cross-section at 50% of the chevron length	83
Figure 63. Comparison of the measured and predicted noise spectra for both the baseline and chevron nozzles at the three operating conditions. Note: the NASA baseline measurements have a core $TTR = 3.0$ and a mixed $TTR = 2.56$ at $M_j = 1.36$ and a core $TTR = 3.6$ and a mixed $TTR = 3.0$ at $M_j = 1.47$ and 1.56 . (a) $M_j = 1.36$, $\theta = 30^\circ \sim 70^\circ$, (b) $M_j = 1.47$, $\theta = 30^\circ \sim 70^\circ$, (c) $M_j = 1.56$, $\theta = 30^\circ \sim 70^\circ$, (d) $M_j = 1.36$, $\theta = 80^\circ \sim 120^\circ$, (e) $M_j = 1.47$, $\theta = 80^\circ \sim 120^\circ$, (f) $M_j = 1.56$, $\theta = 80^\circ \sim 120^\circ$	87
Figure 64. Comparison of the predicted far-field OASPL with the experimental measurements. All data are scaled to the same distance $R/D = 100$. (a) $M_j = 1.47$, $TTR =$, (b) $M_j = 1.56$, $TTR =$	88
Figure 65. Three-dimensional view of the instantaneous streamwise vorticity iso-surfaces. Two iso-surfaces are plotted at the values $\omega_x D/U_j = \pm 5$. The red iso-surface represents a positive value, and the blue, a negative one. (a) Baseline, $M_j = 1.36$. Note: the chevrons are shown as a reference, (b) P05L13W8, $M_j = 1.36$, (c) P05L13W8, $M_j = 1.47$, (d) P05L13W8, $M_j = 1.56$	89
Figure 66. Comparison of the three-dimensional views of the time-averaged axial velocity contours for the baseline nozzle and the chevron nozzle simulations at several axial stations. Normalized by the fully expanded jet velocity U_j . Operating condition: $M_j = 1.56$, $NPR = 4.0$, $TTR = 3.0$	90
Figure 67. Comparison of the vorticity thickness for the baseline and the chevron nozzle jets at the three operating conditions.....	91

Figure 68. Instantaneous contours of density gradients (color contours) and pressure time derivatives (gray backgrounds).....	92
Figure 69. Virtual probes along the lip line where the flow solutions are sampled. The colored contours show the time-averaged Mach number contours of the baseline nozzle jet operating at $M_j = 1.47$, $NPR = 3.5$ and $TTR = 3.0$	93
Figure 70. Comparison of the turbulence intensities between the baseline nozzle jets and the chevron nozzle jets along the lip line. (a) $M_j = 1.36$, tip and valley planes, (b) Three conditions, baseline and P05L13W8 valley plane.	94
Figure 71. Comparison of the power spectral density of u' between the baseline nozzle jets and the chevron nozzle jets at various axial locations along the lip line. (a) $M_j = 1.47$, baseline, (b) $M_j = 1.47$, P05L13W8.	95
Figure 72. Cross correlation coefficients of the axial velocity at $x / D = 4.0$ along the lip line. Operating conditions: $M_j = 1.36$, $NPR = 3.0$, $TTR = 3.0$	96
Figure 73. Variation of time delay for maximum cross correlation with separation distance. The reference flow probe is fixed at $x / D = 4.0$ along the lip line. Operating conditions: $M_j = 1.36$, $NPR = 3.0$, $TTR = 3.0$	96
Figure 74. Comparison of the predicted frequency-dependent phase speeds for all the baseline and chevron nozzle jets. (a) Predicted convection speed, (b) fitted convection speed.	98
Figure 75. A general parabolic shape of nozzle which depends on one design parameter.....	105
Figure 76. Algorithm for the adjoint method for designing a nozzle contour with one design variable.....	106
Figure 77. The general geometry of the nozzle for a two-dimensional case.	109
Figure 78. Algorithm for the adjoint method for designing a nozzle contour.	112
Figure 79. Mesh inside the nozzle domain for two-dimensional calculations.....	113
Figure 80. The distribution of increment dx with grid points along the nozzle centerline.	114
Figure 81. Initial and final nozzle shapes. The black line shows the final geometry and the red line shows the initial shape for quasi-one-dimensional flow.....	116
Figure 82. The convergence of objective function with design cycles on a log-log plot for quasi-one-dimensional flow.....	117
Figure 83. The convergence of the design parameter α with design cycles for quasi-one-dimensional flow.....	117
Figure 84. The distribution of the final, desired and initial pressure distribution (with respect to total pressure p_o) as function of axial distance inside nozzle. The symbols represent the desired pressure distribution, the blue line represents the final pressure distribution, and the red line represents the initial pressure distribution for quasi-one-dimensional flow.....	118
Figure 85. The initial (red), intermediate (green) and final (black) geometry of the rectangular nozzle.	119

Figure 86. The Mach number distribution along the centerline of the nozzle. The red and blue lines show the initial and final Mach number respectively along the nozzle centerline. The desired Mach number is shown by symbols.	120
Figure 87. The pressure distribution (with respect to total pressure p_o) along the centerline of the nozzle. The red and blue lines show the initial and final pressure respectively along the nozzle centerline. The desired pressure is shown by black symbols.	120
Figure 88. The decay of the objective function with design cycles.....	121
Figure 89. Change in the design parameter α with design cycles. The desired value of design parameter is 0.25.....	121
Figure 90. Pressure contours inside the nozzle. The upper half of the nozzle shows the pressure contours for the initial geometry and the lower half shows the pressure contours for the final geometry.	122
Figure 91. The geometry of the nozzle. Calculations were performed for only half the domain. The red line shows the initial geometry. The green line shows the final geometry. The black line shows the geometry that gives the desired pressure distribution.	123
Figure 92. The convergence of the objective function with design cycles on a log – log plot...	124
Figure 93. The convergence of design parameter α_1 with design cycles.....	125
Figure 94. The convergence of design parameter α_2 with design cycles.	125
Figure 95. The convergence of design parameter α_3 with design cycles.	126
Figure 96. The pressure distribution (with respect to total pressure p_o) along the centerline of the nozzle. The red and blue lines show the initial and final pressure respectively along the nozzle centerline. The desired pressure is shown by black symbols.	126
Figure 97. The pressure contours inside the nozzle. The upper half of the nozzle shows the pressure contours for the initial geometry and lower half shows the pressure contours for the final geometry.	127
Figure 98. The distribution of pressure (with respect to total pressure p_o) along nozzle centerline. The red and blue lines show the initial and final pressure respectively along the nozzle centerline. The desired pressure is shown by black symbols.....	128
Figure 99. The decay of objective function with design cycles for the supersonic case with a shock.	129
Figure 100. Pressure contours inside the nozzle domain. Upper half shows the initial flow and lower half shows the final flow.....	130
Figure 101. The distribution of shock parameter Z along nozzle axis for the final design cycle.	131
Figure 102. Description of Geometric Parameters.	133
Figure 103. Directivity pattern of the overall level for Base (solid line), Medium Penetration Chv3 (dashed line), and Larger Penetration Chv6 (dash-dot line).	137
Figure 104. SEL contours resulting from running Base (solid line), Chv3(dashed line), and Chv6 (dash-dot line) in AAM on an FCLP operation.	138
Figure 105. The Pennsylvania State University high speed jet noise facility.....	142


Figure 106. Schematic of dual flow jet exit rig in the NASA Glenn Research Center with the bypass air for low bypass nozzle systems.....	144
Figure 107. Spectra and OASPL comparison of unheated jets from PSU and HFJER issuing from GE nozzle with $M_d = 1.65$, $M_j = 1.56$, and scaled to $R/D = 100$	148
Figure 108. Spectra and OASPL comparison of unheated jets from PSU and HFJER issuing from GE nozzle with $M_d = 1.5$, $M_j = 1.56$, and scaled to $R/D = 100$	148
Figure 109. Spectra and OASPL comparison of single stream jet with heat simulation ($TTR = 2.6$) from PSU and heated jet ($TTR = 2.5$) from HFJER both issuing from GE nozzle with $M_d = 1.65$, $M_j = 1.36$, and scaled to $R/D = 100$	150
Figure 110. Spectra and OASPL comparison of heat simulated jet ($TTR = 3.0$) from PSU and heated jet ($TTR_{mix} = 3.0$) from HFJER both issuing from GE nozzle with $M_d = 1.5$, $M_j = 1.64$, and scaled to $R/D = 100$	151
Figure 111. Spectra comparison among single-flow heated jets ($TTR = 3.2$ and 2.5) and dual-flow heated jet ($TTR_{core} = 3.2$, $TTR_{mix} = 2.7$ with $St_{dual} = f D_j / U_{j mix}$) with $BPR = 0.3$ all from HFJER issuing from GE nozzle with $M_d = 1.5$, $M_j = 1.36$, and scaled to $R/D = 100$	152
Figure 112. Spectra comparison among heat simulated jets ($TTR = 3.0$ and 2.6) from PSU and heated jet ($TTR_{core} = 3.0$, $TTR_{mix} = 2.6$) from HFJER all issuing from GE nozzle with $M_d = 1.65$, $M_j = 1.36$, and scaled to $R/D = 100$	153
Figure 113. Spectra comparison between heat simulated jet ($TTR = 2.2$) from PSU and heated jet ($TTR = 2.25$) from NASA Langley Research Center LaRC) both issuing from CD nozzle with $M_d = 1.5$, $M_j = 1.5$, and $R/D = 100$	154
Figure 114. Spectra comparison of heated jets with HFJER in single-flow ($TTR = 2.2$) and dual-flow ($TTR_{mix} = 2.2$), and LaRC in single-flow jet ($TTR = 2.2$), all issuing from a CD nozzle with $M_d = 1.5$, $M_j = 1.5$, and scaled to $R/D = 100$	154
Figure 115. Spectra comparison among heat simulated jet ($TTR = 2.2$) from measured at $R/D = 280$ and heated jet ($TTR = 2.2$) from HFJER in single-flow measured at $R/D = 140$ both issuing from CD nozzle with $M_d = 1.5$, $M_j = 1.5$, and scaled $R/D = 100$	155
Figure 116. Spectra comparison of heat simulated jets ($M_j = 1.5$, $TTR = 3.2$) from PSU issuing from CD nozzles with $M_d = 1.5$, $D = 1.3$ and 2.5 cm respectively; scaled to $R/D = 100$. .	157
Figure 117. Spectral comparison of experiments measured at various locations from HFJER issuing from CD nozzle with $M_d = 1.5$, $M_j = 1.5$, $TTR_{core} = 2.6$, $TTR_{mix} = 2.2$; scaled to $R/D = 100$	158
Figure 118. Acoustic data acquired in the moderate scale laboratory experiments and the F15 ACTIVE flight test. The observation angle is given by 	159
Figure 119. Schematic of military-style nozzle. a) Baseline nozzle. b) Chevron nozzle. c) Definition of chevron parameters ⁴⁰	164
Figure 120. Acoustic spectra for a $M_d = 1.0$ nozzle and chevron nozzle, operating at $M_j = 1.5$, cold, scaled to $R/D = 100$	166

Figure 121. Schlieren visualization from the measurements operated at $M_j = 1.5$, cold jets respectively conducted with $M_d = 1.0$ nozzle. a) Baseline nozzle. b) Chevron nozzle measured at tip plane. c) Chevron nozzle measured at notch plane.	167
Figure 122. Schlieren images obtained with GE M_d 1.5 baseline nozzles respectively operated unheated with M_j at a) 1.3. b) 1.5. c) 1.7. d) 1.9.....	168
Figure 123. Schlieren images obtained with GE M_d 1.5 baseline nozzle and chevron nozzle operated at $M_j = 1.3$, cold.	168
Figure 124. Spectra comparison from the measurements conducted with GE M_d 1.5 baseline nozzle at Penn State and NASA GRC ⁴⁰ both operated under-expanded at M_j 1.64, TTR = 1.	169
Figure 125. Acoustic spectra and OASPL from the measurements conducted with GE M_d 1.5 baseline and chevron nozzles operated under-expanded at M_j 1.64, TTR = 1.....	170
Figure 126. Spectra comparison from the measurements conducted with GE M_d 1.5 baseline nozzle at Penn State and NASA GRC ⁴⁰ both operated under-expanded at M_j 1.64, TTR = 3.	171
Figure 127. Acoustic spectra and OASPL from the measurements conducted with GE M_d 1.5 baseline and chevron nozzles operated under-expanded at M_j 1.64, TTR = 3.....	172
Figure 128. Acoustic spectra and OASPL from the measurements conducted with GE M_d 1.65 baseline and chevron nozzles operated at $M_j = 1.47$, TTR = 1.	172
Figure 129. Acoustic measurements conducted with GE M_d 1.65 baseline and chevron nozzles operated at $M_j = 1.47$, TTR = 3.	173
Figure 130. Acoustic measurements conducted with GE M_d 1.65 baseline and chevron nozzles under forward flight simulation with $M_f = 0.3$ operated at same conditions as Fig. 13 by NASA GRC ³³ with a jet of exit diameter 5.07".	174
Figure 131. Schematic of the hypothesized flow separation respectively in the laminar boundary layer given by the smooth nozzle and turbulent boundary layer given by the rough nozzle in the small scale jets.	175
Figure 132. Acoustic spectra from the measurements conducted with GE M_d 1.65 baseline nozzles (rough and smooth) operated at $M_j = 1.47$ with a) TTR = 1. b) TTR = 3.	176
Figure 133. Acoustic spectra from the measurements conducted with GE M_d 1.65 baseline nozzles at NASA GRC ⁴³ and PSU with rough and smooth baseline nozzles operated at $M_j = 1.47$ with a) TTR = 1. b) TTR = 3.	176
Figure 135. Acoustic spectra and OASPL from the measurements conducted with GE M_d 1.65 baseline and chevron nozzles (both rough) operated at $M_j = 1.47$ with TTR = 3.	177
Figure 134. Acoustic spectra from the measurements conducted with GE M_d 1.65 chevron nozzles (rough and smooth) operated at $M_j = 1.47$ with a) TTR = 1. b) TTR = 3.	177

4. List of Acronyms

AAM:	Advanced Acoustic Model
AAPL:	Aero-Acoustic Propulsion Laboratory
AFCEE:	Air Force Center for Environmental Engineering
AFRL:	Air Force Research Laboratories
AIAA:	American Institute of Aeronautics and Astronautics
ANOPP:	Aircraft Noise Prediction Program
AR	Nozzle Area Ratio
ARP:	Aerospace Recommended Practice
BASEOPS:	Base Operations
BBSAN:	Broadband Shock-Associated Noise
CAD:	Computer Aided Design
CD:	Converging-Diverging
CFD:	Computational Fluid Dynamics
DES:	Detached Eddy Simulation
DNWG:	Defense Noise Working Group
DoD:	Department of Defense
DOE:	Design of Experiments
DRP:	Dispersion-Relation-Preserving
DTD	Discrete Time Derivation
FCLP:	Field Carrier Landing Practice
FWH:	Ffowcs Williams and Hawkings
GE:	General Electric
GRC:	Glenn Research Center (NASA)
HFJER:	Hot Flow Jet Experimental Rig (NASA GRC)
HSR:	High Speed Research
IBM:	Immersed Boundary Method
JSF:	Joint Strike Fighter
LaRC:	Langley Research Center (NASA)
LES:	Large Eddy Simulation
LIM:	Line Intersection Method
LSAF:	Low Speed Aeroacoustic Facility (Boeing)
MDOE:	Modern Design of Experiments
NASA:	National Aeronautics and Space Administration
NATR:	Nozzle Acoustic Test Rig
NOISEMAP:	Integrated Noise Model (Wyle Laboratories)
NPR	Nozzle Pressure Ratio
NTR	Nozzle Temperature Ratio
OASPL:	Overall Sound Pressure Level
OD:	Optical Deflectometry
PSD:	Power Spectral Density
PSU:	Penn State University
RANS:	Reynolds-Averaged Navier-Stokes
RMS:	Root Mean Square

RNM:	Rotorcraft Noise Model (RNM)
SAE:	Society of Automotive Engineers
SERDP:	Strategic Environmental Research and Development Program
SHJAR:	Small Hot Jet Acoustic Rig
SLA	Stereo Lithography
SPL:	Sound Pressure Level
TTR:	Total Temperature Ratio
TKE	Turbulent Kinetic Energy
UAC:	User Advisory Committee
URANS:	Unsteady RANS

5. Keywords

Adjoint design

Aeroacoustics

Jet noise

Mach wave radiation

Military aircraft

Noise reduction

Shock-associated noise

Turbulence

6. Acknowledgements

The investigators and authors would like to extend their appreciation and acknowledge to the SERDP organization for funding this research program, and would also like to thank the following individuals who contributed to the success of this project:

- Dr. Yongle Du, Dr. Jeremy Veltin, Dr. Ching-Wen Kuo, Ms. Nidhi Sikarwar, Mr. Ben Day and Mr. Adam Goss, who assisted with the experiments and numerical simulations at Penn State in the course of their graduate studies.
- Prof. Dimitri Papamoschou at the University of California Irvine for discussions and assistance with the helium/air mixture jet experiments.
- Dr. John Spyropoulos and Mr. Allan Aubert at NAVAIR, Patuxent River, for their interest in the project and valuable discussions on military fighter aircraft.

7. Abstract

This report describes a combined experimental and computational study of the generation and radiation of jet noise from high performance military fighter aircraft. An emphasis is on the methodology for scaling measurements at small and moderate scale to full scale aircraft engines. In addition, promising concepts for jet noise reduction are explored at small and moderate scale. Numerical simulations are performed to support the experiments and provide additional insight into the noise generation and radiation process. Noise and flow measurements are performed in the Anechoic Jet Noise Research Facility at Penn State University and the Aero-Acoustic Propulsion Laboratory at the NASA Glenn Research Center. Designs for the baseline nozzles are developed by General Electric Aviation. In addition, a computational study of the effect of chevrons on the jet flow is conducted by General Electric and used to design chevron nozzles that are then studied experimentally by NASA and Penn State. The flow and noise experiments conducted at small scale at Penn State use mixtures of helium and air to simulate the effects of jet heating. This enables the jet nozzles to be constructed using rapid prototyping, which reduces the model costs and construction time. The results of the noise measurements are compared with moderate scale experiments using actual flow heating at NASA Glenn. Very good agreement is obtained between the baseline nozzle measurements at both facilities. This establishes both the noise scaling methodology as well as the validity of using gas mixtures to simulate the effects of jet heating. It is also shown how scaling is not always successful when noise reduction devices, such as chevrons, are studied. The experiments at different scales also indicate that care must be taken in establishing the location of the far field, especially for very high speed jets. A methodology is developed to enable measurements at different distances and observer angles to be compared. Numerical simulations are performed for the same jet geometries and operating conditions as in the experiments. The calculations use a multiblock structured grid finite-difference approach. A Detached Eddy Simulation turbulence model is used with the turbulence model removed in the jet external flow. Realistic nozzle geometries are included in the simulations. This enables the flow inside the nozzle to be examined. Comparisons between the predicted and measured flow and noise fields show good agreement. In order to simulate the effects of small geometric features, such as chevrons, an Immersed Boundary Method is implemented. An adjoint design method is also developed and implemented to determine the nozzle contours for minimum shock strength. Finally, the results of the experiments and simulations were used to develop source noise (level) spheres. These were transferred to project partner for use in development of the Advanced Acoustic Model. This model can be used to assess the impact of aircraft operations on communities surrounding military bases. An example of the use of the model to examine the effect of the addition of chevrons on noise contours is given.

8. Objective

The objectives of the project described in this report are:

- To identify and test promising noise reduction concepts for military aircraft engines, in low cost, scale-model experiments.
- To develop a methodology for using data obtained from testing at small and moderate-scale, supported by computations, to reliably predict full scale engine noise.
- To develop a constrained optimization design methods that minimizes shock-associated noise through nozzle internal shaping.
- To assess installation effects on high performance military aircraft engine noise.
- To gain a fundamental understanding of the source mechanisms in military aircraft engines.
- To enhance an existing community noise prediction model.

9. Background

The implementation and testing of noise reduction concepts at full scale is very expensive. This report describes the degree to which scale model testing, including forward flight, with support from numerical computations, can be used to predict the jet noise of full scale military aircraft in flight. Additionally, the development of alternative nozzle designs for noise reduction is included.

The technical approach is centered on jet noise experiments at small and moderate scale. These experiments are supplemented by a complementary computational effort. The experiments include noise measurements of baseline nozzle geometries typical of military aircraft engines. This, in combination with the computations, provides a fundamental understanding of the engine's jet noise sources. A major objective of the project has been to develop a methodology for using data obtained from testing at small and moderate scale, supported by computations, to reliably predict full scale engine noise. A critical component in this process is the inclusion of forward flight effects. Experiments at small and moderate scale are also performed on nozzles with one proven noise reduction concept: nozzle trailing edge chevrons. This establishes the viability (and the limits) of scaling acoustic results from small to moderate scale when the nozzles have such detailed modifications.

Experiments at small scale are used to test additional promising noise reduction concepts. Tests on nozzles with beveled exit planes are included. In addition, to reduce the shock-associated noise, nozzle shapes will be designed to minimize the shock strength over a wide range of operating conditions rather than a single design point.

The following section provides a brief description of high speed jet noise generation mechanisms. This provides the background to the problem. The following section describes the several tasks and results of the experiments and numerical simulations.

High Speed Jet Noise Generation Mechanisms

Engines in military fighter aircraft have very low bypass ratios and their noise is dominated by the core jet exhaust. For example, the General Electric F414-400, which powers the F/A 18 E/F Super Hornets, has a bypass ratio of 0.3, with the bypass flow being used mainly for cooling the primary jet nozzle. Such a low bypass ratio can be contrasted with a typical high bypass ratio of 9:1 found on the GE90. Such high bypass ratio turbofan engines generate thrust by moving a large volume of air in the fan stream at a relatively low velocity. Not only is this configuration much quieter than low bypass ratio turbofans, it is also more fuel efficient. However, military aircraft engines, which must be compatible with the aircraft size and shape and also permit supersonic flight, are forced to have a low bypass ratio. In addition, as noted below, the nozzles are usually operated at off-design conditions. Then, at take-off conditions, the jet noise consists of two primary components: turbulent mixing noise and broadband shock-associated noise. Turbulent mixing noise is generated by the unsteady turbulent motions in the jet plume as the high speed jet exhaust mixes with the ambient air. At subsonic jet exit Mach numbers the noise is associated with the fine-scale details of the turbulence. However, at supersonic conditions, the

turbulent eddies move supersonically with respect to the ambient air and a very strong, highly directional, noise radiation (Mach wave radiation) occurs.

Because of constraints on the internal complexity of the military engine's nozzle, the jet is almost never ideally expanded. That is, the pressure at the jet exit does not equal that of the ambient air. This imbalance results in shock cell structures in the jet plume. These are regions of alternating high pressure and temperature with regions of lower temperature and pressure. These regions are separated by shocks and expansions that form an early periodic cell structure. Broadband shock-associated noise is generated by the interaction in the jet shear layer of the turbulent eddies and this shock-cell structure. The intensity of broadband shock-associated noise is nearly independent of observer angle, though the spectral peak moves to lower frequencies as the observer moves towards the jet inlet. Since the jet mixing noise is highly directional, being concentrated in the jet downstream arc, broadband shock-associated noise is usually the dominant noise component in the forward arc. However, at high power settings the total noise power radiated is dominated by the jet mixing noise.

A common occurrence in experiments with shock containing (imperfectly expanded) supersonic jets is an intense resonant acoustic tone called "screech." Such a phenomenon is common with laboratory unheated jets, but not often found in full scale jet engine exhaust jets. Besides the heat present, turbulence shed from the upstream turbomachinery is an influencing factor in the absence of screech (at full scale). When appropriate this screech is suppressed in laboratory jets with the presence of small disturbance tabs that have an almost immeasurable effect on the jet flow. At operating conditions typical of military fighter aircraft at take-off, the character of the jet mixing noise changes and is said to "crackle." Crackle, as the name suggests, is a broadband noise phenomenon that is characterized by sudden sharp peaks – like the crackling sound made of a piece of paper when it is crumpled, except it is far more intense. This makes the sound far more annoying than a noise at the same intensity but with a smoother, Gaussian behavior.

Combustion noise in a jet engine is produced by the combustion process itself and also by the passage of the hot combustion products through the turbines and jet exhaust. These acoustic sources make up what is generally called "core" noise. Core noise is a function of the temperature, pressure, the physical geometry of the hot gas path through the engine, and the heat release distribution along this path. Core noise can often be noticed at lower throttle settings when jet noise levels are reduced. It is usually characterized by a broadband spectrum that peaks at a frequency of only a few hundred Hertz. This is the frequency of the peak in the jet mixing noise in the peak noise direction for typical military aircraft engines, so core noise is expected to be negligible compared to the jet exhaust noise sources.

Other upstream influences that could affect the engine noise are the presence of a mean velocity deficit, generated by the wake of the turbine center body, and the influence of the cooling flow that is introduced on the F414-400 engine through a fan duct liner¹. This results in a very non-uniform mean velocity profile at the jet exit. In testing under the High Speed Research (HSR) program it was determined that there was a difference in absolute noise level when a nozzle was fed with a non-uniform upstream mean flow, but there was no change in the noise reduction delta achieved by noise reduction devices.

The next sections describe the experiments and numerical simulations conducted under the research program. They are organized according to their task number.

10. Tasks and Results

10.1. Task 1: Nozzle Design and Configuration Control

Task 1.1 Provide Baseline Nozzle Designs

GE completed Task 1.1 by providing PSU and NASA Glenn and Langley Research Centers existing scale model hardware designs of a typical converging-diverging single stream nozzle with three different area ratios, the overall assembly drawing is shown in Figure 1. These scale models had been tested previously at GE Aviation and data can be compared to the small and moderate scale data to be acquired by PSU and NASA, respectively. GE also completed a static engine acoustic test with an exhaust system similar to the scale model hardware and this data can also be used to evaluate scaling between small, moderate, and full-scale acoustic data.

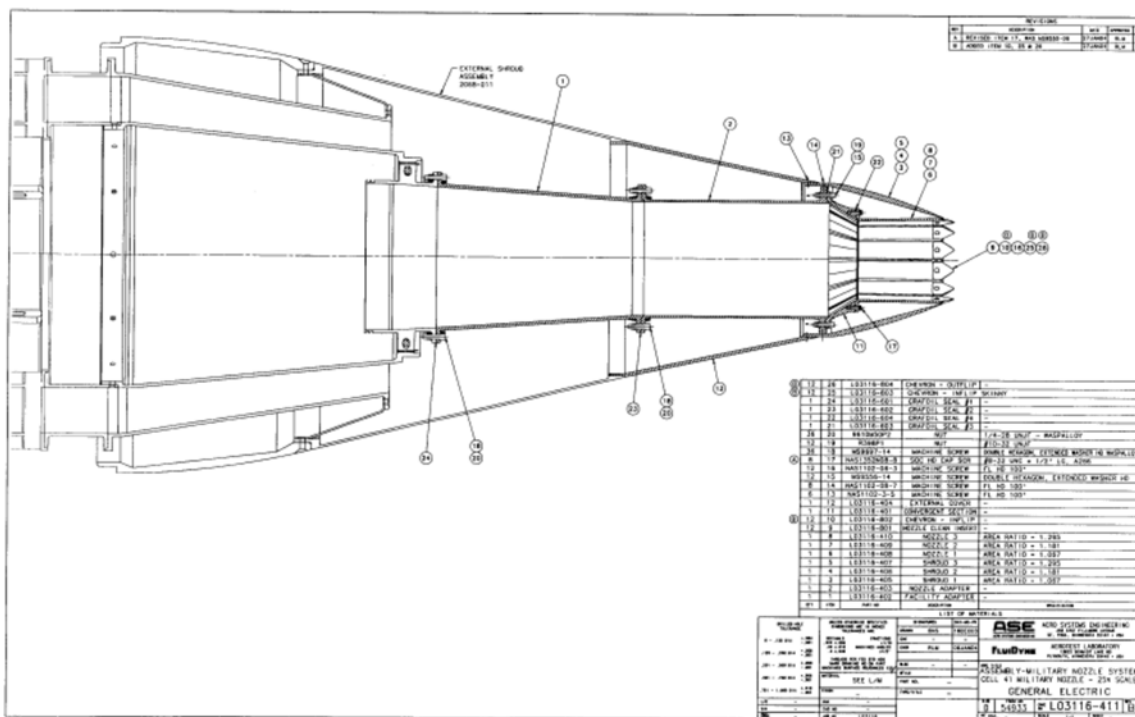


Figure 1 Assembly drawing containing nozzle drawings provided to SERDP team.

GE arranged a loan of the scale model hardware system (shown in Figure 1) built under another government program to NASA to be available for testing. This is the model the designs are based on from Task 1.1 above.

Task 1.2 Conduct CFD Studies of Candidate Chevron Nozzles

GE conducted a RANS (Reynolds Averaged Navier Stokes) based Design of Experiments (DOE) study of candidate chevron designs for future testing in this program. A baseline, no chevron configuration, was run, as well as a twelve chevron designs with different length and penetration parameters. Table 1 shows the parameters that were varied in the CFD (Computational Fluid Dynamics) DOE study. Figure 2 shows a schematic describing the geometric parameters defining the chevrons. The results of this study were compared to look at flow field characteristics and making qualitative assessments of their relative noise characteristics.

Table 1. Chevron CFD DOE parameters

Config	Length	Penetration
0	4.0	0.8
1	4.0	0.4
2	4.0	1.2
3	4.0	1.6
4	4.5	0.4
5	4.5	0.8
6	4.5	1.2
7	4.5	1.6
8	5.0	0.4
9	5.0	0.8
10	5.0	1.2
11	5.0	1.6

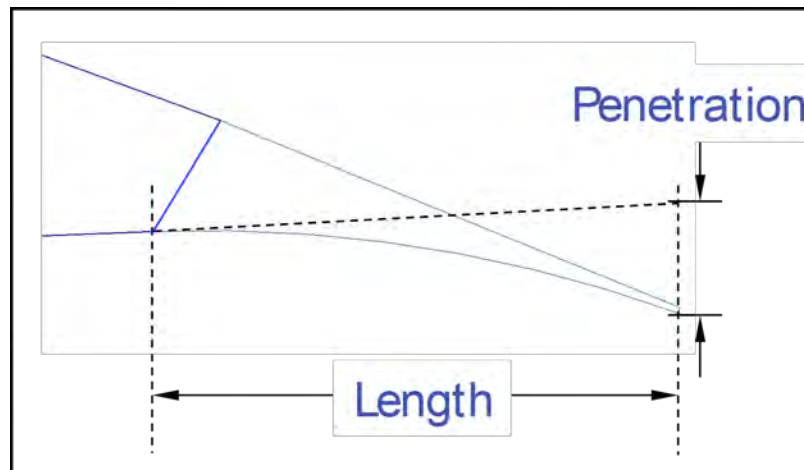


Figure 2. Description of geometric parameters.

The CFD results are compared for different flow quantities, including total temperature, Mach number, and turbulent kinetic energy (TKE) and provide a qualitative link to acoustics through the amount and rate of mixing. This is shown by the length of the potential core, the level and location of the TKE, and the shock strength through Mach number. Figure 3 shows the

total temperature contours through the tip of the chevron for all of the configurations. Differences are subtle for the total temperature.

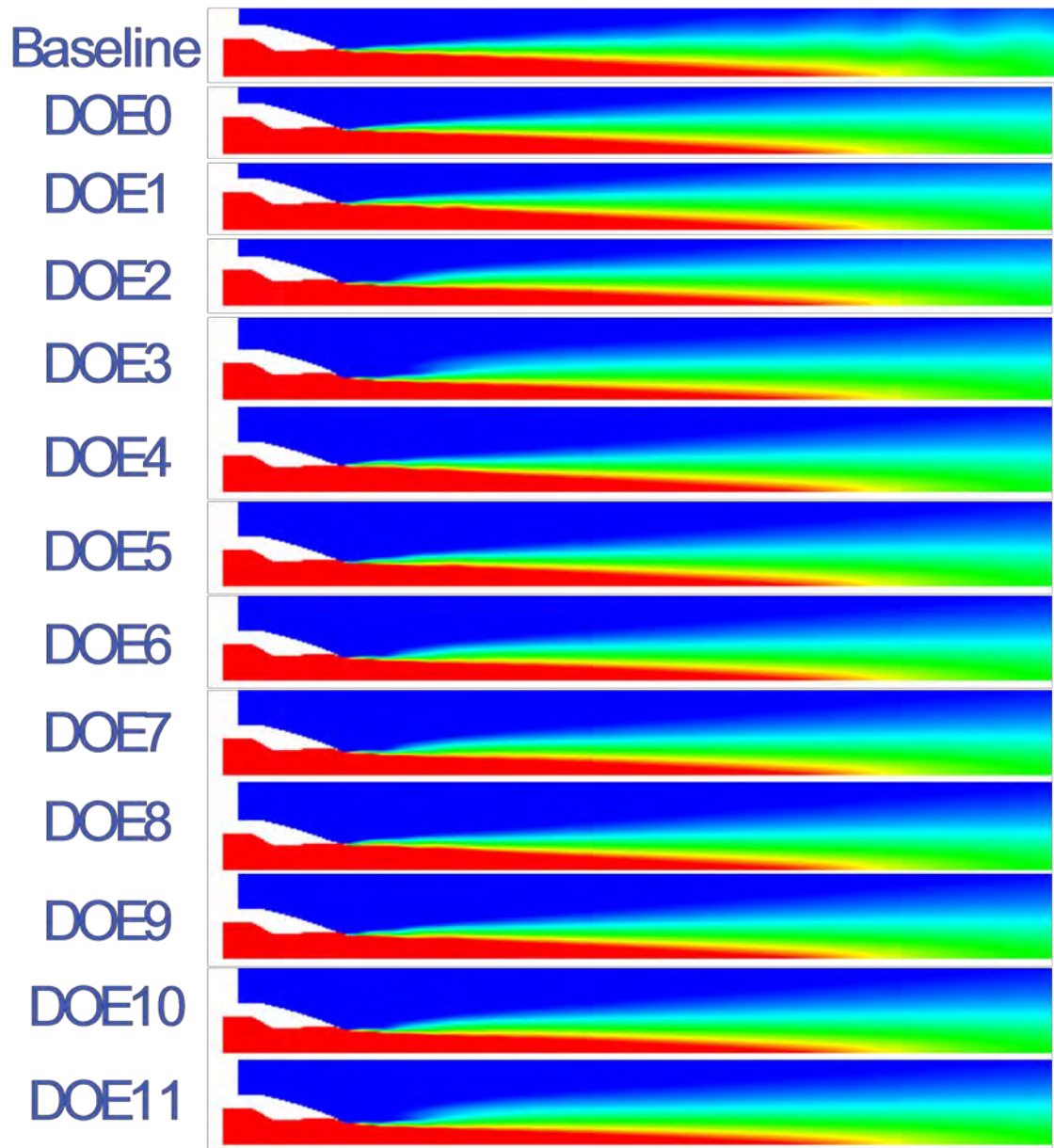


Figure 3 Total Temperature CFD results on a plane through the tip of the chevron.

Figure 4 shows the TKE contours through the tip of the chevron for all of the configurations. There is much more differentiation seen among the various chevron designs in these comparisons. Different chevrons can have drastically different effects on the TKE levels its distribution.

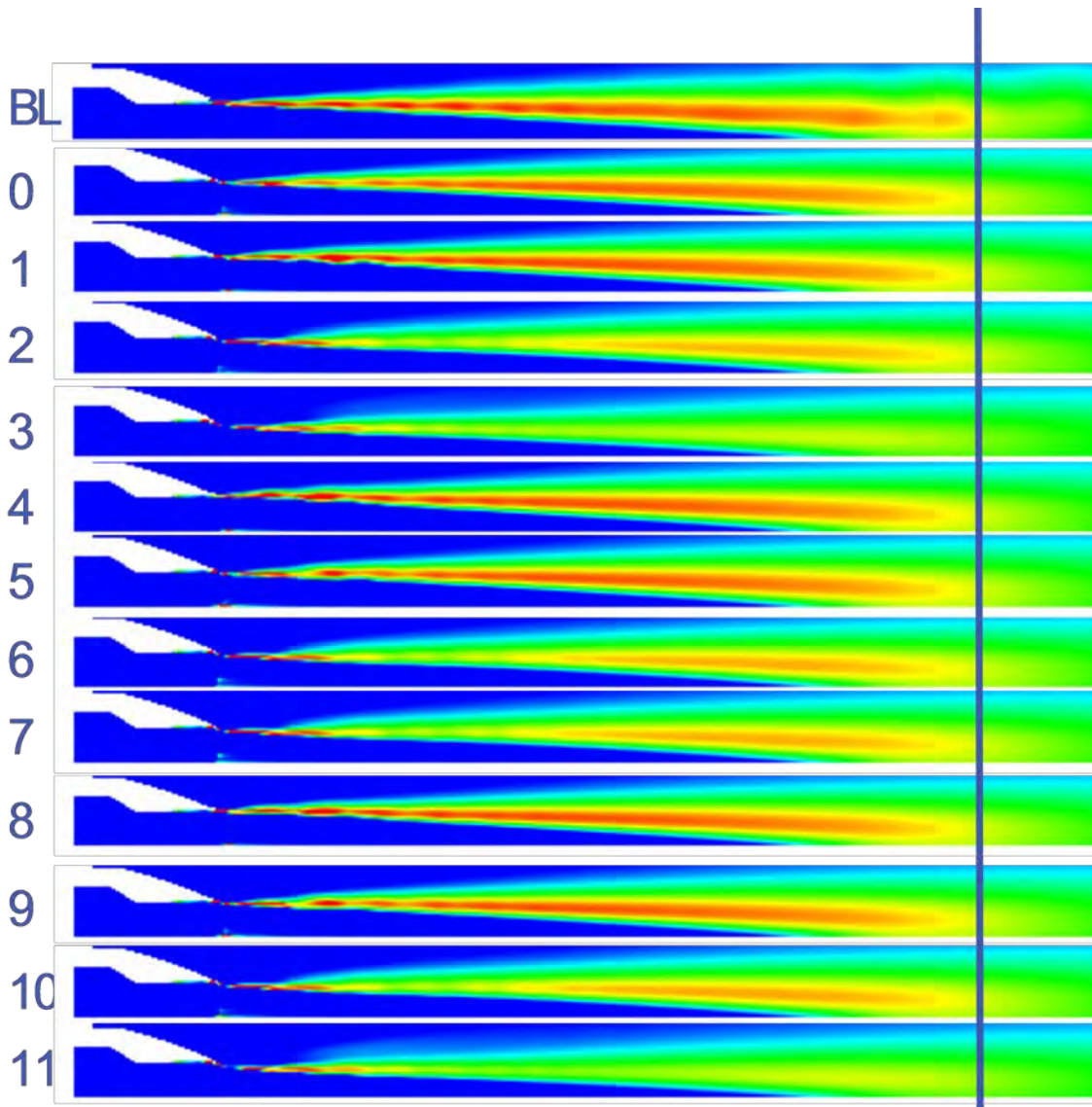


Figure 4 TKE CFD results through the tip of the chevron.

Figure 5 shows total temperature contours through a cross-section of the jet plume at an axial location at $x/D = 0.5$. This comparison shows how the different chevron designs can have a large effect on the shape of the mixing region in the jet plume. Different shapes can provide insight into the level of mixing achieved with different designs.

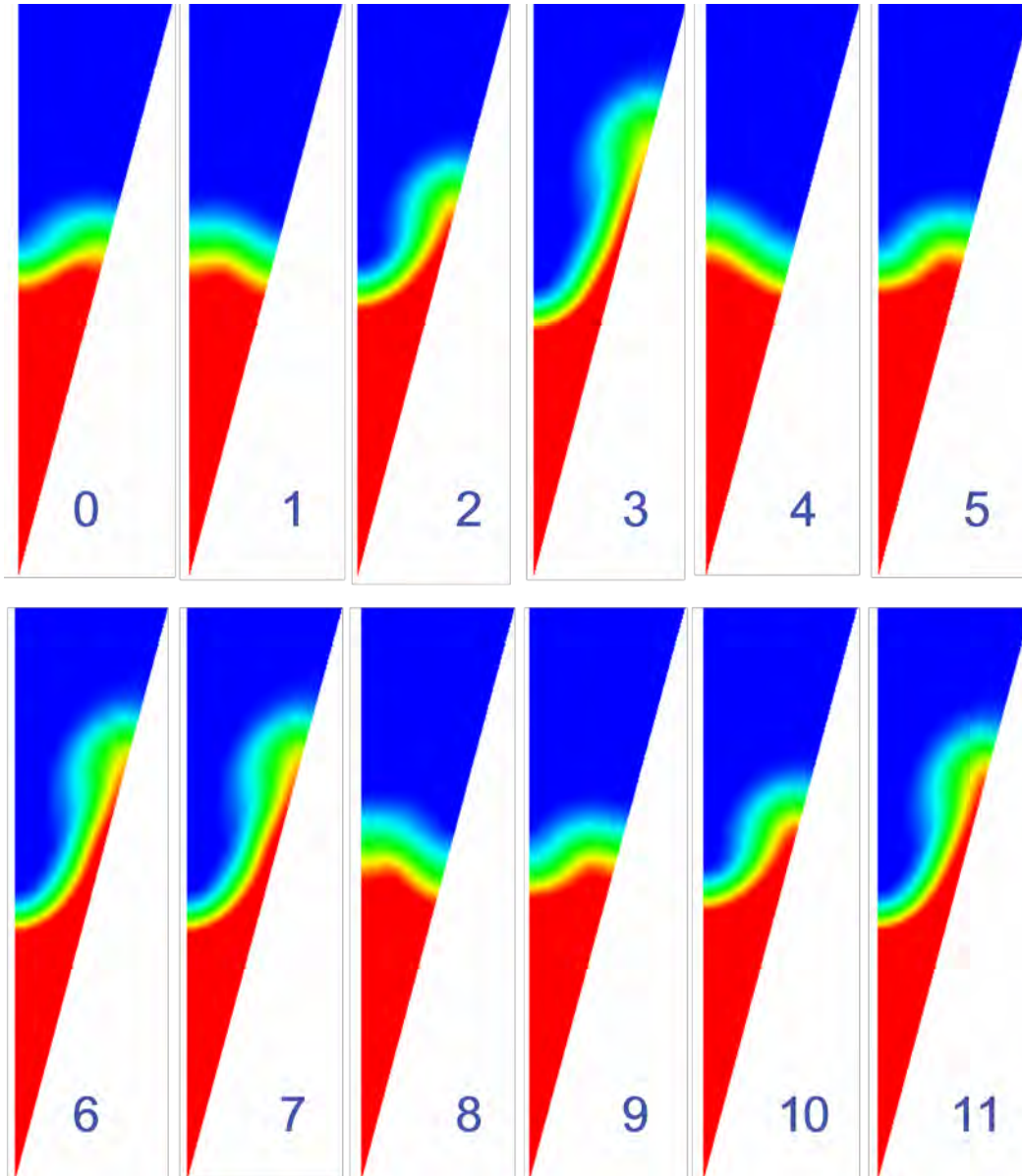


Figure 5 Total temperature contours through the cross-section of the plume at $x/D=0.5$.

Figure 6 shows TKE contours through three cross-sectional cuts through the jet plume for two of the chevron configurations. This shows how different chevron geometries affect the details of the jet plume and how these changes propagate axially.

This CFD study helped PSU select chevron designs for their subsequent testing.

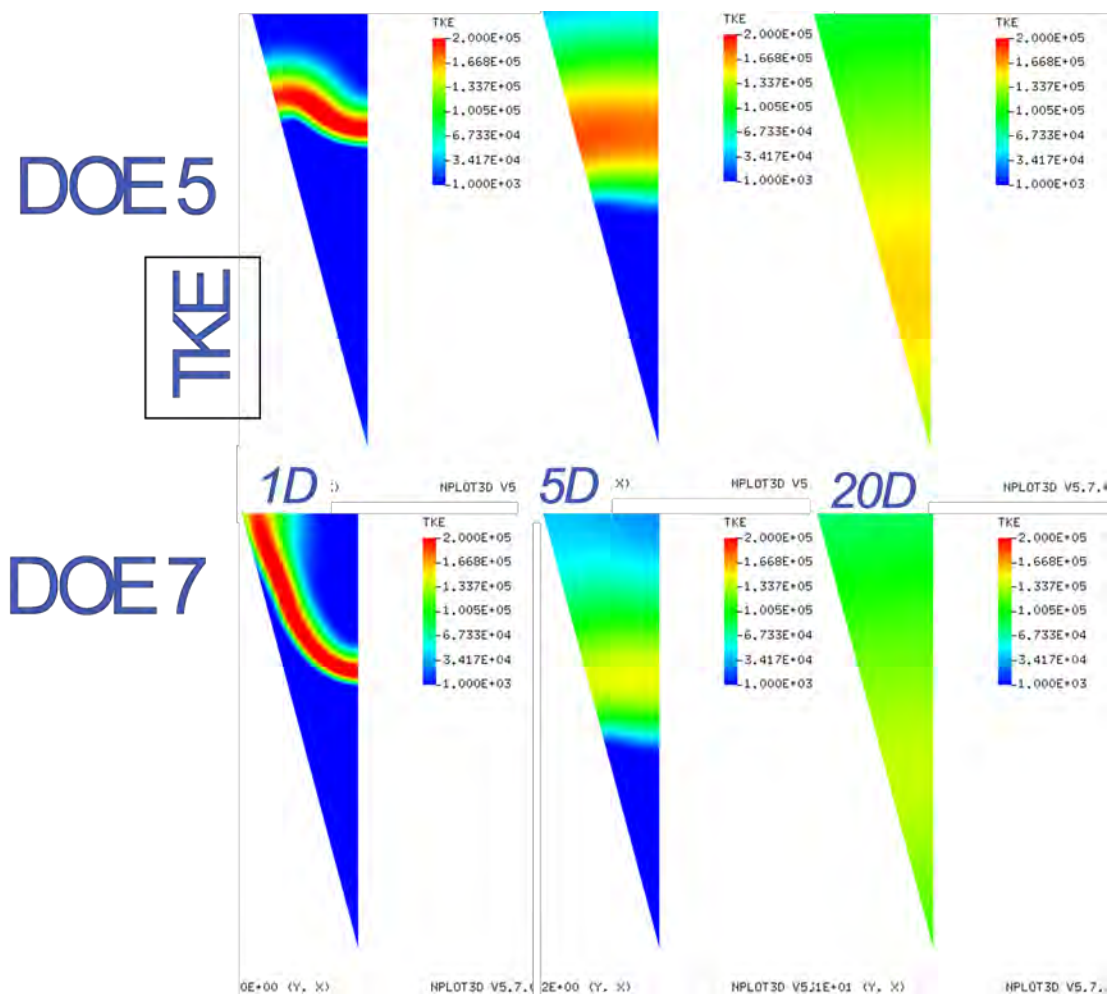


Figure 6 TKE contours through a cross-section of the plume for two chevron configurations, at three axial locations.

Data Comparison between GE and NASA

GE arranged to lend a scale model exhaust system acquired under a separate government contract to NASA so the same model could be tested in two facilities. This model was discussed in the first section. Comparisons were made between the two facilities and a typical comparison will be shown here. The GE data was acquired in Cell 41, GE Aviation's anechoic jet noise facility, with a far field microphone array approximately 22 ft from the nozzle. The NASA data

was acquired at the Nozzle Acoustic Test Rig (NATR) with an upper array mounted from the ceiling of the Aero-Acoustic Propulsion Laboratory (AAPL) facility and a pole mounted array closer to the nozzle that simulates the microphone array at NASA Langley Research Center's facility. The data shown is model scale, on a 40 ft arc and has been corrected to a standard day. Figure 7 shows the Overall Sound Pressure Level (OASPL) directivity for a nozzle pressure ratio

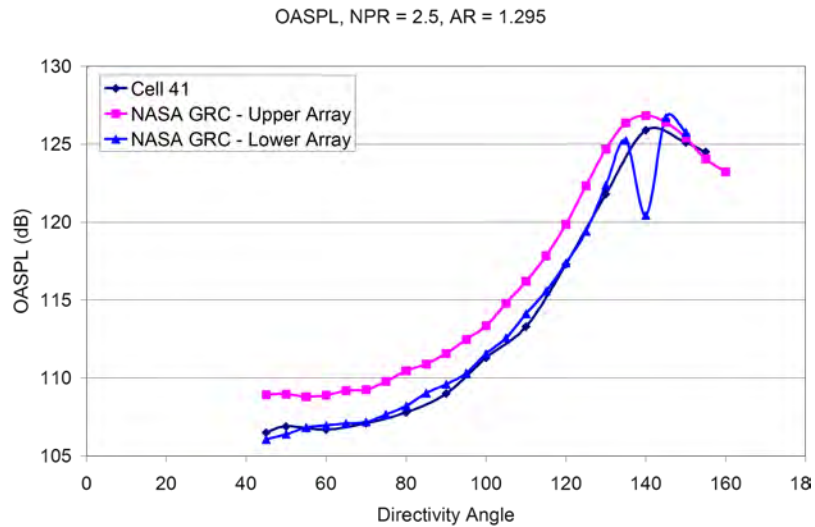


Figure 7. Scale Model Data Comparison, OASPL.

(NPR) of 2.5 and a nozzle area ratio (AR) of 1.295. The GE data and lower array NASA data compare fairly well. NASA's upper array is moderately higher over most angles.

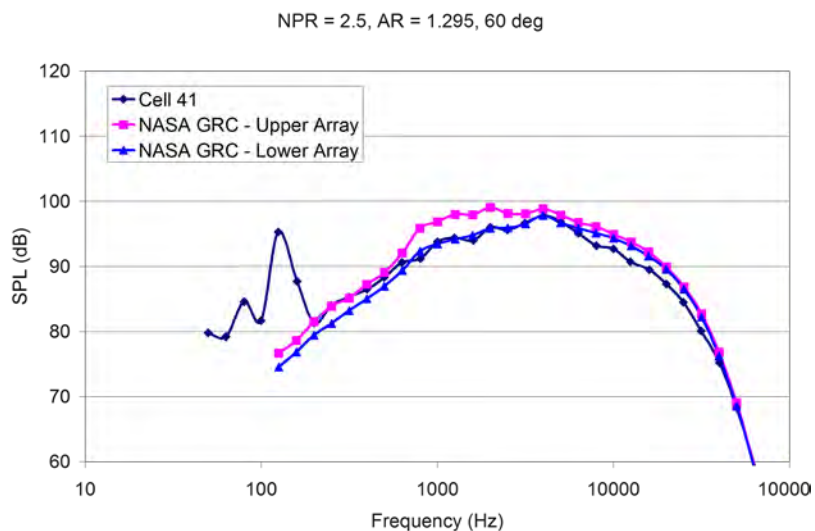


Figure 8. Scale Model Data Comparison, SPL at 60 deg.

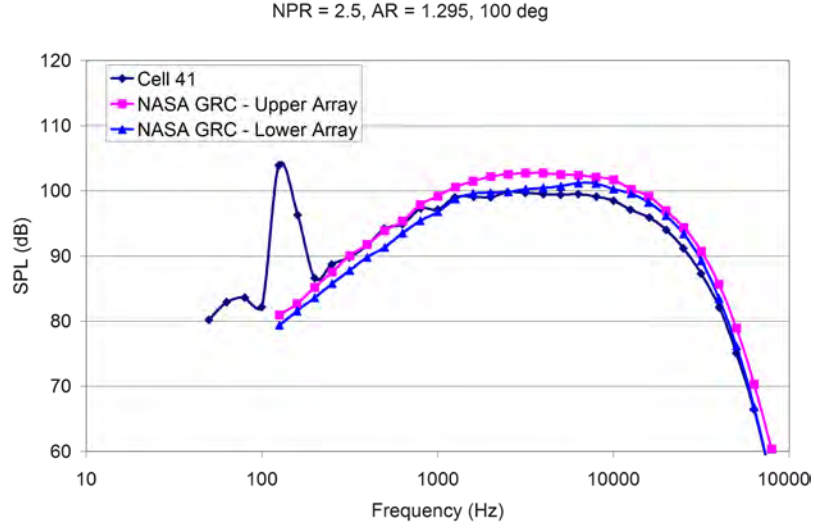


Figure 9 Scale Model Data Comparison, SPL at 100 deg.

Figure 8 through Figure 10 show the SPL spectra comparisons at 60, 100 and 150 degrees to the jet inlet, respectively. In these figures the peak in the low frequencies from the Cell 41 data is from the combustor in the facility. Since this type of data is typically scaled to full scale geometry these frequencies are not important. Again, the data compares fairly well over most of the frequency range. In general the GE and NASA lower array compare more closely, likely because their distances from the nozzle to the microphones is more similar.

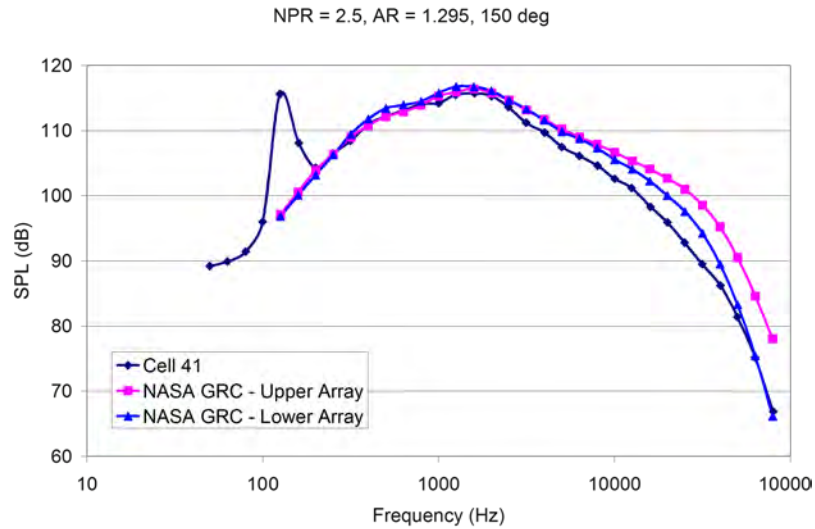


Figure 10 Scale Model Data Comparison, SPL at 150 deg.

Scale Model to Engine Data Comparison

GE conducted static engine acoustic testing as part of another government program with similar nozzle geometry and made some comparisons with the data to investigate scaling issues. The nozzle conditions were not exactly the same between the engine and scale model test due to temperature limitations in the scale model test facility. The pressure ratios were very close and just below a dry military power level (max dry power setting). Three temperatures are shown for the scale model data to provide the noise sensitivity to temperature. The data is for static conditions and are all extrapolated to approximately a 150 ft arc and corrected to a standard day. Figure 11 shows the SPL at 60 deg, measured from the inlet of the engine, for the engine and scale model data at three temperature levels. The abscissa is Strouhal number, which is the frequency normalized by the nozzle diameter and exhaust velocity. Throughout most of the frequency range the comparison is very good. The overall shape of the spectra is captured in the

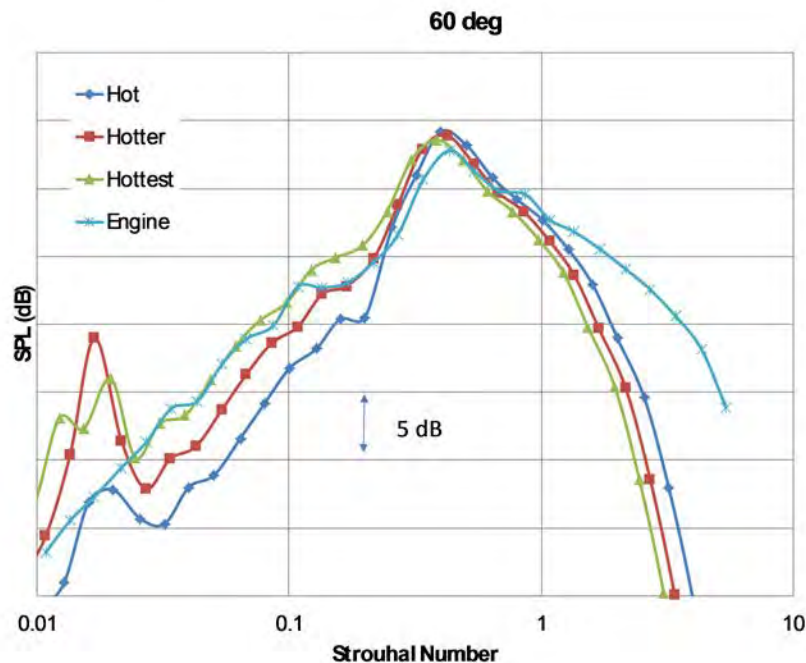


Figure 11 Comparison of engine and scale model data, SPL at 60 deg.

scale model data, including the peak frequency and low frequency noise levels. The broadband shock associated noise is the dominant feature at this angle and is captured well. The engine data does not roll off as fast as the scale model data at high frequencies. This could be due to a number of reasons, including the difference in turbulence exiting the nozzle due to the engine, or other noise sources from the engine.

Figure 12 shows the same comparisons at 90 degrees, to the side of the nozzle exit. Again, the comparison is fairly good. The scale model data again captures the broadband shock associated noise peak fairly well, but continues to roll off faster at the higher frequencies.

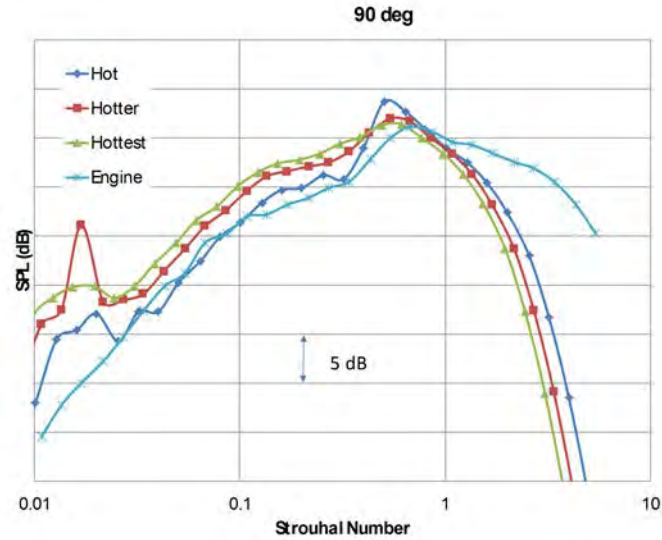


Figure 12. Comparison of engine and scale model data, SPL at 90 deg.

Figure 13 and Figure 14 show the SPL spectra at two downstream or aft angles, 130 and 150, respectively. At these angles the noise spectra do not show any sign of shock noise and contain jet noise. The spectral shapes are fairly close, although there is a small shift in the peak frequency, and the high frequencies continue to differ.

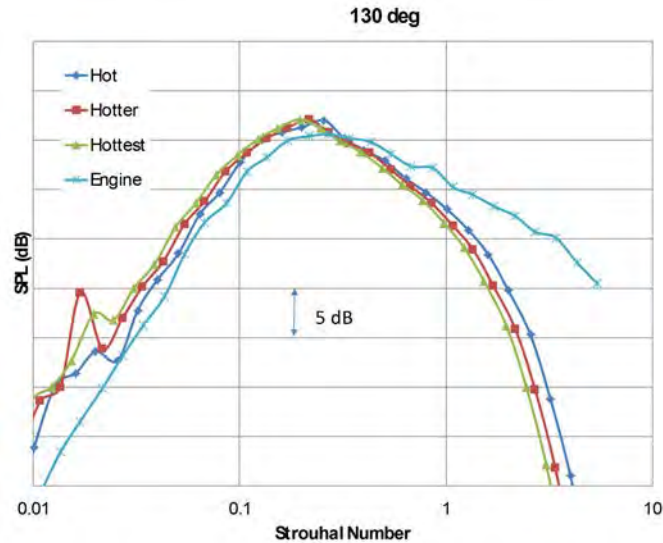


Figure 13. Comparison of engine and model scale data, SPL at 130 deg.

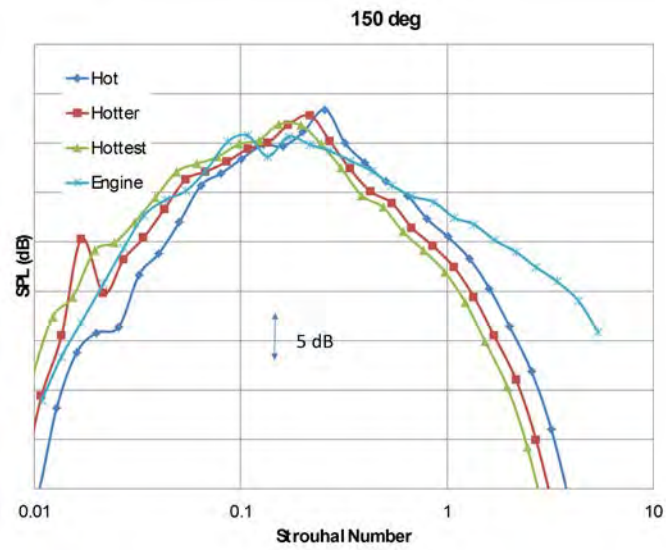


Figure 14. Comparison of engine and model scale data, SPL at 150 deg.

10.2. Task 2. Small Scale Experiments

This section describes activities and results related to the following tasks:

2.1 Baseline Chevron Nozzles and Noise Measurements, 2.4 Baseline Round Jet Noise Measurements: Unheated and 2.5 Baseline Round Jet Noise Measurements: Heated

Jet noise production is well known to be of a distributed nature along the jet, with high frequency noise components radiating from locations close to the nozzle exit and low frequency noise being produced farther downstream, beyond the end of the potential core. Such a distributed source implies that measurements need to be made at a significant distance from the source in order to be in the true geometric (acoustic) far field. The current Task presents measurements of fully expanded jet Mach number $M_j = 1.5$ jets operating with cold air and heat simulated at total temperature ratio $TTR = 2.2$ made at various positions in the acoustic field, some short of the minimum distance required to be in the true geometric far field. A close look is taken at the details of the noise generation region in order to better understand the mismatch between spectra measured at various acoustic field radial locations. A processing methodology is then presented to correct for near-field effects and efficiently compare near and far field spectra with unprecedented accuracy. This technique is then further used to clarify the nonlinear propagation effects that can be observed at high frequencies in high speed jet noise.

Experimental Facilities, Set-Up, and Procedure

Facility and instrumentation descriptions

The experiments presented in this part of the study were conducted in The Pennsylvania State University high speed small scale jet noise facility shown in Figure 15. In order to produce acoustic measurements that can be directly compared to aircraft engine measurements, the temperature of the jet is an important parameter that needs to be replicated. A hotter jet results in

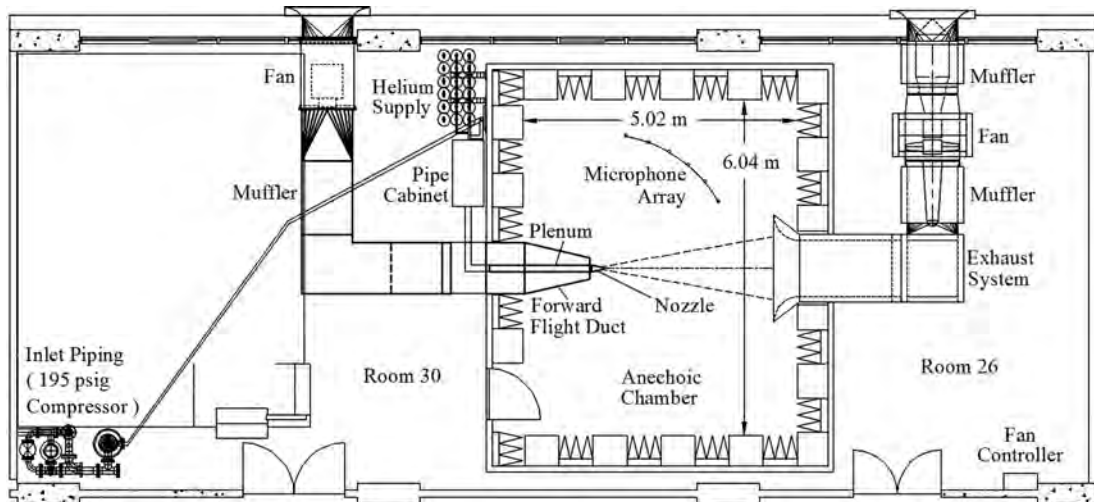


Figure 15. The Pennsylvania State University high speed jet noise facility.

different acoustic characteristics, due to the increase in jet exit velocity and decrease in jet density. Actually heating the air that exhausts through the nozzles is done in facilities such as the one used at the NASA Glenn Research Center². However, it requires an extensive amount of power and infrastructure, raising the overall operating costs of the facility. In order to simulate the flow and acoustic properties of a hot jet, Doty and McLaughlin³ and Papamoschou⁴ have shown the detailed methodology of heated jet simulation via a mixture of helium and air. Recent careful comparisons⁵ with measurements performed in other facilities have shown very good agreement when matching the acoustic velocity of the mixture jet to that of a heated jet following a procedure developed by Doty and McLaughlin³ over 10 years ago and refined ever since.

The anechoic chamber is a 5.02 X 6.04 X 2.8 m room covered with fiberglass wedges and with an approximate cut-off frequency of 250 Hz. An exhaust fan is installed in the downstream direction of the plenum collects the jet exhaust and prevents possible uncontrolled helium accumulation in the anechoic chamber. Acoustic measurements are typically performed using six microphones, hanging from a boom that extends from the plenum stand, as can be seen in Figure 16. The microphone array can freely rotate around a point located at the center of the nozzle exit plane. The microphones are positioned at a grazing incidence to the jet and equally spaced by 10



Figure 16. The Pennsylvania State University high speed jet noise facility.

degrees. The physical distance from each microphone to the nozzle exit is approximately 180 cm (70 in). This distance is sufficient to ensure the microphones are in the far field when testing nozzles up to 1.8 cm (0.7 in) in diameter. The microphones used are 3.2 mm (1/8 in) pressure-field microphones, type 4138 from *Brüel and Kjaer (B&K)*, and type 40DP from *GRAS*. Apart from this fixed 180 cm arc, the microphones can be rearranged with ground supported struts to other desired locations inside the anechoic chamber. Such an arrangement was used in the current study as shown in Figure 17 where each dot represents the pre-selected non-dimensional locations for microphones. The detailed microphone setup is described later in this section.

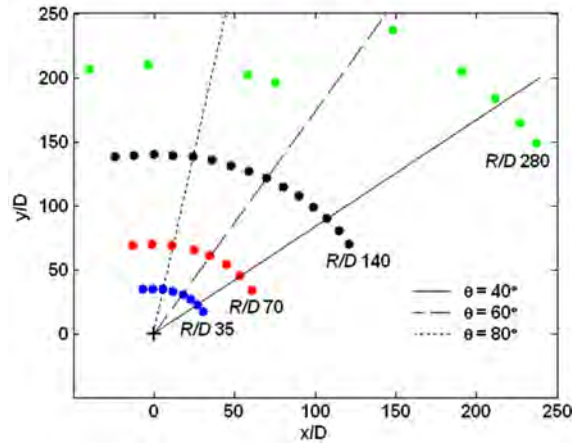


Figure 17. Schematic of non-dimensional measured locations of microphones.

Data acquisition

A flow chart of the data acquisition process is shown in Figure 18. The microphone calibration is performed with a *B&K* acoustic calibrator, model 4231, and the microphone calibration constants are recorded to provide the conversion from the measured voltages to the equivalent pressure. The analog time-domain signals from the microphones are routed through a *Nexus*, *B&K* signal conditioner or a *GRAS* model 12AN power module and then amplified and filtered

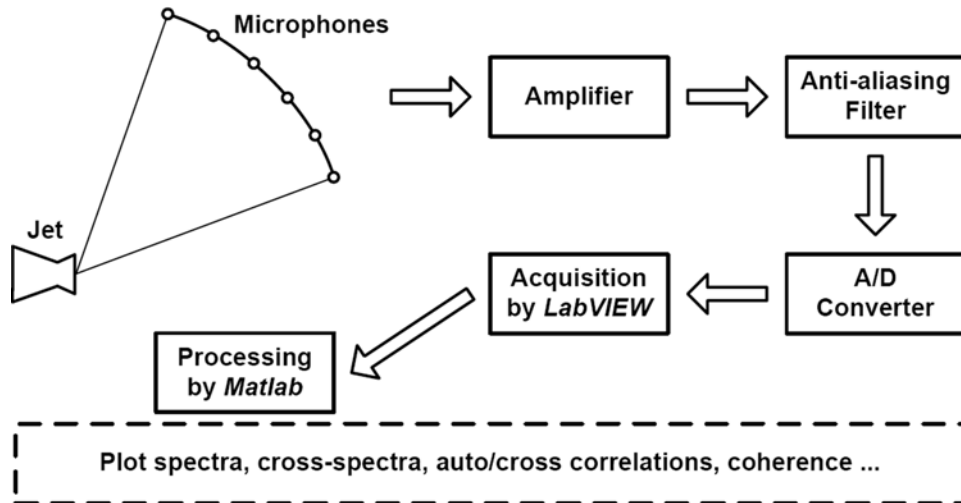


Figure 18. Flow chart of the data acquisition process.

for anti-aliasing, thus enabling their accurate digital conversion in the following acquisition. A high-pass filter is also set to 500 Hz, removing any undesirable low frequency noise that could contaminate the data. A PCI-6123 *National Instruments* DAQ board acquires the time domain data which are then stored in binary files. The sampling rate is set at 300 kHz and 102,400 to 409,600 data point are collected, the reduced dataset being used for helium-air mixture jets in order to reduce the amount of helium used during an experiment. The raw data are then fed into

Matlab for data processing. The raw data are split into 1024 or 4096 points segments and a Hanning window function is applied with 50 percent overlap between each window. The Fast Fourier Transform is calculated in each window and an averaged value is calculated from the 199 segments. This yields the power spectral density (*PSD*) which is then converted to a decibel (dB) scale using a reference pressure of $20 \mu Pa$. Three corrections are then applied to the raw sound pressure level (*SPL*) to compute the lossless *SPL* as explained in Kuo, Veltin and McLaughlin⁶. The corrections, all preceded by Δ adjust the final data for spectral non-uniformities in microphone actuator response ΔC_{act} , microphone free field response ΔC_{ff} , and atmospheric attenuation ΔC_{atm} , respectively. Finally, the spectra are non-dimensionalized to *SPL* per Strouhal number. Equation (1) summarizes the different steps that lead to the *SPL* per unit Strouhal number.

$$SPL(St) = SPL_{raw}(Hz) - \underbrace{\Delta C_{act}(Hz) - \Delta C_{ff}(Hz)}_{\text{Microphone Corrections}} + \underbrace{\Delta C_{atm}(Hz)}_{\text{Atmospheric Correction}} + \underbrace{10 \times \log_{10} f_c}_{\text{Strouhal Number Scaling}} \quad (1)$$

The Strouhal number is defined as $St = f / f_c$, with f_c the characteristic frequency of the jet defined by $f_c = U_j / D_j$, where U_j is the mean jet velocity, and D_j is the fully expanded diameter of the jet plume.

From the *SPL*, given at intervals of Δf , the *OASPL* is calculated from the following formula:

$$OASPL = 10 \log_{10} \left[\Delta Hz \sum 10^{\left(\frac{SPL(Hz)}{10} \right)} \right] = 10 \log_{10} \left[\Delta St \sum 10^{\left(\frac{SPL(St)}{10} \right)} \right] \quad (2)$$

Experimental Overview

This Task reports on experiments and a data processing methodology for acoustic measurements performed on high speed jets. Such laboratory jets are simulations of the exhaust jets of the very low bypass ratio turbofan engines that power today's supersonic (military) aircraft. The research focuses on the processing of data to produce an improved representation of acoustic data. The ultimate goal of the research is to develop methods to alter the jet flow fields to produce lower noise levels, or to alter the noise directivity to produce directions at which the noise is reduced.

Supersonic jet noise has proven to be an extremely difficult phenomenon to control, or even to reduce in any measurable way. Because of this difficulty, it is important to make all measurements as carefully and as accurately as possible. A part of the process of making and reporting accurate measurements is to make a number of comparisons with data from similar experiments conducted by other researchers in other facilities using similar but not precisely identical measurement and processing methodologies.

An example of such a comparison is shown in Figure 19 in which acoustic data obtained with a jet issuing from a 1.8 cm exit diameter nozzle at Penn State are compared with data obtained at the NASA Glenn Research Center (GRC) with a 12.9 cm exit diameter nozzle jet. In this case the nozzles replicated the inside contour of a GE F404 series engine exhaust nozzle to the accuracy of the machining and rapid prototyping process. Acoustic measurements were conducted with the circular microphone arrays set at non-dimensional radial distances that equaled or exceeded 100 (and were centered at the nozzle exit plane). Care was taken to operate

the nozzles at the same pressure ratio and at the same unheated temperature (ratio), and to perform the data processing including the microphone and atmospheric attenuation corrections

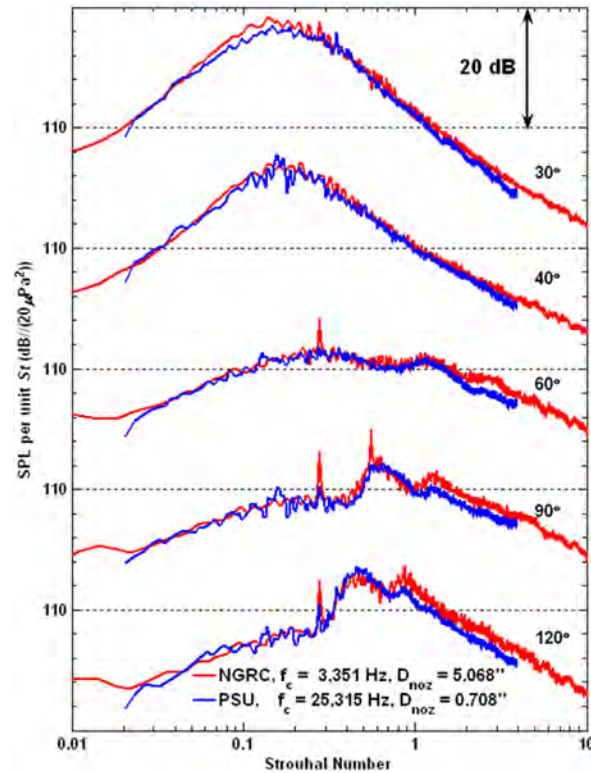


Figure 19. Lossless spectra comparison of unheated jets from PSU and NASA Glenn Research Center both issuing from $M_d = 1.65$ GE nozzle operated at $M_j = 1.56$, and scaled to $R/D = 100$.

following a consistent methodology. For this specific nozzle the area ratio produces a $M_d = 1.65$ exit flow based on isentropic flow, and both jets were operated at a pressure ratio of 4.0 that produces a spatially averaged exit Mach number M_j of 1.56. In such imperfectly balanced flow, a standard shock cell pattern is present and produces broadband shock associated noise (BBSAN) that is easily identified in the spectra recorded at the polar angles of 60°, 90° and 120° from jet axis. The small shock screech components are replicated in frequency but not in amplitude (as was expected, as shock screech is very sensitive to global features that are not possible to reproduce from one facility to another). In the case of these data, the NASA Glenn data were “back propagated” from the measurement location of $R/D = 120$ to the location of $R/D = 100$ of the Penn State measurements (using spherical spreading, $p' \sim 1/R$). Such data are representative of numerous measurement comparisons of cold jets, operated at various over expanded and under expanded conditions using three different area ratio jets as part of a cooperative Penn State/NASA project. With cold jets, the two sets of data are typically in agreement within ± 1.5 dB across the spectra.

Turning now to heated jets, those of primary interest to the aircraft and engine manufacturers and users, the agreement in the data is typically not as close. Presented in Figure 20 are data recorded in three facilities: Penn State, NASA Glenn Research Center and NASA Langley

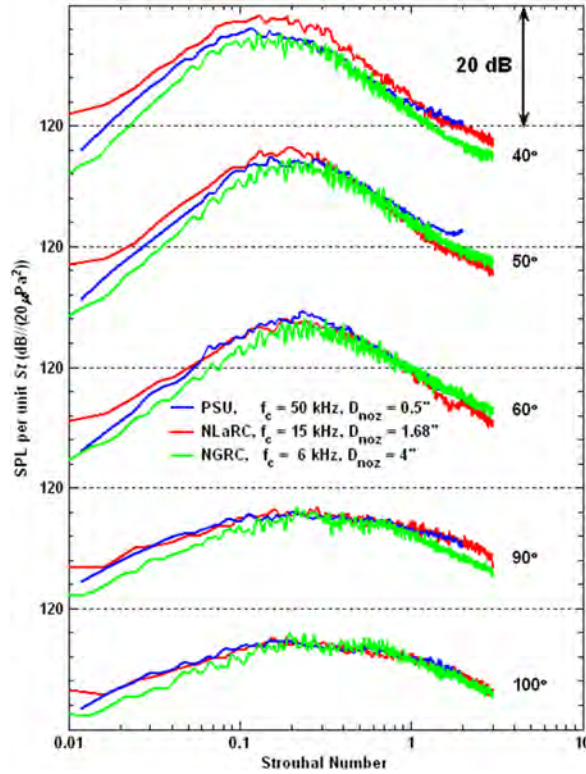


Figure 20. Acoustic measurements from Penn State, NASA Langley Research Center (LaRC), and NASA Glenn Research Center (GRC) conducted with CD nozzle ($M_d = 1.5$, $D = 0.5$) accordingly operated at $M_j = 1.5$, $TTR = 2.2$, and scaled to $R/D = 100$.

Research Center (LaRC). In this case the nozzles had converging-diverging (CD) $M_d = 1.5$ contours, the jets were operated in the perfectly expanded $M_j = 1.5$ condition and all spectra were reported to have been measured in the far field, with the closest microphones located at $R/D = 85$. In general the agreement between spectra acquired in the different laboratories is not as good as was found from the cold jet data. The Penn State data, acquired with helium-air mixture jets to simulate the heated condition, fall for most part between the two NASA data sets. In fact, the discrepancy at low frequencies between the two NASA spectra (at common polar angles) is approximately 5 dB for $\theta = 40^\circ$ to 60° .

The imperfections in the data match led to the examination of the data in more detail from the GRC and LaRC laboratories and from the GRC Small Hot Jet Acoustic Rig (SHJAR), which operates with smaller jet nozzles and with a polar array on a radius $R/D = 50$. All of these data comparisons led to the conclusion that when data are compared with measurements made at common radial distances from the nozzle, sufficiently in the far field, the smaller heated jets at LaRC, GRC SHJAR and Penn State agree across the spectra within ± 1.5 dB over the range of polar angles typical of Figure 19 and Figure 20. When comparisons are made, *in the true geometric far field* between any of these smaller jets and the GRC HFJER, the agreement at the peak amplitude and in the high frequency range is also within ± 1.5 dB but at frequencies below the peak, the discrepancies between spectral levels grow to values as high as 5 dB (± 2.5 dB).

The differences between the measurements at similar R/D locations are not the focus of this report, but have been presented to explain how we were led to the study at hand. In gathering data with which to make comparisons, the usual assumption is that at ranges of $R/D > 50$ extrapolation of data to greater ranges can be quite accurate when using spherical spreading ($p' \sim 1/R$; or 6 dB per doubling of distance). While such scaling is straightforward, it relies on the underlying assumption that the noise radiates spherically and inversely proportional to distance between the source and the microphones and the lateral extent of the noise generation region is assumed to be negligible.

The question of the minimum distance to the true geometric far field was investigated more carefully by examining data recorded from the same jet (in the same laboratory) measured at different ranges. These data were obtained as part of a Penn State/NASA cooperative research program, the results of which are documented by McLaughlin, Bridges and Kuo⁷. First are the comparative data of Figure 21 which show spectra of acoustic measurements performed (at Penn State) in the acoustic field of two supersonic jets exiting from CD nozzles operating fully

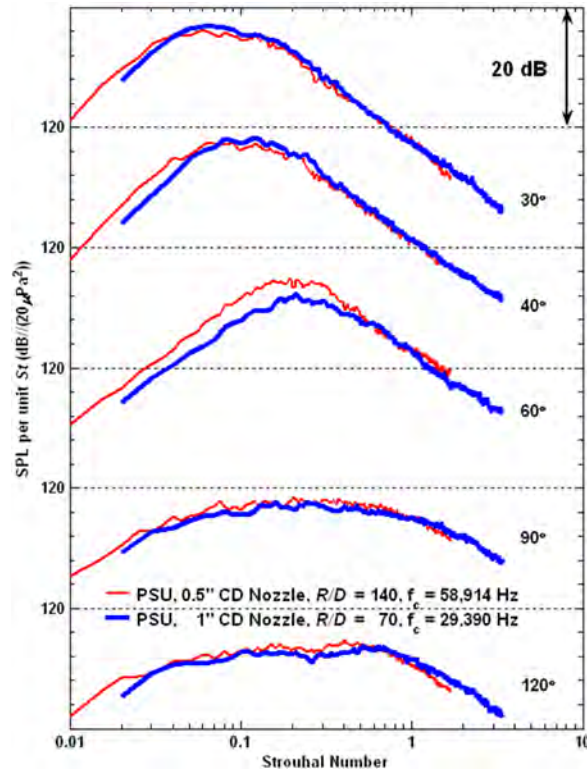


Figure 21. Spectra comparison of heat simulated jets issuing from $M_d = 1.5$ ($AR = 1.18$) CD Nozzle with 0.5" and 1" in diameter operated at $M_j = 1.5$, $TTR = 3.2$, and scaled to $R/D = 100$.

expanded at $M_j = 1.5$ and simulated total temperature ratio of $TTR = 3.2$. The microphones for both jets were positioned at a radius of 1.78 m (70 in) on a polar arc centered at the center of the nozzle exit. Since the two nozzles used in these measurements were 12.7 and 25.4 mm in diameter, the R/D values for the experiments were $R/D = 140$ and 70 respectively. In the data of Figure 21, both sets of data were then scaled (by spherical spreading) to $R/D = 100$. Note that the spectral data are in fair agreement but differences of about 3 dB in magnitude are apparent

between data from the two size nozzles (and R/D positions). The discrepancies are most apparent at frequencies below the peak amplitude level and in the polar angle range from 40° to 60° from the jet downstream axis corresponding to the region of largest gradient in the $OASPL$ with polar angle.

Figure 22 shows very similar data to Figure 21, this time recorded with a heated jet exhausting from the NASA Glenn Research Center Hot Flow Jet Exit Rig (HFJER) facility fitted with a CD nozzle (and a thin annulus of unheated bypass air). In this case the acoustic data were recorded simultaneously with microphones positioned on an arc at $R/D = 147$ and on a linear array displaced parallel from the jet axis by $33 D$. The latter data, which are recorded at an average radius of $R/D \sim 50$, are clearly not in the geometric far field. The plotted data are scaled to a non-dimensional radial position of $R/D = 100$ and discrepancies in the spectral level are observed: as with the Penn State small scale jet measurements of the previous figure.

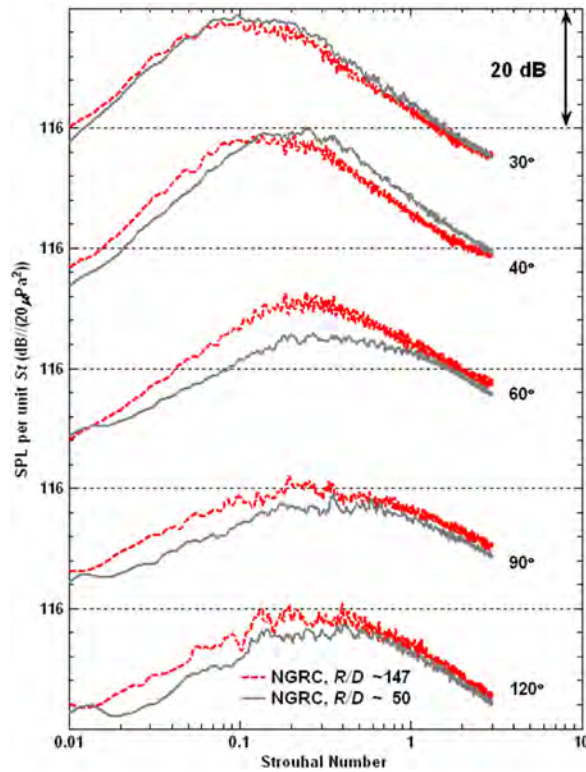


Figure 22. Spectral comparison of experiments measured at various locations from NASA Glenn Research Center (NGRC) issuing from $M_d = 1.5$ (AR = 1.18) CD Nozzle operated at $M_j = 1.5$, $TTR_{core} = 2.6$, $TTR_{mix} = 2.2$, scaled to $R/D = 100$.

Such discrepancies between the measurements made at the threshold of the near to far field and those that are clearly in the geometric far field are significant and render the comparisons of the effect of other parameters, in some cases, less effective. In essence the problem is much more acute with hot and heat-simulated jets, than it is with cold supersonic jets. As demonstrated by Lee and Bridges⁸ and McLaughlin *et al.*⁹, the dominant region of noise sources in hot supersonic jets center around a non-dimensional axial distance $x/D = 13$, whereas the comparable location

for cold jets is around $x/D = 8$. This shift of the dominant region of noise sources as well as the extended length of the source region are enough to distort the spherical spreading scaling of acoustic data to different radial positions when the measuring microphones are on a polar arc originating at the nozzle exit. This reason makes it more important to perform comparison measurements at the same non-dimensional radial positions. Due to physical restrictions and the different requirements of each experiment, such is not always possible when making comparisons to data recorded in experiments performed in past years.

Recently, the distance of 50 diameters has been widely accepted^{10,11,12,13,14,15} as being the outer edge of the near field of high speed jets, and an appropriate distance to make measurements that can then be scaled to farther distances. However, when comparing the data obtained from different non-dimensional distances conducted in the same facility, as shown in Figure 21 for data acquired at Penn State and in Figure 22 for spectra measured at NASA, the agreement is not as precise as the comparisons in Figure 19 and Figure 20. All these measurements were previously thought to meet the criterion of noise spherically radiating to the far field. Albeit, one can easily observe that there is obvious discrepancy in the sound pressure level at low frequencies and an apparent shift of the peak frequency of the spectrum at some polar angles. These comparisons suggest that data previously measured and existing in the literature for some time might not have been made in the true geometric far field. Table 2 summarizes some experiments for which we have been comparing data and the location of their microphones. Many of the data sets that have been widely referenced have been acquired at polar distances less than 100 jet diameters.

Table 2. Testing nozzles and measured distances of acoustic measurements from each facility.

Author	Facility	Nozzle Diameter (D)	Measured Radius (R)	R/D	Reference
Tanna, H. K.	Lockheed-Georgia	2"	144"	72	[13]
Seiner, J. M. <i>et al.</i>	NASA Langley	1.68"	144"	85	[14]
Viswanathan, K.	Boeing LSAF	1.5" up to 4.9"	Sideline array 180"	120 to 37	[12]
Bridges, J. <i>et al.</i>	NASA Glenn, HFJER	4" up to 5"	588"	147 to 117	[15]
	NASA Glenn, SHJAR	2"	100"	50	[2]

It is also noteworthy to mention that the extended range to the true geometric far field is a direct result of the extended noise source region in supersonic jets, particularly those that have been heated. Beginning with Nagamatsu *et al.*¹⁶, it has been established that the noise sources in

supersonic hot jets extend much further downstream than do those in cold subsonic jets. The results of several noise source distribution measurements have been assembled and plotted collectively. Figure 23 and Figure 24 accordingly present the estimated downstream location of the peak noise source in low and high speed jets as a function of non-dimensional frequency (Strouhal number). These data were collected from the literature where measurements were made with improved directional reflecting microphone systems^{17,18,19}, with phased array microphone measurements^{9,20,21} and correlation of multi data sets²². Even data from some early

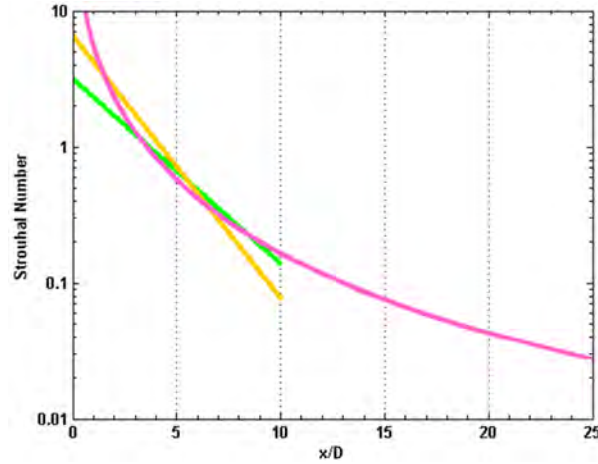


Figure 23. Estimated peak noise emission location as a function of Strouhal number for cold and heated jets operated at $M_j = 1$. Green, Cold Jets^{17,18}; Yellow, Heated Jets²¹; Magenta, Tester et al²².

sound shadow measurements are included, which were conducted by systematically blocking noise generation regions from the acoustic far field^{23,24,25}. With these given peak noise emission

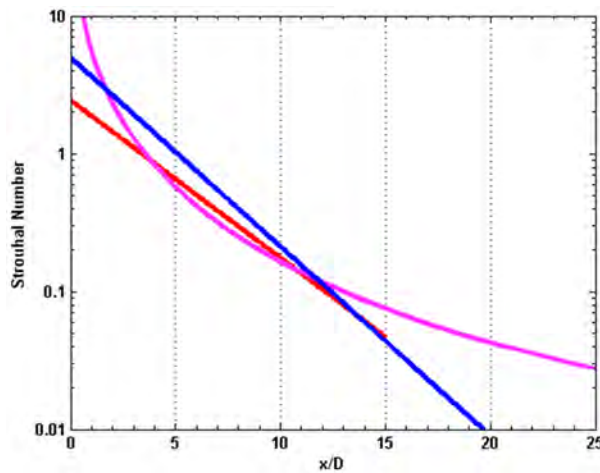


Figure 24. Estimated peak noise emission location as a function of Strouhal number for cold and heated supersonic jets. Red²¹, Blue⁹, Purple²².

locations, one can examine the relationship between the acoustic measurements conducted at pre-selected locations and the noise radiating from these peak noise emission locations.

In an effort to produce measurements that can be reliably used by other organizations and propagated to the far field for noise prediction during an aircraft fly-over, laboratory measurements need to be representative of the true geometric acoustic far field. The goals of this part of the study were to: 1) examine acoustic measurements made in the regions of the acoustic far field (of supersonic jets) where the true geometric far field had not yet been reached, 2) examine the details of the noise production regions within these jets in order to better understand the source of the spectral mismatch measured at various radial locations in the acoustic field, and 3) develop a correction methodology with which measurements previously made in the acoustic far field at ranges shorter than the true geometric far field could be converted to useful geometric far field data.

Regarding the third research goal, an advanced processing method is being developed to allow for a more accurate comparison of acoustic measurements from different distances from the nozzle exit plane. The improved acoustic data scaled to the true geometric far field are referred to as synthesized far field data. Data produced in this fashion can then be used to obtain better comparisons with measurements from other research groups as well as provide the most accurate data to be used in the acoustic modeling for environmental noise predictions. This new correction methodology uses the noise source distribution data that were discussed above. Applying this methodology can also allow one to further identify the nonlinear propagation effects on the spectra that will be demonstrated in the latter portions of this paper.

Experimental procedure and operation conditions

A contoured CD nozzle, designed with the method of characteristics for a nominal Mach number 1.5 and a diameter of 1.27 cm (0.5 in) at the nozzle exit plane was used for the acoustic measurements presented. Two operating conditions were used for these measurements: a pure air cold jet operating on design ($M_j = 1.5$) and a helium-air mixture jet of simulated temperature ratio $TTR = 2.2$ also operating at $M_j = 1.5$. The main properties of these jets are summarized in Table 3 inclusive of the acoustic Mach number $M_a = U_j / a_a$, a_a being ambient acoustic velocity, convective Mach number (M_c), Reynolds number (Re), and Mach wave radiation angle (β_M). Microphone measurements were performed at the locations represented by dots in Figure 17. In

Table 3. Jet operating conditions for measurements conducted with CD nozzle ($M_d = 1.5$).

M_j	TTR	M_a	M_c	Re	β_M
1.5	1	1.25	0.88	686,000	N/A
1.5	2.2	1.85	1.3	486,700	40°

$$M_c \approx 0.7 \times M_a, \quad \beta_M = \cos^{-1}(1 / M_c)$$

this figure, the center of the nozzle exit plane corresponds to the origin and the flow direction is toward the positive values on the x axis. The coordinate system for the microphone locations is originated from the nozzle exit plane. The first group of microphones resides at non-dimensional

distance $R/D = 35$ and 70 from polar angles 30 to 100 degree, as measured from the jet direction, with 10 degree increments. The second group of microphones resides at non-dimensional distance $R/D = 140$ from polar angles 30 to 100 degree with 5 degree increments. The third group of microphones is located at a non-dimensional distance $R/D = 210$ to 280 and polar angles 30 to 100 degree with approximately 10 degree increments. All acoustic measurements acquired at these locations were processed into lossless spectra per unit Strouhal number as a standard processing procedure. These lossless spectra represent the corresponding acoustic field at these pre-selected locations. Only while there is a need, the resulting data will be (back) propagated to certain distance, R_{prop} , assuming spherical spreading of the acoustic field. This “back” propagated SPL is determined from:

$$SPL(St, R_{prop}) = SPL(St, R) + 20 \times \log_{10} (R / R_{prop}) \quad (3)$$

Data processing methodology

The major portion of the processing methodology includes data on the distribution of peak noise emission locations. The first step, therefore, is to acquire a reasonably representative curve of the peak noise source locus for the specific operating conditions. The experimental results conducted at UCI by McLaughlin, Kuo and Papamoschou presented in Figure 24 were selected for this purpose. These results were acquired by phased array microphones. There is a numerical estimation of the peak noise locus in Strouhal number for $M_j = 1.5$ cold and heated jets issuing from a CD nozzle with $M_d = 1.5$. The experimental conditions for the current study were selected as $M_j = 1.5$ cold and $TTR = 2.2$ jets issuing from a CD nozzle with $M_d = 1.5$. The numerical estimation of the peak noise locus can be described as:

$$x / D(St) = 5.1 - 7.3 \times \log_{10} St \quad (4)$$

The next step is to choose a target array of microphones in the geometric far field that will be used to produce estimates of synthesized spectra from the closer measurement array. Figure 25 shows how one position in the geometric far field array relates to the closer acoustic field measurements. The empirical information on the noise source distribution is used to relate the measured spectra to the further distances from the jet. In doing so, there are some changes in the angular and radial position for the spectrum contents measured from microphones as a function of frequency. For each frequency, the distance and polar angle between each microphone in the acoustic field and the locus of the noise generation region can be calculated. Thus for a given frequency band, there is a corrected polar angle θ_f and corrected distance R_f that represents the actual polar location and distance of the microphone with respect to the (estimated) noise source location. The closer the measurement microphones to the jet, the larger the discrepancy between the polar angle measured from the exit plane θ_m and θ_f . The distance of the microphone relative to the noise source also varies similarly. In order to compare measurements performed at two different radial distances, the comparison should therefore be made between the microphone locations relative to the source, not relative to the exit of the jet. Obviously, since the source location is a function of frequency, this means that for each frequency band, a different value of θ_f should be matched. Again, this is schematically represented in Figure 25.

For example, in order to project measurements conducted at $35 D$ to the geometric far field position (at $140 D$), the following steps are followed:

- Choose the geometric far field radius and polar angle upon which to “project” the spectra from the closer measurement position spectra.

- Obtain f for each frequency band the noise source location from the numerical estimation of the locus of peak noise.

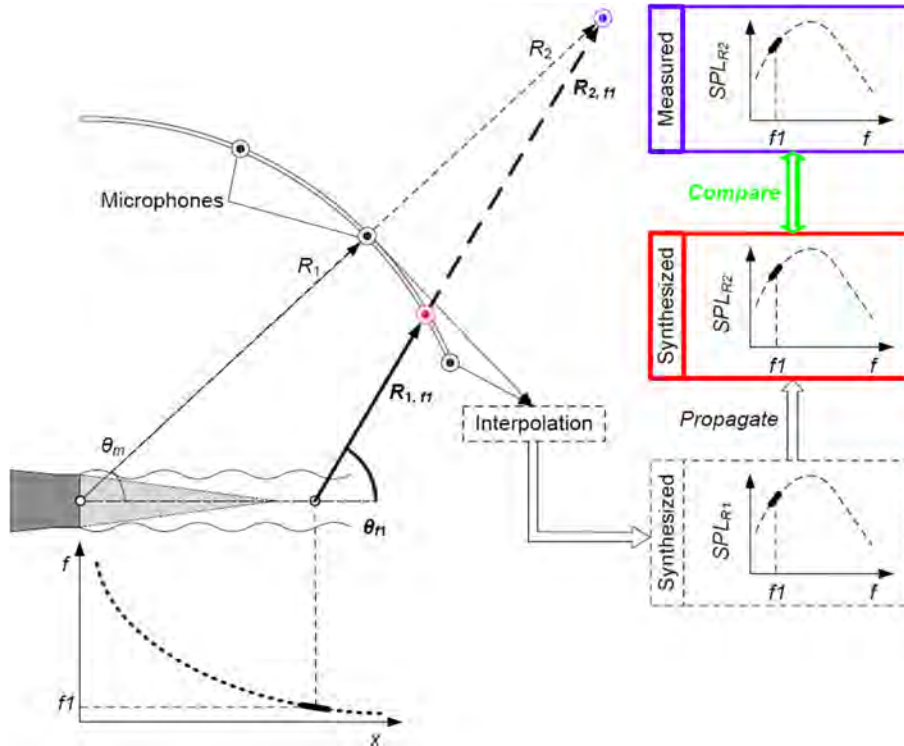


Figure 25. Schematic of the data processing procedure based on the noise source distribution locations for the acoustic measurements conducted at various radial distances.

- For each frequency band, find the values of $\theta_f = \theta_{f1} = \theta_{f2}$ and R_{1f} and $R_{2f} = R_{140D,f}$ corresponding to the measurement obtained at R_{140D} .
- For each frequency band, find the noise radiation path from the R_{140D} measurement to the R_{35D} measurement, and find the values of $R_{35D,f}$.
- Interpolate between the two closest measurements performed at R_{35D} to obtain a spectrum at the exact θ_f angle, and pick up the corresponding SPL for the specific frequency band.
- Assuming spherical propagation, correct the value of the pick-up SPL from $R_{35D,f}$ to the $R_{140D,f}$ distance.

This process can obviously be applied to any two radial distances R_1 and R_2 . Finally, while the whole process is described here with dimensional frequencies for clarity, it can obviously be extended to non-dimensional spectra expressed as a function of Strouhal number.

Correction is most useful at polar angles f for which the sound pressure level shows large variations for small angular displacements (i.e. around the peak noise direction). In doing so, the spectra comparison across various measured radial distances can provide more accurate and useful results.

Results and Discussion

Experimental results are presented in the following section: divided into three sections. Spectra and *OASPL* plots are first presented, highlighting the general features of the noise radiated by the two jets considered (fully expanded $M_j = 1.5$ cold and operated at a simulated $TTR = 2.2$). In the second section, comparisons are made between near-field and far-field measurements, with correction of the spectra using the noise source distribution described earlier. Finally, application of this methodology in the peak noise direction is made in order to have a clear visualization of the effects of nonlinear propagation on the spectra.

Jet noise directionality and spectra

Figure 26 presents the spectra and *OASPL* obtained from the acoustic measurements performed at non-dimensional distance $R/D = 140$. When the jet temperature ratio is raised, the overall sound intensity level is raised accompanied with a downward shift of non-dimensional peak frequency at shallow polar angle from the jet direction as shown in the spectra. The peak noise emission direction alters from 25° for $M_j = 1.5$, $TTR = 1$ jets to 45° for $M_j = 1.5$, $TTR = 2.2$ jets as shown in the *OASPL* plot. This is the acoustic trend for the jets with higher acoustic Mach number (U_j/a) due to the increased nozzle pressure ratio or total temperature ratio.

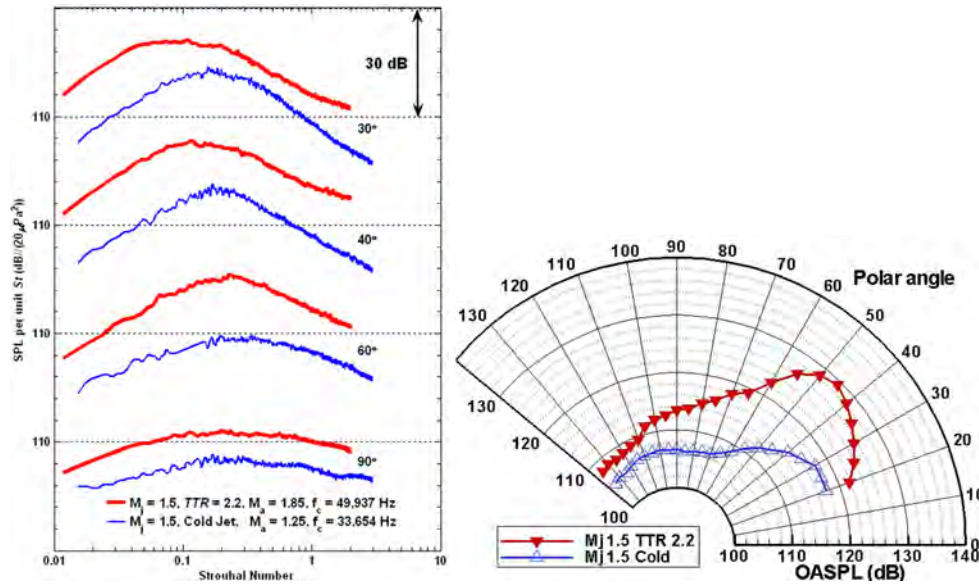


Figure 26. Acoustic measurements from PSU conducted with CD nozzle ($M_d = 1.5$, $D = 0.5$) operated at $M_j = 1.5$, $TTR = 2.2$, and $TTR = 1$, as measured at $R/D = 140$.

Since acoustic measurements were performed at varying radial distances and polar angles, a two dimensional map of the sound field can be reconstructed. Sound intensity contour plots are shown in Figure 27 for three specific frequencies for both the cold and heated jets. The sound intensity contours were plotted by selecting the *SPL* at a specific frequency measured by the microphones at the locations represented by the black dots. Interpolation between these data points allows for the contours to be extrapolated. The selected frequencies correspond to a frequency below, at, and above the peak frequency of the acoustic spectra shown in Figure 26. For the heated jet case, the sound intensity contour presents a broad lobe centered around $\theta = 35^\circ$ for $St = 0.08$, and this lobe shifts to larger polar angle with increase in frequency, up until $\theta =$

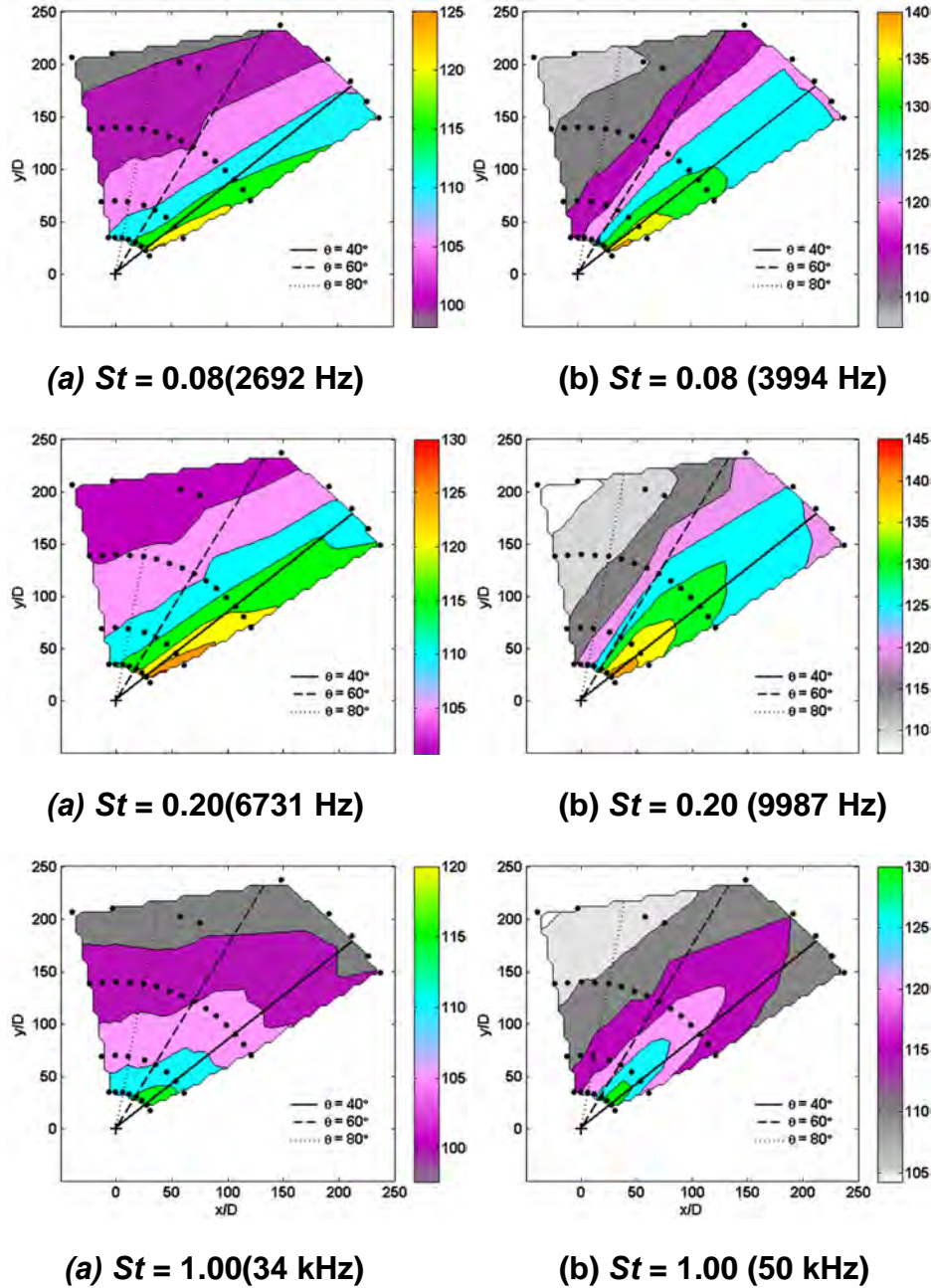


Figure 27. Sound intensity contour plot in for specific frequencies from jets operating at various conditions (a) $M_j = 1.5$, $TTR = 1$, (b) $M_j = 1.5$, $TTR = 2.2$.

45° for $St = 1$. The amplitude of that lobe also varies, being highest at the peak noise frequency, as should be expected. The cold jet case presents somewhat similar results, with lobes that do not rotate with frequency as much. The amplitude of the sound is again, as expected, highest at the frequency corresponding to the peak emission. In both jets, a broadening of the peak amplitude lobe is noted, which is consistent with the more omnidirectional nature of the noise produced by fine scale turbulence.

The observed rotation of the acoustic directivity with frequency is in agreement with turbulence measurements that suggest that the convection velocity of turbulent structures varies with frequency. Such measurements, based on cross-correlations within the jet, have been performed by Harper-Bourne²⁶, by Kerherve²⁷ and by Morris and Zaman²⁸ and demonstrated a somewhat logarithmic variation of the convection velocity with frequency. Similar experimental results from experiments performed at Penn State with an Optical Deflectometry (OD) setup are shown in Figure 28 in the unheated $M_j = 1.5$ jet. Details of the setup are discussed in Ref. 29. The variation of convection velocity with frequency clearly follows the same distribution found by

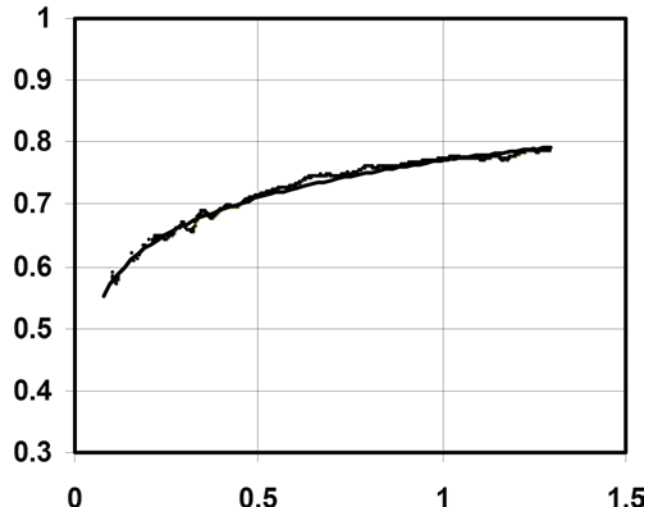


Figure 28. Optical Deflectometer measurements performed with CD nozzle ($M_d = 1.5$, $D = 0.5$) operated at $M_j = 1.5$, $TTR = 1$ measured along nozzle lip line accordingly from $x/D = 4$ to 9. Convection velocity as a function of St .

the investigators noted above. The same distribution has been observed in jets of varying speeds (sub and supersonic) and temperature ratios. As a result, while the cold jet, of speed $U_j = 427$ m/s, has an overall convective Mach number that is subsonic, the high frequency content that approaches 0.8 times the jet speed has a convection velocity that becomes supersonic and therefore radiates Mach waves. This explains the lobe that appears at larger polar angle for the higher frequencies. For the heated case, the majority of the turbulent structures of different length scales travel supersonically, but at different speeds, causing this rotation of the lobe with frequency observed from the acoustic field measurements.

In addition, the optical deflectometry turbulence measurements conducted with the cold pure air jet can be used to provide information on the noise generation region as a function of frequency content. Figure 29 presents autospectra of the optical signal measured along the lip line of the jet and at varying downstream locations $x/D = 4$ to 9. While these measurements are not enough to accurately measure the locus of the noise production region for each frequency component, they do highlight the fact that the highest frequency components are strongest at small downstream locations and the lower frequencies dominate further downstream. The peak of the autospectra shifts from roughly $St = 0.6$ at $x/D = 5$ to $St = 0.1$ or below at $x/D = 9$. The amplitude also monotonically increases, as is expected within the potential core of such a jet, and as mentioned in Ref 16. From experimentally derived estimations^{16,30}, the length of the potential core for this

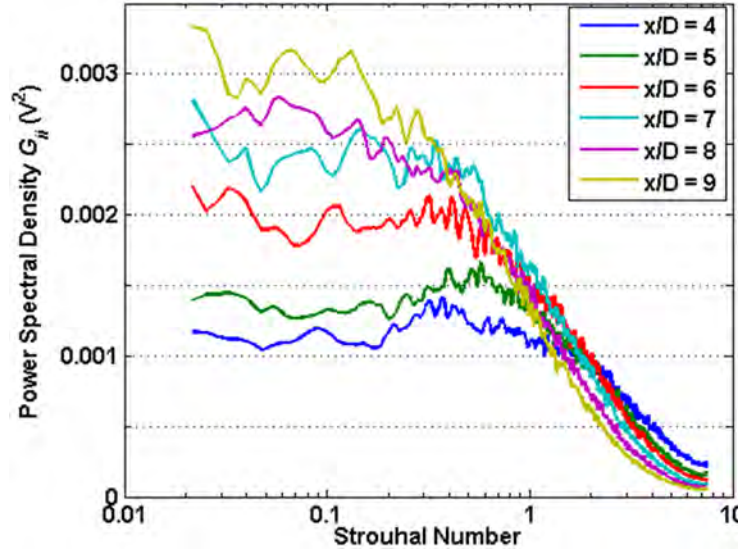


Figure 29. Optical Deflectometer measurements conducted with CD nozzle ($M_d = 1.5$, $D = 0.5$) operated at $M_j = 1.5$, $TTR = 1$ measured along nozzle lip line accordingly from $x/D = 4$ to 9. Density fluctuation level as a function of St .

specific jet is around $7 D$ and the supersonic core length is around $12 D$. These measurements therefore conform to the assumption made for the noise source distribution presented earlier, in Figure 23 and Figure 24: the high frequency noise is mostly generated close to the nozzle exit and the low frequency noise is predominantly produced farther downstream.

Effect of jet noise source distribution in the acoustic measurements

Attention is now paid to comparisons between measurements performed at different radial distances from the jet. Figure 30 presents the *OASPL* polar plot from the measurements acquired at $R/D = 35$, 70, and 140 for both jets. As one can see, there is almost exactly a 6 dB shift

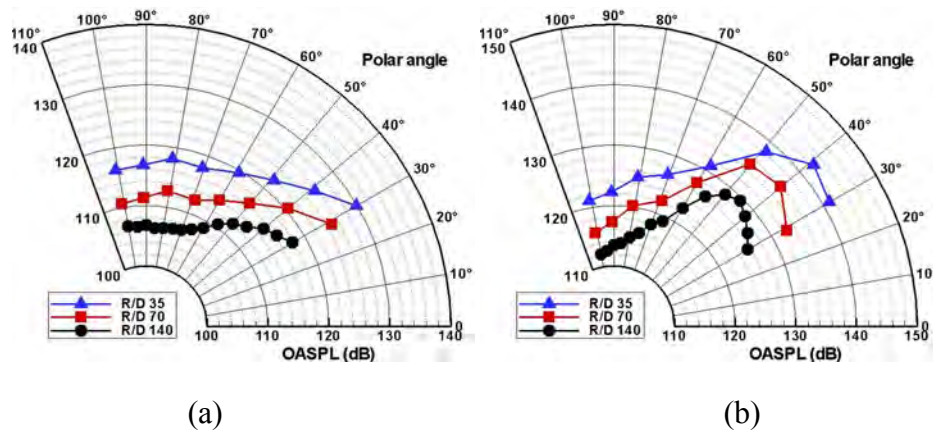


Figure 30. OASPL plot measured at $R/D = 35$, 70, and 140 for jets operated at (a) $M_j = 1.5$, $TTR = 1$, (b) $M_j = 1.5$, $TTR = 2.2$.

between the $R/D = 70$ and $R/D = 140$ measurements for the cold jet, and close to 6 dB between the $R/D = 35$ and $R/D = 70$ locations for the same jet. This suggests that the distance of 70 D is already far enough to be considered to be in the geometric far field, meaning that spectra at any further location can be predicted using spherical spreading. However, for the heated (simulated) case, the linear spherical spreading approximation is inaccurate between $R/D = 70$ and $R/D = 140$: the difference between the measured $OASPL$ is not uniformly 6 dB. Particularly, there is an obvious shift in the peak noise emission direction which shifts from 40° at $R/D = 35$ to 45° at $R/D = 140$.

In a more detailed look, the corresponding spectra can be compared between measurements acquired at $R/D = 35, 70, 140$, and 280 for $\theta = 40^\circ$ for the cold jet and $\theta = 50^\circ$ for the heated case, as shown in Figure 31. These polar angles were chosen since they are around the peak noise direction for the jets considered, which is where a small discrepancy in angular location

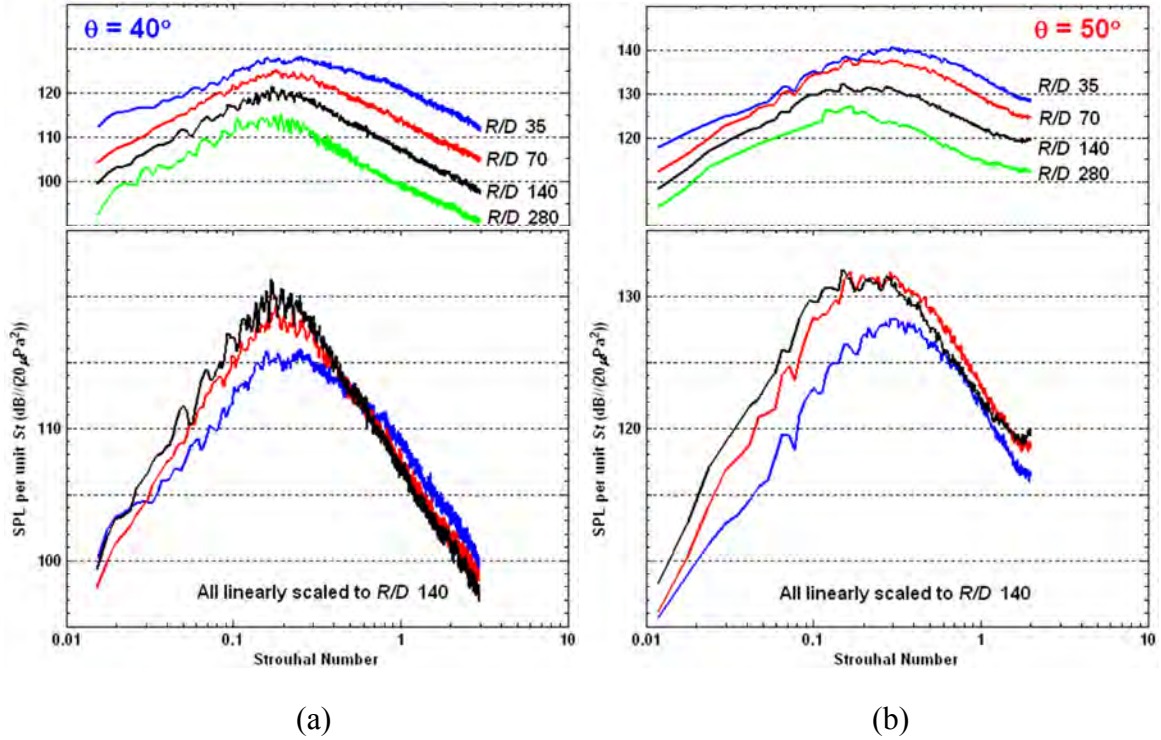


Figure 31. Acoustic measurements conducted with CD nozzle ($M_d = 1.5$, $D = 0.5$) as measured at $R/D = 35, 70, 140, 280$, (a) operated at $M_j = 1.5$, $TTR = 1$, (b) operated at $M_j = 1.5$, $TTR = 2.2$.

relative to the noise source can induce large changes in the spectra. On the top part of each subplot the lossless spectra at each radial location are plotted. On the bottom part of part a) of Figure 31 (the cold jet condition) the spectra for $R/D = 35, 70$ and 140 are presented. Data from the two closest positions have been scaled to the distance $R/D = 140$ using linear propagation (assuming spherical spreading). Looking at part a) of Figure 31, the collapse can be seen to be fairly good between all measured distances except the closest ($R/D = 35$). The last shows some discrepancies as high as 6 dB at low frequencies, but still a good collapse at the high frequencies. This observation is consistent with the $OASPL$ plot that suggested that the distance of 70 D was far enough to be considered as being in the geometric far field. The fact that the high

frequencies still match, even at the closest location with far field locations, highlights the fact that these high frequencies are generated very close to the nozzle exit plane. The heat simulated jet spectra in part b) of Figure 31 show similar results, except that the best collapse is shown between the two furthest locations ($R/D = 140$ and 280). When these data are compared they collapse within ± 1 dB. Spectra measured at $R/D = 70$ or closer and propagated to $R/D = 140$ do not match as well with actual measurements at $R/D = 140$ or further. Discrepancies on the order of ± 2 dB are found between the data from $R/D = 70$ to 140 and much greater if the data at $R/D = 35$ are compared to the further distances. The peak noise frequency for a given polar angle is also seen to shift to lower values further downstream. This heat simulated jet has a noise production region that is more extended in the downstream direction of the jet, so it makes sense that the discrepancies are much higher than in the cold case. Once again, the high frequencies match much better, which highlights the fact that these are produced close to the nozzle exit plane. The exception to this is the high frequency content in the hot jet between $R/D = 140$ and 280 which can be attributed to nonlinear propagation effects, which is discussed in the next section.

The spectra are now corrected for the distributed nature of the noise source as described in the previous section. The noise source distribution discussed earlier in Equation (4) is used as an underlying assumption for this processing. The measurements at $R/D = 70$ are first used in order to reproduce synthesized spectra at $R/D = 140$, and a comparison is made with the actual measurement obtained at $R/D = 140$. The results are presented in Figure 32 parts a) and b) for $\theta = 40^\circ$ for the cold jet and $\theta = 50^\circ$ for the heated case. These polar angles were chosen as

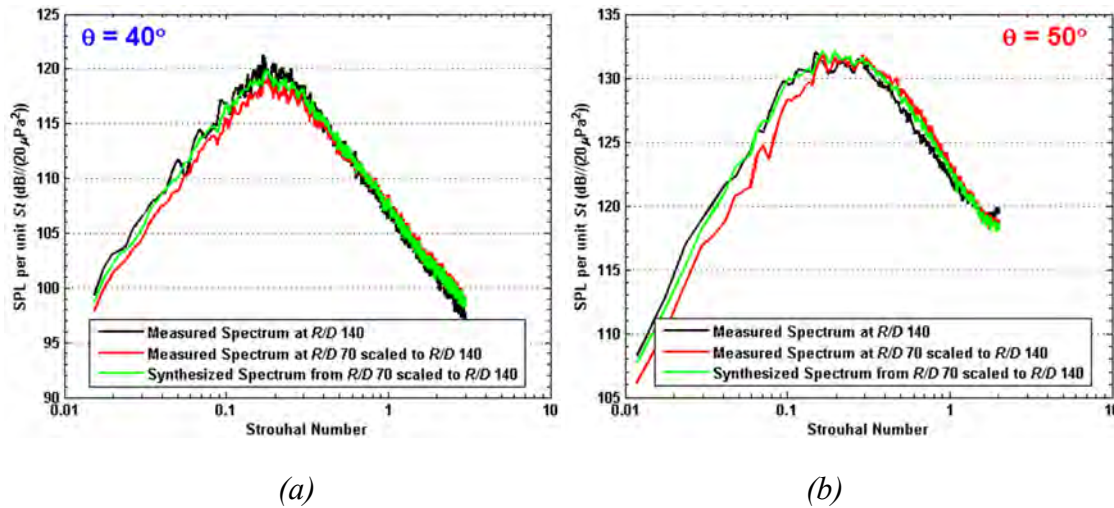


Figure 32. Acoustic measurements conducted with CD nozzle ($M_d = 1.5$, $D = 0.5$) operated at $M_j = 1.5$, $TTR = 1$ for left column and $M_j = 1.5$, $TTR = 2.2$ for right column and corrected with noise source distribution. (a) and (b) spectra from $R/D = 70$ synthesized to $R/D = 140$.

representative cases since they are slightly away from the peak noise direction, which makes them the cases with largest spectral changes with small angular displacement. Similar results were obtained at other polar angles but are not presented here. Subplots a) and b) of the figure represent cases the most relevant to jet noise measurements: comparison between measurements obtained at 70 and 140 diameters from the jet exit plane. It is most important as many groups have published and still publish data measured with microphones located between 50 and 70

diameters. Three spectra are shown in each subplot: the actual spectra measured at $R/D = 140$, and the spectra measured and synthesized from the measurements at $R/D = 70$ used to predict the spectrum at $R/D = 140$. As can be seen for both angles and both TTR values, the agreement between the two measured spectra is not perfect, with about 1 dB discrepancy at most in the cold case and about 2 dB at low frequencies for the hot case. On the other hand, the synthesized spectra and the actual measurements match almost perfectly (within ± 1 dB), allowing a much better comparison between measurements that are not quite in the geometric far field ($70 D$) and others that are far enough to assume spherical spreading of the sound ($140 D$).

As a more extreme case, the same comparison can be made between measurements obtained at 35 and 140 diameters from the jet exit plane, as shown in Figure 33 part a) and b). This time, the discrepancies between the two non-dimensional distances are quite large, especially in the heated case with more than 5 dB differences at low frequencies. The spectra synthesized from the measurements at $R/D = 35$ in order to predict the spectra at $R/D = 140$ does match with excellent

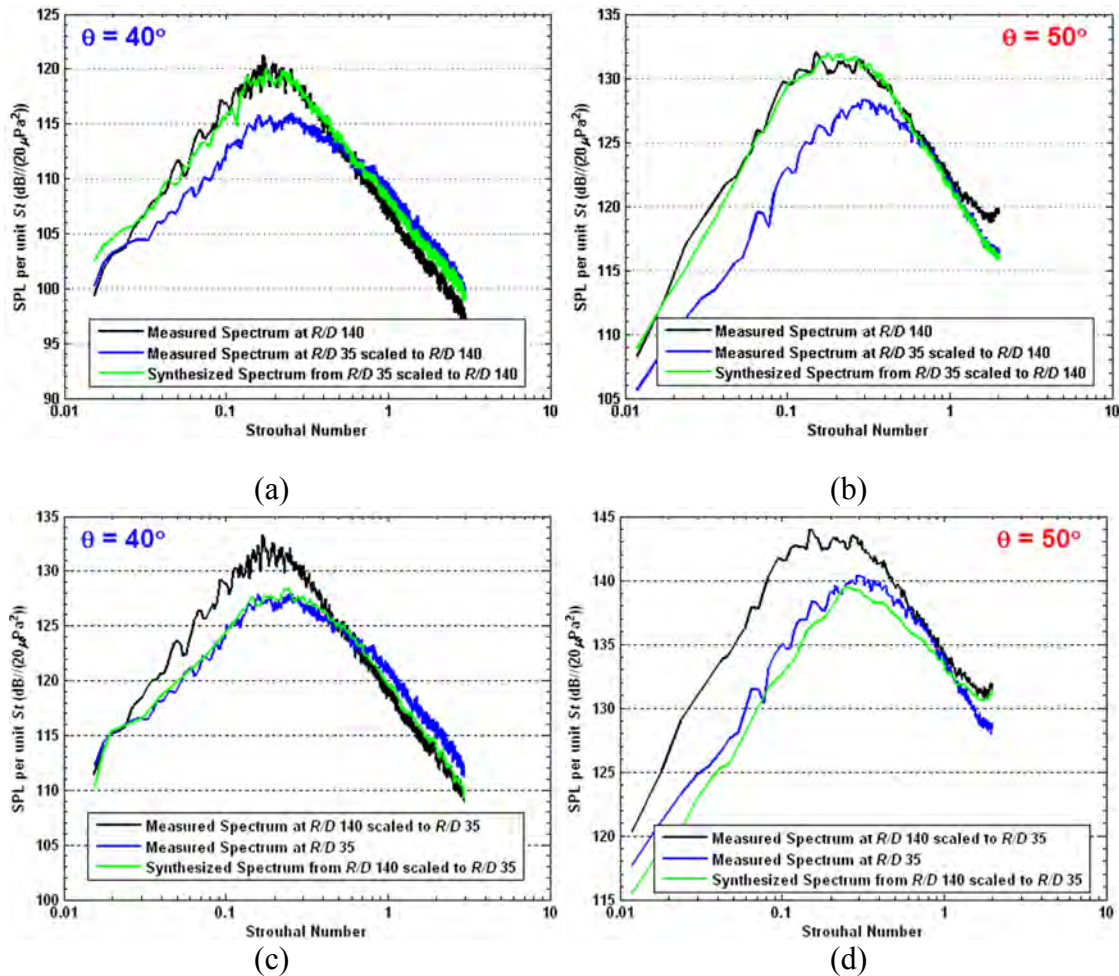


Figure 33. Acoustic measurements conducted with CD nozzle ($M_d = 1.5$, $D = 0.5$) operated at $M_j = 1.5$, $TTR = 1$ for left column and $M_j = 1.5$, $TTR = 2.2$ for right column and corrected with noise source distribution. (a) and (b), spectra from $R/D = 35$ synthesized to $R/D = 140$, (c) and (d), spectra from $R/D = 140$ synthesized to $R/D = 35$.

agreement with the actual measurements at $R/D = 140$. The shift of the peak noise frequency has been completely corrected for, as well as the large discrepancies at the lower frequencies. Similar good results were observed for all polar angles. This provides a very good tool to be able to predict the geometric far field noise spectra from measurements that are in the acoustic far field but not in the geometric far field. This kind of accurate projection is extremely useful for proper prediction of the environmental noise on the ground from flying aircraft predicted from propagation models that use the laboratory source measurement data. Finally, part c) and d) of Figure 33 demonstrates that this projection methodology can be applied in both directions: spectra measured at $140 D$ can be used to reconstruct the spectra that would be measured at $R/D = 35$. The large discrepancies are once again corrected for completely, providing near-perfect collapse of the spectra. As long as the noise source locus can be acquired to accompany the acoustic measurements covering appropriate polar angles, the spectrum at any selected location in the acoustic field can be reasonably synthesized.

These results give confidence in both the validity of the methodology used and the accuracy of the noise source distribution used for the calculation. This strengthens the accuracy and understanding of the scaling methodology when producing comparisons between measurements acquired at various nozzle diameters or from different facilities with disparate radial distances. It also demonstrates that for a highly heated jet, the beginning of the true geometric acoustic far field extends much further than $R/D = 50$, as previously mentioned. The methodology developed is now used to identify nonlinear propagation effects in laboratory-scale experiments.

Examination of nonlinear propagation effects

A previous study at Penn State³¹ showed that there is an energy transfer from mid frequency content to high frequency content, causing the spectrum to lift at the high frequency end when the sound pressure levels in the acoustic field reach levels of approximately 135 dB. Re-examination of this result can be provided using the current methodology to observe the nonlinear propagation effect in a more accurate way. When investigating nonlinear propagation effects, measurements at different radial locations need to be conducted and compared. It typically means that two effects are then causing changes in the spectra: the nonlinear propagation and the effects due to the distributed nature of the noise sources. The methodology developed in the previous sections can therefore be applied to effectively isolate the effects of nonlinear propagation from near-field/far-field effects.

Figure 34 presents the spectra comparison measured at $R/D = 35, 70, 140$, and 280 for $\theta = 40^\circ$, and 70° . There is a trend of the curves lifting at high frequencies at $\theta = 40^\circ$ for the measurements at $R/D = 280$. There are also large differences in the spectral shape at low frequencies, with a shift of the peak. But these are unlikely to be due to the effect of nonlinear propagation, rather to the distributed nature of the noise source. The corresponding values of the Morfey-Howell indicator of nonlinearity³² were calculated to provide direct evidence for the appearance of nonlinearity in the frequency domain. The nonlinearity indicator shows that there is an energy loss around mid frequencies and significant energy gain at high frequencies for $\theta = 40^\circ$ but not for $\theta = 70^\circ$. It is also noted that this high frequency lift is also evident in the hot jet at $\theta = 50^\circ$ at $R/D = 140$. The Mach wave radiation angle of the $M_j = 1.5$, $TTR = 2.2$ jets is approximately 40° calculated with $M_c \sim 0.7M_j$. Thus it is reasonable to observe the phenomena of the nonlinear propagation near $\theta = 40^\circ$, where the noise is significantly louder.

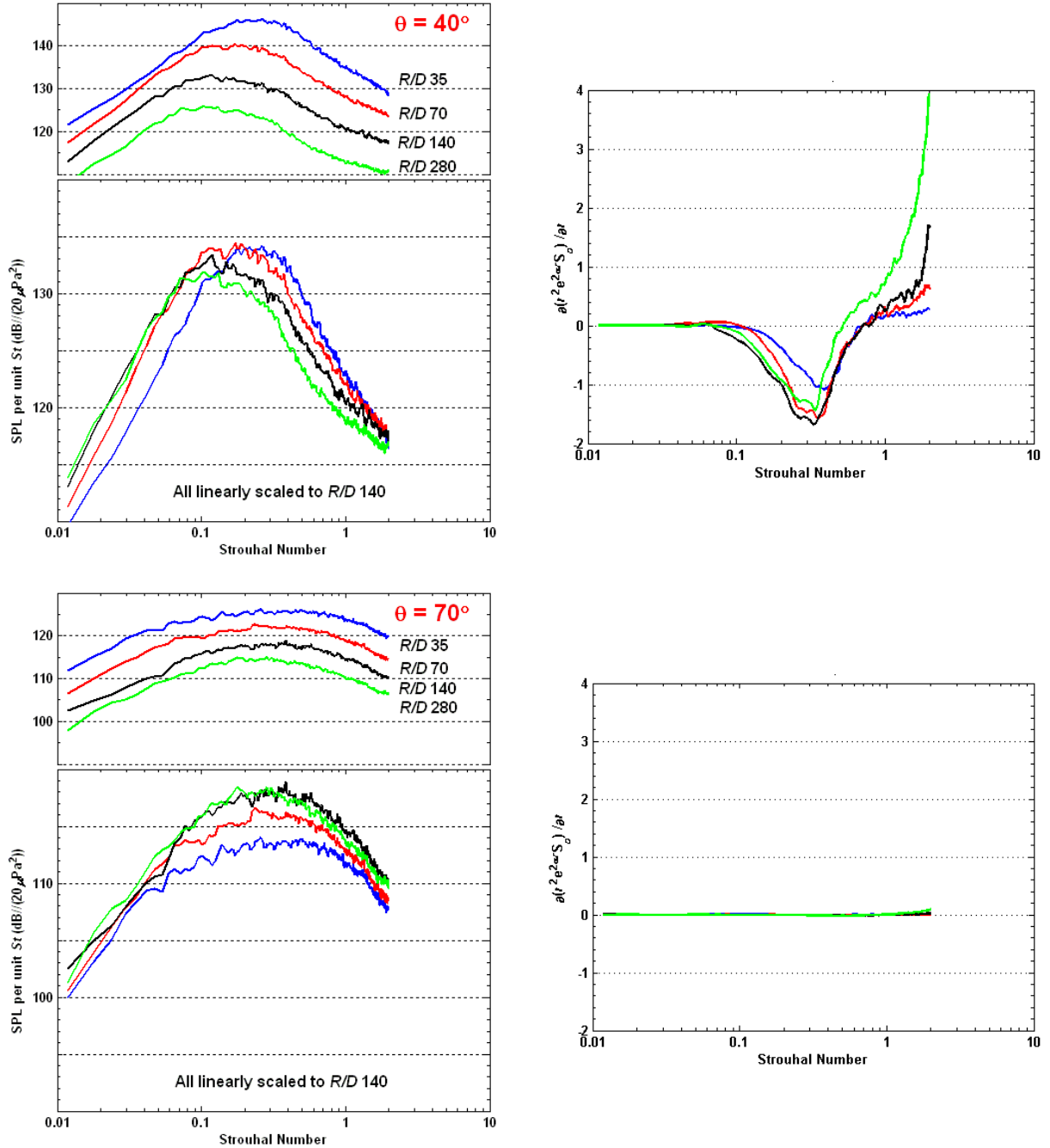


Figure 34 Acoustic measurements conducted with CD nozzle ($M_d = 1.5$, $D = 0.5$) operated at $M_j = 1.5$, $TTR = 2.2$, as measured at $R/D = 35, 70, 140, 280$ for $\theta = 40^\circ$, and 70° and corresponding values of the Morfey-Howell indicator of nonlinearity.

Figure 35 presents the normalized pressure time histories for the measurements at $R/D = 35, 70, 140$, and 280 for $\theta = 40^\circ$. As one can see the pressure fluctuation time histories gradually show less zero crossing and well-described N shape like waveforms as the measured distances advancing. This is evidence of nonlinear propagation in the time domain.

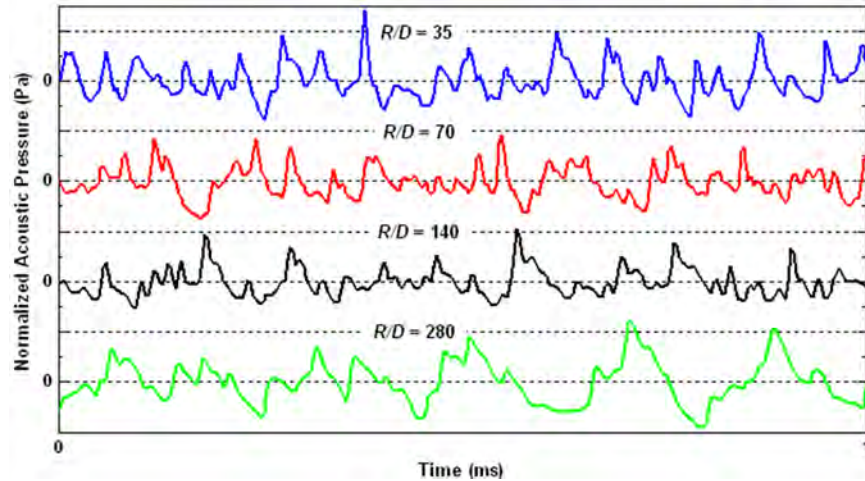


Figure 35. Normalized pressure time histories from acoustic measurements conducted with CD nozzle ($M_d = 1.5$, $D = 0.5$) operated at $M_j = 1.5$, $TTR = 2.2$, $\theta = 40^\circ$, at $R/D = 35$, 70, 140, and 280.

The methodology of including the effect of the jet noise source distribution to observe the nonlinear propagation effect is repeated again here. By first selecting one position of measurement at $R/D = 280$, the noise radiation angle and propagation path are calculated as a function of frequency from the locus of peak noise as shown in Figure 24 to this measured position. The corresponding sound intensity levels then can be collected from the identical radiation path across the measurements at $R/D = 35$, 70, and 140 as a function of frequency. In doing so, the synthesized spectra can be used for comparison as a representative of measurements at $R/D = 35$, 70, and 140. Figure 36 presents the resultant spectra at four polar angles. Due to the unavailability of data at polar angles less than 30 degree for the measurements at $R/D = 35$ and 70, some synthesized spectra were unable to be generated. As one can see from the spectra comparisons at $\theta = 36^\circ$ and 41° , there is a close collapse for the spectra from the measurements at $R/D = 70$ and 140. The spectra from the measurements at $R/D = 280$ consistently show the energy loss across the mid and high frequencies. For the spectra comparisons at $\theta = 47^\circ$ and 58° , the good collapse at low frequency content is maintained within a 1 dB deviation for all measurements. The high frequency ends of the spectra begin to lift up as the values of R/D advances. The energy loss at the mid frequencies only appears in the measurements at $R/D = 280$. These results clearly present the trends from the Morfey-Howell indicator of nonlinearity where there is an energy loss in the mid frequencies transferred to the energy gain at high frequencies. It is therefore quite promising in applying this methodology to observe the nonlinear propagation effects for detailed measurements.

Task 2.1 conclusions

In an effort to produce measurements that can be reliably used by other organizations and propagated to the far field for noise prediction during an aircraft fly-over, laboratory measurements need to be representative of the true geometric far field. The nature of jet noise is such that the noise source is distributed along the jet, with high frequency components being emitted closer to the nozzle exit and the low frequency components radiating from farther

downstream with a dominant sound intensity level. The current task has looked at the details of

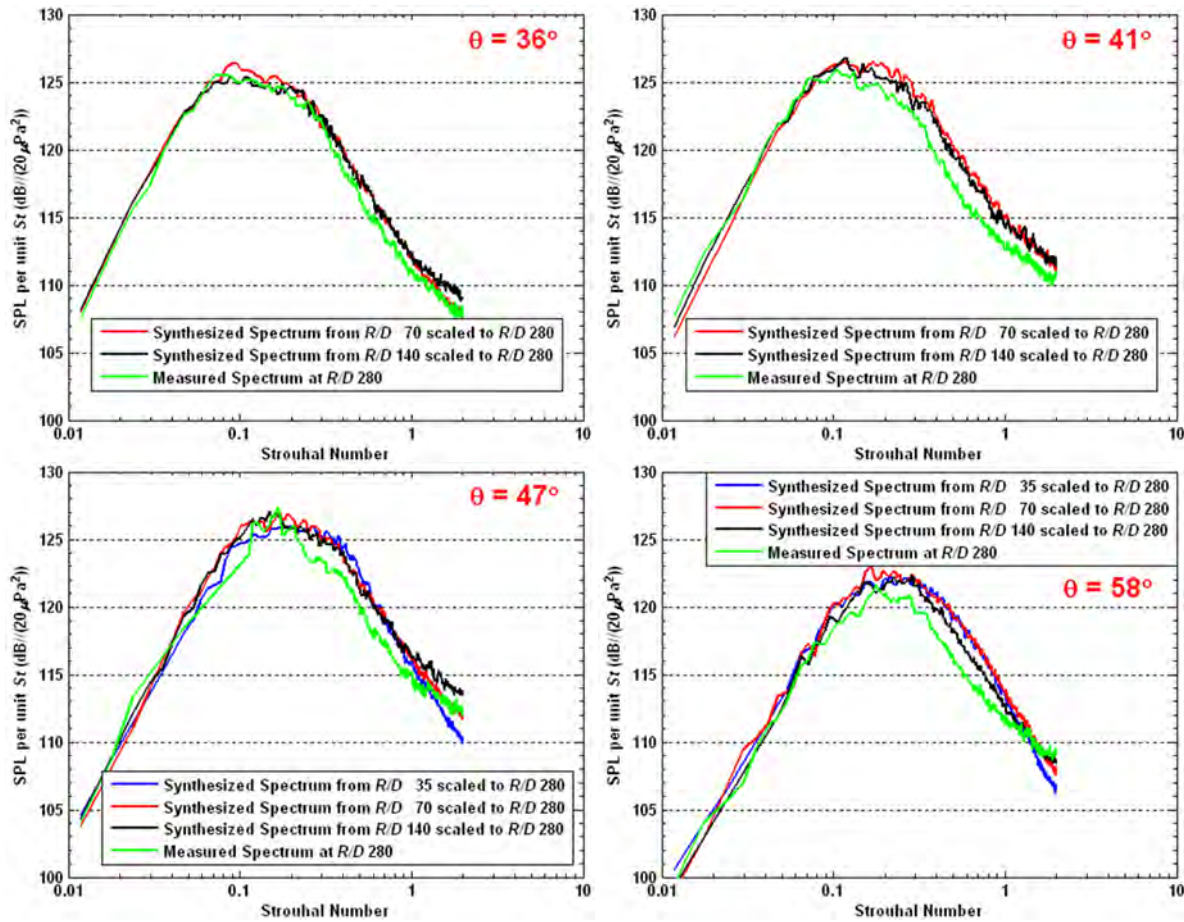


Figure 36. Acoustic measurements conducted with CD nozzle ($M_d = 1.5$, $D = 0.5$) operated at $M_j = 1.5$, $TTR = 2.2$, as measured $R/D = 280$. Synthesized spectra were reconstructed respectively from $R/D = 35$, 70 , and 140 and scaled $R/D = 280$.

the noise production regions within supersonic jets in order to better understand the source of the spectral mismatches between measurements at various radial locations. Based on noise source location measurements by several investigators, an advanced processing method has been developed to allow for a more accurate comparison of spectral measurements from vastly different distances from the nozzle exit plane.

Acoustic measurements conducted at four radial distances with fully expanded both cold and simulated hot jets were presented. Direct comparison of the experimental results demonstrated that measurements at the non-dimensional distance of 70 nozzle diameters do not produce the best accuracy to predict the geometric far field. Discrepancies among the measurements acquired at various radial locations were observed and documented. By using reliable measurements of the jet noise source distribution, synthesized spectra were obtained from acoustic field measurements (35 to 70 diameters) to accurately reproduce measured spectra in the geometric far field (140 diameters). This methodology strengthens the accuracy and understanding of the scaling methodology when making comparisons with the measurements obtained from nozzles of different sizes or from different facilities with disparate radial locations.

of the microphones. Moreover, it can be concluded from these data that for very hot exhaust jets such as the ones encountered in military aircraft, the threshold distance of the geometric far field is located much further than the non-dimensional distance $R/D = 50$ used for subsonic cold jets.

The current methodology has been extended to examine the nonlinear propagation effects. The phenomenon of nonlinear propagation in the trial case is observed in the frequency domain by the Morfey-Howell nonlinearity indicator and in the time domain with the pressure time histories. For a detailed spectral comparison, the synthesized spectra provide a better accuracy in examining the identical noise radiation path with the appropriate propagation distance as a function of frequency content. The spectral comparison depicts well the energy loss at mid frequencies and the energy gain at high frequencies.

Task 2.2. Effect of Empennage on Noise Directivity

In order to fully validate the measurements made at Penn State with full scale measurements, integration of the military-design nozzles into an accurate representation of a F35 empennage was performed. The empennage is expected to affect the acoustic spectra by reflecting and scattering some of the acoustic waves, in a way similar to that observed by Papamoschou³³. It may also affect the entrained flow field, with possibly more or less effect with the presence of forward flight. Figure 37 a) shows a picture of the 1/48 empennage model mounted on the baseline nozzle. The empennage and nozzle scales were evaluated to be dimensionally accurate within 10% error with the published specifications of the JSF from the website of Lockheed Martin.

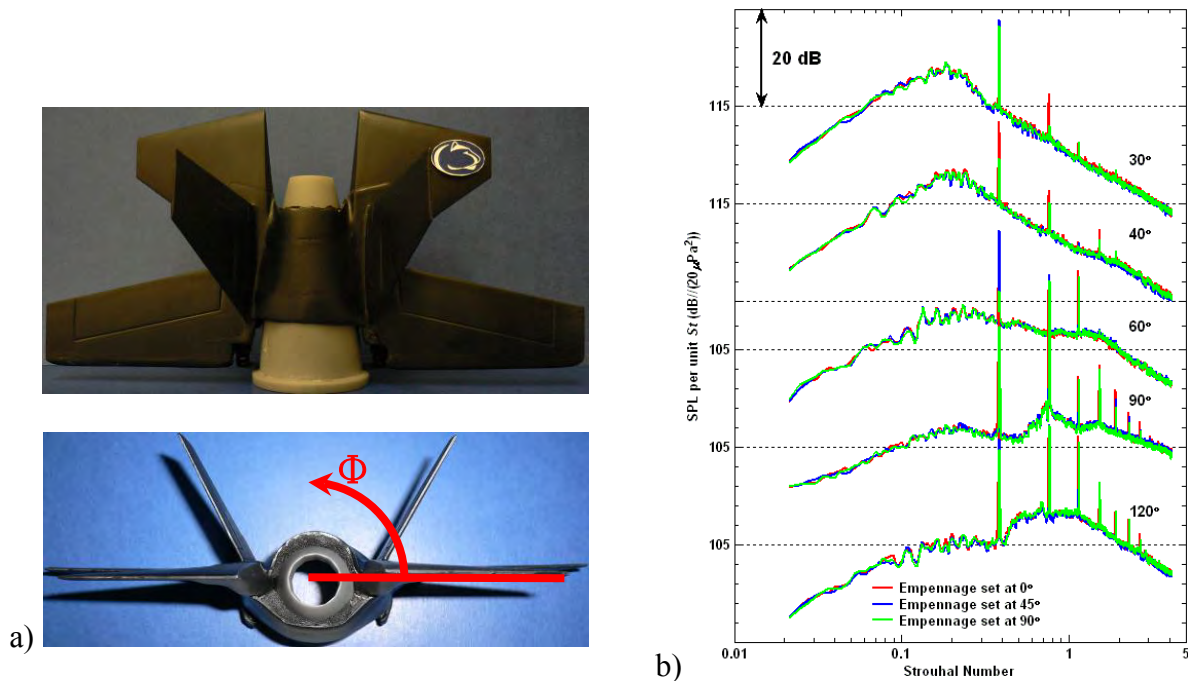


Figure 37 a) 1/48 scale aircraft model end view with model rotating azimuthal angle, ϕ , where red line represents the measured plane of microphone array. b) Spectra comparison from measurements conducted with GE M_d 1.5 baseline nozzle operated at M_j = 1.36, cold accompanied with empennage set at $\phi = 0^\circ, 45^\circ$, and 90° respectively.

A series of measurements were conducted with military-style nozzle of design Mach number 1.5 for a variety of cold jet conditions with M_j varying from 1.3 to 1.7, with and without the empennage model. The experiments include three various azimuthal angles for the empennage model, as defined from the picture of Figure 37 a). For all values of M_j tested and all azimuthal angles, no effect was observed due to the presence of the empennage. Figure 37 b) shows sample spectra, acquired at $M_j = 1.36$ where this jet condition at least shows the subtle modification on the screech intensity level. The spectra present a perfect overlap among all different values of ϕ . Extension of these measurements with the addition of a surrounding forward flight simulating flow also showed no acoustic effects of the empennage model.

Task 2.3 Tests of Additional Noise Reduction Concepts

The emergence of louder, more powerful fighter aircraft has led to research into supersonic jet noise reduction devices. Noise emitted towards the ground is most important during the takeoff segment of the flight profile (which results in jet exhaust flow that is typically over-expanded). Laboratory measurements are important so that noise reduction concepts can be evaluated early in the design process. In the past, acoustic measurements from the heated anechoic facility at the Pennsylvania State University have been compared to acoustic measurements from larger scale heated anechoic facilities with excellent results. This was demonstrated in the previous sections. Beveled exits for subsonic nozzles rotate the jet plume and primarily reduce noise through the subsequent rotation of the acoustic field. This is not the case for beveled exits on supersonic converging-diverging nozzles. The jet plume from such nozzles has been examined and shown to deflect less than 5 degrees for both over- and under-expanded flows. Therefore the measured noise reduction in converging-diverging nozzles results from an alteration of the noise generation mechanisms. A new method of rotating the exit plane about the centerline has been used to create the beveled nozzles. This results in an extension of the bottom lip and a shortening of the top lip. Beveled nozzles with the exit plane rotated 24 and 35 degrees have been tested in addition to a baseline nozzle. Results show that for heated jets, noise in the peak emission direction was reduced by 3-4 dB on the long lip side of the nozzle. For over-expanded flows there was very little gain or reduction in the sideline broadband shock associated noise. Similar magnitudes of noise reductions were still present with the forward flight capability being used.

As the public pays more attention to and requests the reduction of noise levels around airports and military bases there is a strong need to reduce aircraft noise, especially that of military aircraft. The noise produced by military aircraft while taking off from aircraft carriers has a long term negative effect on the crews of these vessels. Efforts are currently being made to develop new methods to reduce the noise produced by such aircraft. Many new design concepts, which alter the nozzle shape, have already been investigated. These include chevrons, corrugations, non-axisymmetric geometries, and beveled nozzles. Research is being conducted to better understand these designs and improve them through an understanding of their noise suppression mechanisms. The most successful of these methods achieves its results through faster mixing in the shear layer and a decrease of the perimeter and the length of the potential core with downstream distance from the nozzle exit. Both chevrons and corrugations are examples of designs that use this method. Additionally, nozzle geometry has been altered to rectangular or elliptic nozzles to attempt to achieve a noise benefit at different azimuthal angles (such as decreased noise levels in the major axis plane, but with increased levels in the minor axis).

The high speed jet noise laboratory at the Pennsylvania State University (PSU) has contributed to these studies of jet noise source generation and suppression mechanisms for some time. In the past, studies were performed on a purely converging beveled nozzle³⁴, and the investigation of rectangular nozzles with thrust vectoring³⁵. More recently, studies described in this report have been performed that focus on more realistic and accurate representations of military style nozzle geometries and noise reduction concepts for these nozzles. These studies were performed in collaboration with NASA and GE Aviation and used nozzles which replicated the exhaust installed on the F-18 aircraft. This nozzle uses multi-faceted flat sections in both the convergent and divergent sections of the nozzle. These sections can slide between each other to allow for the

control of the exit and throat area and thus the area ratio of the nozzle. The control of the area ratio allows the engine to be operated more efficiently with a wider flight envelope. Baseline nozzle measurements were performed on these small scale nozzles (1/35 full scale) at PSU^{5,7}, with good agreement demonstrated between moderate scale data acquired at NASA Glenn Research Center (GRC). Afterwards experiments were performed at PSU to investigate the noise reduction potential of chevrons on the supersonic military-style nozzle³⁶.

Purely converging beveled nozzles have been shown to produce a significant deflection of the jet plume. It appeared that there was also an accompanying rotation of the acoustic field. Until recently, the same was believed to be true for supersonic converging-diverging beveled nozzles. A recent study by Viswanathan and Czeh³⁷ documented the use of a bevel on a converging-diverging supersonic nozzle. The present task aims to extend these results with a slightly different methodology in the design of the nozzle bevel. The laboratory facility at PSU allows for reliable, inexpensive measurements that, early in the design process, can help select the most-promising

Experimental facilities, set-up, and procedure

The Pennsylvania State University high speed jet noise facility was described in an earlier section of this report (see Figure 15). The air for the facility is supplied by a CS-121 compressor combined with a KAD-370 air dryer, both of which were manufactured by Kaeser Compressors. The compressor fills a tank which then supplies the air for the piping system. The air flow is controlled using a series of pressure regulators and control valves located within a piping cabinet near the workstation, which supplies air to the plenum within the chamber. The end of the plenum was designed in such way that different geometry jet nozzles can be easily attached and tested. A pitot probe is embedded in the middle section of the plenum which, via a calibrated pressure transducer, provides the total pressure upstream of the nozzle. The facility uses helium-air jet mixtures to simulate heated air jets. The partial pressures of both the helium and air can be regulated in the piping cabinet to produce the desired result. This methodology was demonstrated and developed by Doty and McLaughlin. The anechoic chamber walls are covered with fiberglass wedges and it has an approximate cut-off frequency of 250 Hz. Located at the opposite wall of the plenum is an exhaust collector and fan which minimizes any possible helium accumulation.

Additionally this facility has been upgraded to include a forward flight simulation capability in the noise measurements. Air is drawn from an upstream fan and exhausted through a square nozzle (15 inches wide) in an open jet surrounding the jet nozzle. This system can simulate forward flight around the jet stream up to a Mach number of 0.17 (58 m/s).

Acoustic measurements are currently performed using six microphones, each of which is supported by a boom that extends from the plenum stand, which can also be seen in Figure 16. The microphone array can be freely rotated around a point located at the center of the nozzle exit plane. The microphones are positioned so that the ends are at a grazing incidence to the centerline of the jet exhaust and are equally spaced every 10° from the jet axis. The average physical radial distance of all the microphones to the nozzle exit is 70 inches. When testing jet nozzles smaller than 1 inch in diameter this allows for the microphones to be considered in the

acoustic far field. Because the microphones are assumed to be located in the acoustic far field, spherical spreading can be applied to the data to propagate it to different (far-field) radial positions.

Model geometry of military-style supersonic converging-diverging beveled nozzles

The results presented in this task were conducted with military style nozzles representative of aircraft engines of the F404 (used in the F-18 aircraft) family. The inner contours of the military style nozzles were provided by General Electric Aviation. Such military engines have nozzles which are capable of varying their geometry to produce different exit to throat area ratios to adapt for different flight regimes. The expansion portion of these nozzles contains a flap and seal configuration that consists of 12 flat segments that are interleaved to facilitate area adjustment of the operational nozzles. For this research, one exit to throat area ratio was selected at a typical configuration for a takeoff scenario of one of these aircraft. The area ratio selected was 1.295. The nozzles were then designed with the same multi-faceted (12 segments) conical inside contour. The nozzles were fabricated using a rapid prototyping technique of fused deposition modeling with ABS plastic with a 0.254 mm (0.01 in.) standard layer thickness. More details concerning these military style supersonic nozzles can be found in Kuo, Veltin, and McLaughlin.

A beveled nozzle is a nozzle which has the exit plane rotated at an oblique angle to the nozzle axis instead of perpendicular to it. For a supersonic converging-diverging nozzle, there are many ways in which a bevel could be added to the end of the nozzle. The methodology created and used for the present task was to rotate the exit plane with the center of rotation at the center of the original exit plane. This extends the bottom lip of the nozzle and shortens the top of the nozzle. This method was chosen because it results in a projected area ratio (exit area perpendicular to the flow) of the bevel exit which is closest to the baseline area ratio. For the angles used, the percent change in perpendicular exit area was less than 0.3%. A two-dimensional cross sectional drawing of this methodology can be seen in Figure 38 as well as an

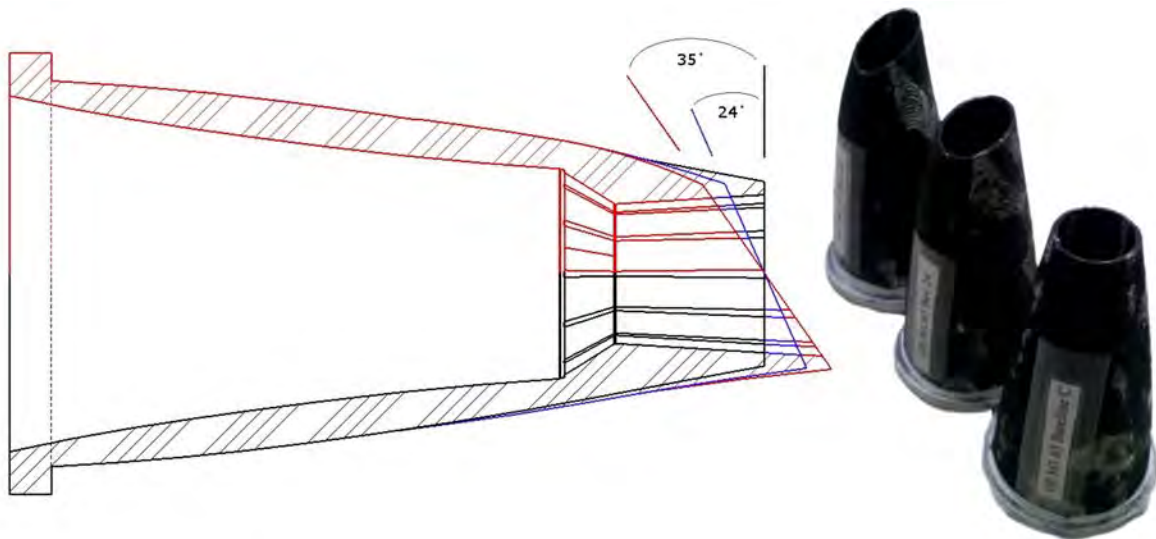


Figure 38. The Beveled Nozzles – Left: 2-D Cross-Sectional Drawing; Right: Image of Rapid Prototyped Nozzles.

image of the actual rapid-prototyped nozzles. There were three nozzles used in this study: the Baseline (0° bevel), Bevel24 (24° bevel), and Bevel35 (35° bevel). For these beveled nozzles the azimuthal angle, ϕ , is taken to be 0° on the long lip side and 180° on the short lip side. This angle convention is shown in Figure 39.

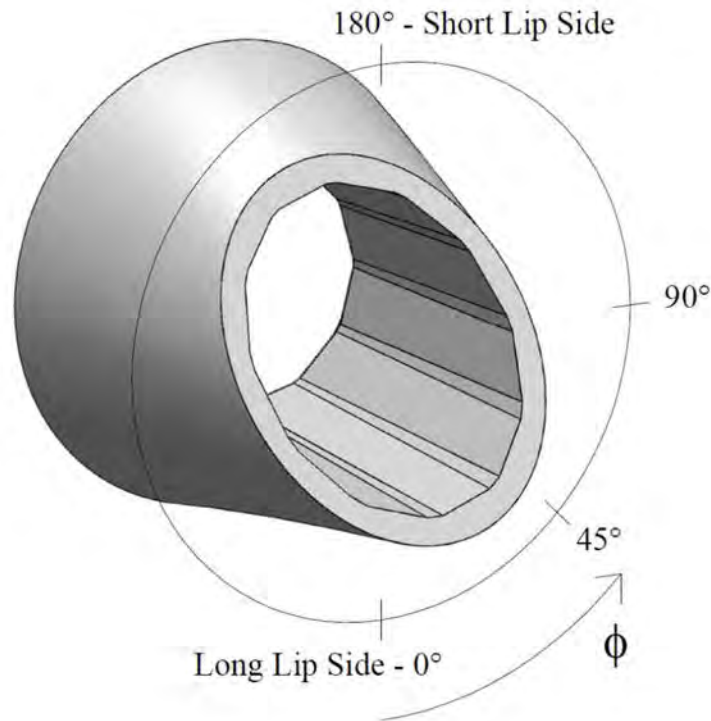


Figure 39. Schematic Showing the Convention for the Azimuthal Angle (ϕ).

Experimental Results

Flow-field images

The three different beveled nozzles were tested at many different nozzle pressure ratios (*NPR*). The jet exit Mach number can be calculated from the nozzle pressure ratio using the isentropic flow relations. The design Mach number of the nozzle is the Mach number at the exit if the flow is expanded from the high pressure to exactly ambient pressure. Therefore when a nozzle has a nozzle pressure ratio applied which results in a jet Mach number which is lower than the design Mach number, the flow is said to be over-expanded. When they are the same, the flow is perfectly expanded, and when the exit pressure is higher than the ambient pressure (jet Mach number higher than design Mach number) the flow is under-expanded. Typical military jet engines have over-expanded flow during the takeoff portion of the flight profile.

Figure 40 shows nine different shadowgraph images taken during the experiments. A shadowgraph is a light refraction technique that can be related to the strength of the gradient of the density field within the flow. It is best for visualizing shock waves. Settles gives a detailed

analysis of shadowgraphy³⁸. Figure 40 contains the shadowgraphs for all three nozzles ($TTR = 1$) when over-expanded, nearly perfectly expanded, and under-expanded. It is important to note that because of the method used to create shadowgraph images, the flow appears to be two-

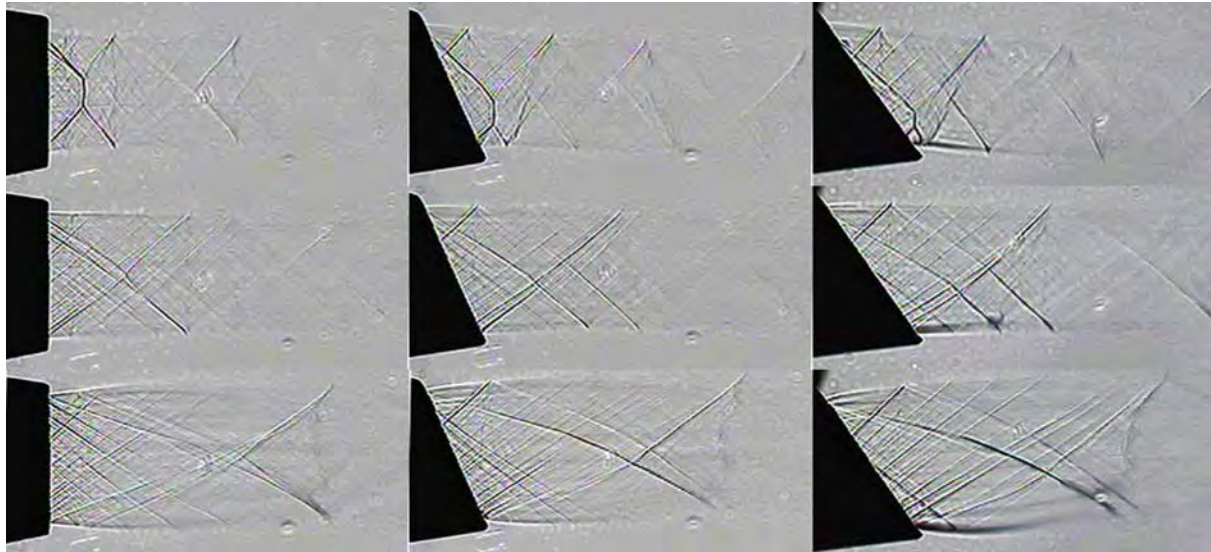


Figure 40. Shadowgraph Images – Top Row: $M_j = 1.4$; Center Row: $M_j = 1.6$; Bottom Row: $M_j = 1.9$. Left: Baseline Nozzle; Middle Bevel24 Nozzle, Right: Bevel35 Nozzle

dimensional. This however is not the case, as the turbulent flow from these jet exhaust nozzles is fully three-dimensional.

For the baseline nozzle, the shock cell structure within the jet plume can clearly be seen for the over-expanded and under-expanded flow. As would be expected, the nearly perfectly expanded flow from the baseline nozzle shows only weak shocks, which result because the nozzle is a straight walled converging-diverging nozzle instead of a contoured converging-diverging nozzle designed to eliminate non-uniformities in the velocity at the nozzle exit.

The shadowgraph images of the beveled nozzles show how the flow changes because of the extension of the bottom lip, and the shortening of the top lip. The first thing that should be noticed is the deflection of the flow when compared to the baseline nozzle flow. The over-expanded flow ($M_j = 1.4$) is deflected towards the long lip side, with an average deflection of 3.4° for the Bevel24 nozzle and of 5.3° for the Bevel35 nozzle. On the other hand, the under-expanded flow ($M_j = 1.9$) is deflected towards the short lip side, with an average deflection of 3.5° for the Bevel24 nozzle and of 5.77° for the Bevel35 nozzle.

The second thing to be seen is the change in the shock cell structure. Both the over-expanded and under-expanded flows show the shock cell shifting down towards the long lip. Additionally, the strength of the shock appears to increase as the bevel nozzle angle increases.

In addition to the cold jet shadowgraph images, schlieren images were also taken, this time with helium-air mixture jets. Figure 41 shows three schlieren images of the flow with helium-air being used to simulate a total temperature ratio, TTR , of 3. In these images the strong index of refraction of the turbulent helium-air mixture, located in the shear layer, masks the shock cell

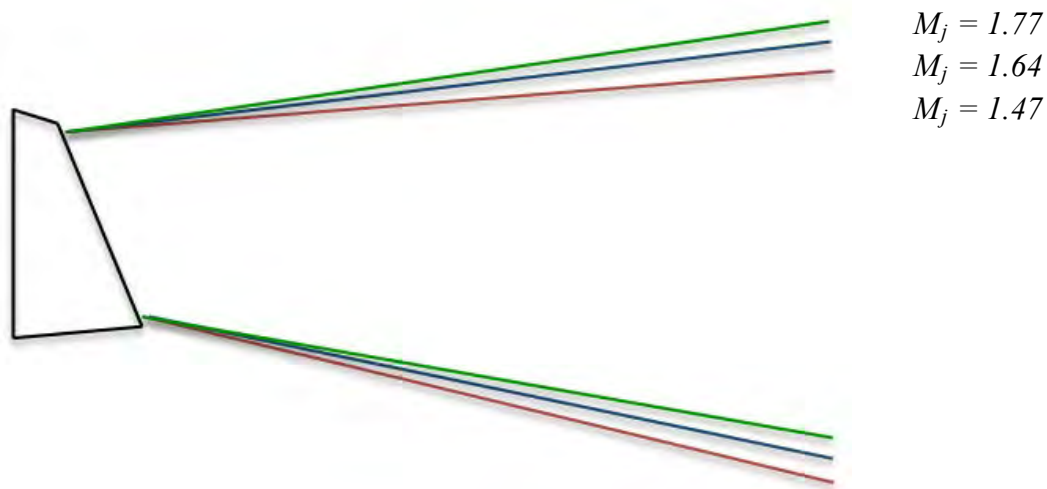


Figure 41. Top – Schlieren Imagery of the Bevel24 Nozzle with M_j (from Left to Right) = 1.47, 1.64, 1.77. Bottom – Comparison of the Flow Exit Angles at $M_j = 1.47, 1.64, 1.77$.

structure located more in the inner portion of the jets. The strong Mach wave radiation can also be seen for all three conditions. Also shown in Figure 41 is a schematic that compares the deflection angles for the three conditions. Again the small deflection angles can be seen here.

Beveled nozzle thrust estimates

As noted by Viswanathan and Czech cutting back the nozzle on the top portion actually produces additional thrust when the jet is operating at an over-expanded pressure ratio in comparison with the baseline nozzle. The additional thrust is a result of the reduction of drag that occurs on the nozzle for all downstream positions in which the local pressure within the nozzle has expanded to a pressure below the exterior ambient pressure. Figure 42 shows a plot of the pressure distributions calculated from simple quasi-one-dimensional isentropic flow theory for an approximation to the beveled nozzle (for an over-expanded nozzle pressure ratio condition). The portion of the pressure distribution on the long lip side of the nozzle, where the pressure is substantially lower than ambient, produces a net drag on that portion of the nozzle. In the upper portion of the nozzle (the short lip side) there is almost no drag on any portion of the nozzle.

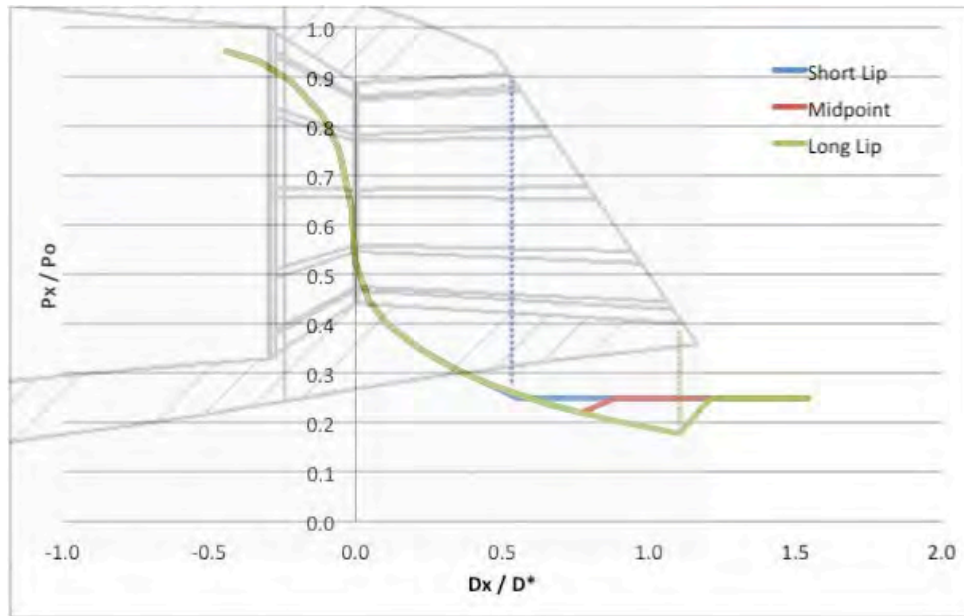


Figure 42. Overlay of the Pressure Distribution inside the Nozzle at the Short Lip Side, Midpoint, and Long Lip Side

At a altitude, in c cruise operation, an aircraft nozzle would be operating at s substantially higher pressure ratio and the long lip side of the nozzle would have a much longer portion of positive thrust. Very simple calculations of this type suggest that a beveled nozzle of roughly this shape could be designed to sacrifice less than 1 % of its thrust over the range from take-off to high altitude cruise.

Acoustic results and noise reduction

The acoustic field that results from the exhaust of military style nozzle jets is complicated. In its simplest form it can be reduced to the peak emission noise, and the broadband-shock associated noise (BBSAN) components. The peak emission noise is a lower frequency, higher amplitude noise when compared to the BBSAN. Also, the peak emission noise is typically radiated at angles of 40 to 50 degrees from the jet downstream axis, whereas BBSAN is emitted at higher angles to the jet axis in the sideline direction. When evaluating any noise reduction method, the changes, when compared to the baseline nozzle, in the peak emission noise and BBSAN must be considered. Table 4 presents the entire run conditions performed in this task. Relevant and meaningful acoustic comparisons were selected from all of these conditions.

Acoustic measurements were first taken with the baseline nozzle with no beveled exit, for a range of flow conditions. These measurements were followed with those made with beveled nozzles of two different bevel configurations. Each of the two nozzles were rotated to two azimuthal angles so the long lip of the nozzle was closest to the microphone array, then the nozzle was rotated 180°, so the short lip was pointed towards the microphone array. The sound pressure level spectrum from all polar angles was then recorded for both of these configurations.

Table 4. Nozzle parameters and jet conditions for all experiments run for this task

Nozzle	Jet Mach Number (M_j)	TTR	Polar Angle (θ) of 1st Mic	Azimuthal Angle (ϕ)	M_f
Baseline	1.2 , 1.3 , ... , 2.1 , 2.2	1	20° , 80°	-	0
Bevel24	1.2 , 1.3 , ... , 2.1 , 2.2	1	20° , 80°	0° , 180°	0
Bevel35	1.2 , 1.3 , ... , 2.1 , 2.2	1	20° , 80°	0° , 180°	0
Bevel24	1.4 , 1.5 , 1.65 , 1.8 , 1.9	1	20° , 80°	45° , 90°	0
Bevel35	1.4 , 1.5 , 1.65 , 1.8 , 1.9	1	20° , 80°	45° , 90°	0
Baseline	1.47 , 1.64 , 1.77	3	20° , 80°	-	0
Bevel24	1.47 , 1.64 , 1.77	3	20° , 80°	0° , 45° , 90° , 180°	0
Bevel35	1.47 , 1.64 , 1.77	3	20° , 80°	0° , 45° , 90° , 180°	0
Baseline	1.47	1	20° , 25° , 80° , 85°	-	0.17
Bevel35	1.47	1	20° , 25° , 80° , 85°	0° , 45°	0.17
Baseline	1.47	3	20° , 25° , 80° , 85°	-	0.17
Bevel35	1.47	3	20° , 25° , 80° , 85°	0° , 45°	0.17

Figure 43 shows the spectrum for five different polar angles emitted from the long lip for a heat simulated over-expanded flow condition from all three nozzles. Below the spectrum is the variation in OASPL over a range of polar angles for all three nozzles. Figure 44 is similar, but shows the noise produced from the short lip side of the beveled nozzles. It can be seen that on the long lip side there is a reduction in peak emission noise of about 4 dB for the Bevel35 nozzle,

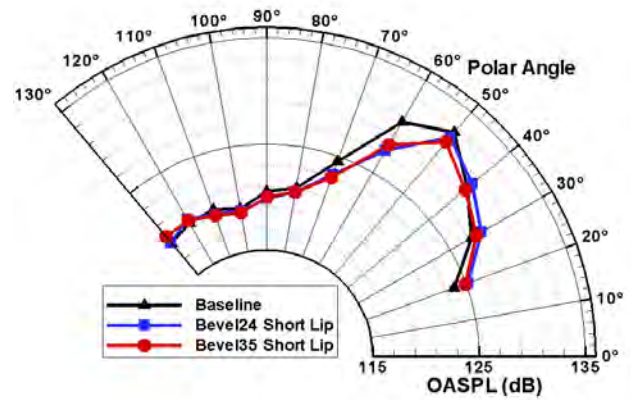
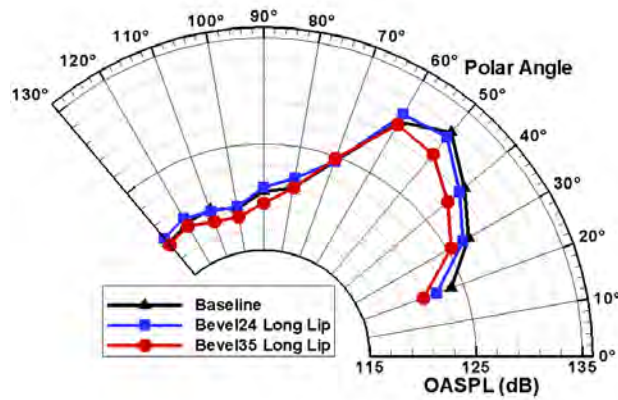
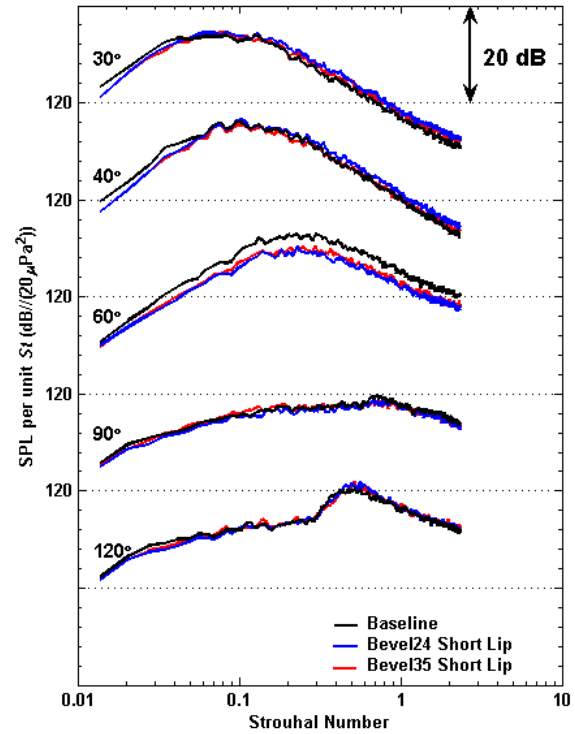
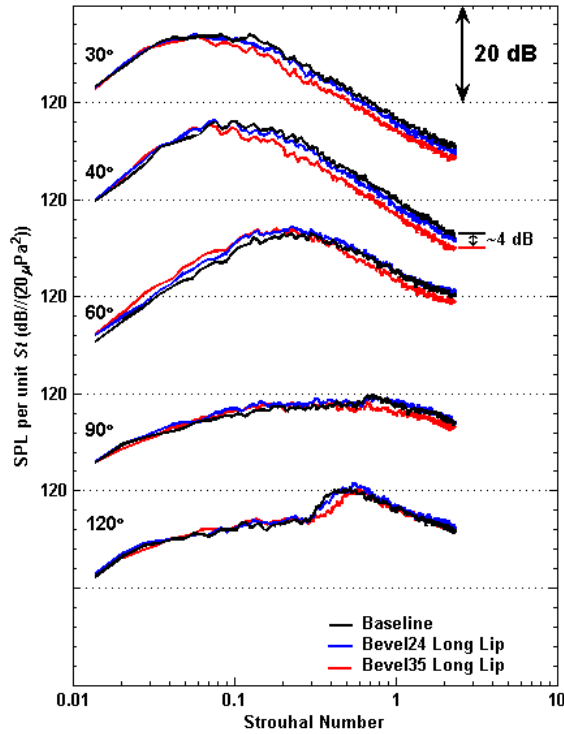


Figure 43. Spectra and OASPL Comparison of Heated jets, measured at $\phi = 0^\circ$ (Long Lip Side), issuing from GE C-D $M_d = 1.65$ Beveled Nozzle, with $M_j = 1.47$, $TTR = 3$, $D_{noz} = 0.708''$, $f_c = 42693$ Hz, Scaled $R/D_j = 100$

Figure 44. Spectra and OASPL Comparison of Heated jets, measured at $\phi = 180^\circ$ (Short Lip Side), issuing from GE C-D $M_d = 1.65$ Beveled Nozzle, with $M_j = 1.47$, $TTR = 3$, $D_{noz} = 0.708''$, $f_c = 42693$ Hz, Scaled $R/D_j = 100$

with slightly less than that for the Bevel24 nozzle. There is very little noise reduction or gain in the BBSAN. On the short lip side, there is a slight increase in peak emission noise, with almost

no change to the BBSAN. The *OASPL* comparison reinforces these conclusions for the noise on the long lip side, with noise reduction being seen in the low polar angles (20°-50°) and similar noise levels for all other polar angles. The *OASPL* measured from the short lip side can be seen to be nearly identical to the baseline nozzle.

Figure 45 and Figure 46 show similar spectra as Figure 43 and Figure 44, but for a nearly perfectly expanded flow with a total temperature ratio of 3. It is noted that for noise, the perfectly expanded pressure ratio condition is normally of much less importance than the over-expanded condition that occurs at take-off. It is included here to help complete our understanding of the noise generation physics. For this perfectly balanced case, a reduction of about 3 dB can be seen in the peak noise emission on the long lip side. On the short lip side, there is very little change. From examination of the BBSAN it can be noticed that both beveled nozzles increase the SPL at the peak by about 6-7 dB. This is expected following examination of the shadowgraph images in Figure 40 that showed stronger shocks in the nearly perfectly expanded flow.

A more in depth azimuthal investigation on the noise field was then conducted with measurements taken of the noise emitted at azimuthal angles of 45° and 90°. The relevance of the higher degree azimuthal measurements is that during take-off, the quadrant containing the 45° to 90° direction most closely aligns with sideline microphones in aircraft noise certification.

Figure 47 shows the comparison at a heat-simulated over-expanded condition between these two new azimuthal angles with the baseline measurements, and the long lip side for reference. Only the Bevel35 nozzle is shown in this comparison. Both the spectra and the *OASPL* for all polar angles show that the noise produced at an angle of 45° is nearly identical to the baseline nozzle noise. The noise produced at an angle of 90° (directly in between the short and long lip) can be seen to be louder than the baseline nozzle. The magnitude of gain at 90° is similar to the magnitude of reduction seen on the long lip side.

Figure 48 shows a comparison between the azimuthal angles for the nearly perfectly expanded heat-simulated nozzle condition. The same trends as seen in the under-expanded case can be seen here with the addition of a noise gain at all azimuthal angles in the upstream direction. This was previously noticed and believed to be due to the increasing strength of the shock cell structure. The magnitude of reduction and gain for the perfectly expanded jet is slightly less than that of the over-expanded jet.

Next, the noise characteristics of the beveled nozzles, in the presence of forward flight, was investigated. Figure 49 shows the spectral and *OASPL* comparison for the over-expanded heat-simulated condition between the static noise and the noise with a forward flight Mach number of 0.17. Figure 50 shows the spectral and *OASPL* comparison between the baseline nozzle and the Bevel35 nozzle measured at two azimuthal angles, the long lip side ($\phi = 0^\circ$) and $\phi = 45^\circ$. When comparing the long lip side and the baseline, there is still a reduction of approximately 4 dB in the peak noise direction. Additionally, at high polar angles in the upstream direction there is a reduction of about 2 dB that was not present in for static tests. This could be due to the forward flight stream lessening the strength of the shock cells in the beveled nozzle jet. The noise produced at $\phi = 45^\circ$ is also no longer identical to the baseline nozzle noise. There is a slight reduction when compared to the baseline at very low polar angles (20° - 40°) and an increase at

intermediate polar angles (60° - 80°).

Conclusions

Acoustic measurements from small-scale heated jets issuing from supersonic converging-diverging nozzles have been previously shown to compare very well to acoustic measurements from larger scale heated jets. This study examined the noise reduction potential of the concept of beveling the nozzle exit. Beveled exits for supersonic converging-diverging nozzles have only sparsely been explored. When using a new method of creating the nozzle exit bevel (which rotates the exit plane base on the center, thereby extending the bottom lip and shortening the top lip) the results show very good potential for noise reduction. The deflection angle of the jet plumes issuing from supersonic converging-diverging beveled nozzles is very small ($<5^\circ$).

For over-expanded jets without forward flight there is a noise reduction of ~ 4 dB on the long lip side in the peak noise emission direction; for nearly perfectly expanded jets there is a noise reduction of ~ 3 dB. In addition, the short lip side does not show an increase in noise of the same magnitude as the reduction on the long lip side. The BBSAN is affected very little for the over-expanded jets, whereas there is a noticeable rise in the peak of the BBSAN for the nearly perfectly expanded jets due to the presence of stronger shock cells.

The noise field produced by supersonic converging-diverging beveled nozzles appears to be at a minimum on the long lip side then approaches the baseline noise levels when an azimuthal angle of 45° is reached. The noise then increases at an angle of 90° , then decreases back down to baseline levels on the short lip side. Assuming the long lip side would be oriented in the downward direction on an aircraft, such nozzles would produce a modest noise reduction for very little thrust loss penalty.

Finally, the presence of a forward flight stream did not negatively affect the noise reduction seen on the long lip side of the beveled nozzle. Similar magnitudes of reduction were seen as in the static tests.

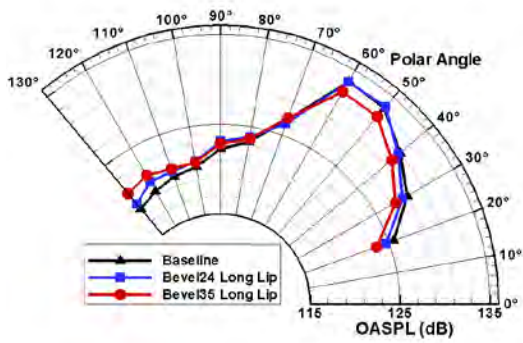
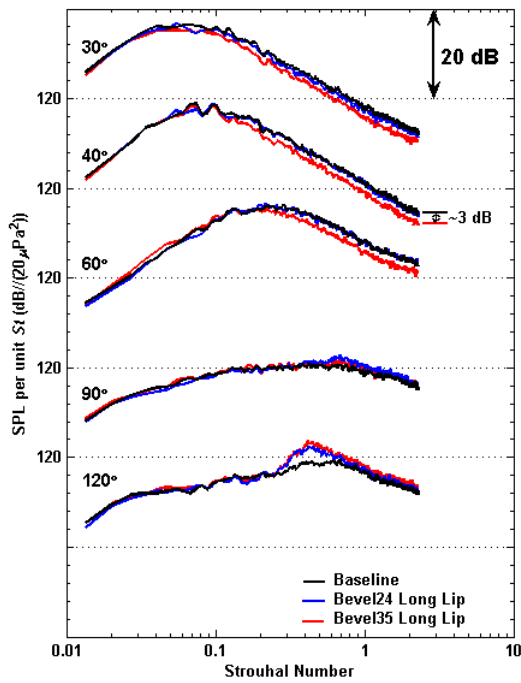


Figure 45. Spectra and OASPL Comparison of Heated jets, measured at $\phi = 0^\circ$ (Long Lip Side), issuing from GE C-D $M_d = 1.65$ Beveled Nozzle, with $M_j = 1.64$, $TTR = 3$, $D_{noz} = 0.708''$, $f_c = 43644$ Hz, Scaled $R/D_j = 100$

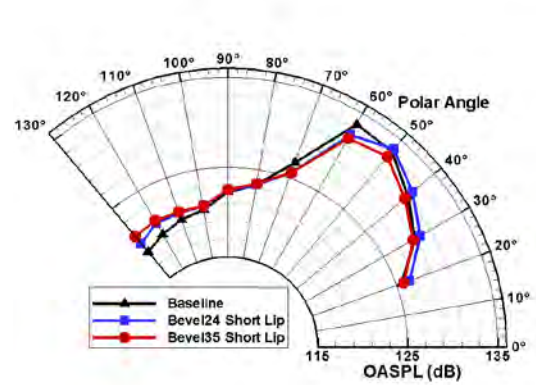
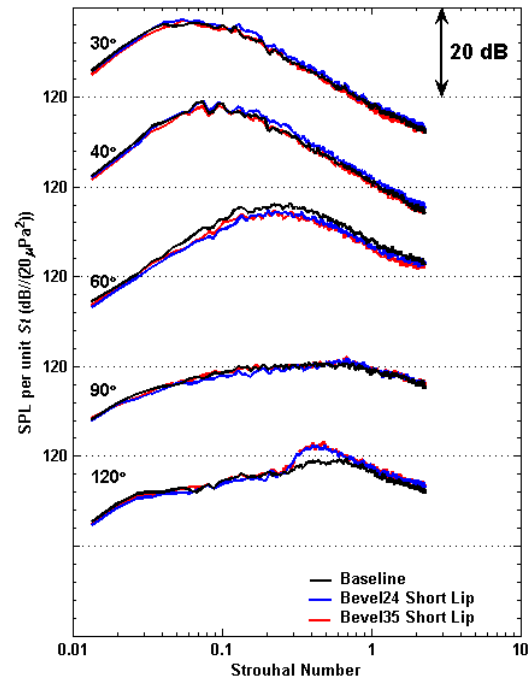


Figure 46. Spectra and OASPL Comparison of Heated jets, measured at $\phi = 180^\circ$ (Short Lip Side), issuing from GE C-D $M_d = 1.65$ Beveled Nozzle, with $M_j = 1.64$, $TTR = 3$, $D_{noz} = 0.708''$, $f_c = 43644$ Hz, Scaled $R/D_j = 100$

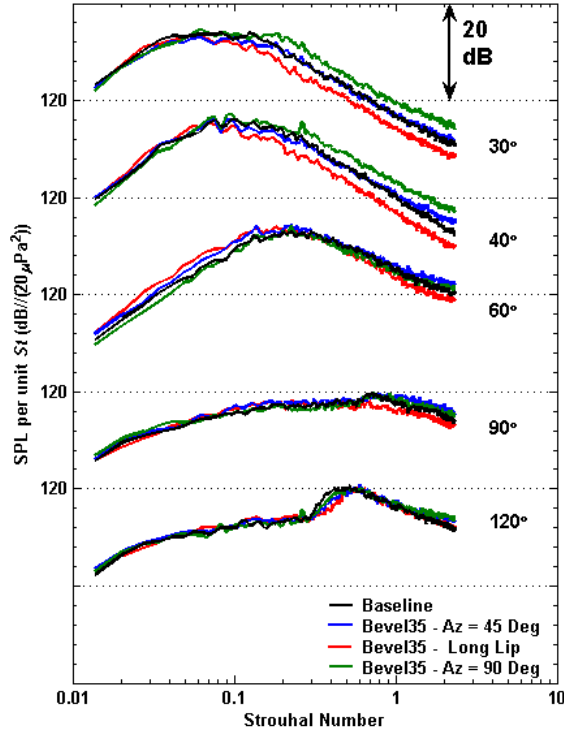


Figure 47. Spectra and OASPL Comparison of heated jets issuing from GE C-D $M_d = 1.65$ Beveled Nozzle, with $M_j = 1.47$, $TTR = 3$, $D_{noz} = 0.708''$, $f_c = 42693$ Hz, Scaled $R/D_j = 100$. The beveled nozzle jet data are shown for various azimuthal angles.

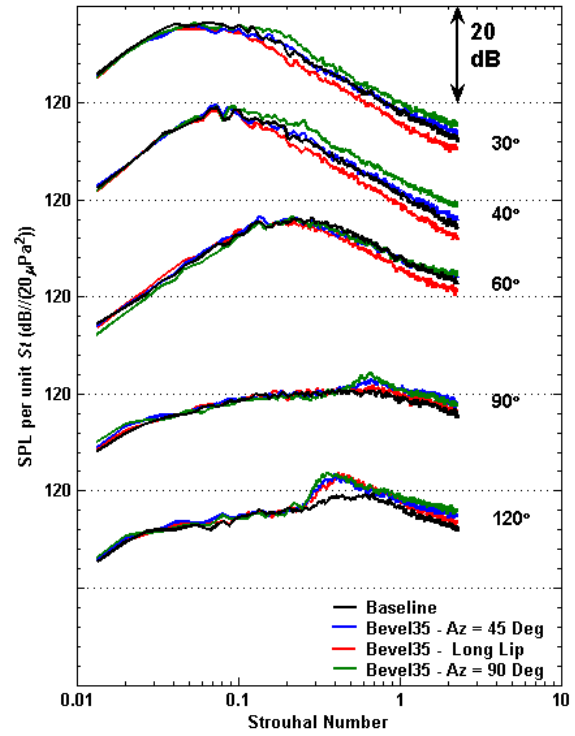


Figure 48. Spectra and OASPL Comparison of heated jets issuing from GE C-D $M_d = 1.65$ Beveled Nozzle, with $M_j = 1.64$, $TTR = 3$, $D_{noz} = 0.708''$, $f_c = 43644$ Hz, Scaled $R/D_j = 100$, again at various azimuthal angles.

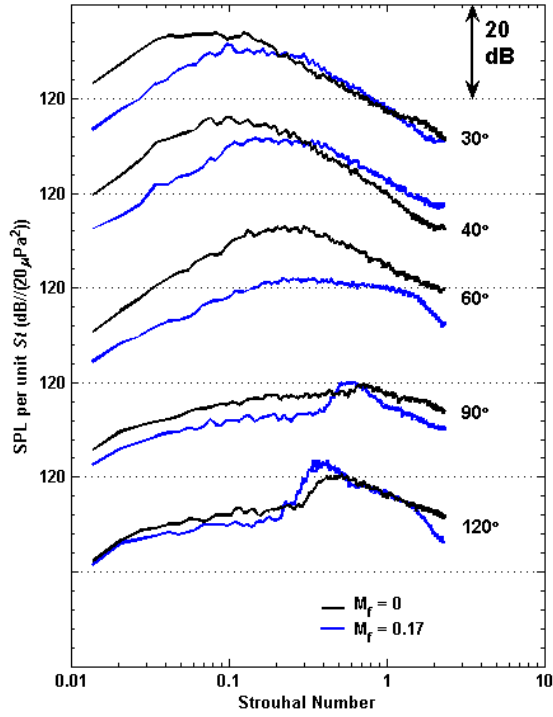


Figure 49. Spectra and OASPL Comparison of Heated Baseline jet with and without Forward Flight, issuing from GE C-D $M_d = 1.65$ Beveled Nozzle, with $M_j = 1.47$, $TTR = 3$, $D_{noz} = 0.708''$, $f_c = 42693$ Hz, Scaled $R/D_j = 100$. The forward flight data have been corrected for outer stream shear layer refraction.

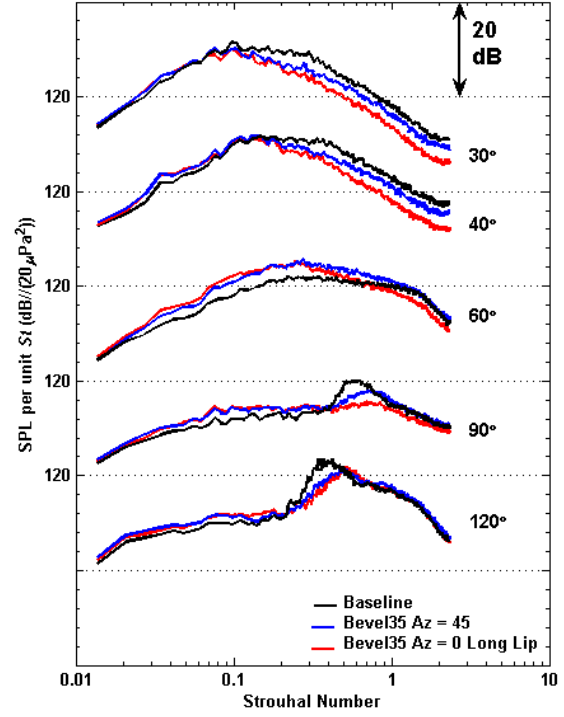


Figure 50. Spectra and OASPL Comparison of Heated jets issuing from GE C-D $M_d = 1.65$ Beveled Nozzle, with Forward Flight of $M_f = 0.17$, with $M_j = 1.47$, $TTR = 3$, $D_{noz} = 0.708''$, $f_c = 42693$ Hz, Scaled $R/D_j = 100$

10.3. Task 3: Moderate Scale Noise Experiments

Task 3.1. Noise Measurements for Baseline Nozzles

Moderate Scale Noise Measurements for Baseline Nozzles

Moderate scale baseline experiments were performed in the Aero-Acoustic Propulsion Laboratory (AAPL) at the NASA Glenn Research Center shown in Figure 51. The AAPL is a 20 m radius geodesic dome treated with acoustic wedges. The AAPL contains the Nozzle Acoustic Test Rig (NATR), which produces a 53 inch diameter simulated forward flight stream (referred to as free jet) reaching Mach numbers of 0.35 and contains the High Flow Jet Exit Rig (HFJER), a dual-stream jet engine simulator capable of replicating most commercial turbo-fan engine temperatures and pressures³⁹.

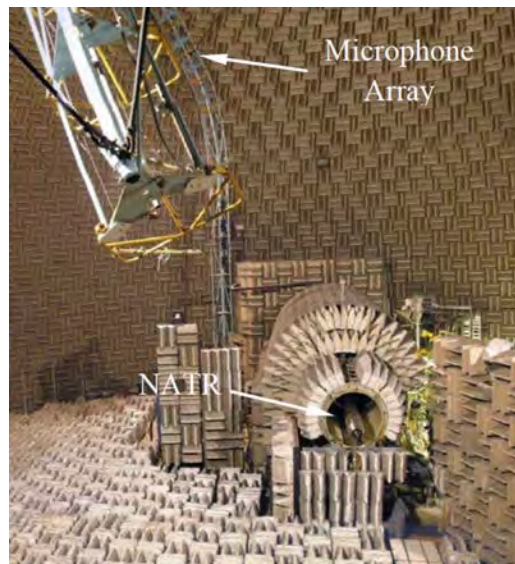


Figure 51. A photograph of the Aero-Acoustic Propulsion Laboratory (AAPL) showing the Nozzle Acoustic Test Rig (NATR).

The nozzle and fan-core splitter shown in Figure 52 were mounted on the HFJER. The fan-core splitter was changed to alter the bypass ratio of the nozzle system. Representative, military-style, convergent-divergent nozzles with throat diameters equal to 4.5 inches were used in the experiments. The nozzles were formed from conical convergent and divergent sections and had facets cut in the internal surfaces of the nozzles to simulate divergent seals. Internal Pockets were machined in the trailing edges of the nozzles as shown in Figure 52. Baseline metal inserts that resulted in smooth nozzle flow lines were used in the pockets for the experiments described in this task. For the experiments described in Task 3.2, chevrons were used in place of baseline metal inserts.

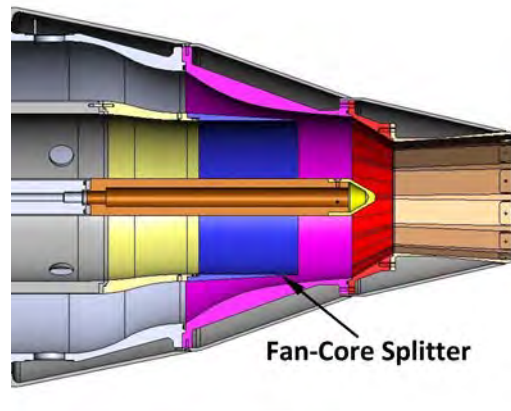


Figure 52. The $M_d = 1.65$ nozzle mounted on the fan stream of the HFJER.

One use of the data was to determine the validity of experiments conducted in small-scale, single-stream jet rigs used to predict noise from military aircraft engines. The impact of bypass flow on the radiated noise is shown in Figure 53. The nozzle pressure ratio, NPR, is the ratio of the jet stagnation pressure to the ambient pressure. The nozzle temperature ratio, NTR, is the ratio of the jet stream temperature to the ambient temperature.

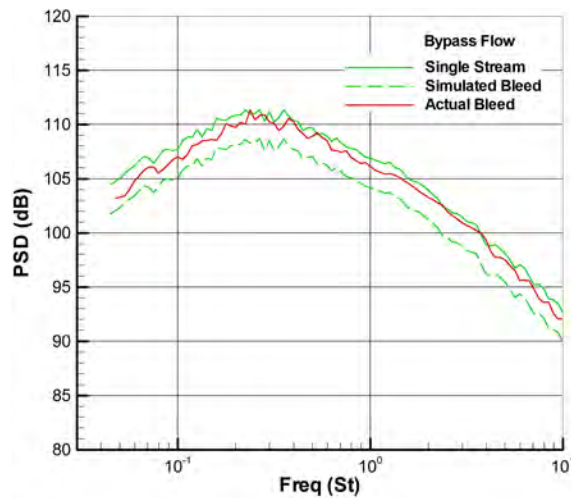


Figure 53. Acoustic data acquired at a 90° observation angle for $NPR_c = 2.5$ and $NTR_c = 3.0$.

The subscripts “c” and “f” refer to the core and fan streams, respectively. The single stream data were acquired by operating the core stream at the specified temperature and pressure with no bypass flow. The “Actual Bleed” data were obtained by operating the core and fan streams at $NPR_c = NPR_f = 2.5$, the core stream at $NTR_c = 3.0$, and the fan stream at $NTR_f = 1.0$. The resulting bypass ratio was 0.28. The “Simulated Bleed” data were obtained by operating the core stream at fully mixed conditions which represent the conditions that would be obtained if “Actual Bleed” flow mixed completely before exiting the nozzle. Observation angles greater

than 90° are in the downstream direction relative to the nozzle trailing edge. These results show that an uncertainty of 2dB can be expected when single-stream rigs are employed and that the single stream jet should be operated at the core stream conditions of the engine.

The photographs in Figure 54 show fluorescent oil applied to the nozzle trailing edge. The photographs were taken before and after operating the jet exit rig at representative takeoff conditions. Separation regions near the nozzle trailing edge are visible in the photograph taken after completion of the test.

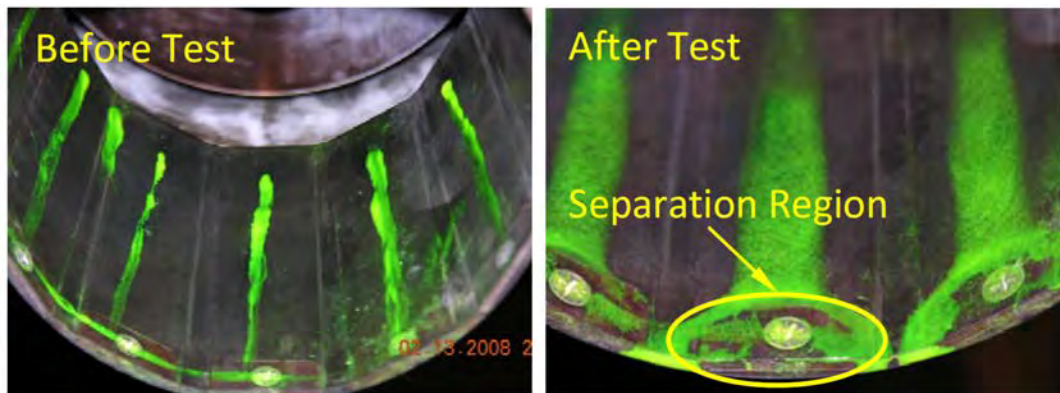


Figure 54. Photographs of fluorescent oil applied to the nozzle trailing edge. The

Substantial documentation of the jet noise spectral directivity of these moderate scale tactical nozzles can be found in the papers written jointly with Penn State University comparing the moderate and small scale jet noise results.

Task 3.2. Noise Measurements for Chevron Nozzles

Moderate Scale Noise Measurements for Chevron Nozzles

The impact of chevron design on acoustic radiation of over-expanded jets was investigated. Chevron penetration, length, and width were varied in an MDOE (Modern Design of Experiments) investigation that resulted in the development of modeled noise reduction for a range of observation angles and jet operating conditions. The chevron designs were guided by extensive prescreening of computational fluid dynamic (CFD) results. The CFD studies showed that altering the levels of the three selected parameters significantly impacted the jet plume TKE. The chevrons appeared to have little impact on shock strength. The effects of forward flight, bypass flow, and nozzle design Mach number on chevron acoustic performance were investigated.

An MDOE (Modern Design of Experiments) investigation was conducted in the AAPL at NASA Glenn Research Center (see Task 3.1 for a facility description) using the nozzles described in Task 3.1 and shown in Figure 55. The nozzle design Mach number was equal to 1.51. The conditions used in the experiments are shown in Table 5. The free jet Mach number is given by M_{fj} and ΔV is the difference in the fully expanded jet velocity and the free jet velocity ($V_{fe} - V_{fj}$). The MDOE study was a full factorial, two-level investigation with three parameters.



Figure 55. The nozzles used in the chevron experiments.

A center point was included in the design to check for model curvature. The chevron design space is shown in Figure 56.

The corresponding chevron parameters are listed in Table 6. Also shown in Table 6

Table 5. Experimental cycle points

Setpoint	NPR _c	NPR _b	NTR _c	NTR _b	M _{fj}	$\Delta V/V_{fe}$
44100	3.00	3.00	3.00	1.00	0.00	
44540	3.50	3.50	3.00	1.00	0.00	
44053	2.00	2.00	2.40	1.00	0.30	0.80
44083	2.50	2.50	2.80	1.00	0.30	0.83
44103	3.00	3.00	3.00	1.00	0.30	0.85
44543	3.50	3.50	3.00	1.00	0.30	0.86

are the configuration designations (quantities in parentheses) used to identify each chevron configuration. The chevrons are identified by two digits following the penetration (P), length (L), and width (W) so a chevron designation of P03L08W06 indicates a chevron with 0.30 inches penetration, 0.75 inches length, and 60% width.

Table 6. Chevron parameters

Parameter	Low Level	High Level	Center
Penetration (inches)	0.3 (P03)	0.6 (P06)	0.45 (P05)
Length (inches)	0.75 (L08)	1.75 (L18)	1.25 (L13)
Width (% facet width)	60 (W06)	100 (W10)	80 (W08)

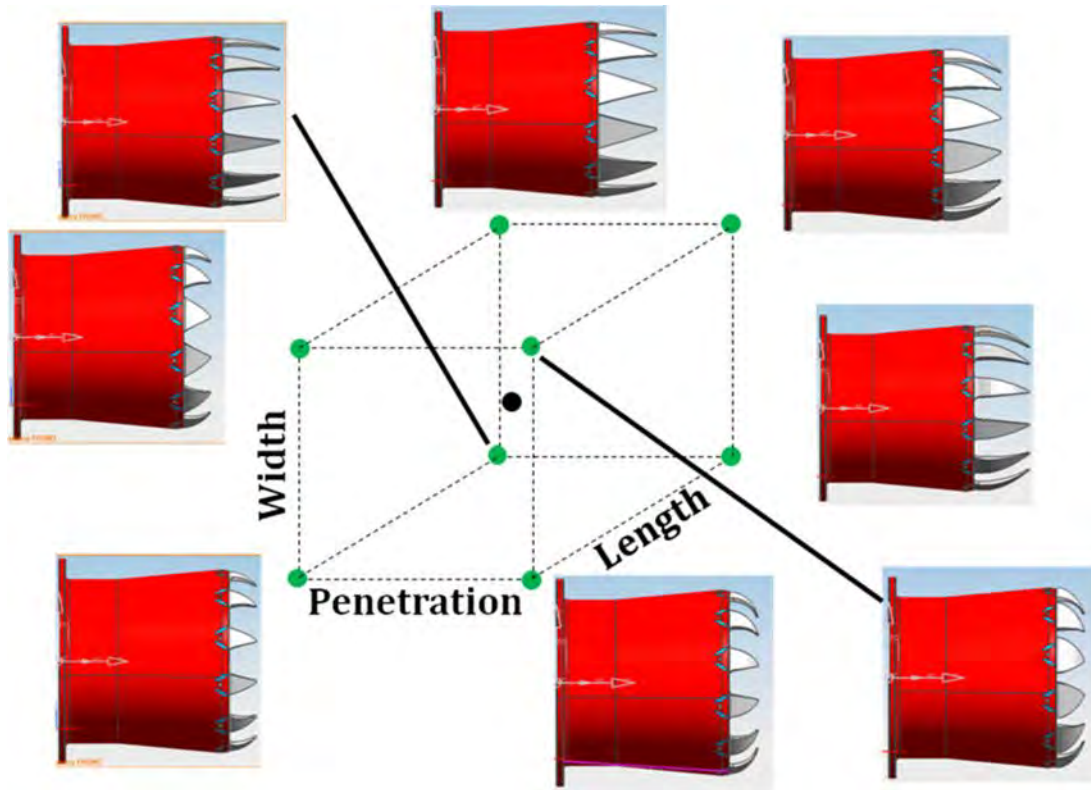


Figure 56. The chevron design space used in the MDOE study.

Results from the MDOE study are shown in Figure 57 and Figure 58 for the P03L08W06 and P06L18W10 chevrons, respectively. The results for the baseline nozzle with no chevrons are also shown in the Figures. The “Measured” spectra are from the experiments and the “Model” spectra were obtained from the MDOE models. While a few of the chevron designs resulted in limited broadband shock noise reduction (relative to the baseline) as occurs in Figure 57 (a), many chevron designs resulted in an increase in broadband shock noise as observed in Figure 58 (a). Most chevron designs produced significant reductions in acoustic radiation in the peak jet noise direction [see Figure 57 (b) and Figure 58 (b)]. The spectra obtained with the MDOE models are in close agreement with the measured agreement. The equations for the modeled spectra can be found in Ref. 40.

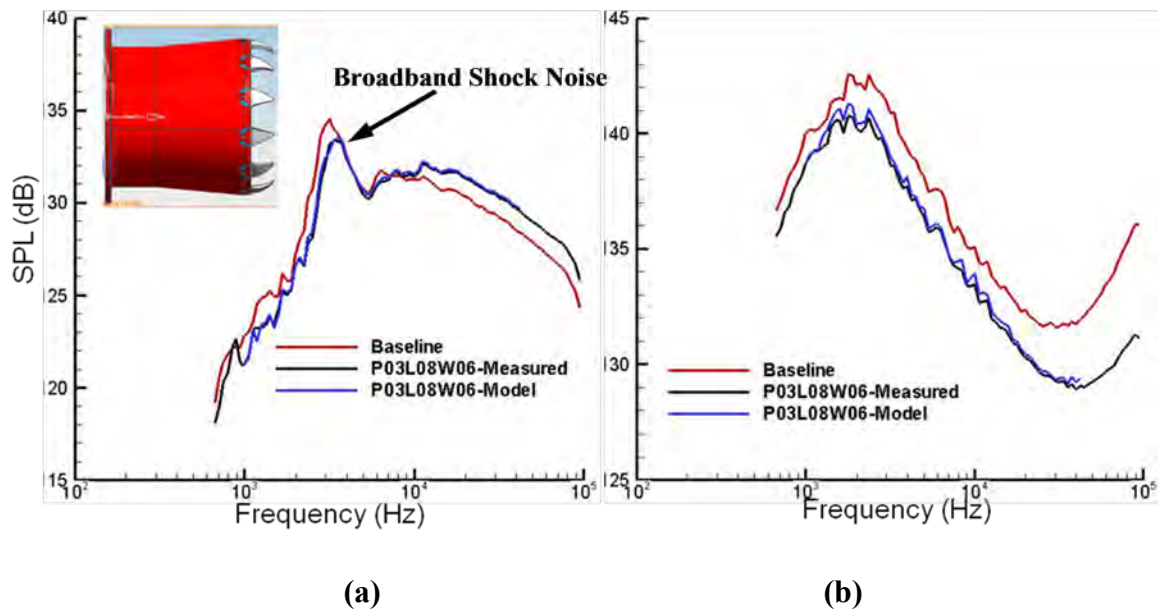


Figure 57. One-third octave band modeled and measured spectra for the P03L08W06 chevrons and the average baseline spectra at setpoint 44543 and observation angles equal to (a) 80° and (b) 160°.

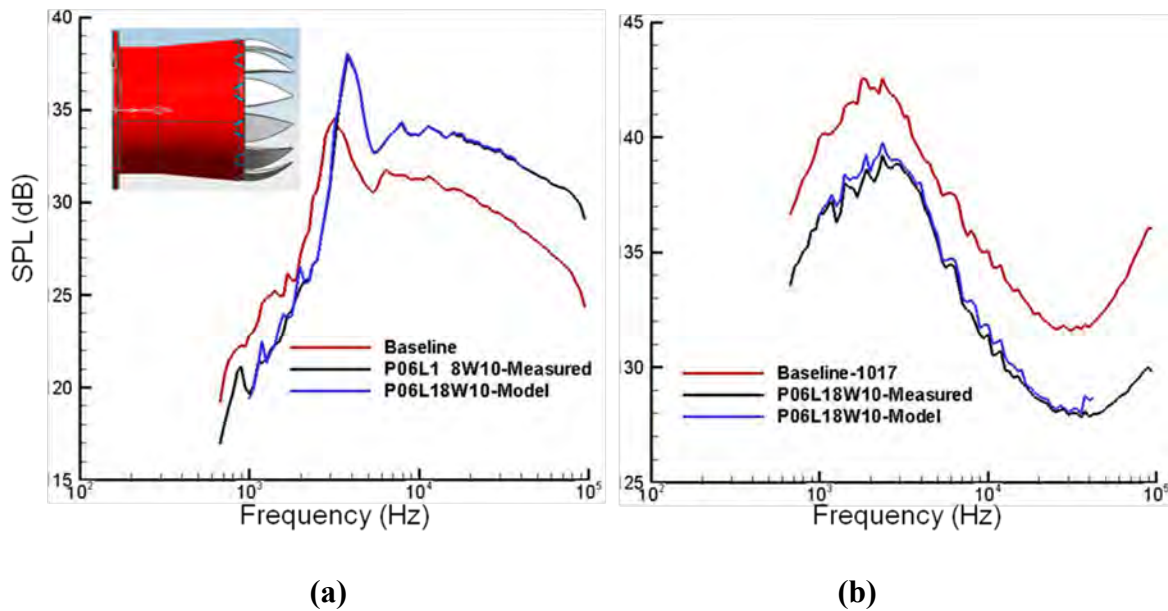


Figure 58. One-third octave band modeled and measured spectra for the P06L18W10 chevrons and the average baseline spectra at setpoint 44543 and observation angles equal to (a) 80° and (b) 160°.

10.4. Task 4. Numerical Simulations of Jet Noise

This section describes the methodology development and results associated with the following tasks: **Task 4.1 – Noise Predictions for Ideally Expanded Jets**; **Task 4.2 – Noise Predictions for Shock-Containing Jets**. In addition, simulations are described for a nozzle fitted with chevrons.

This section describes a methodology combining advanced CFD technologies and the acoustic analogy for the simulation of jet noise from chevron nozzle geometries with engineering accuracy and efficiency. A multiblock structured mesh topology is used to represent complex nozzle geometries, including the faceted inner contours, finite nozzle thickness and chevrons. The impact of chevrons on the near-field noise sources and far-field noise radiation is simulated using the Immersed Boundary Method to overcome the difficulties in grid generation. A modified block interface condition is used for the complex multiblock mesh topology to avoid the centerline singularity. A non-matching block interface condition is developed to allow the grids to be greatly refined around the chevrons for a higher accuracy of simulation without significantly increasing the mesh size. To enable efficient calculations, a dual time-stepping approach is used in addition to parallel computation. The sub-iterations in the fictitious time are accelerated using both multigrid and implicit residual smoothing. A modified version of the Detached Eddy Simulation (DES) approach is used. Noise predictions are made with the permeable surface Ffowcs Williams and Hawkings (FWH) solution.⁴¹ Noise predictions are presented for chevron nozzles and baseline nozzles at the same operating conditions. A good agreement of the predicted noise spectra is found for each $St \approx 3.0$. Encouragingly, the frequencies and amplitudes of the broadband shock-associated noise are captured precisely. Details of the statistical properties in the jet shear layer are presented. These include the mean flow and the turbulence intensities, the two-point space-time correlations and associated length and time scales and convection velocities for both baseline and chevron nozzles.

Introduction

Due to their noise reduction benefit and low performance penalty, chevron nozzles are presently the most popular jet noise reduction concept in both commercial and military applications. The previous experimental research has shown that chevrons usually lead to a reduced low-frequency noise level, but some high frequency noise penalties may occur^{42,43,40}. The ultimate goal of the chevron design is to reduce the low-frequency noise, while preventing the high-frequency noise penalty and thrust loss. However, due to an insufficient database of noise measurements and the difficulty of experimentally acquiring details of the near-field noise sources for supersonic hot jets, the understanding of this noise reduction concept remains limited.

With advances in computer technology, some subsonic jet noise simulations have been performed for chevron nozzles to supplement the experimental research. Two approaches have been adopted for chevron nozzle jet simulations. The first one excluded the actual nozzle geometries from the simulations (see Shur et al.⁴⁴) to avoid the great difficulty in creating a body-conformal mesh. An inlet boundary condition was imposed at the nozzle exit, using the solutions acquired from separate steady jet flow solutions in which the nozzle geometries were

included. The effects of the chevrons were simulated by well-calibrated mass/momentum source models at the nozzle exit. In the second approach, realistic chevron geometries were included and body-conformal meshes were created, despite the large effort needed for mesh generation. For example, Liu et al.⁴⁵ used an unstructured tetrahedral mesh with 65M elements to examine the near-field noise sources of supersonic cold jets. Uzun et al.⁴⁶ generated a multi-block, body-conformal, overset structured mesh to study the near-nozzle noise generation mechanism of a $M_j = 0.9$ cold jet. The mesh had 512 blocks and approximately 100 million grid points in a very confined computational domain. Xia et al.⁴⁷ used a traditional fully-matching multi-block structured mesh with 12.5 million grid points to simulate a $M_j = 0.9$ hot jet from a chevron nozzle. The agreement with the experimental acoustic measurements was found to be within $St \approx 2.0$, but the disparity between the low frequency noise levels and the experimental measurements was as much as 10dB at observer angles of 30° and 90° and an observer distance of $R/D = 40$.

The present numerical study proposes a compromise between these two approaches for chevron nozzle simulations. Jet noise simulations are performed for a military style chevron nozzle at several off-design conditions, and compared with the baseline nozzle operating at the same conditions to evaluate the noise reduction.

The remainder of this section begins with descriptions of the nozzle models and the related experimental studies. Then the numerical issues involved in jet noise simulations are discussed. The simulation results are then presented in section. Specifically, far-field noise predictions are compared with the acoustic measurements. Details of the turbulent jet flow are analyzed to reveal the noise source characteristics. Finally conclusions are drawn and some remaining problems that exist in the current study are summarized.

Nozzle models and experimental studies

In recent experimental studies, military-style baseline nozzles, mounted with different designs of chevrons, have been tested independently at the Pennsylvania State University (PSU) and the NASA Glenn Research Center (GRC). Apart from the different nozzle model sizes (small-scale models measured at PSU and moderate-scale models measured at NASA GRC), another experimental difference also existed in the acoustic measurements^{40,48}. The PSU measurements of single-stream jets used helium/air gas mixtures to simulate the heating effect, while the NASA GRC measurements had an extra annular cold bypass flow surrounding the heated core jet. The current numerical research of the baseline nozzle matches the small-scale measurements at PSU, and the chevron nozzle matches the moderate-scale nozzle at NASA GRC, both with a single-jet flow. Uncertainties could be introduced in both measurements^{40,48,49}, but a good scaling of the noise spectra has been observed⁷. However, some caution must be used when the comparisons between the predictions and the experiments are evaluated.

Figure 59 shows a sketch of the military-style baseline nozzle, mounted with the center-point chevron design *P05L13W8* from NASA GRC. The design Mach number of the baseline nozzle (without chevrons attached) is $M_d = 1.5$. The nozzle throat has a diameter of 0.631 inches for the small-scale model, and 4.45 inches for the moderate-scale model. 12 chevrons are attached at the

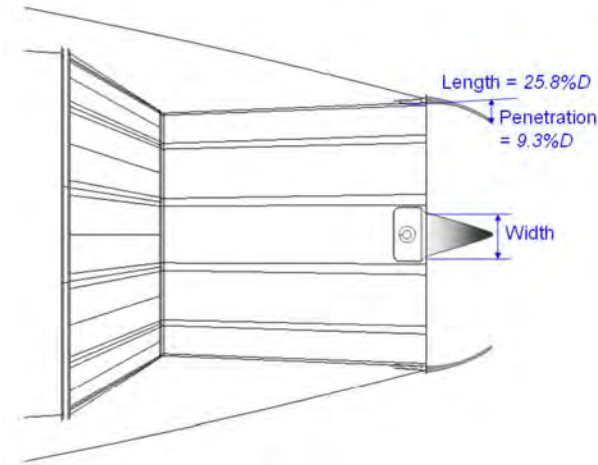


**Figure 59. The military-style nozzle with chevrons and three geometric parameters.
(Only 4 out of 12 chevrons are shown for clarity)**

nozzle exit to match the faceted inner contours. The chevrons have a penetration of 0.45 inches ($9.3\%D$), a length of 1.25 inches ($25.8\%D$), and a width of 80% of the facet width.

Table 7 lists the operating conditions at which the experimental measurements and the numerical simulations are conducted. Three off-design hot jets are studied with $NPR = 3, 3.5$, and 4 , and $TTR = 3.0$. These correspond to $M_j = 1.36, 1.47$ and 1.56 respectively.

Table 7. Operating conditions

NPR	TTR	M_j	T_j / T_∞	M_a
3.0	3.0	1.36	2.190	2.013
3.5	3.0	1.47	2.095	2.135
4.0	3.0	1.56	2.018	2.223

Numerical Issues

Simulation strategy

To make the most effective use of limited computer resources, a hybrid method combining advanced CFD technology with an acoustic analogy is used for the jet noise simulations. The approach focuses on resolving the larger turbulent eddies accurately, but sacrifices the accuracy of very fine turbulent structures in return for lower computational resource requirements. This approach is justified by the observation that the former are the dominant noise sources for high speed jets, and the latter are associated with noise 20dB or more below the large scale mixing noise.

As a first step, the Unsteady Reynolds-Averaged Navier-Stokes (URANS) equations are solved to simulate the development of the unsteady turbulent noise sources in the jet flow. Following the idea of model-free LES computations⁵⁰, a new variant of the Detached Eddy Simulation

(DES), which deactivates the turbulence model in the DES region and lets the numerical dissipation provide the removal of unresolved turbulent scales, is used for turbulence modeling. This avoids excessive dissipation in the mixing layers. A fourth-order Dispersion-Relation-Preserving (DRP) scheme⁵¹ is used for spatial discretization. The dual-time stepping method is used to advance the development of the unsteady turbulent jet flow, and multigrid and implicit residual smoothing are used to accelerate the convergence of the sub-iterations.

Once the unsteady turbulent jet flow has reached a statistically stable state, the flow solutions are sampled every two physical time steps on a set of Ffowcs Williams and Hawkins (FWH) acoustic data surfaces surrounding the shear layers. Based on the permeable surface solution⁵², the numerical integration of the unsteady flow solution at the retarded time gives the time-history of the acoustic pressure at the far-field observers.

Immersed Boundary Method

Rather than using a fully body-conformal mesh, the Immersed Boundary Method (IBM)^{53,54} is used to represent the chevron geometries in the chevron nozzle simulations. A sketch of the principle of the IBM is shown in Figure 60. Some of the grid points (for example, grid point A) are immersed within the surface and the governing equations are modified at such grid points to emulate the effect of solid boundaries on the external flow. The actual boundaries of complex

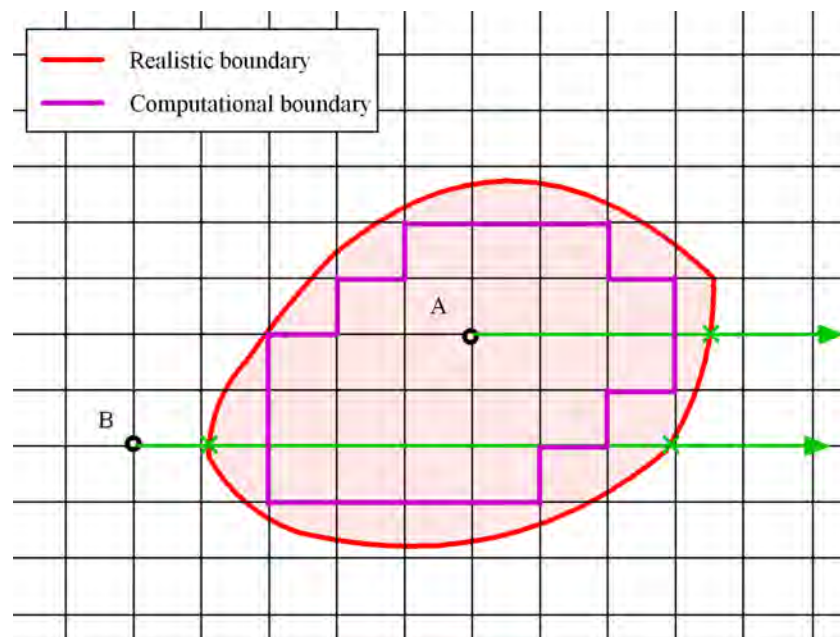


Figure 60. Sketch of the immersed boundary method

surfaces are replaced by the connection of the outermost points of the immersed grids. Clearly, the finer the grids are near the solid bodies, the more accurate the IBM will be. This simulation strategy trades accuracy in return for a less-expensive but still satisfactory simulation. The emulation technique by Shur et al.^{44,55} has shown that the effects of small geometric features, such as chevrons and tabs, on jet flows can be satisfactorily captured without requiring a fully body-conformal mesh over all the fine geometry details.

Imposition of boundary conditions is a key factor in developing an IBM algorithm. Numerous techniques have been proposed. The Discrete-Time Derivation (DTD) of the Brinkman Penalization Method is used in the current research. In this method, the continuity and energy equations are kept unchanged and the momentum equations are modified at the grid points inside the solid body. Specifically, the momentum at the immersed grid points is set to zero and remains unchanged during the computation. In the case of a moving surface, such as in forward flight, the velocity would be set to that of the moving body.

Computational Mesh

A multiblock structured mesh with 6.35M grid points, as shown in Figure 61, is created for the chevron nozzle simulations. The jet flow simulation is performed in a relatively compact physical domain, yet the outer boundaries are still placed far away from the jet core region, so that proper boundary conditions can be imposed to minimize any unphysical reflection of sound waves back into the computational domain. Measured from the nozzle exit, the computational domain extends to $62D$ in the jet flow direction. Away from the centerline in the radial direction, the outer boundary extends to $16D$ at the nozzle exit, and $23D$ at the downstream boundary. Four outer blocks form an O-type topology in the axial cross-section, which allows a fine grid distribution in the annular jet mixing layer. Surrounded by the four outer blocks, a center block is created around the jet axis to avoid the centerline singularity. A finite nozzle thickness is meshed. This is needed to trigger the unsteadiness of the jet flow. The grids are refined significantly around the jet potential core. The average grid sizes are $0.024D$ from the nozzle exit to $x/D = 4$, and $0.047D$ from $x/D = 4$ to $x/D = 10$, which results in an estimate of the highest resolvable Strouhal number of approximately 4.0. In the circumferential direction, 121 grid points are used to represent the non-circular faceted nozzle contour, though the resolution is increased in the vicinity of the chevrons.

A small region around the chevrons is refined significantly in order to improve the accuracy of the IBM. Three times the number of grid points are used in the circumferential direction, and double the number of grid points are used in the radial direction, as compared with the grid density in the main computational domain. The mesh without local grid refinement (5.89 million points) is used for the baseline nozzle simulations. It should be noted that, in a test case, the chevron nozzle mesh has been used for the simulation of the baseline nozzle jet with $M_j = 1.7$ and almost identical far-field noise spectra are predicted. Therefore, it is believed that the local refinement has little impact on the baseline nozzle simulations, and the results of baseline nozzle simulations shown below are all performed without the local grid refinement.

A preprocessing code has been developed to mark the immersed grid points automatically using the Line Intersection Method (LIM)⁵⁶. A line is drawn from each grid point, through the solid surface, to a far-field point at the edge of the computational domain. An odd number of intersections of the line with the solid surface indicates that the grid point (for example, A in Figure 60) is immersed inside the solid body. An even number indicates that the grid point is a regular grid point (for example, B in Figure 60) in the flow region. In Figure 62, the regions with red color show the immersed grid points, for which the governing equations are modified to emulate the effects of the chevrons on the jet flow.

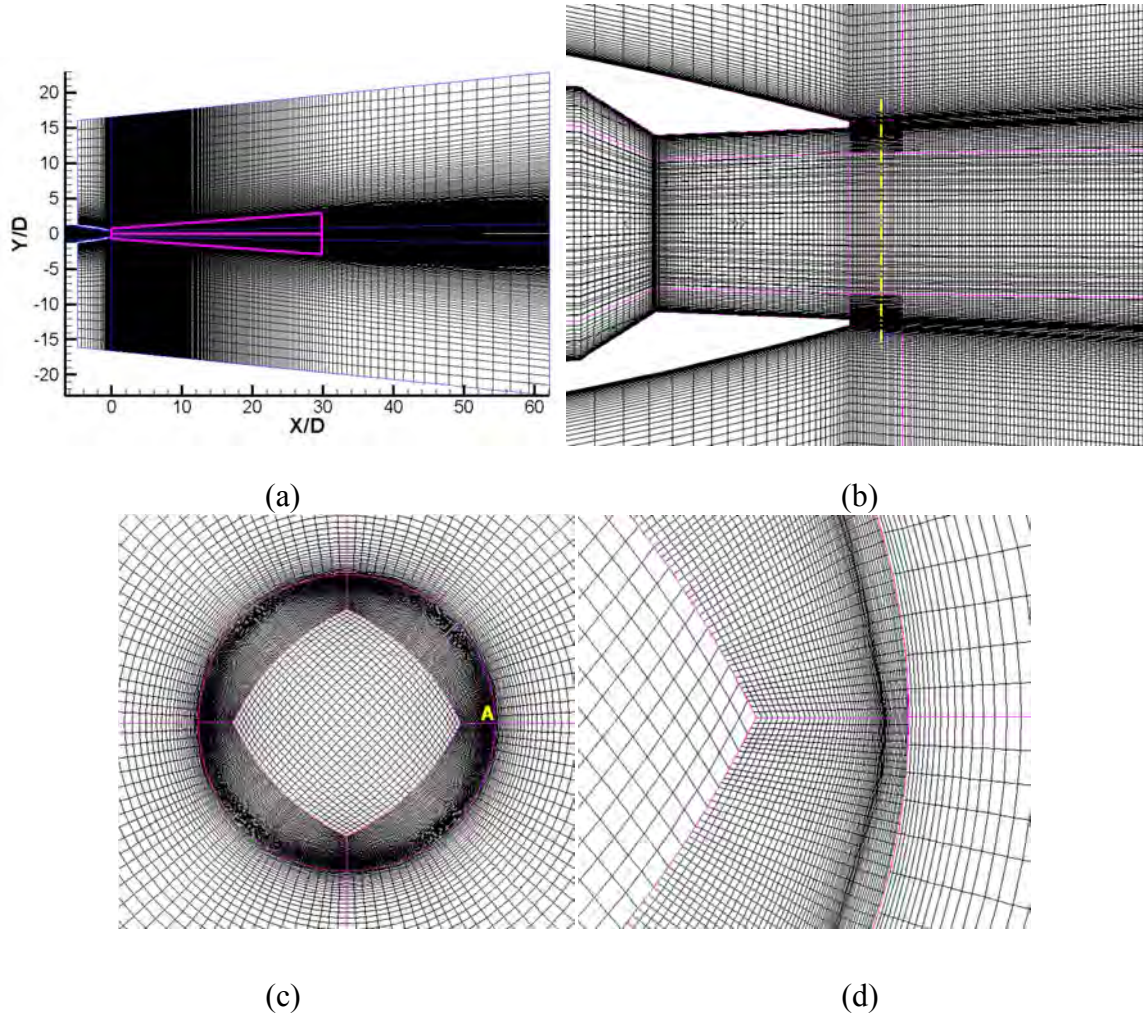
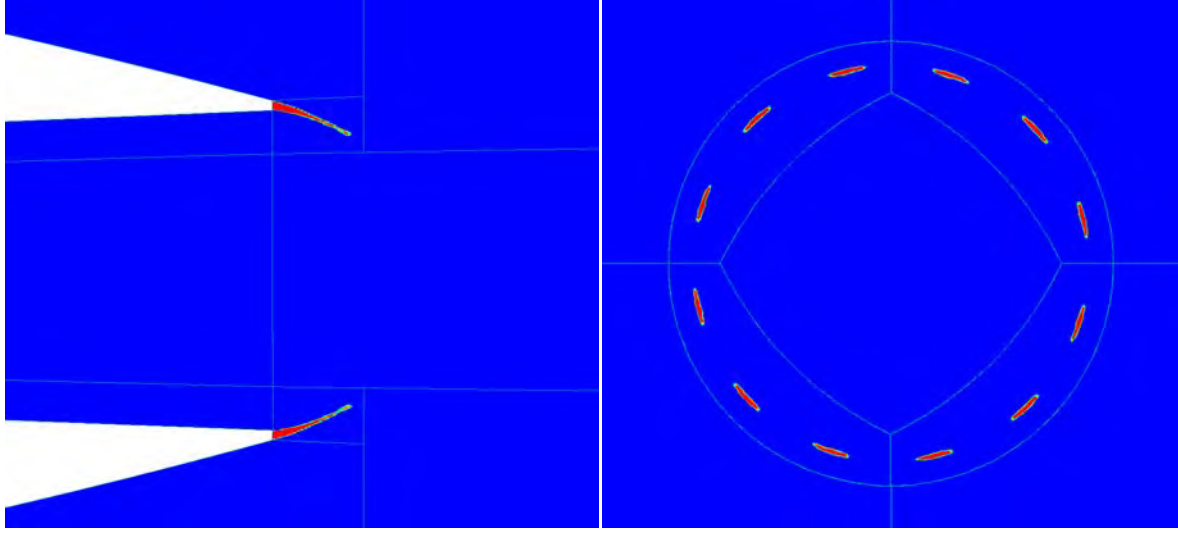


Figure 61. Computational mesh for the chevron nozzle simulations. The grids around the chevrons are refined significantly to improve the IBM representation of chevrons.

No local grid refinement is used in the baseline nozzle simulations. (a) Full computational domain and the FWH integration surface (pink lines). (b) A symmetric plane through one chevron tip. (c) An axial station at about 50% of the chevron length. (d) Grid details around point A.

Boundary conditions

A non-reflecting boundary condition is important to avoid the contamination of the acoustic solution by the reflections at the outer boundaries back into the computational domain. Many previous researchers^{46,47} have used a sponge zone to damp the reflecting waves, which requires a prior knowledge of the time-mean flow solution and extra computational loads. In the current numerical studies, Dong's modified version of radiation boundary condition⁵⁷ is imposed on the lateral and downstream boundaries. A numerical test with an initial Gaussian pressure pulse embedded in a moving medium has shown that this radiation boundary condition produced a similar solution to that with the sponge zone method. The other boundary conditions are: a total



(a)

(b)

Figure 62. The IBM representation of the chevron geometries. The region with red color shows the immersed grid points. (a) A symmetric plane through one chevron tip. (b) An axial cross-section at 50% of the chevron length

inlet condition is imposed at the nozzle inlet, where the total pressure and total temperature are fixed. A no-slip adiabatic wall condition is imposed on the nozzle wall, except that, for a small section of inner wall starting from the nozzle inlet, a slip wall condition is set up to initiate the boundary layers.

For the multiblock mesh topology shown in Figure 61(d), special treatments are required at the block interfaces since the grid transformation matrices are not continuous at the block interfaces. The characteristic interface condition proposed by Kim and Lee⁵⁸ is used. However, it should be noted that their original equations are not easy to implement, especially when the mesh-orientations are not the same across the block interface. Therefore, an analysis has been performed to directly manipulate the residuals of the conservative form of Navier-Stokes equations. This is described here.

Block interface condition.

This section describes a way to simplify the governing equations of the block interface condition for very complex mesh topologies in general curvilinear coordinates. Following Kim and Lee's notation, the corrected conservative form of the Navier-Stokes equations at the block interface can be written as:

$$\frac{\partial Q}{\partial t} = Res = -S(L + S_c) \quad (5)$$

where, L and S_c are given by Kim and Lee, and Res represents the residuals of the semi-discretized equations. The eigenmatrix S is defined as,

$$S = \begin{bmatrix} \frac{\rho}{2c} & \widetilde{\xi}_x & \widetilde{\xi}_y & \widetilde{\xi}_z & \frac{\rho}{2c} \\ \frac{\rho H}{2c} - \frac{\rho \tilde{U}}{2} & \overrightarrow{B}_{0x} & \overrightarrow{B}_{0y} & \overrightarrow{B}_{0z} & \frac{\rho H}{2c} + \frac{\rho \tilde{U}}{2} \\ \frac{\rho u}{2c} - \frac{\rho \widetilde{\xi}_x}{2} & u \widetilde{\xi}_x & u \widetilde{\xi}_y - \rho \widetilde{\xi}_z & u \widetilde{\xi}_z + \rho \widetilde{\xi}_y & \frac{\rho u}{2c} + \frac{\rho \widetilde{\xi}_x}{2} \\ \frac{\rho v}{2c} - \frac{\rho \widetilde{\xi}_y}{2} & v \widetilde{\xi}_x + \rho \widetilde{\xi}_z & v \widetilde{\xi}_y & v \widetilde{\xi}_z - \rho \widetilde{\xi}_x & \frac{\rho v}{2c} + \frac{\rho \widetilde{\xi}_y}{2} \\ \frac{\rho w}{2c} - \frac{\rho \widetilde{\xi}_z}{2} & w \widetilde{\xi}_x - \rho \widetilde{\xi}_y & w \widetilde{\xi}_y + \rho \widetilde{\xi}_x & w \widetilde{\xi}_z & \frac{\rho w}{2c} + \frac{\rho \widetilde{\xi}_z}{2} \end{bmatrix} \quad (6)$$

with,

$$S^{-1} = \begin{bmatrix} \frac{|v|^2(\gamma-1)}{2\rho c} + \frac{\tilde{U}}{\rho} & \frac{\gamma-1}{\rho c} & -\frac{u(\gamma-1)}{\rho c} - \frac{\widetilde{\xi}_x}{\rho} & -\frac{v(\gamma-1)}{\rho c} - \frac{\widetilde{\xi}_y}{\rho} & -\frac{w(\gamma-1)}{\rho c} - \frac{\widetilde{\xi}_z}{\rho} \\ \overrightarrow{B}_{1x} & -\frac{\gamma-1}{c^2} \widetilde{\xi}_x & \frac{\gamma-1}{c^2} \widetilde{\xi}_x u & \frac{\gamma-1}{c^2} \widetilde{\xi}_x v + \frac{1}{\rho} \widetilde{\xi}_z & \frac{\gamma-1}{c^2} \widetilde{\xi}_x w - \frac{1}{\rho} \widetilde{\xi}_y \\ \overrightarrow{B}_{1y} & -\frac{\gamma-1}{c^2} \widetilde{\xi}_y & \frac{\gamma-1}{c^2} \widetilde{\xi}_y u - \frac{1}{\rho} \widetilde{\xi}_z & \frac{\gamma-1}{c^2} \widetilde{\xi}_y v & \frac{\gamma-1}{c^2} \widetilde{\xi}_y w + \frac{1}{\rho} \widetilde{\xi}_x \\ \overrightarrow{B}_{1z} & -\frac{\gamma-1}{c^2} \widetilde{\xi}_z & \frac{\gamma-1}{c^2} \widetilde{\xi}_z u + \frac{1}{\rho} \widetilde{\xi}_y & \frac{\gamma-1}{c^2} \widetilde{\xi}_z v - \frac{1}{\rho} \widetilde{\xi}_x & \frac{\gamma-1}{c^2} \widetilde{\xi}_z w \\ \frac{|v|^2(\gamma-1)}{2\rho c} - \frac{\tilde{U}}{\rho} & \frac{\gamma-1}{\rho c} & -\frac{u(\gamma-1)}{\rho c} + \frac{\widetilde{\xi}_x}{\rho} & -\frac{v(\gamma-1)}{\rho c} + \frac{\widetilde{\xi}_y}{\rho} & -\frac{w(\gamma-1)}{\rho c} + \frac{\widetilde{\xi}_z}{\rho} \end{bmatrix} \quad (7)$$

with the definitions,

$$\begin{aligned} \overrightarrow{B}_0 &= \frac{|v|^2}{2} \overrightarrow{l}_\xi + \rho (\vec{v} \times \overrightarrow{l}_\xi) \\ \overrightarrow{B}_1 &= \left[1 - \frac{|v|^2(\gamma-1)}{2c^2} \right] \overrightarrow{l}_\xi - \frac{1}{\rho} (\vec{v} \times \overrightarrow{l}_\xi) \\ H &= \frac{|v|^2}{2} + \frac{c^2}{\gamma-1} \quad (\text{Entropy}) \end{aligned} \quad (8)$$

where, \overrightarrow{l}_ξ is the unit normal vector at a grid point on the block interface, defined by $\overrightarrow{l}_\xi = (\widetilde{\xi}_x, \widetilde{\xi}_y, \widetilde{\xi}_z)$, in which $\widetilde{\xi}_x = \xi_x / |\nabla \xi|$, $\widetilde{\xi}_y = \xi_y / |\nabla \xi|$, and $\tilde{U} = \widetilde{\xi}_x u + \widetilde{\xi}_y v + \widetilde{\xi}_z w$.

The amplitudes of the characteristic waves are:

$$S^{-1}\delta Q = \begin{bmatrix} \frac{\delta p}{\rho c} - \delta \tilde{U} \\ \left(\delta \rho - \frac{\delta p}{c^2}\right) \tilde{\xi}_x + \left(\delta \vec{v} \times \vec{l}_\xi\right)_x \\ \left(\delta \rho - \frac{\delta p}{c^2}\right) \tilde{\xi}_y + \left(\delta \vec{v} \times \vec{l}_\xi\right)_y \\ \left(\delta \rho - \frac{\delta p}{c^2}\right) \tilde{\xi}_z + \left(\delta \vec{v} \times \vec{l}_\xi\right)_z \\ \frac{\delta p}{\rho c} + \delta \tilde{U} \end{bmatrix} \quad (9)$$

Notice that the eigenvalues are redefined as $\Lambda = [U - c|\nabla \xi|, U, U, U, U + c|\nabla \xi|]$, and minor errors in equation (10) of the reference 58 are corrected.

Equation (5) reveals the relationship between Res and $L + S_c$:

$$\begin{aligned} Res &= -S(L + S_c) \\ L + S_c &= -S^{-1}Res \end{aligned} \quad (10)$$

Application of the characteristic interface condition will change L , and thus result in new residuals:

$$\begin{aligned} Res^* &= -S(L^* + S_c) \\ &= -S[(L^* + S_c) - (L + S_c) + (L + S_c)] \\ &= Res - S(L^* - L) \\ &= Res - S\Delta L \end{aligned} \quad (11)$$

This shows that the block interface condition imposes some corrections on the original residuals calculated by one-sided difference operators, i.e.

$$\Delta Res = -S\Delta L \quad (12)$$

When the mesh-orientation remains the same across the block interface, two blocks have the same normal vector at the interface, for instance, $\vec{l}_\xi^L = \vec{l}_\xi^R$, and the same eigenmatrix S and its inverse S^{-1} . The corrections to L for the left block can be written as:

$$\begin{aligned} \Delta L^L &= L^{*L} - L^L \\ &= (L^R + S_c^R - S_c^L) - L^L \\ &= (L^R + S_c^R) - (L^L + S_c^L) \\ &= -(S^{-1})^R Res^R + (S^{-1})^L Res^L \\ &= -(S^{-1})^L (Res^R - Res^L) \end{aligned} \quad (13)$$

Equation (13) can be shown to be correct for arbitrary mesh orientations of the right block.

When the mesh is locally refined as shown in Figure 61, multiple pairs of non-matching block interfaces are created at the location where the grid density changes. A non-matching block interface condition has been developed for flow variable communication. Since grid points of one block may not be coincident with grid points in the other block, the flow solutions are first interpolated with a Lagrange interpolation method using the information from its neighbor, and then the same block interface condition can be used as the fully-matching version.

Results

Far field noise

Using the solution to the FWH equation, the far-field noise predictions are made with approximately 5800 samples of the instantaneous near-field flow solutions. The predictions are compared with the acoustic measurements at PSU and NASA GRC. Considering that a 2 ~ 3 dB deviation is usually observed for the noise spectrum and OASPL measurements of the same nozzle using different facilities⁵⁹ or the different scale of nozzles using the same facilities^{48,7}, the agreement is said to be “good” if the disparity between the predictions and the experiments is within 3dB.

Figure 63 presents the predicted far-field noise spectra at different downstream observer angles ranging from 30° to 120° as well as the far-field acoustic measurements acquired at NASA GRC and PSU. No experimental measurements for the particular chevron nozzle jets are available at present. The relatively large oscillations of the predicted noise spectra are attributed to a short record length. Overall, the “good” agreement extends to $St \approx 3$ as expected since the computational grids are designed to resolve the highest frequency up to $St \approx 4$. In the resolved frequency range, the disparities of the prediction from the acoustic measurement are well below 4dB, except that there are over-predictions at mid to high frequencies for the baseline nozzle jets at some shallow polar angles. The peak-noise frequency shift to the low-frequency range as the observer angle decreases is captured well for all three jets. Specifically,

- At all upstream directions ($\theta > 90^\circ$), the predictions have an excellent agreement with the experimental measurements. The frequencies and the amplitudes of the BBSAN component are captured precisely. The discrepancy at discrete frequencies is less than 4dB.
- In the peak noise radiation direction, at approximately around $\theta \approx 50^\circ$, the agreement of the noise spectra with the acoustic measurements is as good as those at the upstream observers.
- However, above $St \approx 0.3$, an intriguing but consistent trend is observed for the baseline nozzle jets. Below the peak noise radiation direction (about $\theta \approx 50^\circ$), the agreement deteriorates as the jet Mach number increases. At 30°, the over-prediction increases from less than 2dB for the $M_j = 1.36$ jet to more than 8dB for the $M_j = 1.56$ jet. While, above the peak noise radiation direction, the agreement improves as the jet Mach number increases. At 70°, the over-prediction decreases from approximately 5dB for the $M_j = 1.36$ jet to less than 3dB for the $M_j = 1.56$ jet.

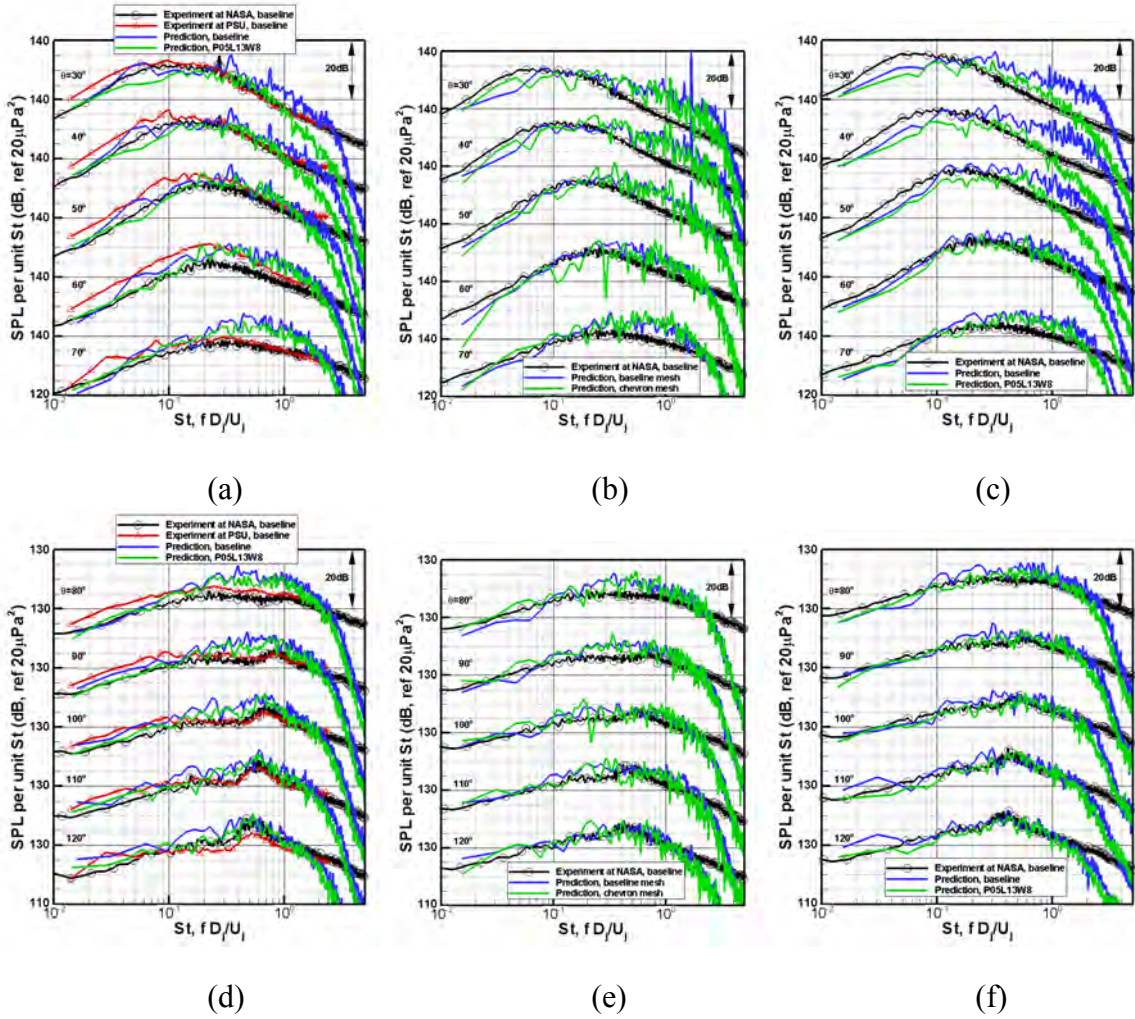


Figure 63. Comparison of the measured and predicted noise spectra for both the baseline and chevron nozzles at the three operating conditions. Note: the NASA baseline measurements have a core $TTR = 3.0$ and a mixed $TTR = 2.56$ at $M_j = 1.36$ and a core $TTR = 3.6$ and a mixed $TTR = 3.0$ at $M_j = 1.47$ and 1.56 . (a)

$M_j = 1.36, \theta = 30^\circ \sim 70^\circ$, (b) $M_j = 1.47, \theta = 30^\circ \sim 70^\circ$, (c) $M_j = 1.56, \theta = 30^\circ \sim 70^\circ$,
 (d) $M_j = 1.36, \theta = 80^\circ \sim 120^\circ$, (e) $M_j = 1.47, \theta = 80^\circ \sim 120^\circ$, (f)
 $M_j = 1.56, \theta = 80^\circ \sim 120^\circ$.

- No obvious over-prediction of the noise spectra are found for the chevron nozzle jets.

A mismatch of the predicted noise spectra with the experimental measurements is found in most publications. Grid resolution is often referred to as one of the important reasons. As a test case, a noise simulation of the baseline nozzle jet with $M_j = 1.47$ has been conducted using the chevron nozzle computational mesh for which the grids are significantly refined near the nozzle exit. The predicted noise spectra with the two meshes are almost identical at all the polar angles,

suggesting that further grid refinement cannot improve the accuracy of the noise prediction. A similar over-prediction of the high-frequency noise level has also been found with very fine grids in other publications^{60,61,62}.

Before a discussion of the noise reduction effect, it should be noted that two issues make it difficult to evaluate the accuracy of the predicted noise level and the noise reduction quantitatively:

- The statistical requirement: Theoretically, the record lengths should be long enough to meet statistical certainty requirements as well as a good resolution at low frequencies. Due to the long CPU time for the jet flow simulation, only 5800 samples (less than 2% of the experimental record length) are obtained at the far field observers. Large oscillations are still present in the predicted noise spectra, especially at low frequencies.
- The experimental uncertainties: The experiments at NASA GRC have an annular bypass cold flow surrounding the heated core jet and its impact on the jet flow and the noise radiation is not well understood.

In Figure 64 (a) and (b), the predicted OASPL for the $M_j = 1.47$ and $M_j = 1.56$ jets are compared with the experimental measurements for the baseline nozzle. Overall, the measurements with different scales of nozzle models showed a $2 \sim 3$ dB disparity. A good agreement is found between the predictions and the acoustic measurements at PSU or NASA GRC. It is also

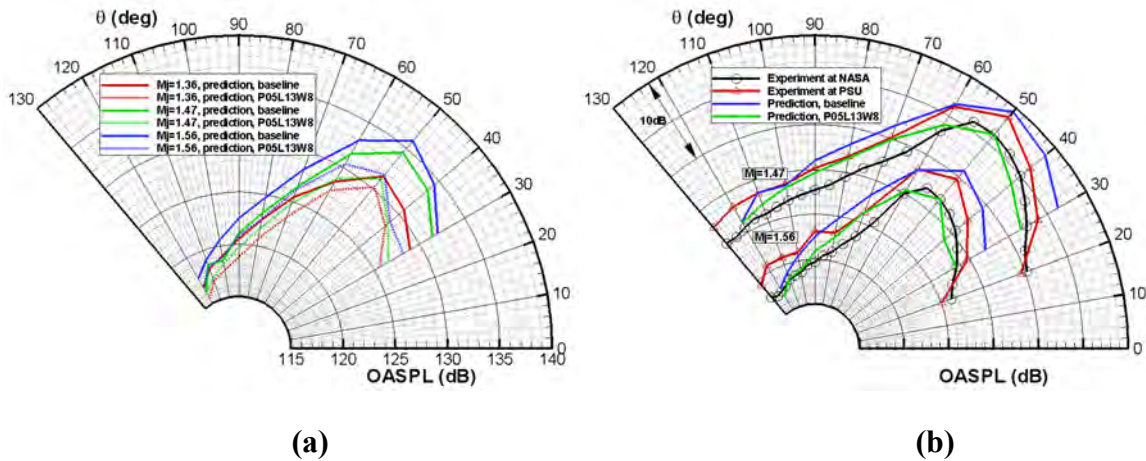


Figure 64. Comparison of the predicted far-field OASPL with the experimental measurements. All data are scaled to the same distance $R/D = 100$. (a)

$M_j = 1.47$, $TTR = 3.0$, (b) $M_j = 1.56$, $TTR = 3.0$.

observed that the predictions show that the chevron nozzle jet has a lower overall noise level over a wide range of polar angles as compared to the baseline nozzle jet operating at the same condition. However, the noise reductions at other observer angles are expected to be over-predicted, because of the over-prediction of the noise levels for the baseline nozzle jets at mid to high frequencies.

Near field properties

A direct impact of the chevrons on the jet flows can be identified clearly from a three-dimensional view of the vorticity iso-surfaces, shown in Figure 65. Two iso-surfaces are plotted at values of $\omega_x D / U_j = \pm 5$. The red iso-surface indicates a counter-clockwise rotating vortex, and the blue color indicates a clockwise rotating vortex, if viewed from the downstream direction. Driven by the pressure imbalance at the inner and outer surfaces, a lateral secondary flow is induced and thereafter creates a pair of strong vortices from each chevron as the flow travels downstream. No well-organized vortex structures are found in the baseline nozzle jets. As the pressure ratio and hence the jet velocity increase, the vortices become stronger, expand further in the radial direction, and keep well-organized for a longer distance, until they break down at a downstream position of approximately $x/D \approx 1.8$. Therefore, it can be expected that the chevrons have the least impact on the jet flow operating at $M_j = 1.36$, but the most significant

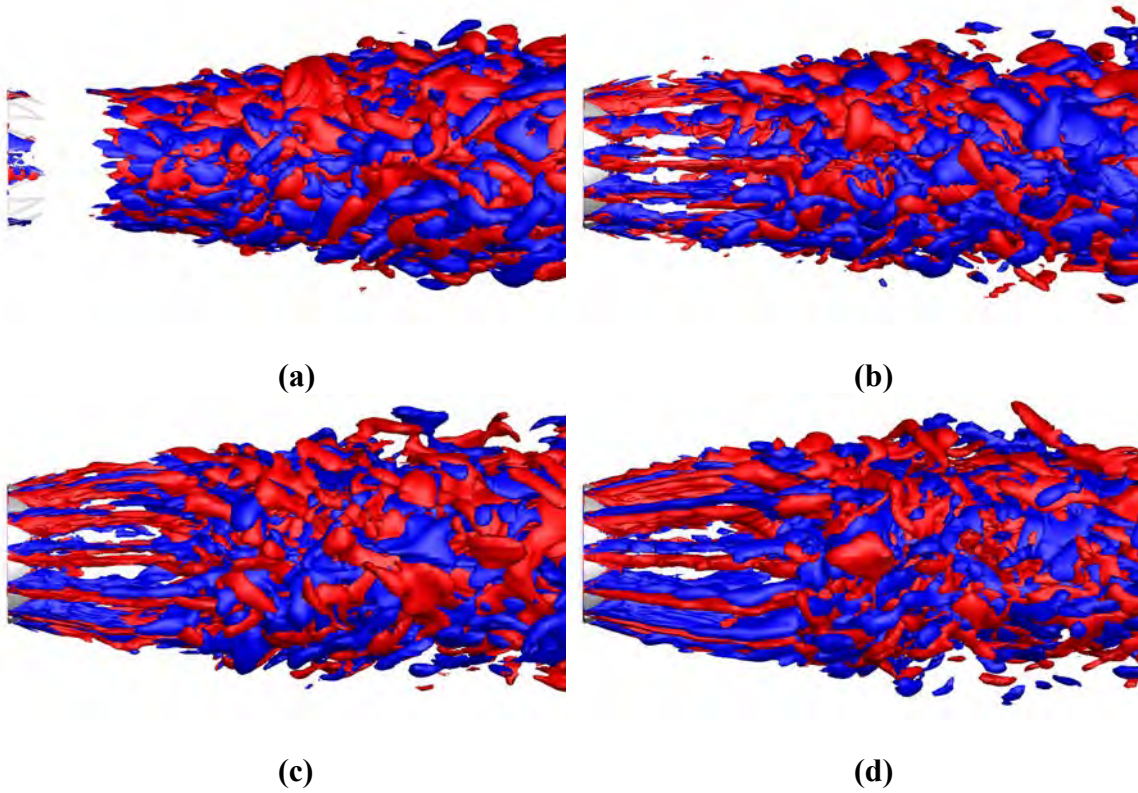
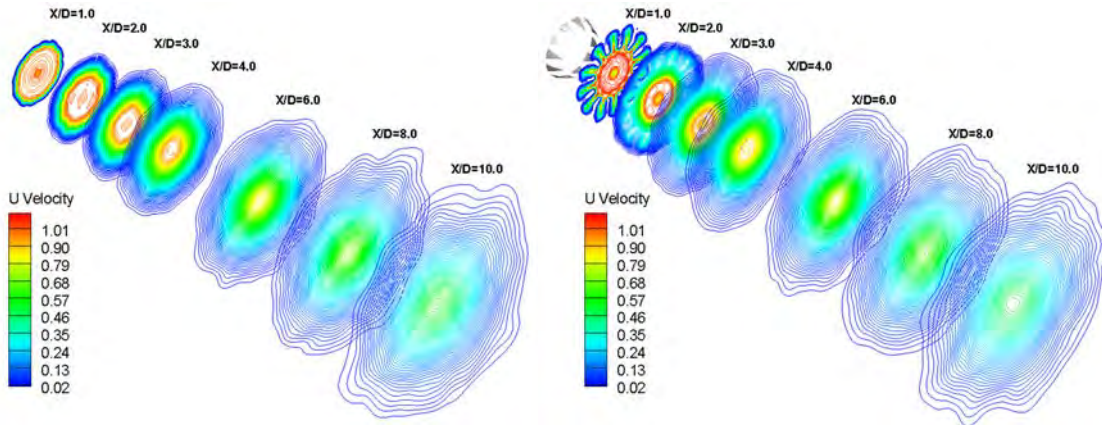


Figure 65. Three-dimensional view of the instantaneous streamwise vorticity iso-surfaces. Two iso-surfaces are plotted at the values $\omega_x D / U_j = \pm 5$. The red iso-surface represents a positive value, and the blue, a negative one. (a) Baseline, $M_j = 1.36$. Note: the chevrons are shown as a reference, (b) P05L13W8, $M_j = 1.36$, (c) P05L13W8, $M_j = 1.47$, (d) P05L13W8, $M_j = 1.56$.

impact on the jet flow with $M_j = 1.56$.

The well-organized vortices induce strong transverse flows downstream of the chevrons. Figure 66 shows a comparison of time-averaged axial velocity contours at several axial stations for the baseline nozzle and the chevron nozzle operating at $M_j = 1.56$. Similar observations are found for the other two operating conditions. The figures are plotted with the same orientation and color scales, allowing a direct comparison of the jet flows from the two different nozzles. A high speed region spreads in the radial direction in the chevron valley plane when the streamwise vortices bring the high-speed flow away from the jet core. An opposite trend is found in the tip plane. Consequently, as compared to the baseline nozzle jet, a lobed pattern of the velocity contours matching the azimuthal distribution of the chevrons appears at the axial station $x/D = 1.0$ for the chevron nozzle jet. This indicates a dramatic change in enhanced turbulent mixing induced by the streamwise vortices. The velocity contours show a weak but discernible lobed shape at $x/D = 2.0$ and resume the similar pattern as the baseline nozzle jet at further downstream locations after the streamwise vortices break down.



(a) Baseline

(b) P05L13W8

Figure 66. Comparison of the three-dimensional views of the time-averaged axial velocity contours for the baseline nozzle and the chevron nozzle simulations at several axial stations. Normalized by the fully expanded jet velocity U_j . Operating condition:

$$M_j = 1.56, NPR = 4.0, TTR = 3.0.$$

The enhanced turbulent mixing can be quantified by examining the vorticity thickness shown in Figure 67. The vorticity thickness δ_ω is defined by:

$$\delta_\omega = \frac{U_{max}}{\left| \partial U / \partial(r) \right|_{max}} \quad (14)$$

where, U is the time-averaged axial velocity and r is the radial coordinate. In the valley plane, the streamwise vortices bring the high speed flow away from the jet core, creating a strong lateral flow and a thick initial vorticity thickness. An opposite trend happens in the tip plane, except that the contraction is blocked by the high pressure jet core. The difference in the tip plane and the valley plane is reduced after the streamwise vortices break down. However, the increased lateral jet flow development reduces the axial velocity gradient in the radial direction,

and thus significantly increases the vorticity thickness. Similar observations have been found in the experimental measurements by Kuo.

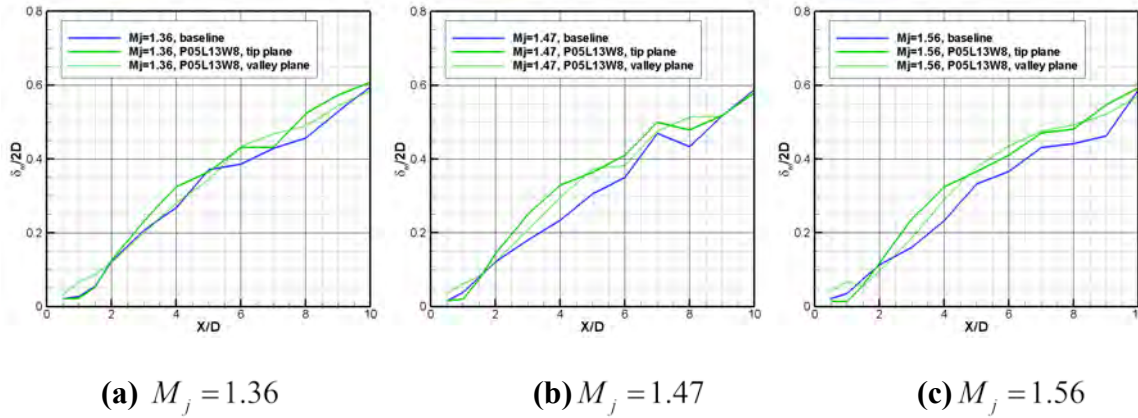


Figure 67. Comparison of the vorticity thickness for the baseline and the chevron nozzle jets at the three operating conditions.

For a clearer view of the noise generation characteristics, Figure 68 shows snapshots of the density gradients and the pressure time-derivatives of the jets using the same contour levels. While the density gradients illustrate the shock cell structures in the jet plume, the pressure time-derivatives, shown in the acoustic field, show the propagation of acoustic waves. Two distinct types of sound waves can be identified in all the jets. One is the strong Mach wave radiation propagating in the downstream direction, and the other is a weak sound propagation in the upstream direction. Consistent with Lui and Lele's findings^{63,64}, with a simplified model of a three-dimensional turbulent shear layer and a single shock-cell, the current simulations of realistic jets show that the oscillating shock cells produce acoustic emissions at the places where they interact with the shear layer. A new observation is that the contact of the shock cell and the mixing layer does not necessarily produce acoustic radiation in isolation. As shown in Figure 68(a), for the $M_j = 1.36$ jet, no strong acoustic waves are seen from the tips of the first two shock cells, while for the $M_j = 1.56$, strong acoustic emissions appear at the tip of the first shock cell. This can be attributed to the low radiation efficiency of the undeveloped mixing layer: the interaction between the shock cell structure and the mixing layer barely produces noticeable acoustic radiation unless the turbulence intensity is large enough. Also the noise source mechanism is related to the multiple, partially coherent interactions of the mixing layer turbulence with the entire shock cell system. However, it should be noted that, since the instantaneous values are plotted in the figures, it is not correct to draw conclusions about the magnitude of acoustic pressures by just examining the pressure time-derivative contours.

Apart from the differences discussed above, it is observed that strong Mach wave radiation starts at farther upstream locations in the baseline nozzle jets, but only appears after the streamwise vortices break down at $x/D \approx 1.8$ in the chevron nozzle jets. This difference is small at the lower jet Mach number of $M_j = 1.36$, but becomes very significant as the jet Mach number rises to $M_j = 1.56$. This suggests that the highly-directional Mach wave radiation in this region might contribute to the over-prediction of the noise levels at low polar angles for the baseline nozzle

jets. The baseline nozzle simulations overestimate the instability of the mixing shear layer. The

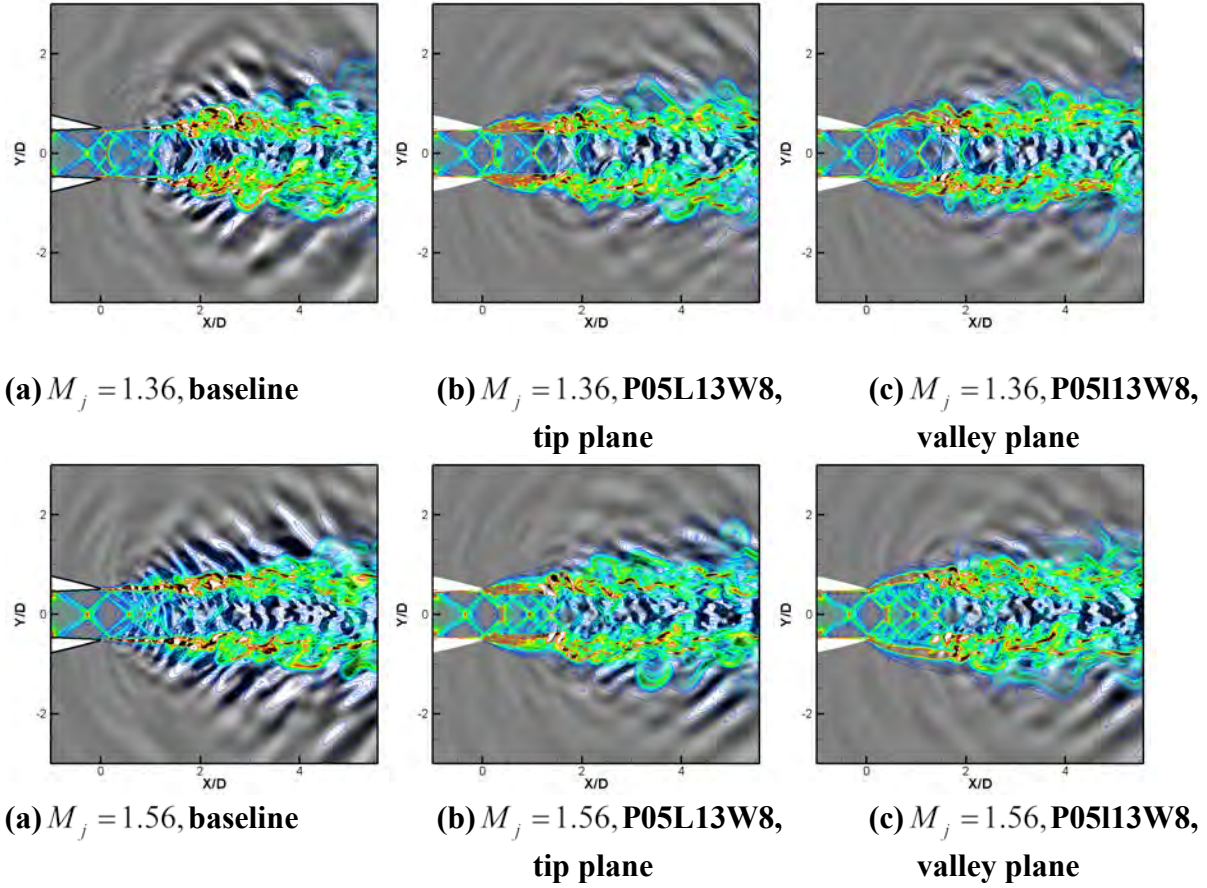


Figure 68. Instantaneous contours of density gradients (color contours) and pressure time derivatives (gray backgrounds).

mixing layer becomes fully turbulent with higher turbulence levels further upstream for the baseline nozzle jets in the jet flow simulations than it should in reality.

Statistical characteristics of the turbulent mixing layers

To predict the statistical characteristics of the turbulent mixing layer, thirty virtual probes are inserted in the flow field along the lip line to record the unsteady flow solutions, as shown in Figure 69. Twenty probes are located up to the downstream location $x/D = 5.0$ with a separation distance of $0.25D$ between two neighboring probes to quantify the rapid development of the turbulent shear layer. The remainder is inserted until $x/D = 10.0$ with an increased separation distance of $0.5D$. For the chevron nozzle simulations, this plane is slightly displaced from the chevron valley. The flow fluctuations are recorded at these virtual probes to calculate the two-point space-time correlations.

The correlation function of the axial velocity fluctuations is defined as:

$$R_{11}(x, \xi, \tau) = \overline{u'(x, t)u'(x + \xi, t + \tau)} \quad (15)$$

where, ξ is the separation distance between a fixed flow probe at a streamwise location x and a downstream traveling flow probe. From two-point space-time correlation measurements, an integral temporal scale L_τ , spatial scale L_Δ , and convection velocity U_c can be estimated to characterize the temporal and spatial evolution of the turbulent mixing layer^{65,66}. The two-point space-time correlation measurements and the turbulence intensities can be related to the noise source models of different acoustic analogy theories^{67,68}.

Figure 70 (a) shows the RMS values of the axial velocity perturbation u' along the lip line for the $M_j = 1.36$ baseline nozzle jet and the $M_j = 1.36$ chevron nozzle jet in the tip plane and the valley plane. The peak moves upstream and has a larger amplitude in the valley plane as compared to the turbulent mixing layer in the tip plane. But the difference decreases at farther downstream locations after the streamwise vortices induced by the chevrons breakdown, an observation consistent with the experimental measurements. In comparison to the baseline nozzle jet, the peak amplitude increases in the valley plane but decreases in the tip plane.

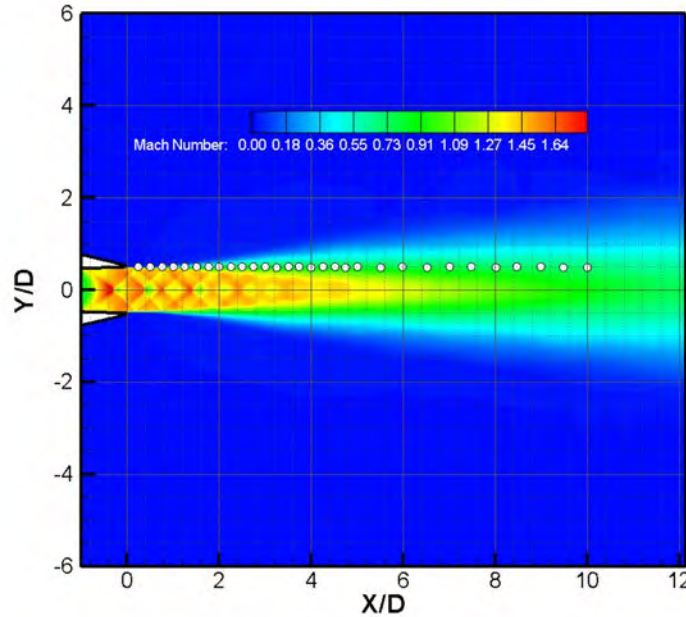


Figure 69. Virtual probes along the lip line where the flow solutions are sampled. The colored contours show the time-averaged Mach number contours of the baseline nozzle jet operating at $M_j = 1.47$, $NPR = 3.5$ and $TTR = 3.0$.

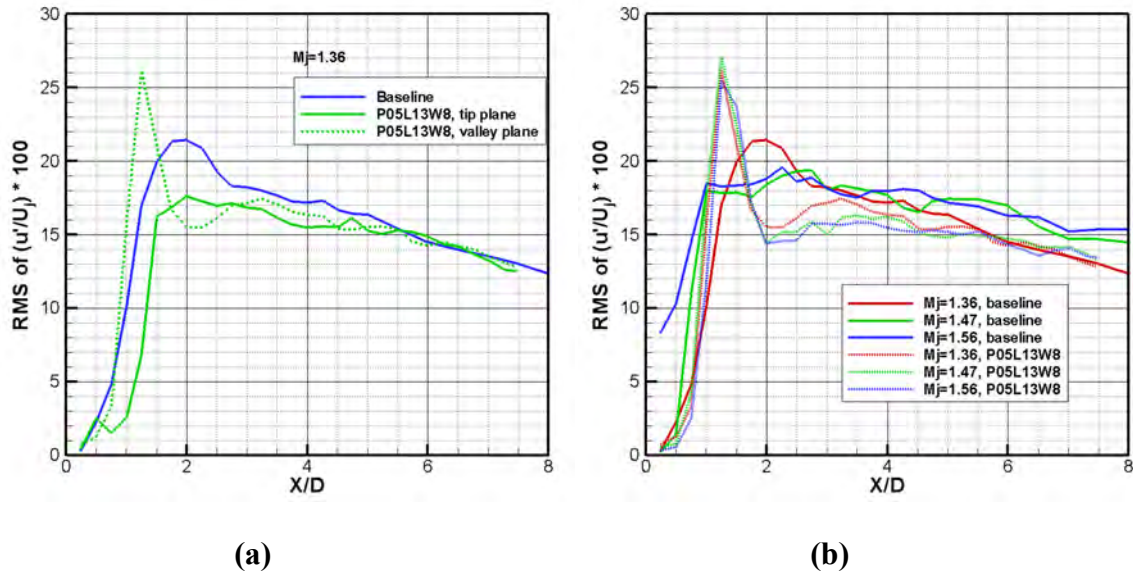


Figure 70. Comparison of the turbulence intensities between the baseline nozzle jets and the chevron nozzle jets along the lip line. (a) $M_j = 1.36$, tip and valley planes, (b) Three conditions, baseline and P05L13W8 valley plane.

Comparison of the turbulence intensities for the baseline and chevron nozzle jets at all the three operating conditions is shown in Figure 70 (b). For the baseline nozzle jets, the transition point of the shear layer from quasi-laminar to fully turbulent shifts upstream as the jet velocity increases. The higher the jet velocity, the faster the shear layer becomes fully turbulent, but the slower the turbulence intensity drops with downstream distance. As compared to the baseline nozzle jets, a significant difference appears within the first two nozzle diameters for the chevron nozzle jets. As well as the increased peak turbulence intensity near the nozzle exit in the valley plane, it is observed that the turbulence intensity is reduced in most of the jet flow downstream due to the enhanced turbulent mixing induced by the chevrons.

To examine the details of the turbulent mixing layer development, Figure 71 shows the power spectral density of u' (normalized by the fully expanded jet velocity U_j) at several locations for the baseline and chevron jets with $M_j = 1.47$. All profiles downstream of the axial location $x/D = 2.0$ for all jets show similar energy spectra with slightly different intensities. These spectra exhibit typical mixing-layer turbulence characteristics, with a dominant low-frequency energy-containing region, and an inertial high-frequency sub-range rolling off of a approximately with the Kolmogorov law $f^{-5/3}$. This suggests that the mixing layer becomes fully turbulent after $x/D = 2.0$ and the self-similarity is correctly captured.

In Figure 71, however, a significant difference is found within the first two nozzle exit diameters. For the baseline nozzle jet with $M_j = 1.47$ (similar observations appear for the baseline jet with $M_j = 1.56$), an abrupt increase of the energy spectra at lower Strouhal numbers is found and the peak becomes more broadband or disappears. For the chevron jet with $M_j = 1.47$ (similar characteristics are exhibited by the chevron jets operating at the other two jet conditions and the baseline jet with $M_j = 1.36$), a gradual increase of the intensity over the entire frequency range is

seen and a strong peak appears at the frequency corresponding to $St \approx 0.3$. The peak is identified as the shear layer instability, corresponding to a particular frequency of the disturbance that is selectively amplified in the shear layer. Experimental measurements exhibit a similar behavior at a Strouhal number $St \approx 0.3 \sim 0.5$ ^{69,70}.

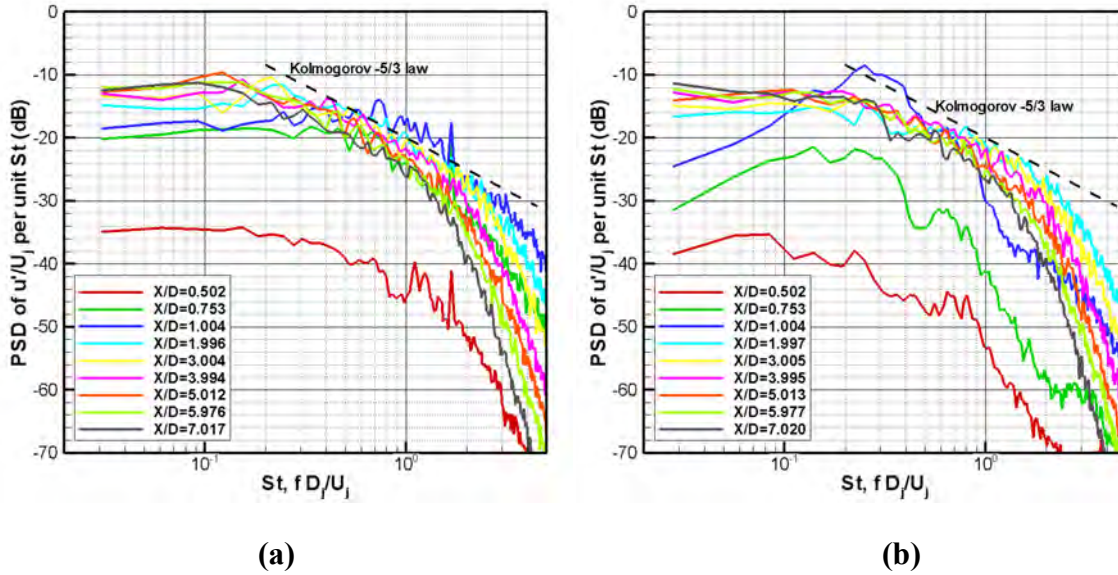


Figure 71. Comparison of the power spectral density of u' between the baseline nozzle jets and the chevron nozzle jets at various axial locations along the lip line. (a)

$M_j = 1.47$, baseline, (b) $M_j = 1.47$, P05L13W8.

Considering that significant over-predictions of the noise level appear only for the baseline jets with $M_j = 1.47$ and 1.56 , these results suggest that the initial development of the mixing layer is most likely responsible for these mismatches. A thin initial mixing layer is observed for these two jet conditions, but the shock-induced separation for the baseline nozzle jets with $M_j = 1.36$ (see Figure 68 (a)) and the enhanced mixing induced by the streamwise vortices in the chevron nozzle jets help to alleviate the problem. Effects of the initial boundary on the jet noise simulations have been discussed by Bodony and Lele⁷¹. More recently, Bogey et al. studied a $M_j = 0.9$ subsonic jet with a prescribed Blasius laminar profile and velocity perturbations excited by different tripping procedures at the nozzle exit. Similar over-predictions at high frequencies are observed using even a significantly finer mesh with 256 million grid points. Additional numerical studies are required in the future to test this speculation.

Figure 72 shows the two-point space-time correlation of the axial velocity fluctuation for the over-expanded jet with $M_j = 1.36$. The reference probe is fixed at $x/D = 4.0$. All correlations are normalized by the auto-correlation of each signal at zero time delay to derive the correlation coefficients ρ_{11} . At larger separation distances, the peaks of the correlation functions are less well resolved, mainly because the record length is quite short (approximately 5800 samples) and the correlation is largely contributed by the low frequency, large wavelength turbulent structures. Based on the two-point space-time cross correlations of the axial velocity perturbation u' along

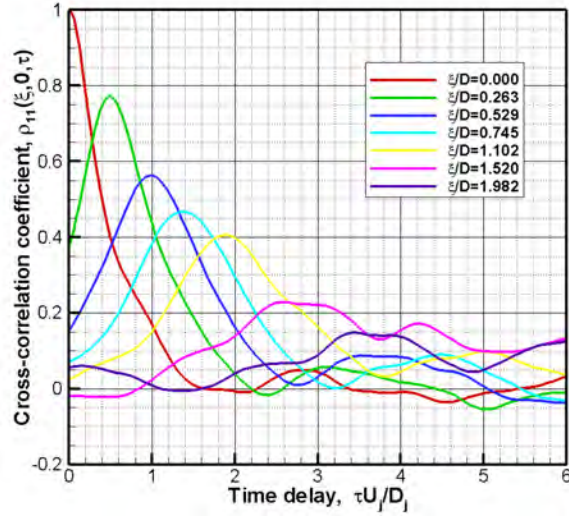


Figure 72. Cross correlation coefficients of the axial velocity at $x/D = 4.0$ along the lip line. Operating conditions: $M_j = 1.36$, $NPR = 3.0$, $TTR = 3.0$.

the lip line, a time scale L_τ in the moving reference frame can be defined as the time delay to the $1/e$ decay point of the envelope of the space-time correlation functions, and a length scale L_x defined as the separation distance to the $1/e$ decay point of the correlation at zero time delay $\tau = 0$. The variation of time delay for maximum correlation with the separation distance is shown in Figure 73. Except for the poorer prediction of the correlation peaks at larger separation distances because of the short record length, a linear dependence is found for both definitions of

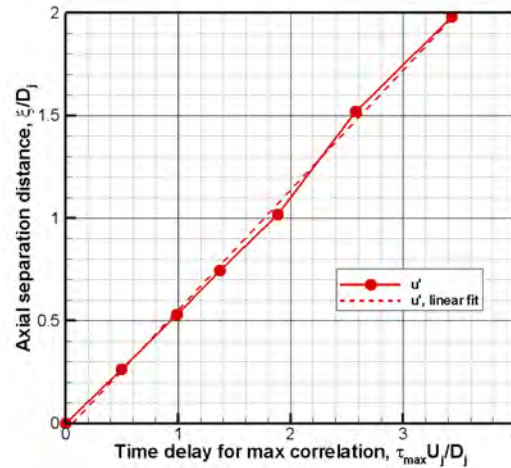


Figure 73. Variation of time delay for maximum cross correlation with separation distance. The reference flow probe is fixed at $x/D = 4.0$ along the lip line. Operating conditions: $M_j = 1.36$, $NPR = 3.0$, $TTR = 3.0$.

the correlation functions. The slope of the curve represents the overall convection speed of the turbulent eddies.

Table 8 summarizes the predictions for all jets. However, no attempt is made to quantitatively evaluate the effects of the chevrons on the statistical characteristics of the turbulent structures, considering that the small changes might be contaminated by several issues: (1) measurements of the turbulent fluctuations at the same locations along the lip line are subject to differences, considering the strong radial convection of the turbulent eddies for off-design supersonic jets; (2) analysis shows that the record length is not enough to meet statistical confidence requirements; (3) analysis shows that the evolution of the turbulent mixing layer is not accurately predicted in the baseline nozzle simulations. Despite these uncertainties, the comparison shows that all jets have similar statistical integral scales at the axial location of $x/D = 4.0$. Consequently, similar noise radiation directivity is observed as shown in the noise spectra in Figure 63.

Table 8. Predicted integral scales of the turbulent structures for all jets. Calculated at $x/D = 4.0$ along the lip line based on the second-order cross correlation of the axial velocity fluctuations.

Nozzles	M_j	$L_t U_j / D_j$	L_x / D	U_c / U_j	U_c / U_∞
Baseline	1.36	2.13	0.263	0.542	1.091
P05L13W8	1.36	1.87	0.254	0.517	1.041
Baseline	1.47	1.49	0.242	0.555	1.184
P05L13W8	1.47	1.76	0.240	0.515	1.100
Baseline	1.56	1.66	0.248	0.553	1.229
P05L13W8	1.56	1.64	0.228	0.560	1.245

Figure 74 (a) shows the predicted frequency-dependent phase velocities for all the jets to reveal the characteristics associated with different scales of turbulent eddies. The frequency-dependent phase velocity is calculated as:

$$U_c(f) = 2\pi f / \left(\frac{d\Phi(f)}{d\xi} \right) \quad (16)$$

where, $\Phi(f)$ is the phase delay of the complex cross spectrum at a downstream location with a separation distance ξ relative to the fixed probe. Due to an insufficient record length, large oscillations are found in the predictions. The results fitted with a logarithmic function $U_c / U_j(St) = A \ln St + B$ are shown in Figure 74 (b). All jets show an increasing phase velocity with frequency. There are only slight differences between the baseline nozzle jet and the chevron

nozzle jet at the same operating condition, or between the jets from the same nozzle at different operating conditions.

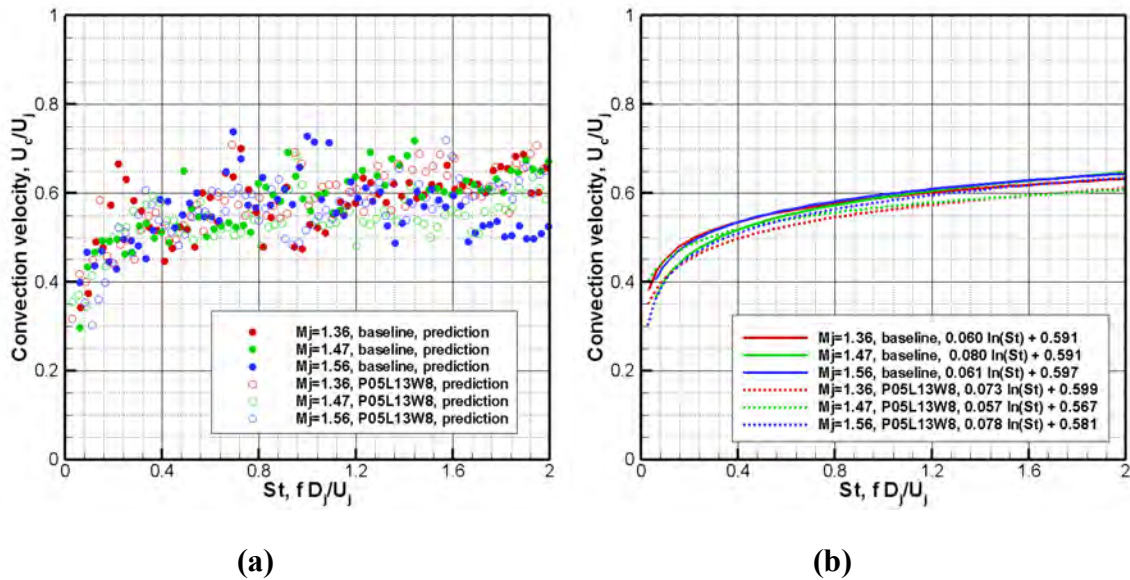


Figure 74. Comparison of the predicted frequency-dependent phase speeds for all the baseline and chevron nozzle jets. (a) Predicted convection speed, (b) fitted convection speed.

Conclusions for Task.4

In this task, jet flow simulations and noise predictions have been performed for a military-style baseline nozzle and a chevron nozzle operating at three off-design conditions with a hybrid method combining advanced CFD technologies and the acoustic analogy. The immersed boundary method with local grid refinement is used to avoid the difficulty in creating a body-conformal mesh for the chevrons.

Although the baseline nozzle simulations show over-predictions of the SPL at mid to high frequencies at some shallow polar angles, a good agreement of the predicted noise spectra with the acoustic measurements is found for both the baseline and the chevron nozzle jets. More encouraging is that the frequencies and amplitudes of the BBSAN components are captured accurately at all the three off-design conditions for both the baseline nozzle and the chevron nozzle.

Jet flow visualization shows that a pair of strong vortices is generated by each chevron. The vortices change the shock cell structures. The enhanced turbulent mixing induced by the streamwise vortices increases the turbulence intensity near the nozzle exit but reduces the turbulence intensity at further downstream locations.

The two-point space-time correlations are used to reveal the statistical characteristics of the turbulent eddies. The results show that chevrons induce a small change of the overall convection speed, integral time and length scales, and the frequency-dependent phase speed of the turbulent eddies. However, considering the numerical uncertainties, more detailed analysis is required to gain an in-depth knowledge of the statistical characteristics of the turbulent eddies under the impact of chevrons.

Two particular problems remain in the current methodology. The first is the insufficient record length of the flow and acoustic signals. It is shown that a sufficiently long record length is important for an accurate estimate of the noise reduction effect, because the actual noise reduction is small and a short record length produces large oscillations of the noise spectra. The second is the over-prediction of sound pressure levels at mid to high frequencies at some low polar angles for the baseline nozzle jets. The reason for these over-predictions remains uncertain. Numerical tests have shown that grid refinement does not improve the solution. Instead, analysis suggests that the initial boundary layer thickness and the initial development of the turbulence in the jet mixing layer are most likely to be responsible. Calculations with a refined definition of the nozzle boundary layer have not shown a reduction in the over-prediction. A remaining approach is to generate a turbulent unsteady flow at the nozzle using synthetic turbulence. This is the subject of ongoing research.

Tasks 4.3 & 4.5: Adjoint Design Method – Analytical Development and Application to Nozzle Design

Background and Motivation

The traditional method of design in aerodynamics has been to depend on the designer's intuition. Designers would make a design and then test it in a wind tunnel to determine its performance. With the introduction of computers, the field of aerodynamic design was revolutionized. Designs were first tested computationally and then actual wind tunnel testing was done. This saved cost because experiments can be very expensive and time-consuming. Computational experiments became the tool for design. However even these computational methods needed several iterations to reach an optimal design. These numerical experiments need a large amount of computations, and one can not be sure to have reached the optimal design. An optimal design is the design which optimizes a certain cost function within the given constraints. A method was needed which would give the direction in which one should perturb the geometry to reach the optimum value of cost function. The need for automatic designs came in to the picture with efforts to reduce the number of computational experiments done in order to reach a final optimal design. For automatic design the gradients of a cost function with respect to the design parameters are used to find the direction of steepest decent. But the traditional automatic design methods may still require considerable computational cost to calculate the gradients. Adjoint methods are methods that do not need as much computation as traditional methods to compute the needed gradients.

Adjoint methods have been used in optimal control theory since 1971. Nowadays, adjoint methods are being used for design in computational fluid dynamics more extensively. Jameson^{72,73,74,75,76,77} first used control theory in the field of aerodynamic design. He developed continuous adjoint methods for various governing equations including the potential, the Euler and the Navier-Stokes equations. An optimal design is the design which optimizes the defined cost function within the given constraints. The cost function could be taken to be either the lift or drag coefficients or some difference relative to a desired flow behavior. It can be chosen to describe any other property with the given constraints such as airfoil chord, wing volume for fuel, or weight. Giles⁷⁸ made important contributions to the use of adjoint methods in aerodynamic design. He developed an adjoint equation for the quasi-one-dimensional Euler equation⁷⁹.

Lions⁸⁰ used adjoint methods to develop an optimization technique for systems that are governed by partial differential equations. The adjoint equations have been used in optimal control theory for a long time. Pironneau⁸¹ used the adjoint equations for the first time in fluid dynamics for design work, but Jameson revolutionized the use of adjoint methods for aerodynamic design. He used them to find a geometry that optimizes a certain cost function. Jameson et al.^{72,73,74} developed adjoint methods for potential flow, and the Euler and Navier-Stokes equations. These methods were then developed for two and three dimensional wing designs and also for a full aircraft^{75,76}. The 'discrete' adjoint approach had been used by Elliott⁸² and Neilson and Anderson^{83,84} working with unstructured grids. Another interesting work is described by Mohammadi⁸⁵ where automatic differentiation software is used to take an original CFD code as input to provide the adjoint code.

Discrete and continuous adjoint approaches

The adjoint equations are formulated from the governing equations. They also depend on the choice of the cost function. The cost function is the property that is being minimized: such as lift or drag. For optimization of a design, it is necessary to find the perturbation in the cost function due to a perturbation in the geometry or other control parameters and a corresponding perturbation in the flow field. The goal of adjoint methods is to find the linearized perturbation of the cost function which is the gradient of the cost function with respect to the design parameters. Depending on the approach, adjoint methods can be divided into two kinds: discrete adjoint and continuous adjoint methods. When the governing equations are discretized first and then the adjoint equations are formulated, using the discretized governing equations, then the approach is known as the discrete approach. It is not necessary to discretize the adjoint equations in this case. When the governing equations are continuous and the adjoint equations are formulated using these equations, and then the adjoint equations are discretized in order to solve them, the approach is known as the continuous approach.

Objective

The objective of this task is to show how to redesign a jet nozzle contour such that the pressure distribution on the nozzle centerline matches a desired pressure distribution. Adjoint methods can be used to find the geometry that gives this desired pressure distribution. For the supersonic case, when there are shocks in the nozzle, this method can be used to find the geometry such that the shock strength is the cost function. Then, for example, broadband shock associated noise could be controlled by controlling the shock strength. The use of the adjoint method for this optimization will save on the computational cost of the nozzle design.

This section is divided into four parts. The first has given an introduction to the problem. The next section describes the formulation of adjoint methods in the context of finding the shape that gives the desired geometry. It describes how the formulation is different for one and two-dimensional cases. Both subsonic and supersonic cases are considered. The numerical methods used are explained in detail in the same section. Then, the results of the use of adjoint methods for subsonic and supersonic cases for both one and two-dimensional examples are given. Finally, conclusions and ideas for future work are presented.

The General Adjoint Approach

In this section, the formulation of the adjoint equation and the numerical technique to solve it are explained for the quasi-one-dimensional Euler equations. Here, the continuous approach has been used. The formulation of the adjoint equations for the two-dimensional Euler equations, their solution and discretization is explained later in this section. The duality of the adjoint solution is also explained.

Adjoint for quasi-one-dimensional Euler equation

The adjoint approach can be outlined by considering a simple example. Say the governing equations (quasi-Euler, Euler or Navier-Stokes) are given by,

$$R(U) = 0 \tag{17}$$

where U is the flow solution and R is a nonlinear differential operator. The solution will depend on the geometry of the problem. If the geometry is perturbed there will be a perturbation in flow field U which is given by u . The governing equation can be linearized with respect to u to give,

$$Lu = f \quad (18)$$

Let the cost function or objective function be given by $J(U)$. For aerodynamic design, the cost function will be a function of U . Changes in geometry will result in changes in U and consequently changes in the cost function. The linear perturbation of the cost function $I(u)$ can then be written as an inner product over the domain,

$$I(u) = (g, u) \quad (19)$$

for some given function g , where the inner product is given by,

$$(g, u) = \int_D g u dD. \quad (20)$$

If a direct approach is used for design, $I(u)$ is determined separately for each design variable by defining the appropriate geometry perturbation and solving the equation for u . In the adjoint approach this can be determined without explicitly calculating the perturbed flow field u . This is achieved by solving the adjoint equation. To formulate the adjoint equation introduce a Lagrange multiplier v such that,

$$I(u) = (g, u) - (v, Lu - f) \quad (21)$$

v has been introduced to enforce the constraint that u must satisfy Equation (18). The adjoint linear operator L^* is defined by the identity,

$$(v, Lu) = (L^*v, u) \quad (22)$$

for all u, v satisfying appropriate homogeneous boundary conditions. Using this, the identity

$$I(u) = (v, f) - (L^*v - g, u) = (v, f) \quad (23)$$

is obtained, provided v is the solution of the adjoint equation,

$$L^*v - g = 0 \quad (24)$$

The adjoint approach provides exactly the same answer as the direct linear perturbation analysis. The advantage of the adjoint formulation of the objective function is that only one adjoint equation needs to be solved in order to get the sensitivities to all the geometric parameters.

Problem formulation (quasi-one-dimensional Euler equations)

The nozzle is confined in $-1 \leq x \leq 1$.

The equations are the quasi-one-dimensional Euler equations, given by

$$R(U, h) = \frac{d}{dx}(hF) - \frac{dh}{dx}P = 0 \quad (25)$$

where,

$$U = \begin{Bmatrix} \rho \\ \rho q \\ \rho E \end{Bmatrix}, \quad F = \begin{Bmatrix} \rho q \\ \rho q^2 + p \\ \rho q H \end{Bmatrix}, \quad \text{and } P = \begin{Bmatrix} 0 \\ p \\ 0 \end{Bmatrix} \quad (26)$$

Also,

$$p = (\gamma - 1)\rho \left(E - \frac{q^2}{2} \right) \quad (27)$$

and,

$$H = E + \frac{p}{\rho}. \quad (28)$$

$h(x)$ represents the half height of the nozzle duct. For small perturbations in the duct shape $h(x)$ linearized equations can be formed.

Let $\tilde{h}(x)$ represents the perturbation in $h(x)$. The linearized equation is given by,

$$Lu - f \equiv \left(\frac{d}{dx}(hAu) - \frac{dh}{dx}Bu \right) - \left(\frac{d\tilde{h}}{dx}P - \frac{d}{dx}(\tilde{h}F) \right) = 0 \quad (29)$$

where u is the perturbation in the flow variable U , $A = \partial F / \partial U$ and $B = \partial p / \partial U$.

Let the objective function be the difference in the pressure distribution from a desired pressure distribution on the centerline of the nozzle. That is,

$$J = \frac{1}{2} \int_{-1}^1 (p - p_d)^2 dx \quad (30)$$

The cost function sensitivity is given by,

$$I = \frac{dJ}{dh} \tilde{h} = \int_{-1}^1 (p - p_d) \frac{dp}{dU} \frac{dU}{dh} \tilde{h} dx \quad (31)$$

but,

$$\frac{dU}{dh} \tilde{h} = u \quad (32)$$

hence,

$$I = \int_{-1}^1 (p - p_d) \frac{dp}{dU} u dx \quad (33)$$

Introduce the Lagrange multiplier v . A constraint on the objective function can be enforced by letting,

$$J = \frac{1}{2} \int_{-1}^1 (p - p_d)^2 dx - \int_{-1}^1 v^T R dx \quad (34)$$

This ensures that the flow satisfies the equation of motion (25). That is, $R = 0$. Then,

$$I = \frac{dJ}{dh} \tilde{h} = \int_{-1}^1 (p - p_d) \frac{dp}{dU} u dx - \int_{-1}^1 v^T (Lu - f) dx \quad (35)$$

Set, $dp / dU = g^T$, Then, consider

$$\int_{-1}^1 v^T \left(\frac{d}{dx}(hAu) - \frac{dh}{dx}Bu \right) dx \quad (36)$$

Integration by parts gives,

$$\int_{-1}^1 v^T L u dx = (v^T h A u)_{-1}^1 - \int_{-1}^1 \left(\frac{dv^T}{dx} h A u - v^T \frac{dh}{dx} B u \right) dx \quad (37)$$

Let,

$$hA^T \frac{dv}{dx} - \frac{dh}{dx} B^T v = L^* v \quad (38)$$

Then,

$$\int_{-1}^1 v^T L u dx = \left(v^T h A u \right)_{-1}^1 - \int_{-1}^1 \left(L^* v \right)^T u dx \quad (39)$$

and,

$$\begin{aligned} I &= \int_{-1}^1 (p - p_d) g^T u dx + \int_{-1}^1 v^T f dx - \int_{-1}^1 \left(L^* v \right)^T u dx - \left(v^T h A u \right)_{-1}^1 \\ &= \int_{-1}^1 v^T f dx - \int_{-1}^1 \left(L^* v - (p - p_d) g \right)^T u dx - \left(v^T h A u \right)_{-1}^1. \end{aligned} \quad (40)$$

Now we can set

$$L^* v - (p - p_d) g = 0 \quad (41)$$

This equation is the “Adjoint Equation” that can be solved for v . This eliminates the dependence of cost function sensitivity on u except at the boundaries. Inlet and exit conditions can be chosen to eliminate the explicit dependence of I on u . That is,

$$\left(v^T h A u \right)_{-1}^1 = 0 \quad (42)$$

At a boundary where the flow equations have n incoming characteristics, and hence n imposed boundary conditions, the adjoint equations will thus have $(3-n)$ boundary conditions corresponding to an equal number of incoming adjoint characteristics.

Then,

$$I = \int_{-1}^1 v^T f dx \quad (43)$$

Now, I provides the rate of change or sensitivity of the objective function with respect to change in the design parameter or parameters.

Example problem

Assume that the duct shape is a function of a parameter α ,

$$h(x) = \alpha + (1 - \alpha) x^2 \quad (44)$$

Figure 75 shows the geometry of the duct with the throat area being equal to α .

Note that,

$$\frac{\partial h}{\partial \alpha} = 1 - x^2 \quad (45)$$

Now return to the flow equation,

$$R(U, h(\alpha)) = 0 \quad (46)$$

The objective function is given by $J(U, \alpha)$. Linearization with respect to α gives,

$$h = h + \frac{dh}{d\alpha} d\alpha \text{ and } F = F + \frac{dF}{d\alpha} d\alpha. \quad (47)$$

Also,

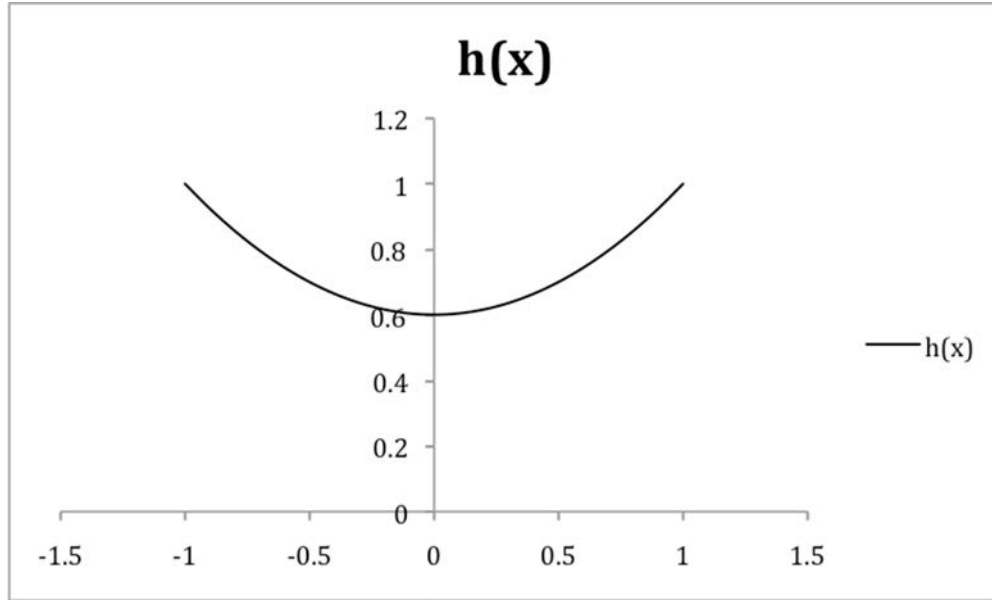


Figure 75. A general parabolic shape of nozzle which depends on one design parameter.

$$Lu = \frac{d}{dx}(hAu) - \frac{\partial h}{\partial x}Bu \quad (48)$$

and,

$$f = \frac{\partial^2 h}{\partial x \partial \alpha} P - \frac{d}{dx} \left(\frac{dh}{d\alpha} F \right) \quad (49)$$

Hence $Lu = f$ can be solved for u .

The design process is summarized in Figure 76. First assume a value for the design parameter α , say α_0 . The geometry for this value of design parameter is given by equation (44). The governing equations (25) are then solved for the flow properties ρ , p , E and u for the geometry corresponding to this value of design parameter. The value of objective function corresponding to this geometry can now be obtained using equation (30). The adjoint equations (41) are now solved with boundary conditions (42) for the adjoint variables v_1 , v_2 and v_3 . Now, the values of the adjoint variables and flow properties are known inside the domain. These values can be used to find the value of the sensitivity of the cost function with respect to the design parameter. The sensitivity of the cost function with respect to the design parameter is given by (43) and can directly be obtained using the adjoint variables and f . The flow source term f can be obtained using the equation (49). The new value of the design parameter(s) is found based on the steepest descent method. The process is repeated until the objective function reaches the desired minimum value.

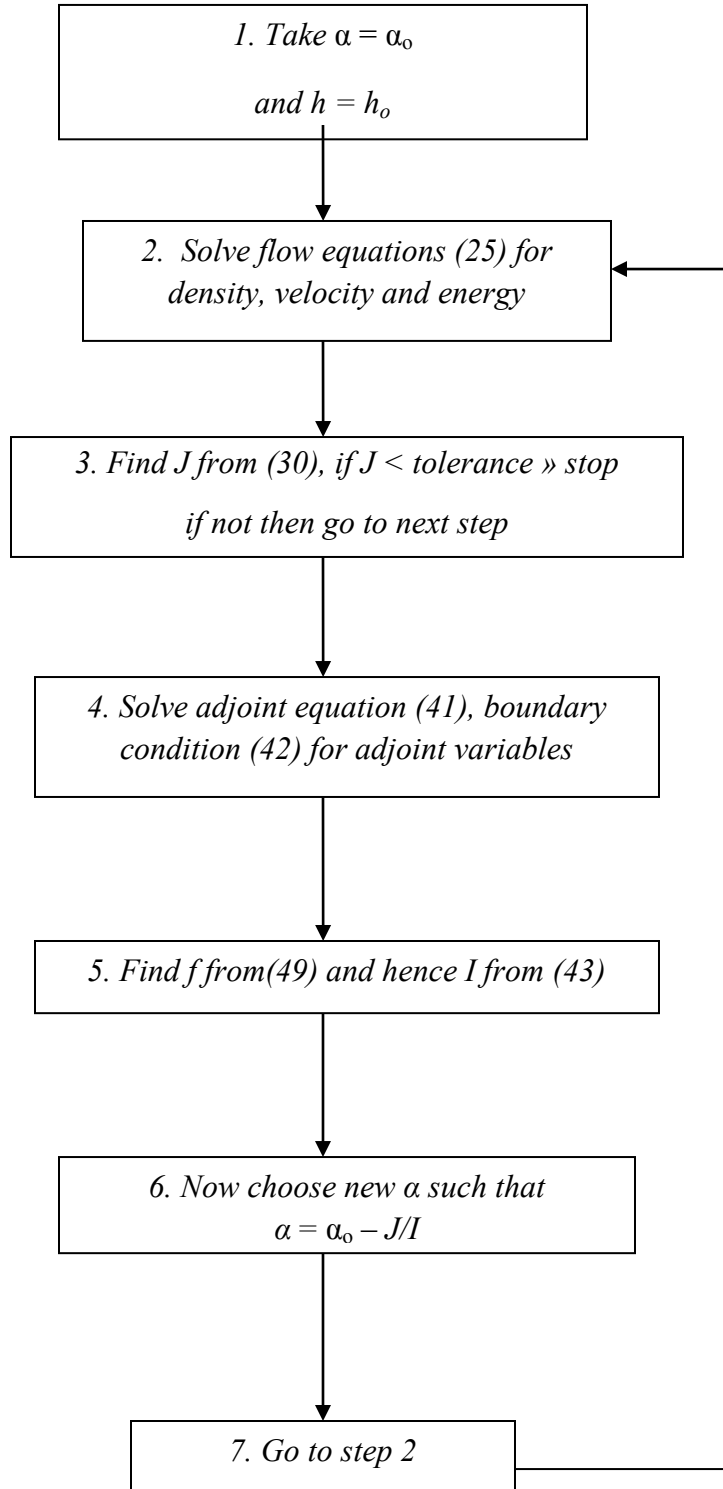


Figure 76. Algorithm for the adjoint method for designing a nozzle contour with one design variable.

Numerical implementation

Finite difference discretization is used to solve the flow equations (25) numerically. The equations are considered in conservative form in order to be able to capture the any shock that might occur. MacCormack's explicit technique⁸⁶ is used for discretizing the governing equations. The MacCormack scheme is implemented in two steps. The first step is known as the predictor step and is given by,

$$U_i^* = U_i^t - \frac{dt}{dx} \left((hF)_{i+1}^t - (hF)_i^t \right) + \frac{\partial h}{\partial x} \bigg|_i p_i^t + S_i^t \quad (50)$$

where, U^* is the intermediate flow solution. The second step is the corrector step which is given by,

$$U_i^{t+dt} = 0.5(U_i^t + U_i^*) - \frac{dt}{dx} 0.5(U_i^* - U_{i-1}^*) + S_i^{t+dt} \quad (51)$$

An artificial dissipation with a coefficient equal to 0.4 is always used to capture the shock when there is shock in the solution. The artificial dissipation terms S_i^t and $S_i^{t+\Delta t}$ are given by,

$$S_i^t = \frac{C_x |p_{i+1}^t - 2p_i^t + p_{i-1}^t|}{p_{i+1}^t + 2p_i^t + p_{i-1}^t} (U_{i+1}^t - 2U_i^t + U_{i-1}^t) \quad (52)$$

$$S_i^{t+\Delta t} = \frac{C_x |p_{i+1}^* - 2p_i^* + p_{i-1}^*|}{p_{i+1}^* + 2p_i^* + p_{i-1}^*} (U_{i+1}^* - 2U_i^* + U_{i-1}^*) \quad (53)$$

The grid is uniform in the entire domain. A fine grid with 151 points is used to obtain the numerical solution of the problem. Local time stepping is implemented to reach a steady state solution as a time accurate solution is not necessary. A very small time step (5×10^{-6}) is used to obtain a stable numerical solution. CFL number is taken to be 0.0255.

Theory of Two Dimensional Adjoint Equations

This section discusses the formulation of the two dimensional adjoint equations. A Cartesian coordinate system is used to define the geometry. The physical space is transformed to a uniform computational domain. The starting point is a system of nonlinear partial differential equations describing a steady flow within the computational domain. Curvilinear coordinates (ξ, η) are used. Using these coordinates, the partial differential equations describing the flow can be written as,

$$R(U, \alpha) = 0 \quad (54)$$

where, U is the flow solution, α are the design parameters and R is a nonlinear differential operator that depends on the mapping from (x, y) to (ξ, η) . Changing the shape changes the mapping and hence R . Linearization of R will give the linear partial differential equation,

$$Lu = f \quad (55)$$

where, u is the perturbation in the flow field and f is the change due to the mapping.

Let J be the objective function and α a vector of design variables. The aim is to find the sensitivity of the objective function with respect to the design variables. If $J = J(U, \alpha)$ then,

$$\delta J = \frac{\partial J^T}{\partial \alpha} \delta \alpha + \frac{\partial J^T}{\partial U} \delta U \quad (56)$$

Similarly,

$$\delta R = \frac{\partial R}{\partial \alpha} \delta \alpha + \frac{\partial R}{\partial U} \delta U = 0 \quad (57)$$

Multiplying equation (57) by v^T and subtracting from δJ , given by (56), gives,

$$\delta J = \frac{\partial J^T}{\partial \alpha} \delta \alpha + \frac{\partial J^T}{\partial U} \delta U - v^T \left(\frac{\partial R}{\partial \alpha} \delta \alpha + \frac{\partial R}{\partial U} \delta U \right) \quad (58)$$

Thus,

$$\delta J = \left(\frac{\partial J^T}{\partial \alpha} - v^T \frac{\partial R}{\partial \alpha} \right) \delta \alpha + \left(\frac{\partial J^T}{\partial U} - v^T \frac{\partial R}{\partial U} \right) \delta U \quad (59)$$

If v chosen to satisfy the adjoint equation,

$$\frac{\partial J^T}{\partial U} - v^T \frac{\partial R}{\partial U} = 0, \quad (60)$$

then the sensitivity of the objective function will be independent of the flow solution perturbation δU .

Problem Formulation

Consider the domain for the problem as the upper half of the nozzle as shown in Figure 77. Only the upper half is considered because the nozzle is assumed to be symmetric about the centerline. The governing equations for the flow are Euler's equations. In conservative form Euler's equations are,

$$\frac{\partial U}{\partial t} + \frac{\partial F}{\partial x} + \frac{\partial G}{\partial y} = 0 \quad (61)$$

where,

$$U = \begin{Bmatrix} \rho \\ \rho u \\ \rho v \\ \rho E \end{Bmatrix}, \quad F = \begin{Bmatrix} \rho u \\ \rho u^2 + p \\ \rho uv \\ \rho uH \end{Bmatrix}, \quad \text{and} \quad G = \begin{Bmatrix} \rho v \\ \rho uv \\ \rho v^2 + p \\ \rho vH \end{Bmatrix} \quad (62)$$

The equations are transformed to a curvilinear coordinate system for the purpose of solving the equations numerically. The transformation matrix is defined by,

$$K = \begin{bmatrix} \frac{\partial x}{\partial \xi} & \frac{\partial x}{\partial \eta} \\ \frac{\partial y}{\partial \xi} & \frac{\partial y}{\partial \eta} \end{bmatrix} \quad (63)$$

and the Jacobian by,

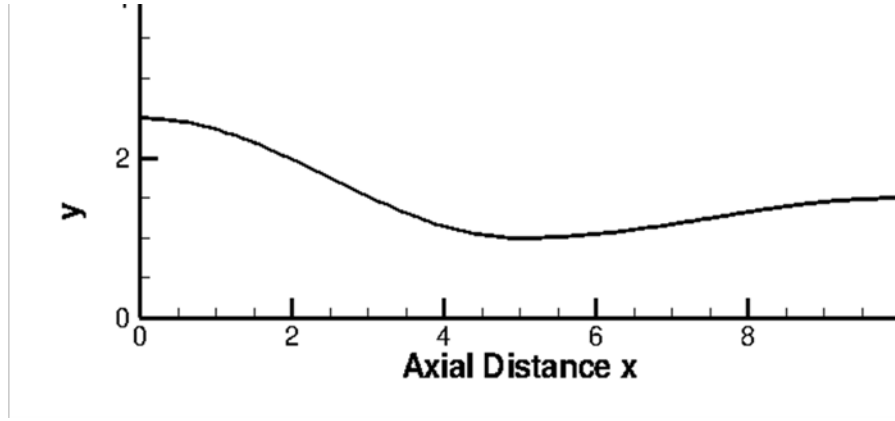


Figure 77. The general geometry of the nozzle for a two-dimensional case.

$$J_c = \frac{\partial x}{\partial \xi} \frac{\partial y}{\partial \eta} - \frac{\partial x}{\partial \eta} \frac{\partial y}{\partial \xi} \quad (64)$$

Introduce the contravariant velocity components,

$$\begin{Bmatrix} U' \\ V' \end{Bmatrix} = K^{-1} \begin{Bmatrix} u \\ v \end{Bmatrix} = \frac{1}{J} \begin{bmatrix} \frac{\partial y}{\partial \eta} & -\frac{\partial x}{\partial \eta} \\ -\frac{\partial y}{\partial \xi} & \frac{\partial x}{\partial \xi} \end{bmatrix} \begin{Bmatrix} u \\ v \end{Bmatrix} \quad (65)$$

Then, in the transformed plane (ξ, η) , the equations are,

$$\frac{\partial U'}{\partial t} + \frac{\partial F'}{\partial \xi} + \frac{\partial G'}{\partial \eta} = 0 \quad \text{in } D \quad (66)$$

where,

$$U' = J \begin{Bmatrix} \rho \\ \rho u \\ \rho v \\ \rho E \end{Bmatrix}, \quad F' = J \begin{Bmatrix} \rho U' \\ \rho U' u + \frac{\partial \xi}{\partial x} p \\ \rho U' v + \frac{\partial \xi}{\partial y} p \\ \rho U' H \end{Bmatrix}, \quad \text{and } G' = J \begin{Bmatrix} \rho V' \\ \rho V' u + \frac{\partial \eta}{\partial x} p \\ \rho V' v + \frac{\partial \eta}{\partial y} p \\ \rho V' H \end{Bmatrix}. \quad (67)$$

Now, the linearization of the fluxes with respect to the design parameter gives,

$$F \rightarrow F + \frac{\partial F}{\partial U} \frac{\partial U}{\partial \alpha} \tilde{\alpha} \quad \text{and} \quad G \rightarrow G + \frac{\partial G}{\partial U} \frac{\partial U}{\partial \alpha} \tilde{\alpha} \quad (68)$$

If these relationships are introduced into the equations of motion (66), terms independent of $\tilde{\alpha}$ will cancel each other and terms involving the square of $\tilde{\alpha}$ are neglected as they are assumed to be small. The linearized equation can then be written,

$$Lu = f \quad (69)$$

where,

$$Lu = \frac{\partial}{\partial \xi} \left[(Ay_\eta - Bx_\eta)u \right] + \frac{\partial}{\partial \eta} \left[(-Ay_\xi + Bx_\xi)u \right] \quad (70)$$

$$f = \frac{\partial}{\partial \xi} \left[\left(F \frac{\partial}{\partial \alpha} y_\eta - G \frac{\partial}{\partial \alpha} x_\eta \right) u \right] + \frac{\partial}{\partial \eta} \left[\left(-F \frac{\partial}{\partial \alpha} y_\xi + G \frac{\partial}{\partial \alpha} x_\xi \right) u \right] \quad (71)$$

where,

$$A = \frac{\partial F}{\partial U} \text{ and } B = \frac{\partial G}{\partial U}. \quad (72)$$

The desired pressure distribution on the nozzle centerline is specified, and a nozzle contour is to be found that gives this desired distribution. Let the cost function be defined as the difference between the pressure at the centerline and the desired pressure at the centerline. The goal is to minimize this cost function. The cost function is defined as,

$$J = \frac{1}{2} \int_0^{\xi_m} (p - p_d)^2 d\xi \quad (73)$$

where p_d is the desired pressure distribution at the nozzle centerline, p is the calculated pressure distribution at the nozzle centerline, and ξ_m is the maximum value of ξ , that is,

$$0 \leq \xi \leq \xi_m. \quad (74)$$

Now, multiply the governing equation by v^T and subtract from the cost function. This gives,

$$J = \frac{1}{2} \int_0^{\xi_m} (p - p_d)^2 d\xi - \int_0^{\xi_m} v^T R d\xi$$

The cost function sensitivity is given by,

$$I = \frac{\partial J}{\partial \alpha} \tilde{\alpha} = \int_0^{\xi_m} (p - p_d) \frac{\partial p}{\partial U} u d\xi - \int_0^{\xi_m} v^T (Lu - f) d\xi \quad (75)$$

$$(76)$$

where, $u = (\partial U / \partial \alpha) \tilde{\alpha}$. That is,

$$I = \int_0^{\xi_m} \left((p - p_d) \frac{\partial p}{\partial U} u - v^T Lu \right) d\xi + \int_0^{\xi_m} v^T f d\xi \quad (77)$$

Integration by parts and rearrangement leads to,

$$I = \int_0^{\xi_m} \left((p - p_d) \frac{\partial p}{\partial U} u + \frac{\partial v^T}{\partial \xi} (Ay_\eta - Bx_\eta) \right) d\xi + \int_0^{\xi_m} v^T f d\xi + v^T (Ay_\eta - Bx_\eta) u \Big|_0^{\xi_m} \quad (78)$$

The adjoint equation is chosen such that,

$$I = \int_0^{\xi_m} v^T f d\xi \quad (79)$$

Thus the adjoint equation is,

$$(p - p_d) \frac{\partial p}{\partial U} u + \frac{\partial v^T}{\partial \xi} (Ay_\eta - Bx_\eta) = 0 \quad (80)$$

with the boundary conditions for the adjoint equation being,

$$v^T (Ay_\eta - Bx_\eta) u \Big|_0^{\xi_m} = 0 \quad (81)$$

The process is summarized in Figure 78. First, take a set of guessed values of the design parameters α , say α_0 and find the geometry corresponding to this set of design parameters. The governing equations (66) are then solved for the geometry corresponding to this set of design parameters for the flow properties ρ , p , v , E and u . The value of the objective function corresponding to this geometry can now be obtained using equation (73). The adjoint equations (80) are now solved with the boundary conditions (81) to obtain the adjoint variables v_1 , v_2 , v_3 and v_4 . The value of the gradient of the cost function with respect to the design parameter then can be directly obtained by equation (79) using the adjoint variables. A new value of design parameter(s) is found based on the steepest descent method. The process is repeated until the objective function reaches a desired minimum value.

Supersonic case with shocks

In the case of supersonic flow a shock may occur in the flow domain inside the nozzle. For example if the pressure ratio p_a/p_o equals 0.67 a shock forms near the nozzle exit. This discontinuity in the flow makes the objective function discontinuous at the location of the shock, since the objective function is chosen to be the integral of the pressure difference between the actual and desired values along the nozzle centerline. With this discontinuity in the flow the adjoint equations cannot be solved. To remove the discontinuity in the objective function the objective function is redefined as,

$$J = \frac{1}{2} \int_{\xi_1}^{\xi_m} \left\{ \lambda_1 Z^2 + \lambda_2 \left(\frac{dZ}{d\xi} \right)^2 \right\} d\xi - \int_{\xi_1}^{\xi_m} v^T R d\xi \quad (82)$$

where Z is a function to be defined below. The gradient of the objective function with respect to the design parameter(s) (also known as the sensitivity) is then given by,

$$I = \int_{\xi_1}^{\xi_m} Z \frac{\partial p}{\partial U} u d\xi - \int_{\xi_1}^{\xi_m} v^T (Lu - f) d\xi, \text{ where } u = \frac{\partial U}{\partial \alpha} \tilde{\alpha} \quad (83)$$

Hence, in this formulation, Z replaces $(p - p_d)$. Here $\xi_1 \leq \xi \leq \xi_m$ is the centerline coordinate. In the present case, $\xi_1 = 0$. Integration by parts and rearrangement leads to,

$$I = \int_0^{\xi_m} \left(Z \frac{\partial p}{\partial U} u - v^T Lu \right) d\xi + \int_0^{\xi_m} v^T f d\xi \quad (84)$$

The adjoint equation is chosen such that,

$$I = \int_0^{\xi_m} v^T f d\xi \quad (85)$$

Thus the adjoint equation is,

$$Z \frac{\partial p}{\partial U} u + \frac{\partial v^T}{\partial \xi} (Ay_\eta - Bx_\eta) = 0 \quad (86)$$

with the boundary conditions for the adjoint equation being chosen such that,

$$v^T (Ay_\eta - Bx_\eta) u \Big|_0^{\xi_m} = 0 \quad (87)$$

During the derivation of the adjoint equation it is also necessary to enforce the condition,

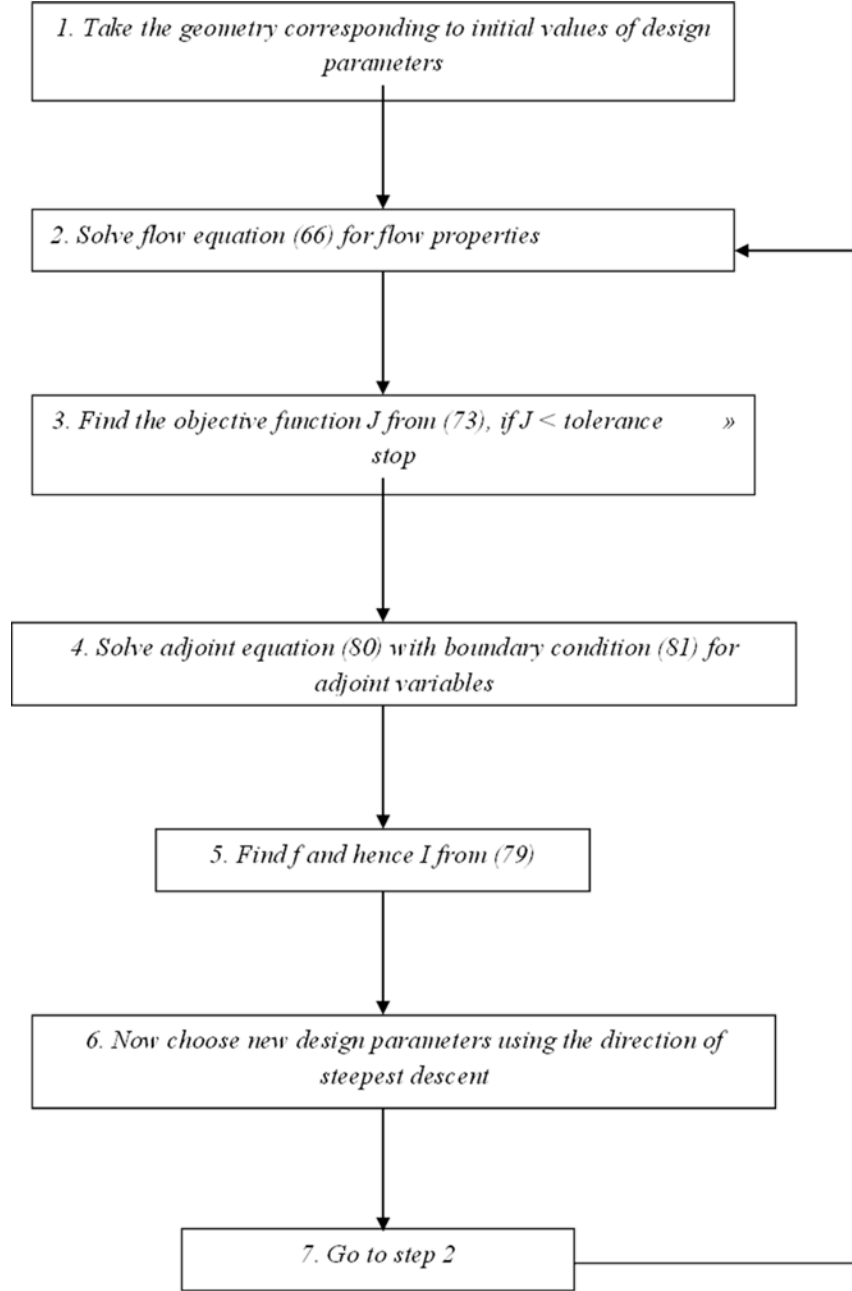


Figure 78. Algorithm for the adjoint method for designing a nozzle contour.

$$\left[Z \frac{d\delta Z}{d\xi} \right]_{\xi_1}^{\xi_m} = 0 \quad (88)$$

From this it is chosen that $Z(\xi_1)=Z(\xi_m)=0$. Then Z is calculated numerically in the domain. The values of λ_1 and λ_2 are chosen such that the equation,

$$\lambda_1 Z - \lambda_2 \frac{d^2 Z}{d\xi^2} = p - p_d \quad (89)$$

has a smooth solution for Z .

The solution procedure is,

1. solve the flow equation
2. solve for the shock parameter Z
3. solve the adjoint equation
4. calculate the value of the objective function
5. correct the design parameter in the direction of steepest descent.

Numerical implementation

The two-dimensional physical space is mapped to a uniform computational space. Cartesian coordinates (x,y) are transformed to a uniform computational domain (ξ,η) . Every constant ξ line corresponds to a constant x line and every constant η line corresponds to a contour in the y direction. The grid distribution is uniform in the η direction but it is not uniform in ξ direction. Figure 79 shows the grid inside the domain. The distribution of the increment dx is shown in Figure 80. This distribution is chosen such that the flow in the convergent and divergent sections is captured accurately. There is more clustering near the outflow and less clustering near the inflow. A fine grid with 201×21 points is used to obtain the numerical solution of the problem. A very small time step (5×10^{-7}) is used to obtain a stable numerical solution. The CFL number is taken to be 0.0068.

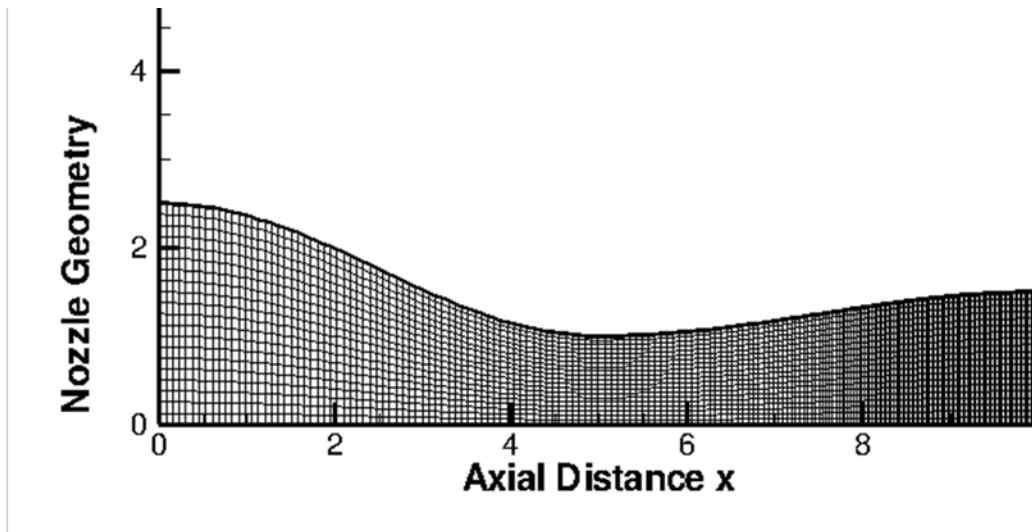


Figure 79. Mesh inside the nozzle domain for two-dimensional calculations.

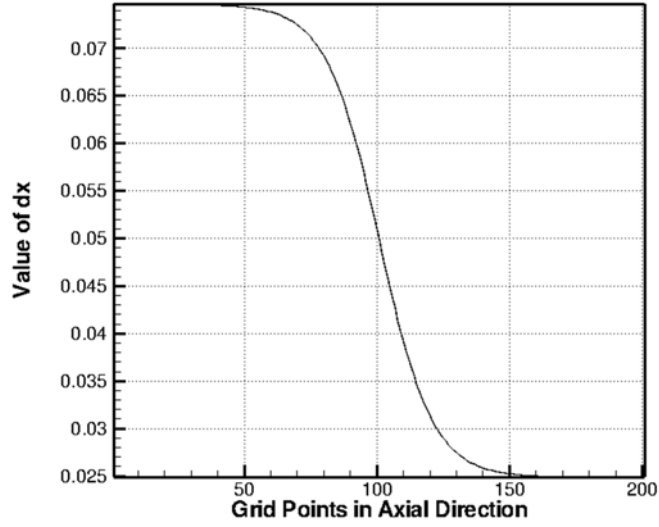


Figure 80. The distribution of increment dx with grid points along the nozzle centerline.

Local time stepping is used to obtain the steady state solution. The second order explicit finite difference MacCormack scheme is used to find the flow solution. It is a predictor corrector scheme. The first step is given by,

$$u_{i,j}^* = u_{i,j}^t - \frac{dt}{d\xi} (f_{i+1,j}^t - f_{i,j}^t) - \frac{dt}{d\eta} (g_{i,j+1}^t - g_{i,j}^t) + S_{i,j}^t \quad (90)$$

where u^* is the intermediate flow solution. The second step is given by,

$$u_{i,j}^{t+\Delta t} = 0.5(u_{i,j}^t + u_{i,j}^*) - \frac{dt}{d\xi} 0.5(f_{i,j}^* - f_{i-1,j}^*) - \frac{dt}{d\eta} 0.5(g_{i,j}^* - g_{i,j-1}^*) + S_{i,j}^{t+\Delta t} \quad (91)$$

Where $u_{i,j}^t, g_{i,j}^t$ and $f_{i,j}^t$ are the components of the vectors defined by equation (66) at the grid point i, j and time step t .

Artificial dissipation with a coefficient 0.4 is used to smooth the shock when there is shock in the solution. The artificial dissipation factors are $S_{i,j}^t$ and $S_{i,j}^{t+\Delta t}$, given by,

$$S_{i,j}^t = \frac{C_x |p_{i+1,j}^t - 2p_{i,j}^t + p_{i-1,j}^t|}{p_{i+1,j}^t + 2p_{i,j}^t + p_{i-1,j}^t} (u_{i+1,j}^t - 2u_{i,j}^t + u_{i-1,j}^t) + \frac{C_y |p_{i,j+1}^t - 2p_{i,j}^t + p_{i,j-1}^t|}{p_{i,j+1}^t + 2p_{i,j}^t + p_{i,j-1}^t} (u_{i,j+1}^t - 2u_{i,j}^t + u_{i,j-1}^t) \quad (92)$$

$$S_{i,j}^{t+\Delta t} = \frac{C_x |p_{i+1,j}^* - 2p_{i,j}^* + p_{i-1,j}^*|}{p_{i+1,j}^* + 2p_{i,j}^* + p_{i-1,j}^*} (u_{i+1,j}^* - 2u_{i,j}^* + u_{i-1,j}^*) + \frac{C_y |p_{i,j+1}^* - 2p_{i,j}^* + p_{i,j-1}^*|}{p_{i,j+1}^* + 2p_{i,j}^* + p_{i,j-1}^*} (u_{i,j+1}^* - 2u_{i,j}^* + u_{i,j-1}^*) \quad (93)$$

Results and discussion

In the previous section it was shown how adjoint methods could be used to determine a nozzle shape with particular flow characteristics. To assess the method further, a desired pressure

distribution is taken to correspond to a known nozzle shape. For this known shape, the pressure distribution at the nozzle centerline is calculated by solving the Euler equations (one or two dimensional). Then the shape is perturbed from the desired one. The first design cycle uses this new shape to find the flow solution. Then the adjoint solution and hence the gradient of the objective function with respect to the design parameter(s) is determined. This gradient is used to calculate the next value of design parameter as follows,

$$\alpha^{new} = \alpha^{old} - \frac{J}{\left(\partial J / \partial \alpha\right)} \quad (94)$$

Here α^{new} is the new value of the design parameter, α^{old} is the previous value of the design parameter, J is the objective function corresponding to the previous value of the design parameter, and $\partial J / \partial \alpha$ is the gradient of the objective function with respect to the previous value of the design parameter (calculated using adjoint methods).

When there are several design parameters $\{\alpha_i\}$,

$$\alpha_i^{new} = \alpha_i^{old} - \frac{J}{\left(\partial J / \partial \alpha_i\right)} \quad (95)$$

Either (94) or (95) is iterated until the value of the objective function reaches a desired limit: usually a small value. It generally takes small number of iterations to reach to the desired limit. This is discussed in detail along with a discussion of the individual cases.

Quasi-one-dimensional and two-dimensional cases are considered to determine the nozzle shape that gives the desired pressure distribution on the nozzle centerline. Both subsonic and supersonic flows are considered. The findings are compared with earlier results by Giles and Jameson. Two different kinds of nozzle geometries are considered for the two-dimensional case – one with one design parameter and other with three design parameters.

Quasi-one-dimensional nozzle

A convergent-divergent nozzle is considered here. The use of the adjoint method to determine a geometry which gives the desired pressure distribution is demonstrated. The nozzle under consideration has a very simple shape given by a parabola. That is,

$$h(x) = \alpha + (1 - \alpha)x^2 \quad (96)$$

The parabola depends on a single parameter α . As discussed earlier, the flow inside a nozzle depends mainly on the axial position and area ratio. Hence, the quasi-one-dimensional equations (25) are considered to determine the flow properties inside the nozzle.

Figure 81 shows the geometry of the nozzle. Note that the actual equations are quasi-one-dimensional. The exact shape changes with the value of the design parameter α . The desired pressure distribution corresponds to value of $\alpha = 0.8$. This geometry is shown in black in the figure. This is the value that is needed to be reached by the adjoint design method. To start the design procedure, the initial value of α is taken to be 0.68, the corresponding geometry is shown by the red line in Figure 81. The corresponding pressure distribution is found numerically at the nozzle centerline for a subsonic case. The geometry is parabolic and the area ratio (A_e/A_o) is

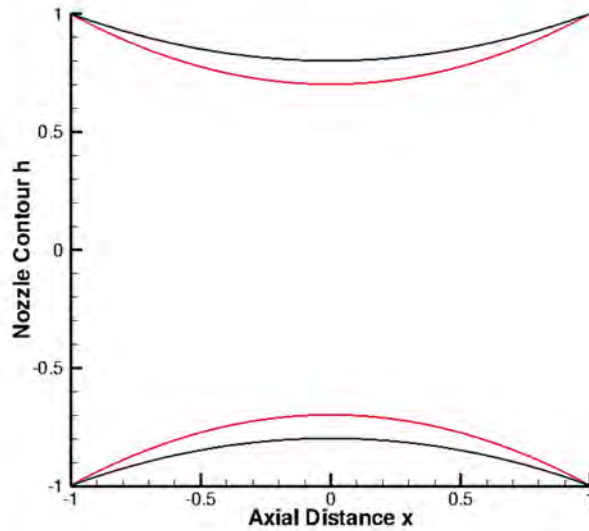


Figure 81. Initial and final nozzle shapes. The black line shows the final geometry and the red line shows the initial shape for quasi-one-dimensional flow.

equal to one and so is the pressure ratio. To ensure that there is a flow inside the nozzle, a small velocity has been assigned at the inflow. The flow accelerates inside the nozzle and then it decelerates to have the exit Mach number equal to the inlet Mach number. After the first design cycle, the value of α obtained is 0.6779. This value of α is now used to obtain the next value of α . The MacCormack scheme is used to determine the flow solution.

The decrease in the value of $(p-p_d)^2$ (that is, the difference in the desired and numerical pressure) is rapid initially and gradual afterwards. Hence the objective function drops rapidly for the first few design cycles and then drops more gradually as shown in Figure 82. The objective function shows a very good rate of convergence as does the design parameter as shown in Figure 83. It took approximately 17 design cycles to converge to a value of $\alpha = 0.80009$. The corresponding value of objective function is $73.93 (N/m^2)^2$, which is a drop from its initial value of $8.563 \times 10^4 (N/m^2)^2$.

Figure 84 shows the initial, final and desired pressure distributions. The initial pressure distribution is given by red in the figure. The final pressure distribution is given by blue which overlaps the desired pressure distribution (symbols). The maximum difference between initial and final pressure distributions is approximately $20000 N/m^2$. The difference between the desired and final pressure distributions is negligible. Hence, from now onwards, there is no need for additional design cycles and it can be observed from the α and objective function convergence plots, Figure 82 and Figure 83, that the change is negligible after a certain number of design cycles.

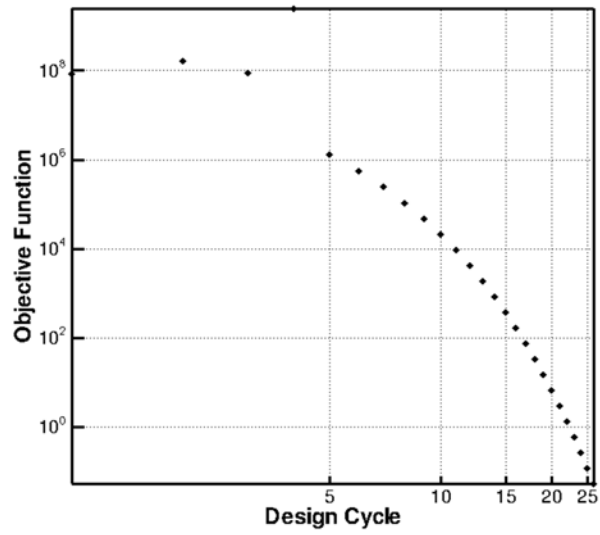


Figure 82. The convergence of objective function with design cycles on a log-log plot for quasi-one-dimensional flow.

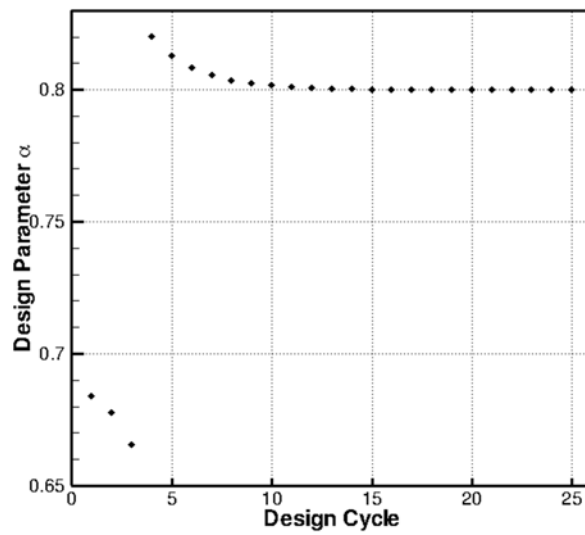


Figure 83. The convergence of the design parameter α with design cycles for quasi-one-dimensional flow.

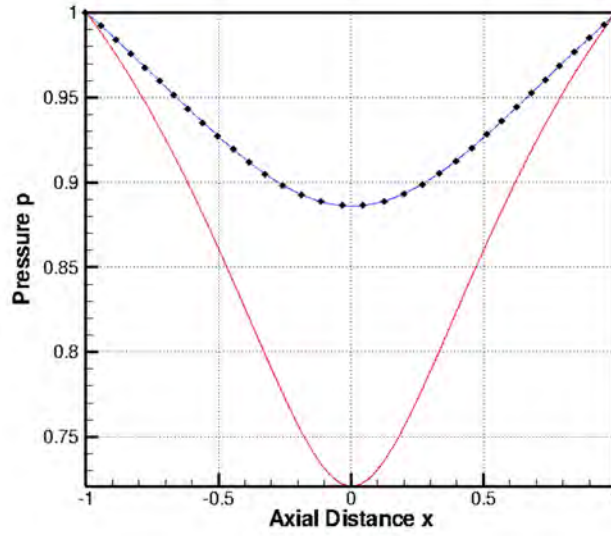


Figure 84. The distribution of the final, desired and initial pressure distribution (with respect to total pressure p_0) as function of axial distance inside nozzle. The symbols represent the desired pressure distribution, the blue line represents the final pressure distribution, and the red line represents the initial pressure distribution for quasi-one-dimensional flow.

Two-dimensional Nozzle

A two-dimensional nozzle is considered for this case. The flow is considered to be inviscid and the two-dimensional compressible inviscid equations are used as the governing equations in conservative form. Two different cases are considered in this section. First, a simple case where the nozzle geometry depends on only one design parameter is studied. A subsonic flow solution is found for this case. The second case is where the nozzle geometry depends on three design parameters. All three design parameters are varied and design iterations are performed to obtain the desired centerline pressure distribution. First the subsonic case is presented and then a case where a shock forms inside the nozzle is presented.

One Design Parameter

To demonstrate the design method a simple case is considered first. A nozzle shape is introduced that is governed by only one design parameter. This parameter is denoted by α . The nozzle contour is given by the equations,

$$\begin{aligned} y &= 1.75 - (0.5 + \alpha) \cos((0.2x - 1)\pi) & 0 \leq x \leq 5 \\ y &= 1.25 - \alpha \cos((0.2x - 1)\pi) & 5 \leq x \leq 10. \end{aligned} \quad (97)$$

Figure 85 shows the nozzle geometry for different values of design parameter α . First, the desired pressure distribution is calculated for $\alpha = 0.25$. The nozzle shape for this value of α is shown by the black line in Figure 85. Now, to start the design cycle, a different initial value of

$\alpha = 0.1$ is considered. This nozzle shape is shown by the red line in Figure 85. It is chosen such that the initial geometry is quite different to the desired geometry.

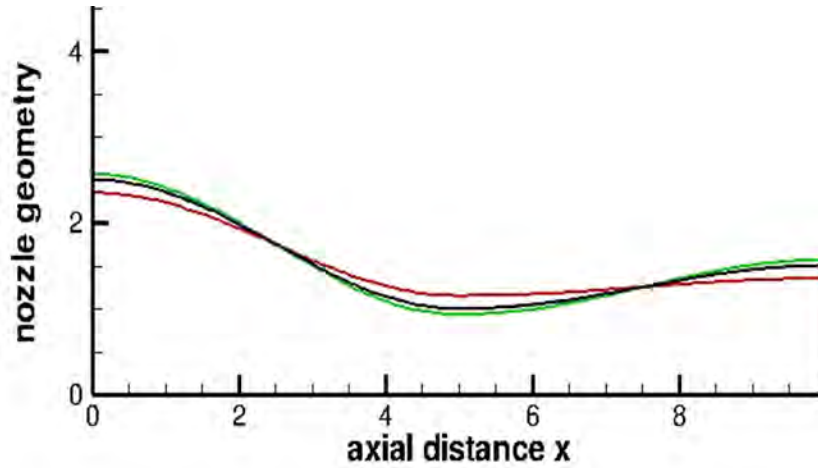


Figure 85. The initial (red), intermediate (green) and final (black) geometry of the rectangular nozzle.

After the first design cycle, the estimated value of α has changed to 0.1722. This value is used to find the next value of α . The adjoint equations are solved for this value of α and then the gradients are used to find the next value of α as explained earlier in this chapter. The process can be summarized in the following steps:

1. Define the geometry for a given set of parameters.
2. Solve the flow equations (66).
3. Find the objective function. If it is less than the tolerance – stop, otherwise move to the next step.
4. Solve the adjoint equations (80) with boundary condition (81).
5. Calculate the gradient of the objective function with respect to the design parameter(s).
6. Correct the geometry in the direction of steepest descent.
7. Return to step 2.

This procedure gives the value of α to be 0.2497 in 10 design cycles. For this value of design parameter the flow properties in the nozzle match closely with the desired values (Figure 86 and Figure 87). The decay of the objective function with design cycles is shown in Figure 88, it decays rapidly initially and then it decays steadily to close to zero. The convergence of α on the log-log plot is shown in Figure 89. These convergence rates are lower than the convergence rates of the one-dimensional solution. It was observed that after 10 design cycles α keeps on fluctuating and does not converge any further. It reaches the proximity of the desired value and then it keeps oscillating around that. The reason for the oscillations can be given by the fact that pressure distribution is already close to the desired pressure distribution and further design cycles are not really useful. It could also be the limit of the resolution of the numerical solution.

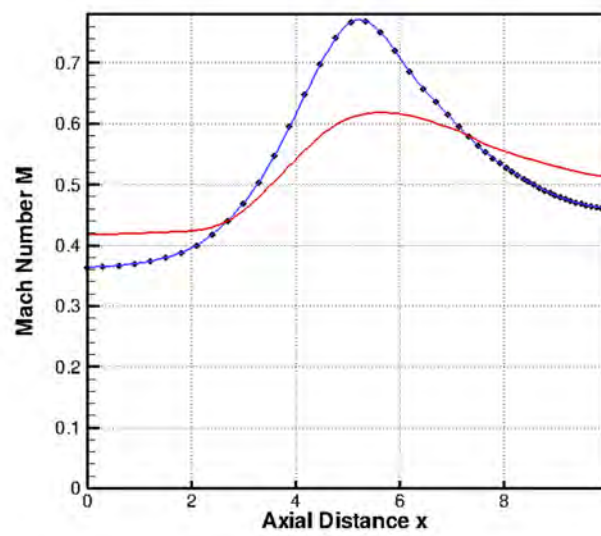


Figure 86. The Mach number distribution along the centerline of the nozzle. The red and blue lines show the initial and final Mach number respectively along the nozzle centerline. The desired Mach number is shown by symbols.

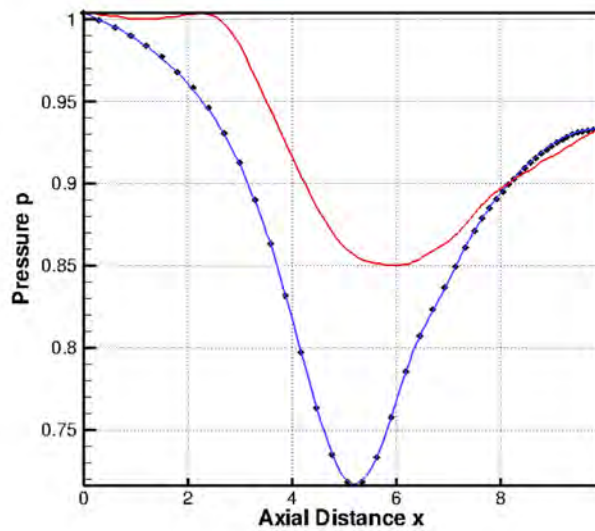


Figure 87. The pressure distribution (with respect to total pressure p_0) along the centerline of the nozzle. The red and blue lines show the initial and final pressure respectively along the nozzle centerline. The desired pressure is shown by black symbols.

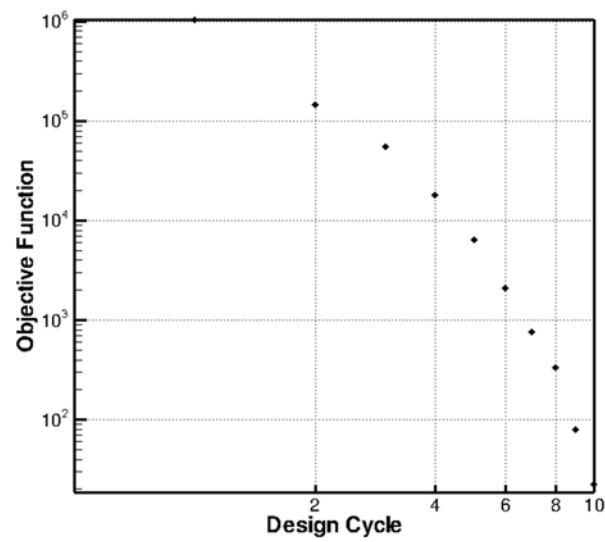


Figure 88. The decay of the objective function with design cycles.

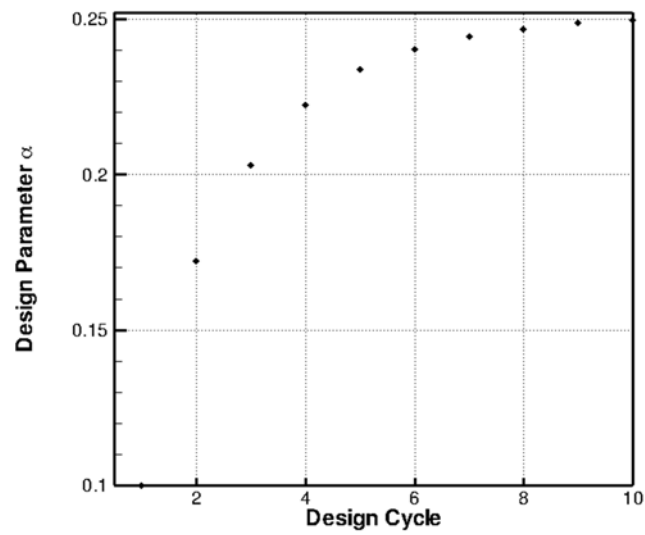


Figure 89. Change in the design parameter α with design cycles. The desired value of design parameter is 0.25.

Figure 86 and Figure 87 show the distribution of Mach number and pressure respectively at the nozzle centerline. The value of p_e/p_o is kept constant and is equal to 0.93 to ensure subsonic flow inside the nozzle. The initial and final flow properties are quite different from each other. The final flow properties are equal to the desired flow property, which shows that very good convergence is achieved through this method. The flow solutions for the initial and final geometries inside the whole nozzle domain are shown for a case of subsonic flow in Figure 90. It can be noticed that the initial and final flows are quite different especially at the nozzle throat. A low-pressure zone extends for the final flow at the throat which is same as the desired condition.

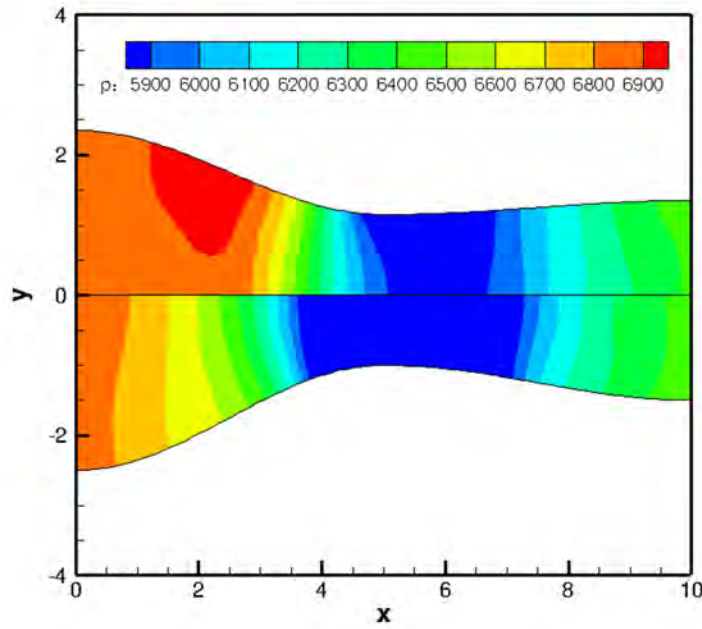


Figure 90. Pressure contours inside the nozzle. The upper half of the nozzle shows the pressure contours for the initial geometry and the lower half shows the pressure contours for the final geometry.

Three design parameters case

In this section a more complicated nozzle geometry is considered to show the advantage of the adjoint method. In this case the nozzle geometry depends on three design parameters. This is a more practical case as adjoint methods are most cost effective when there are several design parameters. The design parameters are denoted by α_1 , α_2 and α_3 . The nozzle contour equations are,

$$\begin{aligned} y &= 1.75 - (0.5 + \alpha_1) \cos((0.2x - 1)\pi) - \alpha_2 \cos((0.2x - 1)\pi) + \alpha_3 \cos((0.2x - 1)\pi) & 0 \leq x \leq 5 \\ y &= 1.25 - \alpha_1 \cos((0.2x - 1)\pi) - \alpha_2 \cos((0.2x - 1)\pi) + \alpha_3 \cos((0.2x - 1)\pi) & 5 \leq x \leq 10 \end{aligned} \quad (98)$$

The equation (98) is such that α_2 and α_3 can be combined to give one new design parameter. Then the geometry will depend only on two design parameters. Breaking up the geometry into more parts gives the freedom of perturbing the geometry in more places.

The use of the adjoint design methods is demonstrated here to calculate more than one gradient of the objective function. The initial area ratio (A_e/A_o) is equal to 0.6 and the pressure ratio (p_e/p_o) corresponding to ideal subsonic flow is 0.92. A subsonic case with $p_e/p_o = 0.93$ has been considered here.

The desired geometry corresponds to values of α_1 , α_2 and α_3 of 0.25, 0.25 and 0.25 respectively. The initial geometry is taken to be such that the values are 0.1, 0.1 and 0.1 respectively. This gives exactly the same geometry as was considered for the one parameter case. These geometries are shown in Figure 91. The red line shows the initial geometry. The black line shows the desired

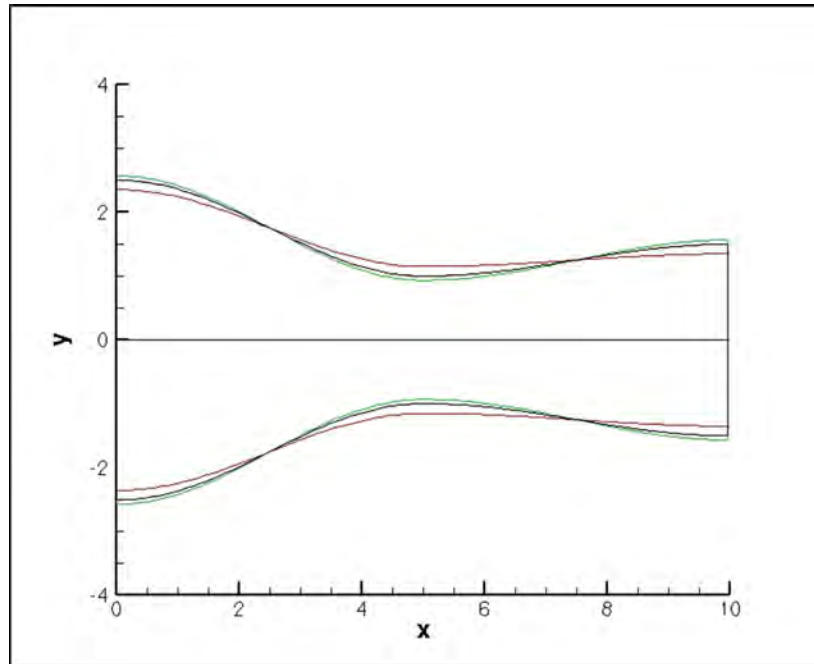


Figure 91. The geometry of the nozzle. Calculations were performed for only half the domain. The red line shows the initial geometry. The green line shows the final geometry. The black line shows the geometry that gives the desired pressure distribution.

geometry and the green line shows the final geometry given by the adjoint design. After the first design cycle the values of α_1 , α_2 and α_3 are found to be 0.1721, 0.1721 and 0.0280 respectively. These values are used to find the next values of α_i . The adjoint equations are solved for the geometry given by these values and then the gradients are used to find the next value of α_i , as explained earlier.

In this case it took approximately 7 design cycles to converge to the desired shape. It can be observed that the final and desired geometry match quite well (Figure 91). The value of the

objective function after 7 design cycles is equal to $36.38 (N/m^2)^2$, which is a decrease from an initial value of $1.042 \times 10^6 (N/m^2)^2$. So it has dropped by a more than four orders of magnitude. The convergence of the objective function is shown in Figure 92. It is observed that the objective function drops rapidly initially and then it gradually approaches zero. The rate of convergence is higher than the one in the case of one parameter only. From the log – log plot it can be seen that the objective function keeps on oscillating about a small minimum value. This may be due to the resolution limit of the grid in the flow simulation.

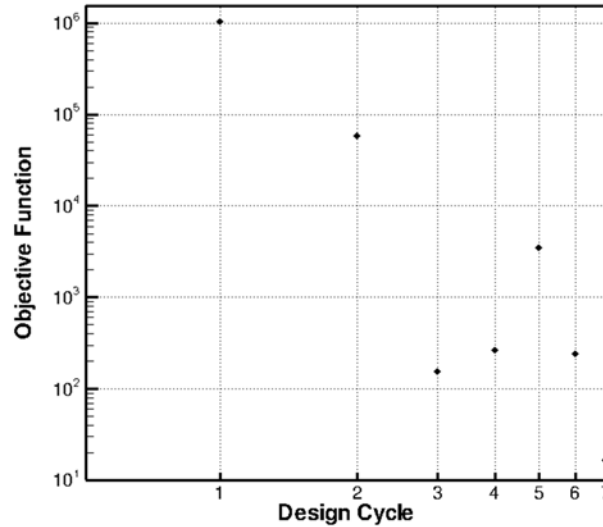


Figure 92. The convergence of the objective function with design cycles on a log – log plot.

The convergence of the α_i are shown in Figure 93, Figure 94 and Figure 95. One interesting thing about the results is that although the final geometry matches quite well with the desired geometry (as do the flow properties), the design parameters do not individually meet the desired design parameters. The set of design parameters for which the desired pressure distribution was found is $(0.25, 0.25, 0.25)$ whereas the final set converged values of design parameters is $(0.1502, 0.1502, 0.049794)$. The geometry contour given by (98) is same for these two sets of design parameters which means that although the design parameters do not reach the desired set of values, the geometry does. These values effectively reach their final value in just three design cycles but they keep on oscillating around those values with more design cycles. The method could have been truncated at three design cycles where the objective function has a value equal to $154.2 (N/m^2)^2$.

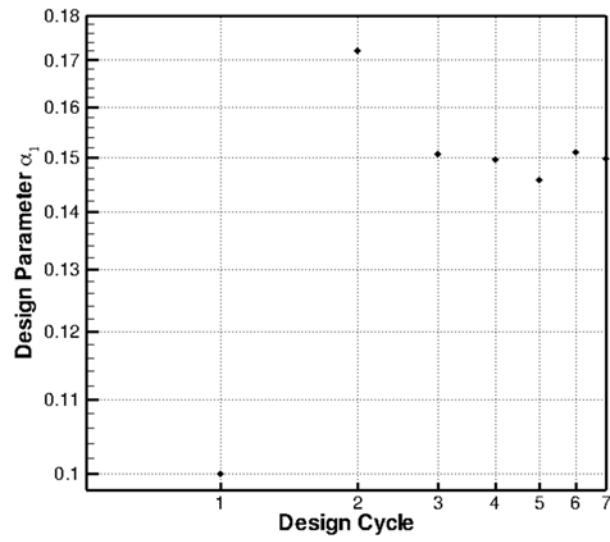


Figure 93. The convergence of design parameter α_1 with design cycles.

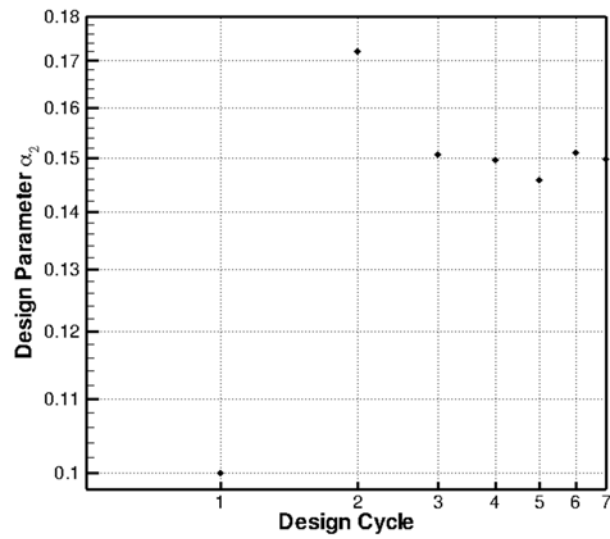


Figure 94. The convergence of design parameter α_2 with design cycles.

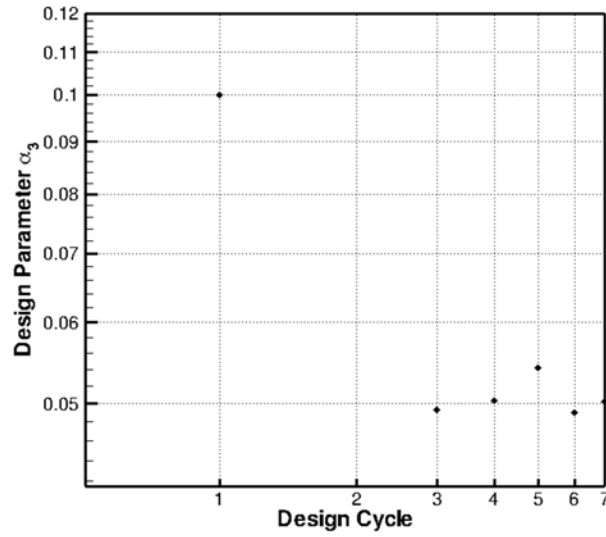


Figure 95. The convergence of design parameter α_3 with design cycles.

Pressure contours in the nozzle domain for the initial and final geometries are shown in Figure 96. It can be seen that the initial and final flows are quite different. The red and blue lines in the Figure 96 respectively show the initial and final pressure distribution on the nozzle centerline.

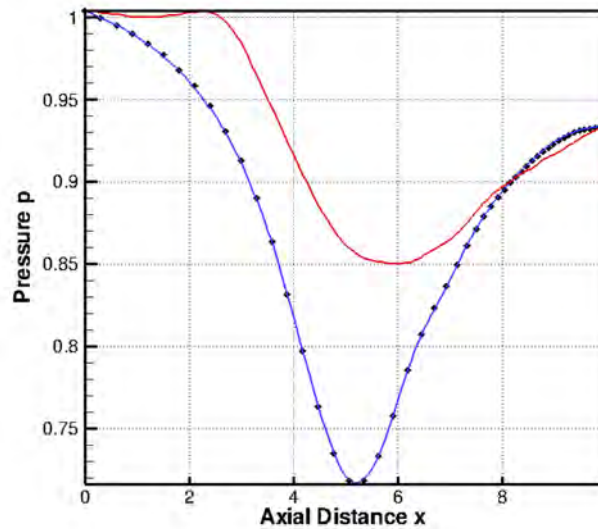


Figure 96. The pressure distribution (with respect to total pressure p_0) along the centerline of the nozzle. The red and blue lines show the initial and final pressure respectively along the nozzle centerline. The desired pressure is shown by black symbols.

The desired pressure distribution on the nozzle centerline is shown by symbols. The flow properties on the nozzle centerline match very well with the desired flow property distribution.

The pressure contours inside the entire nozzle domain are shown in Figure 97. It can be observed from the figure that the initial and final flows are very different although the exit pressure ratio is kept constant for a subsonic flow inside the nozzle.

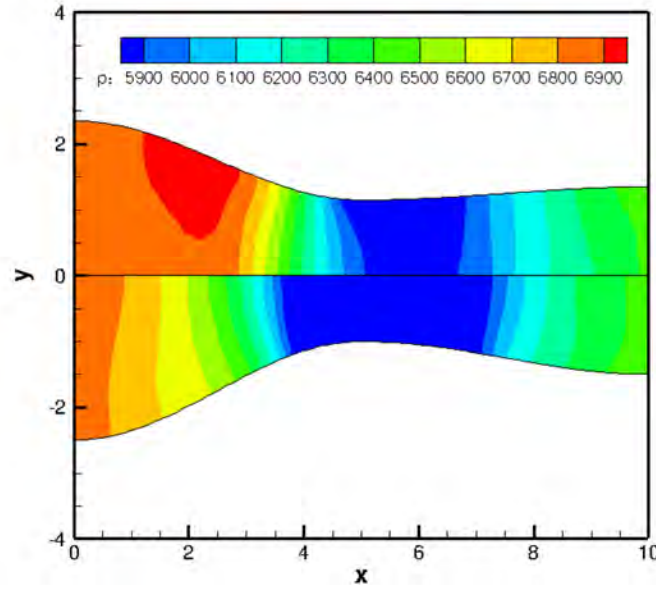


Figure 97. The pressure contours inside the nozzle. The upper half of the nozzle shows the pressure contours for the initial geometry and lower half shows the pressure contours for the final geometry.

Supersonic case with shocks

In this section a case is presented where there is shock in the flow solution. In such a case the flow is not continuous inside the nozzle. Hence, calculations cannot be performed in the same way as for a shock free case. As already discussed previously a new parameter Z is introduced such that new cost function in terms of Z is continuous across the shock. A nozzle contour is considered which depends on three parameters. The design parameters are denoted by α_1 , α_2 and α_3 . The nozzle contour equations are,

$$\begin{aligned} y &= 1.75 - (0.5 + \alpha_1)\cos((0.2x - 1)\pi) - \alpha_2 \cos((0.2x - 1)\pi) + \alpha_3 \cos((0.2x - 1)\pi) & 0 \leq x \leq 5 \\ y &= 1.25 - \alpha_1 \cos((0.2x - 1)\pi) - \alpha_2 \cos((0.2x - 1)\pi) + \alpha_3 \cos((0.2x - 1)\pi) & 5 \leq x \leq 10 \end{aligned} \quad (99)$$

The initial geometry is taken such that the values of design parameters α_1 , α_2 and α_3 are 0.1 , 0.1 and 0.1 respectively. The desired geometry is such that the values of the design parameters α_1 , α_2 and α_3 are 0.25 , 0.25 and 0.25 respectively. The initial area ratio (A_e/A_o) is equal to 0.6 and the pressure ratio corresponding to ideal supersonic flow will be 0.17 . The value of pressure ratio (p_e/p_o) is taken to be 0.67 to ensure shocks in the nozzle. After the first design cycle the values

of α_1 , α_2 and α_3 are found to be 0.1101, 0.11001 and 0.0899 respectively. The flow equation is then solved for the new geometry defined by these values. Then the value of shock parameter is calculated to smooth the cost function. This is an extra step for the discontinuous flows.

In this case it took approximately 32 design cycles to converge to the desired pressure distribution. The final pressure distribution matched very well with the desired pressure distribution even though there is a shock in the flow (Figure 98). This case shows different characteristics than the earlier cases. The objective function does not drop as rapidly. The decay of the objective function with design cycles is shown in Figure 99. The number of design cycles taken is much larger than in the other cases. This value of convergence rate is much smaller than the other cases.

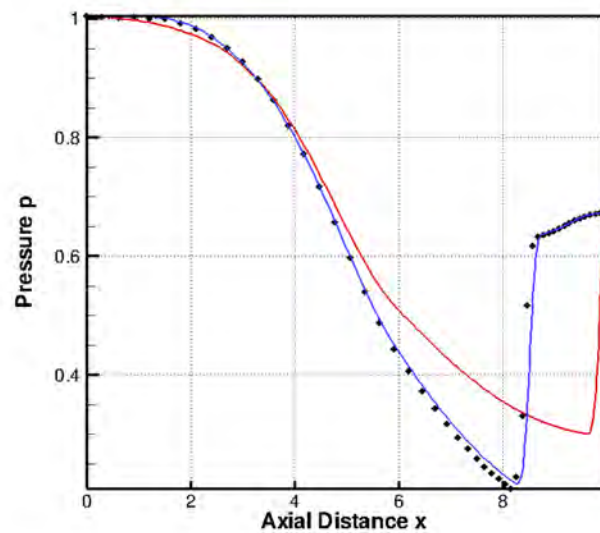


Figure 98. The distribution of pressure (with respect to total pressure p_0) along nozzle centerline. The red and blue lines show the initial and final pressure respectively along the nozzle centerline. The desired pressure is shown by black symbols.

The design parameters gradually converge to the values that are not the originally desired values, but the geometry given by the converged values is very similar to the desired geometry. The set of design parameters for which the desired pressure distribution was found is (0.25, 0.25, 0.25), whereas the final set of the converged values of design parameters is (0.1502, 0.1502, 0.04979). Unlike the previous cases without shocks, these values take several design cycles to converge. It took approximately 32 design cycles to reach close to the desired pressure distribution. It is probable that this reflects the limit of the grid to resolve smaller changes in the pressure distribution.

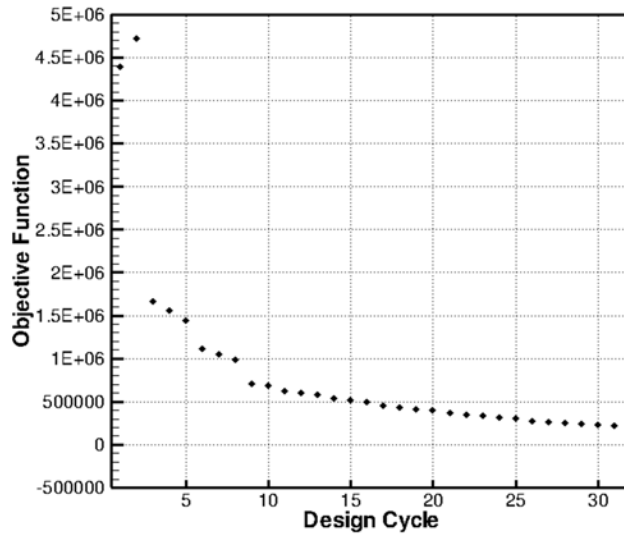


Figure 99. The decay of objective function with design cycles for the supersonic case with a shock.

The full flow solution for the initial (upper) and final (lower) geometries inside the nozzle domain is shown in Figure 100. Pressure contours are shown in the domain. The difference in the two solutions is basically the shock location. The nozzle is sonic at the throat hence the flow upstream of the throat remains the same, whereas the flow downstream changes with each design cycle.

Figure 101 shows the distribution of shock parameter Z along the nozzle centerline for the final design cycle. It is not defined explicitly and is solved for numerically. It can be noticed from the plot of Z that it is like a damping function. The advantage of using this function is that it smoothes the objective function. This is clear from the figure, as it drops rapidly near the exit where the shock is formed.

In this section, the adjoint method has been used to design quasi-one-dimensional and two-dimensional nozzle geometries. The implementation of the adjoint method for nozzle design has presented. Several cases have been considered. The one-dimensional case was presented for a simple geometry, described by only one design parameter. The one-dimensional design was implemented for subsonic flow corresponding to a pressure ratio $p_e/p_o = 0.93$. The two-dimensional case was first implemented for a similar case where the geometry was described by one design parameter and the flow is subsonic. A more complex geometry was then considered. This geometry was described by three design parameters. Both subsonic and supersonic results were presented for this case.

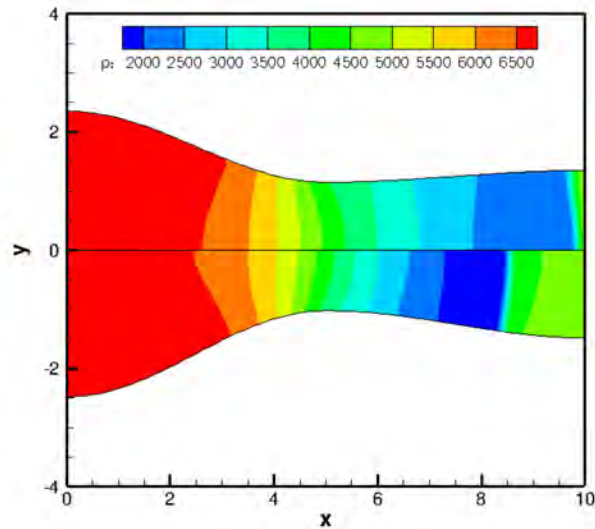


Figure 100. Pressure contours inside the nozzle domain. Upper half shows the initial flow and lower half shows the final flow.

Summary

Adjoint methods have been shown to be very efficient methods for optimization in terms of saving computational cost. In this task, adjoint methods have been developed for quasi-one-dimensional and two-dimensional nozzle flows. The aim is to find a geometry that has an optimum value corresponding to a desired cost function. The cost function has been considered as the difference between the pressure distribution and a desired pressure distribution on the nozzle axis. Adjoint variables are used to find the sensitivity of the cost function with respect to the design parameters. First, a quasi-one-dimensional case has been considered to explain the method. Then more complicated two-dimensional cases were considered. The two-dimensional cases have been demonstrated for a one design parameter case for understanding purposes and then a several design parameters two-dimensional case has been considered. The nozzle operating conditions included both subsonic and supersonic cases. In the supersonic case, when there is a shock present in the nozzle, the cost function has been smoothed. The number of design cycles required to achieve the desired pressure distribution varies with the type of problem (subsonic, supersonic), and type of governing equations (quasi-one-dimensional, two-dimensional). The adjoint equation is similar to the flow equation. Hence its solution takes approximately the same computational effort as the flow equation. Traditional methods of computing the cost function sensitivity require much more computational effort with a new flow solution required for a change in each design parameter. The adjoint solution enables the sensitivity of the cost function to each of the design variables to be determined in a single calculation. In this way, adjoint methods provide a computationally economic design optimization procedure.

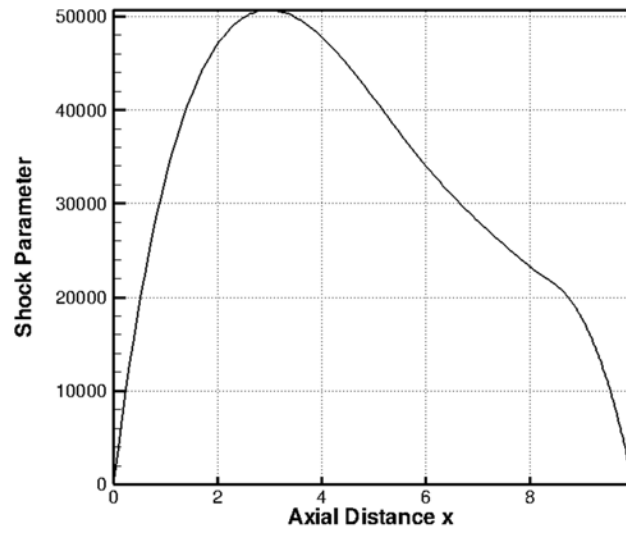


Figure 101. The distribution of shock parameter Z along nozzle axis for the final design cycle.

10.5. Task 5. Integration of Program Elements

Task 5.1 Coordination of Geometries and Operating Conditions

All groups involved in this project would meet once or twice a year at AIAA meetings to coordinate our activities. Foremost among the coordination tasks was agreeing on experimental geometries and operating conditions. Very early in the project it was agreed that all experiments for this project would use the design of 3 existing nozzles that were reasonable replicas of the exhaust of GE Series 404 engines (that power F-18 aircraft) in three area ratio conditions. Table 9 below, documents the geometric and operating parameters used in the baseline experiments.

Table 9. Operating conditions of measurement

Curve ID	Design & Jet Mach No. M_d & M_j	Total Temp. Ratio, TTR TTR_{core} (TTR_{mix})	Acoustic Mach No. M_a	Nozzle Exit Diameter D (cm)	Measured Distance R/D	Char. Freq. $f_c (U_j/D_j)$ Hz	R_e based on TTR_{mix}
PSU	1.65 & 1.56	1.0	1.28	1.8	99	25,315	992,200
HFJER				12.9	116	3,351	7,356,200
PSU	1.5 & 1.56	1.0	1.28	1.7	104	25,321	972,900
HFJER				12.3	121	3,469	6,965,500
PSU	1.65 & 1.36	2.6	1.86	1.7	104	38,031	499,200
HFJER		2.5	1.84	12.3	121	6,200	1,600,000
PSU	1.5 & 1.64	3.0	2.29	1.7	104	47,114	736,600
HFJER		3.6 (3.0)	2.52 (2.29)	12.3	121	5,855	2,088,000
HFJER	1.5 & 1.36	3.2	2.08	12.3	121	6,326	1,219,600
		2.5	1.88			5,706	1,552,900
		3.2 (2.7)	2.08 (1.85)			5,384	1,442,700
PSU	1.65 & 1.36	3.0	2.03	1.8	99	41,694	460,300
		2.6	1.86			38,031	499,200
HFJER		3.0 (2.6)	2.03 (1.86)	12.9	116	5,334	1,675,500
PSU	1.5 & 1.5	2.2	1.85	1.27	140	50,028	485,500
LaRC		2.25		4.27	~100	14,976	844,700
GRC	1.5 & 1.5	2.2	1.85	10.2	147	6,269	2,084,500
		2.6 (2.2)	2 (1.85)				
LaRC		2.25	1.85	4.27	~100	14,976	844,700
PSU	1.5 & 1.5	2.2	1.85	1.27	280	50,028	485,500
GRC				10.2	147	6,269	2,084,500
PSU	1.5 & 1.5	3.2	2.23	1.3	140	58,914	431,200
				2.5	50	29,390	865,100
HFJER	1.5 & 1.5	2.6 (2.2)	2 (1.85)	10.2	147	6,269	2,084,500
					~50		

CAD designs at GE were provided to all participants and, in fact, the actual model nozzles previously used at GE were transferred to NASA for their experiments. Penn State took the nozzle designs and scaled them to have exit diameters of approximately 0.7 inches, a factor of about six times smaller than the GE-NASA nozzles. The Penn State nozzles were referred to as small scale and the GE-NASA nozzles and experiments were referred to as moderate scale. GE and NASA led the way with chevron designs. The following two tables documented the geometries of the chevrons in terms of length, penetration distance and width (as a percentage of 1/12 of the nozzle circumference). (Twelve chevrons were used for all experiments.) Table 10 was generated by GE for their chevron designs. The Chevron parameters are shown schematically in Figure 102.

Table 10. Chevron CFD Design of Experiments (DOE) parameters.

Config	Length	Penetration
0	4.0	0.8
1	4.0	0.4
2	4.0	1.2
3	4.0	1.6
4	4.5	0.4
5	4.5	0.8
6	4.5	1.2
7	4.5	1.6
8	5.0	0.4
9	5.0	0.8
10	5.0	1.2
11	5.0	1.6

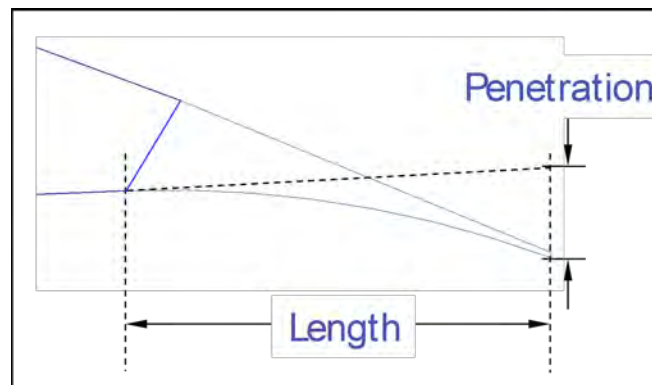


Figure 102. Description of Geometric Parameters.

Table 11 (below) documents the chevron parameters used in the moderate scale chevron experiments described in Task 3.

Table 11. Chevron parameters used in moderate scale experiments

Parameter	Low Level	High Level	Center
Penetration (inches)	0.3 (P03)	0.6 (P06)	0.45 (P05)
Length (inches)	0.75 (L08)	1.75 (L18)	1.25 (L13)
Width (% facet width)	60 (W06)	100 (W10)	80 (W08)

Task 5.2 Update Advanced Acoustic Model

Pennsylvania State University developed methods to reduce noise from military aircraft. One method is the use of chevrons. The effectiveness of two types of chevrons (medium penetration and large penetration) applied to a single engine was provided to research project partner Wyle Laboratories. Wyle Laboratories is responsible for the development of the Advanced Acoustic Model. This is a noise prediction method for the prediction of noise contours based on measured and predicted aircraft noise source characteristics. PSU also combined the effect of chevrons with their twin jet extension⁸⁷ of the SAE ARP 876 jet noise prediction method. The Advanced Acoustic Model⁸⁸ is a time steps simulation model for aircraft noise. Noise sources are represented as spheres, with noise quantified by levels and spectra at a reference distance as a function of the spherical angles. This section describes the method by which chevron effect is added to a noise sphere, either by an extension of the method of Ref. 87 or as a direct application of the differences measured due to chevrons. The effect of chevrons on the noise footprint of a field carrier landing practice operation is presented.

Chevron Effect Software

Program “combine” applies chevron corrections to a netcdf format noise sphere file as used by AAM. Combine is a windows command line program compiled from Fortran source code linked to the netcdf library. The netcdf library is used to access files written in the net common data format. More information on netcdf and how to use its open source library can be found at

<http://www.unidata.ucar.edu/software/netcdf/docs/netcdf-f90>.

The noise characterization of a fixed-wing aircraft for use in the Advanced Acoustic Model is incorporated in a netcdf file, as detailed in Reference 88. The chevron correction levels are in text files with the format detailed in Table 12.

Table 12. File format of chevron correction file

Record	Column	Format	Description
1	1-20	A20	Label to append title in nc file
2	1-2	A2	Spectral content. Must be 'BB'
3	1-2	I2	Number of one-third octave band frequencies
4	*	F	One-third octave band frequencies repeated number of time indicated in record 3
5	*	2I	Number of theta angles
5	*	2I	Number of phi angles. Must be 1
6	*	F	Theta angle (degrees measured from nose of aircraft)
6	*	F	Phi angle (degrees measured from below aircraft - positive to starboard)
7	*	F	Level corrections (decibels - record repeated for each of the one-third octave bands)
Notes: (1)* indicates record is read as list directed - column position is disregarded. (2) Records 6 and 7 are repeated to satisfy record 5 with theta angle incrementing fastest.			

Program “combine” applies the decibel corrections in the text file to a netcdf noise sphere file, using the command line syntax:

```
combine ncfilein chevronfile ncfileout
```

where,

- ncfilein is the name of the netcdf file for the fixed-wing source characterization.
- chevronfile is the text file whose format is detailed in Table 12.
- ncfileout is the name of the netcdf file to be created. It contains all the header information from ncfilein.

The two chevron corrections files accompanying this software are based on the measured chevron corrections, and are called,

- Case0_P03L18W10Chev_coor.txt - medium penetration chevrons
- Case0_P06L18W10Chev_corr.txt - large penetration chevrons

Predicted Noise Spheres and Footprints

PSU expanded the applicability of the SAE ARP 876 method to predict noise emission from twin jet engine aircraft. Using the measured results for single jet nozzles equipped with chevrons, PSU further expanded this method to include the effects of chevrons on full scale aircraft. This expanded method was used to show the change in noise footprint for an F/A-18E/F performing a Field Carrier Landing Practice (FCLP) operation.

Noise spheres were created from the output of PSU’s code for the operating states of the aircraft during this maneuver. Seiner et al.¹ identified the parameters needed to model the F/A-18E/F equipped with GE-F414-400 afterburning turbofan engines. Seiner also related the engine power setting (% N2) of the F/A-18E/F to the aircraft parameter inputs for ANOPP, the NASA developed Aircraft Noise Prediction Program. Veltin et al. used the conditions Seiner published to formulate appropriate parameters for PSU’s coding of SAE ARP 876. Wyle’s modeling of FCLP maneuvers needed two of the conditions Seiner identified. They are listed in Table 13 with the mission profile parameters. The definition for the column headings can be found in Ref.1.

Table 13. Input parameters for SAE ARP 876 code based on F/A-18E/F profile points.

Engine Power (% N2)	Airspeed (kts)	Profile	Mj	Md	Dj (in)	TR=To/Ta	Tj/Ta	Altitude(ft)	Mf	Vj (ft/s)	Ma
86	135	FCLP Pattern	1.185	1.47	16.8	2.91	2.27	582	0.21	1979	1.8
96	150	Take-Off	1.52	1.7	19.9	3.65	2.50	3674	0.21	2645	2.40

The process for creating the noise spheres and footprint contours with and without the two types of chevrons is:

1. Run PSU's SAE ARP 876 code for the conditions in each row of Table 13.
 - Apply the bi-jet correction for all runs
 - Apply no chevron correction for one set of spheres (one for each row in Table 13.) – name spheres Base_001 and Base_002.
 - Apply chevron correction for medium penetration chevrons (P03L18W10Chev) – name spheres Chv3_001 and Chv3_002
 - Apply chevron correction for large penetration chevrons (P06L18W10Chev) – name spheres Chv6_001 and Chv6_002.
2. Create AAM input files using the FCLP track and profile
 - One for each of the three sources: Base, Chv3, and Chv6
 - Insert bank angles such that turns are coordinated
 - List 86400 operations so that DNL metric results in SEL contours
3. Run AAM on each of the input files, generating a grid with SEL at each point
4. Plot contours for all three runs
 - Choose contour values appropriate for 65 DNL contours
5. Calculate contour areas

Effect of Chevrons on Noise Spheres

The predicted effect of adding chevrons to the directivity pattern of the aircraft is shown in Figure 103.

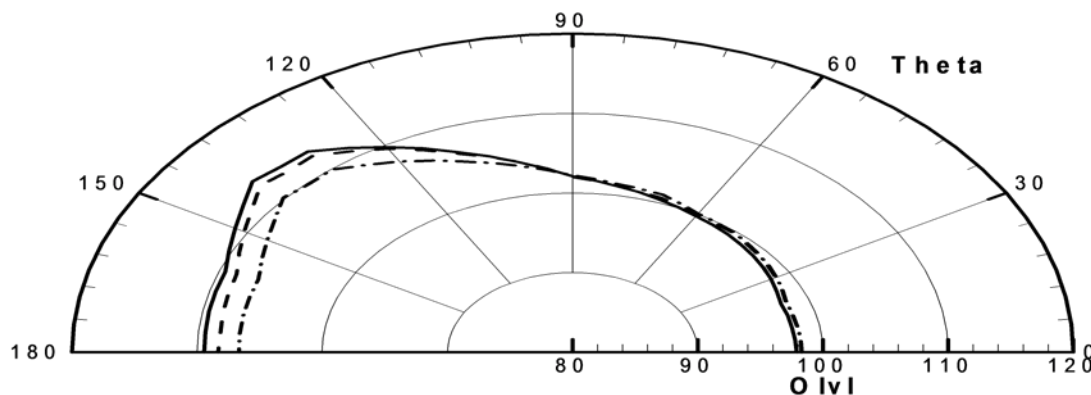


Figure 103. Directivity pattern of the overall level for Base (solid line), Medium Penetration Chv3 (dashed line), and Larger Penetration Chv6 (dash-dot line).

It is important to note that the overall level shown in Figure 103 is calculated from the spectra at each angle theta for phi equal to -90 degrees. There is only spherical spreading of the levels from the origin to the 1000 foot radius of the sphere with no atmospheric absorption removed.

Effect of Chevrons on Noise Contours

The results of running each of the modeled sources on an example FCLP in AAM is shown in Figure 104. As can be seen, the effect of the chevrons reduced the area of the acoustic footprint. The calculated area for each of the contours is listed in Table 14. Medium penetration chevrons reduce the contour areas by 3.5 % to 21%, depending on contour level, while large penetration chevrons reduce contour area by 12% to 55%.

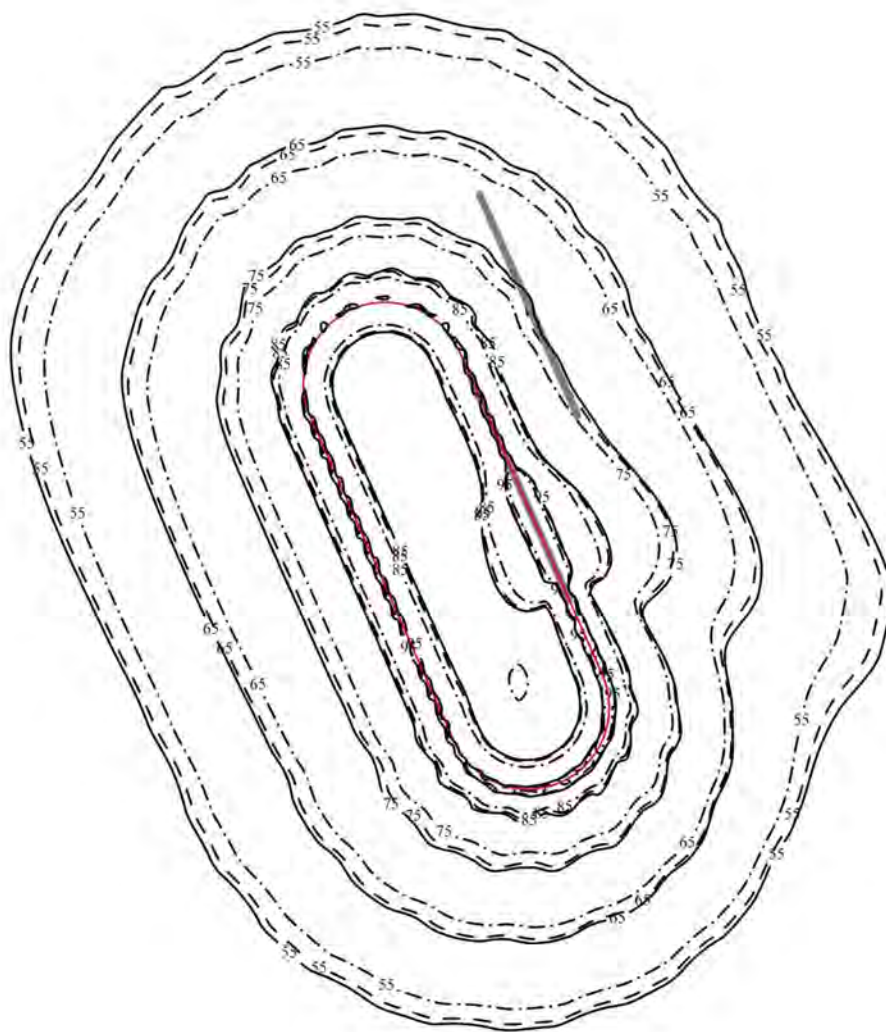


Figure 104. SEL contours resulting from running Base (solid line), Chv3(dashed line), and Chv6 (dash-dot line) in AAM on an FCLP operation.

Table 14. Contour areas, square miles, for each of the sources run in AAM.

Contour Level (dBA)	Source		
	Base	Chv3	Chv6
55	71.17	68.71	62.54
65	41.53	40.29	36.83
75	23.15	22.26	20.09
85	8.68	8.09	6.61
95	1.04	0.72	0.46

Summary for Task 5.2

The effect of chevrons on military aircraft jet noise has been incorporated into AAM. The method is to adjust the noise spheres that AAM uses as sources. Two methods are presented: incorporation into PSU's extension of SAE ARP 876, and direct adjustment of levels in an existing noise sphere. Chevrons were shown to reduce the size of the noise footprint from a Field Carrier Landing Practice operation, with large penetration chevrons yielding greater reduction than medium penetration chevrons.

5.3 Coordination and Transition to the Military

Aircraft noise modeling for military airbases has been performed with NOISEMAP, an integrated noise model. This is now being replaced with the Advanced Acoustic Model (AAM), with a transition period as 3-D noise source spheres become available for more aircraft.

AAM was developed under SERDP Project WP-1304, "Advanced Acoustic Models for Military Aircraft Noise Propagation and Impact Assessment." The final task of this development was to define a transition plan, under the guidance of its User Advisory Committee. The plan consisted of the following elements:

- Technical review of the model by UAC members
- Identification of flight test data suitable for model validation, followed by successful validation
- Delivery to the Defense Noise Working Group (DNWG) for acceptance and distribution
- With AAM incorporating code from NASA's Rotorcraft Noise Model (RNM), a distribution and maintenance plan was jointly developed between DNWG and NASA. DNWG also distributed beta versions of AAM to selected users, including the Air Force Center for Environmental Engineering (AFCEE) for testing. BASEOPS, the interface through which users operate DoD aircraft noise models, was also expanded to accommodate AAM's data requirements. AFCEE submitted AAM for IT testing to certify its installation on networked computers.

DNWG has also sponsored development of 3-D noise sources for use with AAM. An important feature of AAM is that noise sources are separate from the model itself. They do not require the full acceptance testing that software does. For use in environmental studies, sources require approval by Air Force Research Laboratories (AFRL) in the same manner as NOISEMAP sources. Approval by program offices for specific aircraft may also be needed, depending on the aircraft and whether particular details (nonlinear propagation or frequencies outside the customary 50 Hz to 10 kHz range) are needed. Program office review is coordinated by AFRL. 3-D noise data for AAM is in separate files for each aircraft, so there is no need to integrate them into a monolithic database. Some AAM sources (rotorcraft in particular) are owned by agencies other than AFRL or DNWG, so users must obtain those separately.

The implementation of the results of the current project is in the form of one-third octave adjustments that are applied to the noise sphere of a given aircraft. The adjustments are defined in this report, and are thus immediately available. If used in technical analyses, no particular approval is required as long as their origin is appropriately described. If they are used in environmental studies, or analyses that may involve policy decisions, review by AFRL, DNWG or the appropriate program office would be appropriate.

10.6. Task 6. Assessment of Scaling Methodology

Task 6.1 Assessment of scaling methodology for baseline round jets

On the scaling of small, heat-simulated jet noise measurements to moderate size exhaust nozzles

As the engine power of airplanes rises and the frequency of aircraft operations increases, environmental laws are becoming more stringent. While jet noise is not the dominant contributor to the total civilian aircraft noise it once was, it is still a major contributor. Jet noise is the major noise source for military aircraft that have engines of very low bypass ratio and high exit flow temperatures and velocities. The resulting noise poses a health threat to ground crews as well as causes an annoyance to communities in the vicinity of military airbases. Noise control and monitoring for both civil and military airplanes are also growing. Because practical aircraft engine measurements are very time consuming and subject to large uncertainties, there is strong interest in developing more accurate small or moderate model scale experiments which can be conducted in more controlled environments. Clearly it is much cheaper to develop jet noise reduction technologies on small-scale rigs than full-scale engines. However, experimental consistency between model scale and actual engine radiated noise measurements has yet to be fully demonstrated.

The aim of this task was to validate a methodology for using data obtained from testing at small and moderate scale, supported by computations, to reliably predict the full scale engine noise. The approach was to conduct and compare small scale and moderate scale experiments with nozzles representative of military jet engine exhaust nozzles. Comparisons across scales with data obtained in different facilities will provide confidence in the equality of the measurements performed, and in the ability of the methodology to extrapolate the subscale data to the full size aircraft. This task focuses on making extensive comparisons between small scale measurements performed at Penn State and moderate scale data gathered at NASA GRC, in order to determine whether the small scale and heat simulated jets can accurately simulate the acoustics issuing from moderate scale hot jets. A similar study was conducted by Viswanathan⁸⁹ that presented the results of numerous comparisons of moderate size (predominantly) subsonic jets' acoustic measurements. Additionally this work showed comparisons of model supersonic jet acoustic experiments with those of a turbojet engine with an acoustically treated duct between the turbomachinery and the exhaust nozzle. The comparisons showed favorable agreement for both subsonic and supersonic jet flows.

The experiments were performed in two laboratories: the Jet Noise Laboratory at Penn State University and the Aero-Acoustic Propulsion Laboratory at NASA GRC. The High Flow Jet Exit Rig (HFJER) at NASA GRC is one of the largest such facilities in the country. Supersonic air jets with exit diameters of approximately 10 cm are commonly used with jet Mach numbers up to $M_j = 1.7$ and stagnation temperatures exceeding three times standard ambient temperature. The NASA GRC large anechoic geodesic hemispherical dome has a radius of approximately 20 meters. The small scale experiments were performed in the Jet Noise Laboratory at Penn State, with its university size anechoic chamber (with dimensions of 5 x 6 x 2.8 meters). Typical supersonic jet nozzles of exit diameters from 2 to 2.5 cm that operate at pressure ratios up to 4.5 producing exit Mach numbers up to $M_j = 1.7$. This facility does not

include jet heating capability. Instead helium-air mixture jets are used to simulate hot jets. Appropriate mixtures of helium-air can be made to have the desired acoustic velocity of heated jets. When operated at the same pressure ratio of heated air jets, the elevated acoustic velocities also have proportionally increased jet velocities. It is this property that the radiated noise best correlates with. Doty and McLaughlin and Papamoschou⁴ have shown that mixtures of helium and air can be used to simulate the flow and acoustic properties of hot jets with a very high degree of accuracy.

Penn State facility and instrumentation

The Pennsylvania State University high speed small scale jet noise facility was used for the small scale experiments presented in the current study. The facility was described in Reference 5. A schematic is shown here in Figure 105 for convenience. High pressure air, pressurized by a CS-121 compressor combined with a KAD-370 air dryer both manufactured by *Kaeser Compressors*, is provided from the tank, and then the air flow is regulated via pressure regulators and control valves located in a piping cabinet before being fed to a plenum and delivered to the jet nozzle issuing into the anechoic chamber. A pitot probe is embedded in the middle section of the plenum to provide, via a pressure transducer, the total pressure upstream of the nozzle. The helium supply piping is connected to the piping cabinet to provide the helium-air mixture jets in order to simulate the heated jets. The individually partial pressures of the helium and air are both regulated in the piping cabinet. The anechoic chamber walls are covered with fiberglass wedges and it has an approximate cut-off frequency of 250 Hz. An exhaust collector and fan on the opposite wall of the plenum in the anechoic chamber prevents flow circulation and possible helium accumulation.

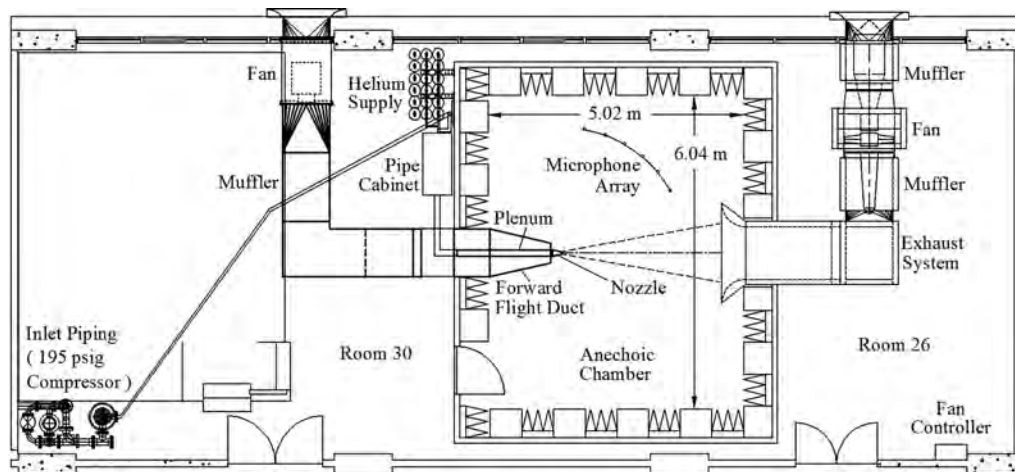


Figure 105. The Pennsylvania State University high speed jet noise facility

Acoustic measurements are currently performed using six microphones, hanging from a boom that extends from the plenum stand. The microphone array is set and aimed to freely rotate around a point located at the center of the nozzle exit plane. The microphones are positioned at a grazing incidence to the jet centerline and equally spaced by 10 degrees. The average physical

radial distance of microphones to the nozzle exit is approximately 1.78 m (70 in). This distance is appropriate enough for the microphones to be considered in the far field when testing nozzles less than 2.5 cm (1 in) in diameter operated in this facility. The microphones are 1/8" pressure-field microphones selected to match the testing nozzles operated at the small scale facility, type 4138 from *Brüel and Kjaer (B&K)*, and type 40DP from *GRAS*. Following calibration corrections, the acoustic data have a frequency response reliably accurate to 120 kHz. This is adequate to define the acoustic frequencies most important to noise studies including those approximately a factor of 10 higher than the peak frequencies in the maximum noise emission direction. The range is not adequate to fully define the noise spectra to the highest non-dimensional frequencies that are typically much less important in supersonic aircraft noise. The acoustic measurements were performed from polar angle $\theta = 30^\circ$ to $\theta = 120^\circ$ measured from the jet downstream direction originated from the nozzle exit plane, with increments of 10 degrees. The microphone calibration is performed with a *B&K* acoustic calibrator, model 4231, and the microphone calibration constants are recorded to provide the conversion from the measured voltages to the equivalent pressure. The analog time-domain signals from the microphones are routed through a *Nexus*, *B&K* signal conditioner or a *GRAS* model 12AN power module and then amplified and filtered for anti-aliasing thus enabling their accurate digital conversion in the following acquisition. A high-pass filter is also set to 500 Hz, removing any undesirable low frequency noise that could contaminate the data. A PCI-6123 *National Instruments* DAQ board is equipped at the operating computer acquiring the time domain data stored in binary files. The data acquisition and storing is accomplished with *LabVIEW* software. The sampling rate is set at 300 kHz for the data acquisition and 102,400 to 409,600 data points are collected, the reduced data set being used for helium-air mixture jets in order to reduce the amount of helium used during an experiment. The raw data are then fed into *Matlab* for the data processing. The raw data are sequentially split into 1024 or 4096 points segments and a Hanning window function is applied with 50 percent overlap between each window. The Fast Fourier Transform (FFT) is calculated in each window and the value is averaged from the 199 segments. This yields the power spectral density (*PSD*) which is then converted to decibels (dB) using a reference pressure of 20 μPa .

NASA GRC facility and instrumentation

Comparisons are presented in this task with acoustic measurements from similar nozzles at a larger scale acquired at the NASA GRC Aero-Acoustic Propulsion Laboratory with the high flow jet exit rig (HFJER) as shown in Figure 51. This facility has a hot jet acoustic rig located in the anechoic geodesic hemispherical dome noted earlier. Jet diameters up to 12.7 cm (5 in) are typically used in this facility for supersonic applications, with the capability to use a co-flow to simulate jets with a small bypass ratio according to the design evolution of modern military engine. The facility can be operated in a single-flow mode as well as a dual-flow mode. When in the dual-flow mode the pressure in both the annular and the core section of the plenum are set to the same value; however, the annular flow was unheated when performing hot jet measurements. A schematic diagram of this dual flow set-up is shown in Figure 106. For the experiments reported in this paper, the cold bypass air comprised 30% of the core flow a value that is roughly what is used in turbojet engines on today's military fighter aircraft. The total temperature ratio of the jets is expressed in terms of the core flow total temperature TTR_{core} , or the total temperature of the flow after it is (hypothetically) fully mixed, TTR_{mix} . Extensive

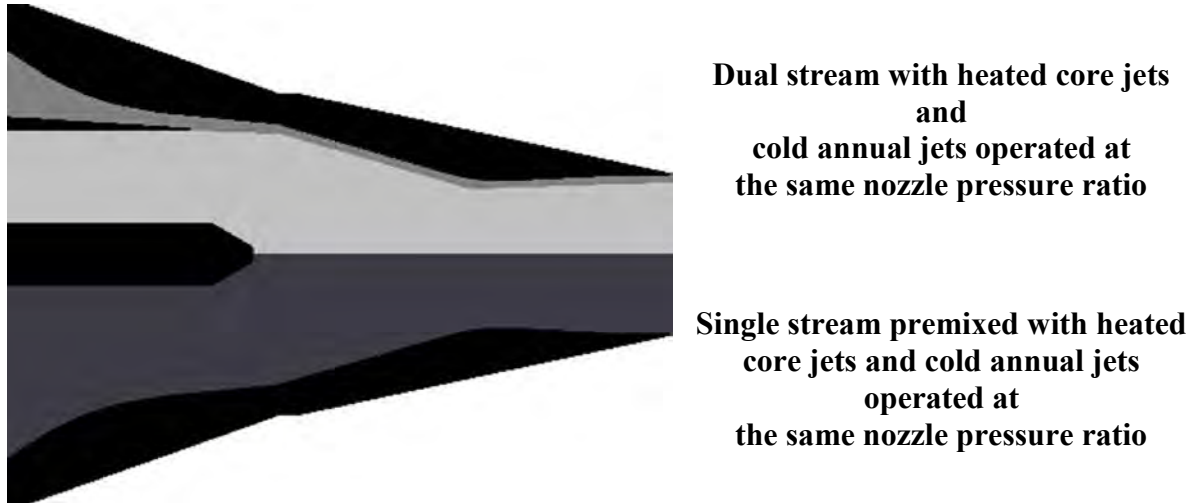


Figure 106. Schematic of dual flow jet exit rig in the NASA Glenn Research Center with the bypass air for low bypass nozzle systems.

description and qualification measurements of this facility can be found in Bridges and Brown². Because the pressure upstream of the nozzle throat in the bypass stream is the same as in the core flow, a reasonable assumption is that the exit Mach numbers of both streams is the same, while the *TTR* of the annular stream is ~ 1 . An arc of microphones with radius approximately 15 m (49 ft) is mounted inside the top of the dome with 24 microphones separated by 5 degree increments.

In addition to the dual flow jet facility, a small hot jet acoustic rig (SHJAR)⁹⁰ also located in the AeroAcoustic Propulsion Laboratory, provided additional single stream hot jet measurements for the current studies. This rig utilizes a microphone arc with 24 microphones separated by 5 degree increments at a radius of 2.5 m (100 in). The nozzle exit diameter used for this rig is 5.08 cm (2 in), thus $R/D = 50$ for these experiments.

In both NASA rigs the microphones were *Bruel and Kjaer* 1/4" microphones (model 4939 with a *B&K* Model 2670 preamp), used without grid caps for maximally flat response and pointed at the nozzle exit. *Bruel & Kjaer Nexus*TM amplifiers provided the signal conditioning. A *DataMAX*[®] Instrumentation Recorder, from RCE Electronics, simultaneously recorded data from all microphones, using a 90 kHz low-pass filter to limit the bandwidth (at 200 kHz sample rate). Eight seconds of data were recorded at each point. Jet flow conditions were recorded during the acoustic data acquisition using a facility computer. Variables such as rig temperatures, pressures, and mass flows, as well as ambient temperature, pressure, and humidity were averaged over the same time that the acoustic record was recorded. The facility data were imported, along with the raw acoustic time series files, into a *Linux* processing workstation for processing. The processing steps mirror that of the PSU facility. Recorded time series were multiplied by amplification factors from the variable gain *Nexus* signal conditioners and by the calibration factor determined by in situ recording of the *Bruel and Kjaer* model 4220 pistonphone. Fourier transforms were computed using FFT algorithms and 10th order Kaiser-Bessel windowing on

16384-point records with 50% overlapping. Power spectral density estimates were created by averaging all 195 transforms and adding back windowing losses, and the resulting PSD were converted to decibels relative to $20\mu\text{Pa}$. Background noise, measured immediately before the data set was acquired, was subtracted and any frequency band within 3 dB of the background was flagged and was not considered in future processing and final plotting.

Data processing and comparison procedure

In both PSU and NASA processing systems, three corrections are applied to the raw *PSD* to compute the normalized, lossless *PSD*. Data were corrected for microphone spectral response characteristics based on the manufacturer's documentation of each individual microphone obtained during factory calibration ($\Delta C_{act}(Hz)$) including appropriate free-field response ($\Delta C_{ff}(Hz)$). The spectra were corrected for daily variations in atmospheric attenuation by calculating the attenuation (ISO 9613 -2:1996) for each microphone using measured ambient pressures, humidities, and temperatures ($\Delta C_{atm}(Hz)$) and adding back the sound lost due to atmospheric attenuation from the jet to the microphone. Finally, the spectra are non-dimensionalized to *PSD* per Strouhal number ($10 \times \log_{10} f_c$). The Strouhal number is defined as $St = f / f_c$, with f_c the characteristic frequency of the jet defined by $f_c = U_j / D_j$, where U_j is the jet velocity, and D_j is the fully expanded diameter of the jet. Equation (100) summarizes the different steps that lead to the *PSD* per unit Strouhal number as explained in Kuo, Veltin and McLaughlin⁵.

$$\underbrace{PSD(St)}_{\text{Lossless Spectrum}} = \underbrace{PSD_{raw}(Hz)}_{\text{Raw Spectrum}} - \underbrace{\Delta C_{act}(Hz) - \Delta C_{ff}(Hz)}_{\text{Microphone Responses}} + \underbrace{\Delta C_{atm}(Hz)}_{\text{Atmospheric Correction}} + \underbrace{10 \log_{10} f_c}_{\text{Strouhal Number Scaling}} \quad (100)$$

From the *PSD*, given at intervals of Δf , the *OASPL* is calculated via the following equation:

$$OASPL = 10 \log_{10} \left[\Delta Hz \sum 10^{\left(\frac{PSD(Hz)}{10} \right)} \right] = 10 \log_{10} \left[\Delta St \sum 10^{\left(\frac{PSD(St)}{10} \right)} \right] \quad (101)$$

The experimental data were processed into lossless spectra per unit Strouhal number to make comparison easier across scales. Most measurements were made at distances close to $R_{raw} = 100 D_j$ or $144 D_j$ depending on the nozzle diameter. Following processing, the resulting data were (back) propagated to $R = 100 D_j$ assuming spherical spreading of the acoustic field to allow direct comparison of data at a common observer distance. This “back” propagated *PSD* is determined from,

$$PSD(St) = PSD(St) + 20 \log_{10} (R_{raw} / R) \quad (102)$$

Heated jet simulation

The density characteristics of heated jets are replicated using gas mixtures in order to produce acoustic measurements in cold small scale facilities that can be directly compared to hot moderate scale experiments or actual aircraft engine measurements. Doty and McLaughlin³ and Papamoschou⁴ have shown that mixtures of helium and air can appropriately simulate the noise of heated jets to a reasonable accuracy by matching density of the heated gas. The features of heated jets are lowered density and increased velocity relative to the speed of sound, and both of these features can be achieved by helium-air mixture jets. However, both parameters, the acoustic velocity a and the density ρ_j cannot be precisely matched simultaneously. Thus, two

independent methods were developed to match either the density ρ_j or the acoustic velocity a from the heated jets. Although there are two matching methods in heated jet simulation, both methods generate very close results. The two matching methods were introduced by Doty and McLaughlin³ and are briefly described below.

The first methodology consists in matching the acoustic velocity between a helium-air mixture and a corresponding hot air jet.

$$a_{heated} = \sqrt{\gamma \mathfrak{R} T_j} \leftrightarrow a_{mix} = \sqrt{\gamma_{mix} \mathfrak{R}_{mix} T_{jmix}} \quad (103)$$

γ_{mix} and \mathfrak{R}_{mix} are dependent on the helium concentration. The proper molar mass of helium can easily be calculated in order to equate a_{heated} and a_{mix} . From there, the partial pressure of helium and air can be computed and the pressure regulators adjusted for the experiment.

The second method consists in matching the density between a heated jet and a helium-air mixture jet, as shown below.

$$\left(\frac{\rho_j}{\rho_\infty} \right)_{heated} = \left(\frac{T_\infty}{T_j} \right)_{heated} \leftrightarrow \frac{\rho_{jmix}}{\rho_\infty} = \frac{T_\infty \mathfrak{R}_\infty}{T_{jmix} \mathfrak{R}_{mix}} = \frac{\mathfrak{R}_\infty}{\mathfrak{R}_{mix}} \left[1 + \frac{\gamma_{mix} - 1}{2} M^2 \right] \quad (104)$$

The molar mass of helium required to equate ρ_{jmix} with ρ_j can be calculated, and from it the partial pressure of helium is once again derived. The two matching methods typically lead to slightly different values for the partial pressures of the mixture. However, as mentioned, experimental results (Refs. 3 and 4) showed that the two methods result in acoustic spectra in agreement within 1 dB across the spectra, and all data presented here uses the acoustic velocity matching method.

Model geometry of military style supersonic nozzle

Besides the experimental results from contoured converging-diverging (CD) nozzle, experiments were conducted with the military style nozzles representative of the exhaust of aircraft engines of the F404 family. While such military engines possess nozzles with variable geometry, adapting to different flight regimes, for this specific research, three nozzles with different exit-to-throat area ratios were used, as specified by GE Aviation. These nozzles were designed with a multifaceted inside conical contour. At Penn State, the nozzles were fabricated via a rapid prototyping technique (stereo lithography); meanwhile, the nozzles of identical inner geometry but seven times larger, built by GE Aviation, were tested at NASA GRC for the moderate scale experiments. These military style supersonic nozzles (GE nozzles) were built with the identical inner geometry at small and moderate scale to demonstrate the scaling of small heat simulated jets to moderate and full size jets (although no full-scale data is presented in this report). More details about these military style supersonic nozzles can be found in Kuo *et al.*⁶. In general, the expansion portion of the flow contour consists of 12 flat segments that are interleaved to facilitate area adjustment of the operational nozzles. Unlike well designed contoured CD nozzles, imperfections at the nozzle exit plane contain weak shock cells, even at perfectly balanced pressure conditions.

Experimental Results

The operating conditions of the data acquired both at Penn State and at NASA GRC are summarized in Table 9. In this table, the jet Mach number M_j relates to the average Mach number of the fully expanded jets and the nozzle total temperature ratio (TTR) is the ratio of the jet stagnation temperature T_o and the ambient temperature T_∞ . For the data from NASA GRC,

when operating the dual flow rig, the values in the column of TTR are accordingly the values of TTR_{core} where the subscript *core* relates to the quantities relative to the core flow and TTR_{mix} where the subscript *mix* relates to the quantities relative to the mixture of the annular and core flow. The values of Reynolds number in this table were computed based on the calculation methodology described by Doty and McLaughlin³. As a first step, comparisons were made between cold, pure air jet measurements obtained at Penn State with similar measurements from NASA GRC. Then, the heat simulated small scale results are compared to the moderate scale hot jet measurements provided by NASA GRC, with discussions of the results included.

Unheated jets measurements

First, comparisons are made between acoustic spectra from cold jets, between small scale measurements acquired at Penn State and moderate scale measurements from NASA GRC. This allows for a direct cross-scale comparison, from jets issuing from nozzles of different sizes but exactly the same geometry, without adding the complication of the heat simulation. Sample spectra are shown in Figure 107 and Figure 108 from two testing nozzles: both jets are operated with a pressure ratio $NPR = 4$, one of them issuing from the $M_d = 1.65$ ($AR = 1.295$) GE nozzle, and the other from the $M_d = 1.5$ ($AR = 1.18$) GE nozzle. The convention adopted here is that M_d is calculated from the known area ratio assuming the Mach number that would be achieved with ideal quasi parallel flow that has been expanded through the given area ratio. In the figure, the Penn State data were acquired with nozzles 1.8 cm (0.7 in) in diameter, and the NASA GRC spectra were acquired at with nozzles 7 times larger. The spectra are spaced apart in pairs by 20 dB for clear elucidation as the polar angle varies and all acoustic levels have been scaled to $R/D = 100$ assuming far field spherical spreading. From both figures the cross-scale spectra comparison exhibits very encouraging results, with spectra from the two rigs agreeing within ± 2 dB over frequencies $0.05 < St < 5$ and angles $30^\circ < \theta < 120^\circ$ as measured from the exhaust axis. The *OASPL* comparisons consistently present good agreement within 2 dB variance across the polar angles. It is noted that this agreement is obtained for jet noise spectra containing not only jet mixing noise, but also significant broadband shock noise from jets operating in the over- and under-expanded condition. This degree of agreement between the data acquired from the two facilities provides a check on the scaling methodology, and validates the quality of cold jet measurements acquired from both facilities. This is an encouraging comparison which validates the potential to develop noise reduction concepts in small scale jets that accurately simulate the acoustics issuing from the actual engine exhausts.

Closer inspection of the details of the small scale nozzles used in conducting the experiments at Penn State shows that the internal nozzle surface is slightly rougher at this scale level in comparison with the moderate scale nozzle. The lip thickness is also not exactly reproduced, due to the limitations of the rapid prototyping technique and the brittleness of the material used. Therefore, the thickness of the boundary layer at the exit plane of the nozzle may not scale perfectly with the moderate scale measurements. In spite of these differences, the comparisons are very good. This observation is in agreement with a previous study from Viswanathan who validated the effect of the state of the flow at the nozzle exit plane. The conclusion from that study was that the radiated noise is insensitive to the state of the flow and the thickness of the boundary layer at the nozzle exit plane, provided the Reynolds number of the jet flow exceeds approximately 400,000.

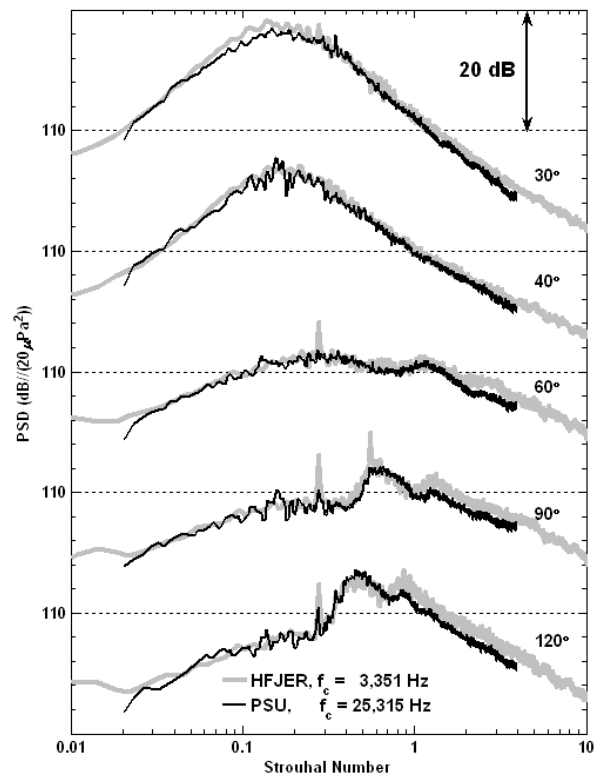


Figure 107. Spectra and OASPL comparison of unheated jets from PSU and HFJER issuing from GE nozzle with $M_d = 1.65$, $M_j = 1.56$, and scaled to $R/D = 100$.

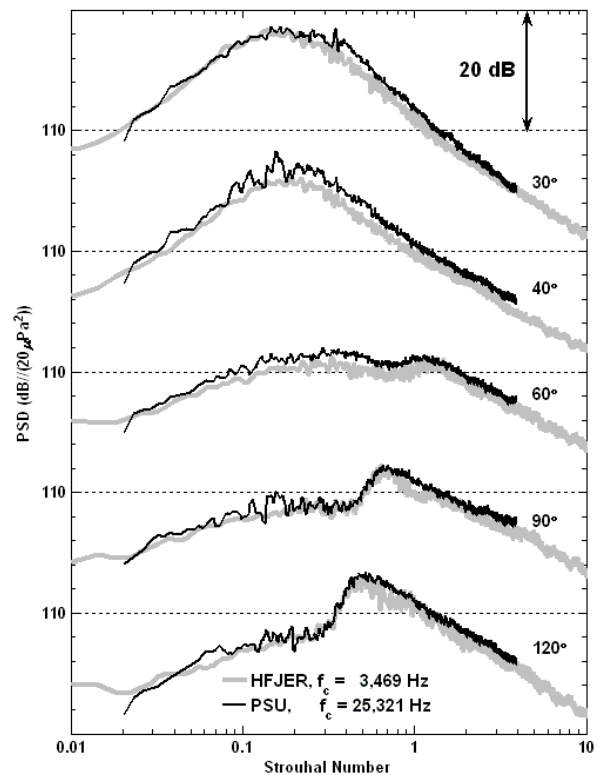


Figure 108. Spectra and OASPL comparison of unheated jets from PSU and HFJER issuing from GE nozzle with $M_d = 1.5$, $M_j = 1.56$, and scaled to $R/D = 100$.

The current comparisons of unheated jet measurements were conducted in the geometric far field, with sound measurements being made well over 100 jet diameters from the nozzle. The term ‘geometric far-field’ is used when the noise is approximated by a point source causing the noise to radiate spherically so the sound intensity is reduced by 6 dB for per doubling of distance from the noise source. By maintaining the far field measurements in treating the noise as a compact point source emitting from the nozzle exit plane, the experimental results can be extrapolated to various non-dimensional distances for comparisons as is commonly done (see Ref. 91, 12, 92). This issue is of particular importance when working with supersonic jets, as discussed below.

The data in Figure 107 and Figure 108 are representative of similar spectra recorded with numerous pressure ratio conditions. Such results show that the small scale jets approximately replicate the acoustics issuing from the moderate scale jets under over-expanded and under-expanded conditions. Moreover, the demonstration of the cross-scale comparison from the unheated jet experiments, measured in the far field, shows that the small scale unheated jets have been able to simulate the acoustic field generated by moderate scale unheated jets. This is an encouraging first step in making cross-scale comparisons with the heated jet measurements.

Heat simulated jets and heated jets measurements

The heat simulated jet experiments were conducted with helium-air mixture jets at Penn State, following the methodology established during previous studies. Figure 109 shows acoustic spectra measured with the GE nozzles with $AR = 1.295$ conducted with single stream jets at both Penn State and NASA GRC. The data recorded using the $M_d = 1.65$ ($AR = 1.295$) GE nozzle operating at a pressure ratio of $NPR = 3.0$ produces an average exit Mach number $M_j = 1.36$, and the simulated temperature ratio $TTR = 2.6$ for Penn State and $TTR = 2.5$ for NASA. All acoustic levels have been adjusted to $R/D = 100$.

Figure 110 shows acoustic spectra measured with the GE nozzles with $AR = 1.18$ conducted at both Penn State and NASA GRC. As mentioned earlier for the experiments measured in the NASA GRC HFJER a small amount of cold bleed flow surrounds the core flow. Although the mixing of this cold stream with the core hot flow is incomplete, a theoretically fully mixed total temperature of the full jet can be calculated to be TTR_{mix} . The mixed flow temperature ratio TTR_{mix} is the simulated temperature ratio chosen for the Penn State helium-air mixture jets in this comparison. In Figure 110, the data recorded using the $M_d = 1.5$ ($AR = 1.18$) GE nozzle operating at a pressure ratio of $NPR = 4.5$ produces an average exit Mach number $M_j = 1.64$, and the simulated temperature ratio $TTR = 3.0$ for Penn State and $TTR_{mix} = 3.0$ for NASA. All acoustic levels have been adjusted to $R/D = 100$. The choice of the mixed total temperature ratio TTR_{mix} in the matching condition will be addressed in the next section.

As in the case of the cold jets, the acoustic data for the small scale experiments compare favorably with the NASA moderate scale data across the frequency range. The individual PSD components are always within 3 dB for both sets of data and most spectral components agree within 2 dB.

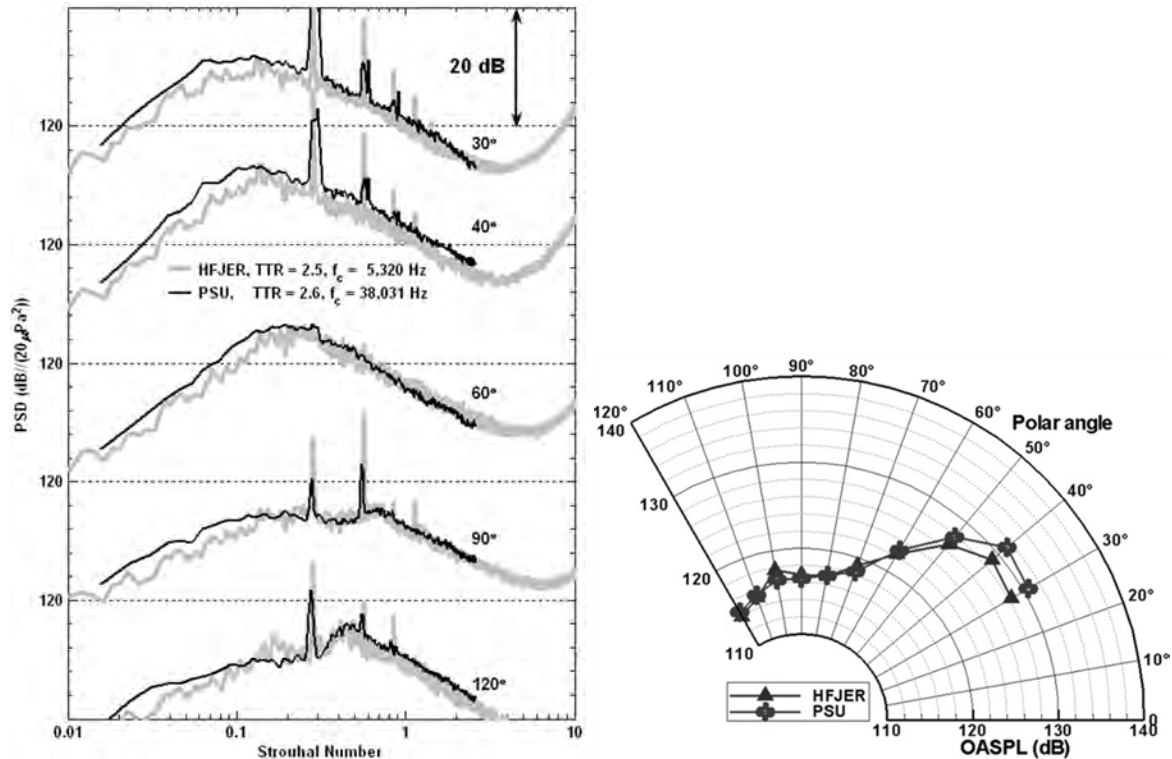


Figure 109. Spectra and OASPL comparison of single stream jet with heat simulation (TTR = 2.6) from PSU and heated jet (TTR = 2.5) from HFJER both issuing from GE nozzle with $M_d = 1.65$, $M_j = 1.36$, and scaled to $R/D = 100$.

The above demonstrations distinctly show that the small heat-simulated jet is capable of reproducing the acoustics issuing from a moderate size heated jet when the precise simulated properties are matched for the over-expanded CD nozzles, which are prevalent in practical supersonic aircraft. These data (and many other comparisons not shown here), show that the scaling of small heat simulated jets measurements are in reasonable agreement provided that comparisons are made in the far field past $R/D = 100$, with identical nozzles, and with matching Mach number and total temperature ratio. In this context “reasonable agreement” can be quantified to state that agreement of individual portions of the spectra agrees within 2 to 3 dB and the overall sound pressure levels agree within 2 dB.

Small unheated bleed flow effect on the noise emission

The most common configuration for the NASA HFJER is with co-annular dual flow with a very low bypass ratio ($BPR = 0.3$) of unheated air. Such a configuration consists of a core flow surrounded by a thin annulus of cold air, whose initial thickness is less than 10% of the core radius (shown schematically in Figure 106). This configuration of nozzle is reasonably close to actual supersonic aircraft engines in which the annular fan flow plays a major role in cooling liner components of the engine. It does however introduce some uncertainty in how best to match these low BPR exhaust jet acoustic experiments to single stream model jets for which a considerable amount of acoustic data are available. The experiments producing acoustic spectra are plotted in Figure 111 as a head-to-head single flow versus dual flow acoustic data comparison.

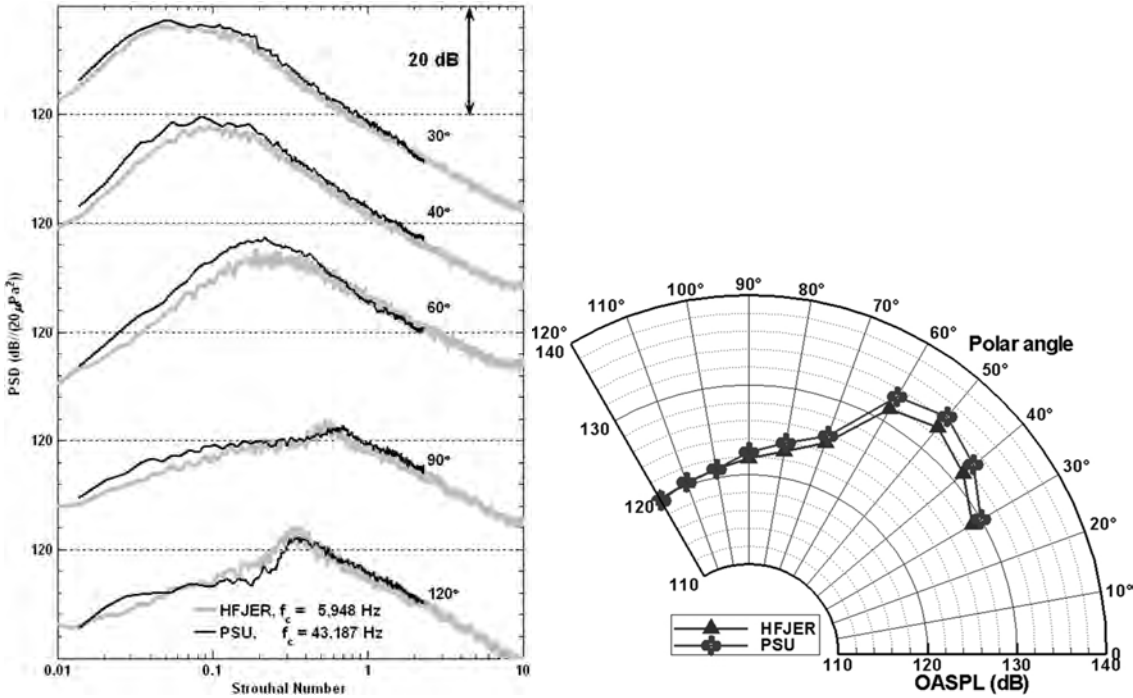


Figure 110. Spectra and OASPL comparison of heat simulated jet ($TTR = 3.0$) from PSU and heated jet ($TTR_{mix} = 3.0$) from HFJER both issuing from GE nozzle with $M_d = 1.5$, $M_j = 1.64$, and scaled to $R/D = 100$.

First, the HFJER was operated both as a single stream jet and in its standard configuration as a dual flow rig with a GE design nozzle with $M_d = 1.5$. Figure 111 compares data from the same facility when the single stream TTR matched the core flow total temperature TTR_{core} ($= 3.2$) and also when it matched to a hypothetical mixed flow temperature ratio TTR_{mix} ($= 2.7$) that assumes the core and cold annular flow to be fully mixed. As noted earlier, the bypass ratio was 0.3 in the dual flow experiment. In Figure 111 the difference between the two single-stream jet noise curves is roughly 3 dB for frequencies below the peak, in line with expectations from increasing jet velocity with increased temperature. The temperature change also affects the shift in peak frequency in the data in the aft quadrant and there is some difference in the high frequency roll-off such that the colder jet produces more high frequency noise at shallow aft angles, but less high frequency noise on the sideline. It is believed that the explanation for this is the rotation of the peak noise emission direction toward steeper angles from the jet (and further from the jet axis) for the hotter single stream jet. The dual stream noise spectra generally lies between the two single-jet curves at low frequencies and follows the higher temperature (core conditions) single jet at high frequencies. For this realistic CD nozzle geometry operating in an over-expanded condition matching the core conditions seems to produce the best match to the more realistic dual stream data.

Having quantified the error in simulating a low-bypass ratio practical CD nozzle with a single-stream jet, the next step is to add the effect of scale. The small-scale rig at Penn State was run in a similar fashion, with two total temperature values that match first the corresponding HFJER TTR_{core} and second, the TTR_{mix} value. The results are plotted in Figure 112. Note that this case

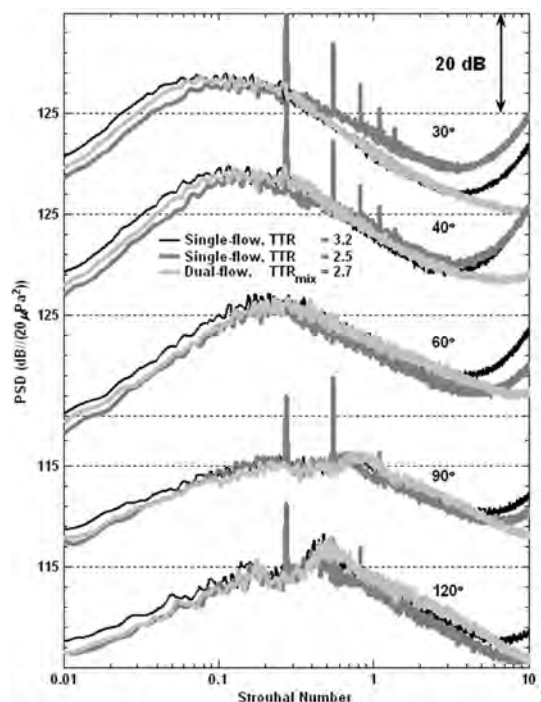


Figure 111. Spectra comparison among single-flow heated jets ($TTR = 3.2$ and 2.5) and dual-flow heated jet ($TTR_{core} = 3.2$, $TTR_{mix} = 2.7$ with $St_{dual} = f D_j / U_{j mix}$) with $BPR = 0.3$ all from HFJER issuing from GE nozzle with $M_d = 1.5$, $M_j = 1.36$, and scaled to $R/D = 100$.

uses a slightly different nozzle than Figure 111, with $M_d = 1.65$; however, both cases are the faceted CD nozzles operating at the over-expanded condition. Here, the jet noise from the two single-stream jets at small scale differ by as much as 5 dB at low frequencies, more than did the same cases in the larger rig. Here the single stream (PSU jet), run at simulated temperatures matching the dual flow fully mixed temperature condition produced better agreement with the dual stream data at low frequencies. At higher frequencies and aft angles, the single-stream jet matching the core conditions of the dual stream jet best agreed with the dual stream jet, in the same way as the medium scale experiment did. It is noted that both the Penn State and the GRC data have shock screech components at virtually identical frequencies that are quite close in spectral level, assuring that the shock structure and details of the shock noise are well represented across the model scales (and with different methods of obtaining a “heated jet”). However, it can be concluded that there are imperfections in the matching of acoustic data between single stream and dual stream ($BPR = 0.3$) jets at frequencies below the peak frequency no matter what matching condition is used.

Confirming experiments

As an additional test of the validity of the Penn State data, comparisons have been conducted with a different data set, namely heated supersonic jet acoustic data measured by Seiner and Norum⁹³ at the NASA Langley Research Center (LaRC). To do this requires that a more common nozzle geometry be used, a convergent-divergent nozzle with a contoured divergent

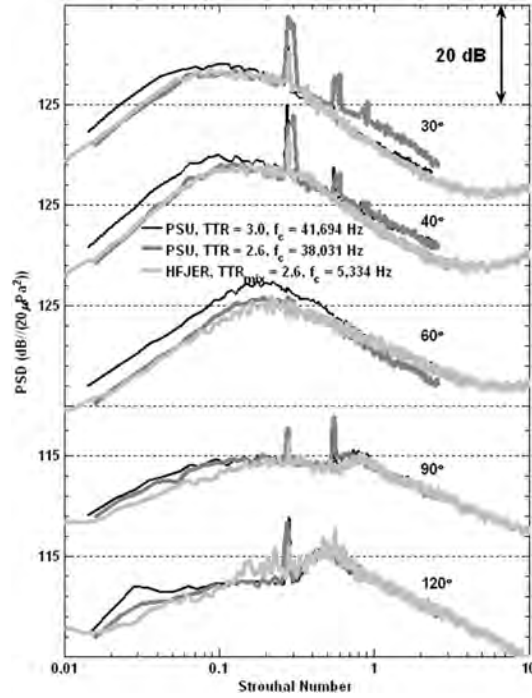


Figure 112. Spectra comparison among heat simulated jets ($TTR = 3.0$ and 2.6) from PSU and heated jet ($TTR_{core} = 3.0$, $TTR_{mix} = 2.6$) from HFJER all issuing from GE nozzle with $M_d = 1.65$, $M_j = 1.36$, and scaled to $R/D = 100$.

section designed using the method of characteristics to be shock-free at its exit at $M_j = 1.5$. Making this change also removes shock-associated noise from the comparison. In this case the LaRC experiments were conducted with a 4.27 cm (1.68 in) exit diameter ideally contoured axisymmetric CD nozzle operating ideally expanded at a $NPR = 3.6$ and $TTR = 2.25$. The Penn State experiments used a 12.5 mm (0.5 in) exit diameter contoured axisymmetric CD nozzle operating at a $NPR = 3.6$ and $TTR = 2.2$. The spectral comparisons are shown in Figure 113, with the data agreeing across the spectra for 90° and 100° to within ± 1.5 dB. The biggest discrepancy in the data, of 4 dB at the peak frequency and 60° polar angle, can be partially accounted for by the differences in the R/D location of the two data sets. As noted earlier, when the distance to the microphones is different between two experiments, differences in spectral level are often most apparent at polar angles around 50 to 60° where the gradient in OASPL with polar angle is the greatest. At the most aft angle shown (40°), the PSU data are less than 3 dB below the LaRC data.

Continuing with the approach of comparing acoustic data acquired at different facilities, Figure 114 presents a comparison of the LaRC single jet data shown in Figure 112 with those of GRC HFJER run in both single-flow ($TTR = 2.25$) and dual-flow ($TTR_{mix} = 2.25$) modes using a contoured axisymmetric CD nozzle with $M_d = 1.5$. The first observation is that for this ideally expanded flow, operation of the GRC HFJER facility in the dual flow mode produces spectra that more closely match the smaller LaRC facility jet spectra than do the spectra in the single jet mode. All three jet data sets agree well at the broadside angles of 100° and 90° . By 60° there appears a systematic discrepancy in levels at frequencies below the peak, where the smaller rig

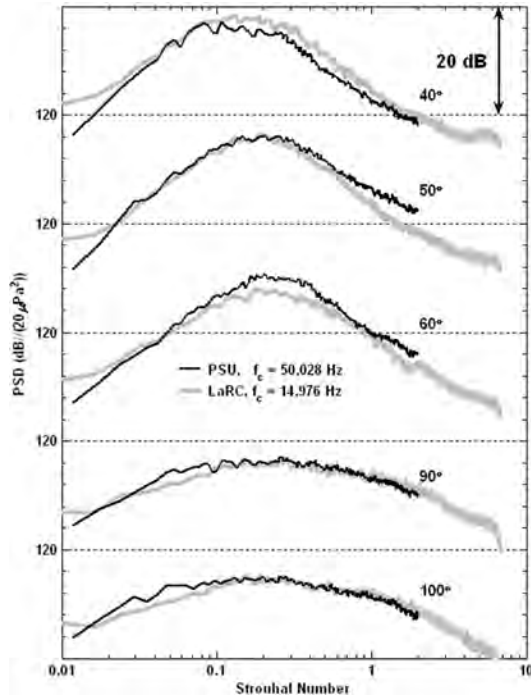


Figure 113. Spectra comparison between heat simulated jet ($TTR = 2.2$) from PSU and heated jet ($TTR = 2.25$) from NASA Langley Research Center LaRC) both issuing from CD nozzle with $M_d = 1.5$, $M_j = 1.5$, and $R/D = 100$.

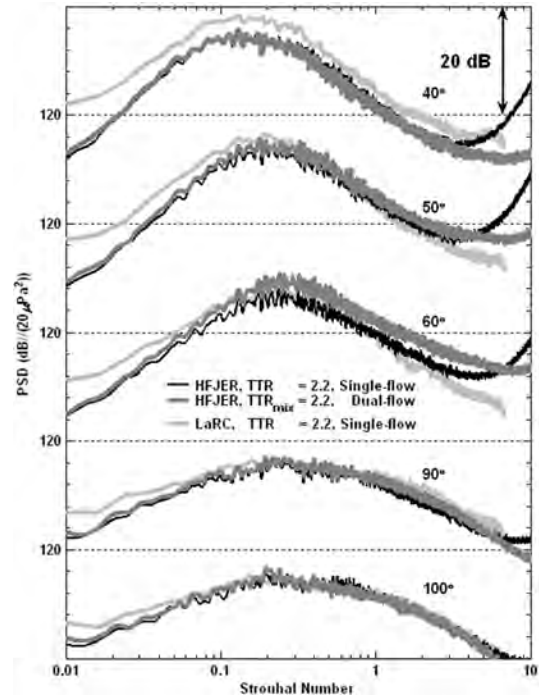


Figure 114. Spectra comparison of heated jets with HFJER in single-flow ($TTR = 2.2$) and dual-flow ($TTR_{mix} = 2.2$), and LaRC in single-flow jet ($TTR = 2.2$), all issuing from a CD nozzle with $M_d = 1.5$, $M_j = 1.5$, and scaled to $R/D =$

produces more noise than the larger rig. At angles aft of 60° the GRC HFJER data are lower than the LaRC data by increasing amounts, being 5 dB different at 40° to the jet axis. At this point it is noted that the feature of higher noise levels at low frequencies for the smaller rigs is consistently present in the data. This feature will be addressed further later in this section of the report.

One other major feature has been present in these datasets that merits attention: the higher frequencies at which the HFJER data show a very strong rise (an upward “hook”). This sharp rise is not visible in raw data, but results from performing the atmospheric attenuation correction to obtain “lossless” data. Such a rise is slightly apparent in both the Penn State and the LaRC data, both of which are not resolved to the same high non-dimensional frequency as is the GRC data. This feature is most significant at the angles of strongest noise emission, e.g., aft angles, and typically appears at supersonic, hot jet conditions, as discussed in Ref. 94. The physical explanation is the presence of strong nonlinear distortion that is present in very high amplitude noise that is undergoing wave steepening (as discussed in several references, for example Ref. 94). It appears from the data presented here, that the increase in sound amplitude in absolute terms going from the ~ 50 mm (2”) nozzles to ~ 100 mm (4”) nozzles is sufficient to cause the onset of nonlinear propagation within the same relative measurement distance.

It is noted that the rising spectral “hook” mentioned in the preceding paragraph is not seen in the Penn State data of Figure 109 and Figure 112. In both those data sets the small scale data agree with the moderate scale NASA data quite well but do not extend in frequency resolution to the point where the lossless spectral content begins to rise. The microphones response limited the resolution. An experiment was conducted however, in which the microphones were placed 280 jet diameters from the nozzle exit over the range of polar angles. The data, presented in Figure 115, show an almost identical shape as the moderate scale data, just shifted to a lower frequency. Such a shift in the location to the onset of the nonlinear distortion is consistent with the

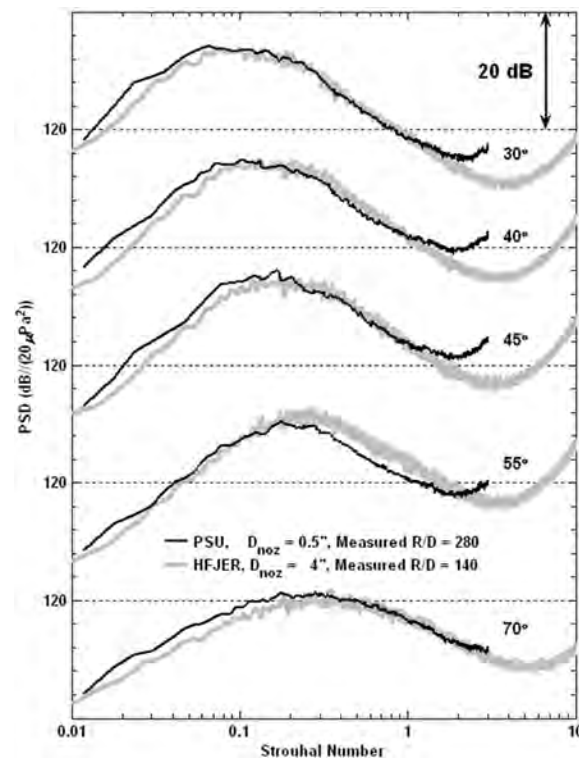


Figure 115. Spectra comparison among heat simulated jet ($TTR = 2.2$) from measured at $R/D = 280$ and heated jet ($TTR = 2.2$) from HFJER in single-flow measured at $R/D = 140$ both issuing from CD nozzle with $M_d = 1.5$, $M_i = 1.5$, and discussion presented by Petitjean *et al.* on the onset of such effects. Additionally Saxena *et al.*⁹⁵ have developed a nonlinear propagation computational model that predicts the general high frequency lift-up feature that is seen in the data of Figure 115. In summary, nonlinear propagation effects require the initially very high sound pressure levels, long propagation ranges within the facility, resolution of the frequency spectra to high frequencies and finally, properly applied correction of the spectra to remove the effect of atmospheric attenuation (to produce lossless data).

To summarize the results of the comparisons made with the data presented in Figure 109 to Figure 115 it is apparent that there is consistency between the single stream Penn State and LaRC data operating at similar jet mean flow (including TTR) conditions with an ideally expanded, shock-free jet flow. For realistic nozzle models running over-expanded conditions, the Penn State and GRC data match well when both are operated in single-stream mode with the

following exceptions. For ideally expanded nozzles, the larger GRC nozzle exhibited a significantly lower noise in the low frequency range (below the peak frequency) at aft angles, than the smaller single-flow rigs. In using single-flow rigs to simulate low bypass ratio jet flows there is a choice to be made whether to match the core conditions or the fully mixed conditions. For the over-expanded realistic nozzle flows, there is a significant impact of the bypass flow. For the ideally expanded shock-free nozzle at $M = 1.5$ there was little impact of the cold bypass stream at this bypass ratio of 0.3. However, the larger rig produced data that were slightly but measurably lower than the smaller rigs for this nozzle. At present these contradictions are unresolved.

At this point it is appropriate to mention the possibility that the annular co-flow that surrounds the core jet could serve to eliminate or reduce the Mach wave radiation as explained by Papamoschou⁹⁶. If the parameters of the annular flow were assumed to be retained following convection through the nozzle, the convection velocity of the turbulence on the outer shear layer would be reduced to below the ambient acoustic velocity thus eliminating Mach wave radiation. It seems rather unlikely that such could be the case in precisely the manner suggested by Papamoschou. It is anticipated that the annular co-flow, which starts upstream of the nozzle throat, would become mostly mixed with the core flow, at least in the outer portion of the jet at the exit of the jet. Thus the criteria used by Papamoschou to predict the parameters for Mach wave elimination are likely not to be satisfied. The outer shear layer however, will certainly be affected, resulting in reduced levels of mean shear which would be expected to slightly reduce the radiated noise, a result that is consistent with observed data.

One focus of future experiments will be to examine the effect of the thin layer of cold air surrounding the hot jet in the dual flow experiments. Recognizing that there remains an unresolved contradiction in the best way to match *TTR* operating conditions when comparing the acoustic data of the dual flow facility with those from the single flow facility, one notices a previously unmentioned issue. The hot jets that compared well using the TTR_{core} were all conducted at a Reynolds number of 2 million or greater. The jets that compared well with the HFJER TTR_{mix} were all at $Re < 900,000$. Although it is premature to draw a definitive conclusion, the lower Reynolds number jet data have a very similar additional noise component that was identified by Viswanathan⁹⁷ with heated subsonic jets at $M = 0.7$.

Near field / Far field measurement issues

During the process of comparing acoustic data acquired in experiments with different scale nozzles it is quite easy to get sidetracked examining data in which not every physical parameter was maintained constant that needed to be. One such example is the microphone radial location during experiments with nozzles of two scales. There is considerable experience with cold jets to conclude that if the microphone(s) are positioned 50 to 70 radii away from a jet (exit plane) then good accuracy can be obtained using the 6 dB per doubling of distance to scale acoustic amplitude levels to a common radius. Such is not the case with hot supersonic jets. Two examples of this effect in the acoustic spectra are shown in Figure 116 and Figure 117.

Figure 116 shows spectra of acoustic measurements performed (at Penn State) in the acoustic field of two supersonic jets exiting from CD nozzles operating at $M_j = 1.5$ ($NPR = 3.6$) and

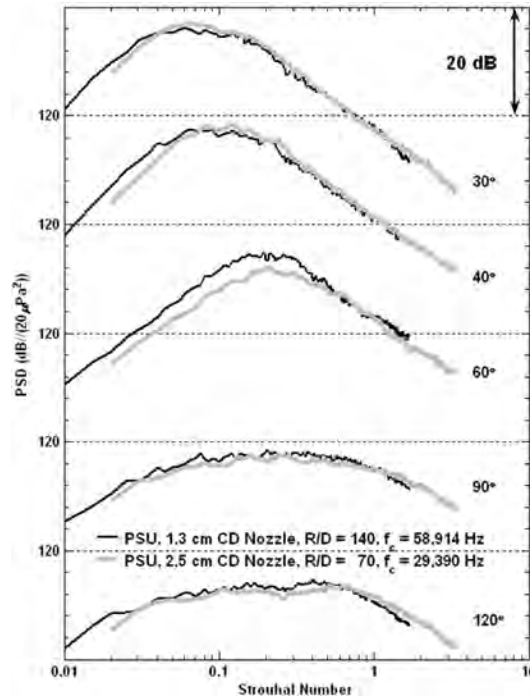


Figure 116. Spectra comparison of heat simulated jets ($M_j = 1.5$, $TTR = 3.2$) from PSU issuing from CD nozzles with $M_d = 1.5$, $D = 1.3$ and 2.5 cm respectively; scaled to $R/D = 100$.

simulated total temperature ratios of $TTR = 3.2$. The microphones for both jets were positioned at a radius of 1.78 m (70 in) on a polar arc originating at the nozzle exit. Since the two nozzles used in these measurements were 12.7 and 2.54 m in diameter, the R/D value for the experiments were $R/D = 140$ and 70 respectively. In the data of Figure 116, both sets of data were then scaled (by spherical spreading) to $R/D = 100$. Note that the spectral data are in reasonable agreement but differences of about 3 dB in magnitude are apparent between data of two size nozzles (and R/D positions). The discrepancies are most apparent at frequencies below the peak amplitude level and in the polar angle range from 40° to 60° from the jet axis corresponding to the aforementioned region of largest gradient in the *OASPL* with polar angle.

Figure 117 shows very similar data as in Figure 116 this time recorded with a heated jet exhausting from the NASA GRC HFJER facility fitted with a CD nozzle and 30% bypass unheated air. In this case the acoustic data were recorded simultaneously with microphones positioned on an arc at $R/D = 147$ and on a linear array displaced parallel from the jet axis by $33D$. The latter data, noted on the figure as at an average radius of $R/D \sim 50$, are clearly not in the geometric far field. The plotted data are scaled to a non-dimensional radial position of $R/D = 100$ and discrepancies in the spectral level are observed as with the Penn State small scale jet measurements of the previous figure.

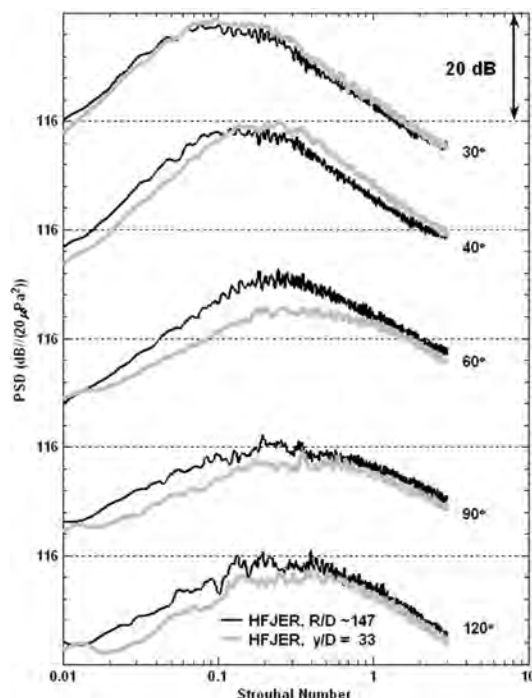


Figure 117. Spectral comparison of experiments measured at various locations from HFJER issuing from CD nozzle with $M_d = 1.5$, $M_j = 1.5$, $TTR_{core} = 2.6$, $TTR_{mix} = 2.2$; scaled to $R/D = 100$.

Such discrepancies between the measurements made at the threshold of the near to far field and those that are clearly in the geometric far field are significant and render the comparisons of the effect of other parameters, in some cases, less effective. In essence the problem is much more acute with heated and heat-simulated jets, than it is with cold supersonic jets. As demonstrated by Lee and Bridges⁹⁸ and McLaughlin *et al.*⁹ the dominant region of noise sources in hot supersonic jets center around a non-dimensional axial distance $x/D = 13$, whereas the location for comparable cold jets is around $x/D = 8$. This shift of the dominant region of noise sources, as well as the extended length of the source region, is enough to distort the spherical spreading scaling of acoustic data to different radial positions when the measured microphones on a polar arc originate at the nozzle exit. This reason makes it more important to perform comparison measurements at the same non-dimensional radial positions.

On the scaling of noise measurements from moderate size jet nozzles to full size engines

The acoustic data obtained in the moderate scale tests conducted at NASA Glenn Research center, described in Task 3.1, were compared to flight data obtained from an F-15 ACTIVE test⁹⁹. The moderate scale tests were performed at similar nozzle pressure ratios and temperatures to those of the real aircraft and with a free jet Mach number close to the aircraft Mach number. A comparison of the model scale and flight data is shown in Figure 118. The acoustic levels obtained from the two tests agree within 2 dB at frequencies below the peak frequency and differ by 5 dB at high frequencies. However, the experiments used an isolated jet

in a simulated flight stream and the flight data included all installation effects that occur in a real aircraft so the agreement between the two data sets is quite remarkable.

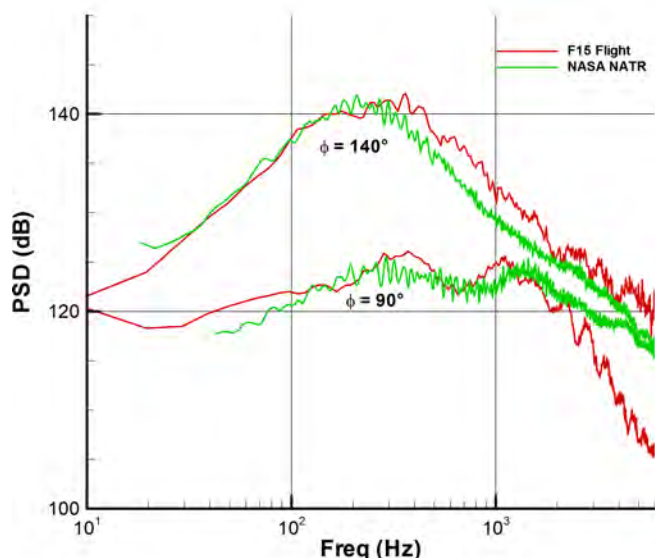


Figure 118. Acoustic data acquired in the moderate scale laboratory experiments and the F15 ACTIVE flight test. The observation angle is given by ϕ .

Concluding remarks for task 6.1

Careful measurements and normalization were employed to produce direct comparisons between small scale jet acoustic measurements made at Penn State and moderate scale measurements from NASA GRC. In most cases the supersonic nozzles were of identical geometries (to engineering accuracy) and closely replicated the exhaust nozzles of GE 404 class turbojet engines. Other experiments were performed with contoured converging-diverging (CD) nozzles producing minimal shock cells in the flow field when operated at perfectly expanded pressure ratios. Initial experiments were performed with unheated, pure air jet flows. For these cold jets, non-dimensional acoustic data measured at identical scaled radial distances were shown to agree within ± 1.5 dB across the spectra at numerous polar angles. The Reynolds numbers for all cold jet data presented exceeded 900,000 and imperfections in nozzle surface roughness and lip thickness did not appear to have any significant effect.

For hot jet comparisons, the small scale (Penn State) experiments simulated the hot-jet velocity conditions of experiments conducted at NASA GRC and NASA LaRC by using helium-air gas mixtures. Comparisons of the acoustic fields (measured in small and moderate sized facilities) of hot jets from practical CD nozzles in typical over-expanded conditions produced very good agreement on *OASPL* and spectra, typically within ± 1.5 dB. Comparisons for ideally expanded nozzles operating at their design Mach numbers showed good agreement between rigs of similar scale (nozzle diameters less than 50 mm (2 in)), but not as good agreement between the small and medium scale rigs, particularly at frequencies below the peak amplitude values.

Realistic exhaust systems often have unmixed bypass flows exiting the nozzle, a feature incorporated into the medium scale rig. For over-expanded jet conditions in realistic CD nozzles, there was an impact of the bypass flow on the noise; the impact on ideally expanded flows from shock-free nozzles was much smaller. Comparisons of the small Penn State rig data with hot jet supersonic jet data from the NASA HFJER operating with low bypass ratio ($BPR = 0.3$) showed reasonable agreement (± 1.5 dB) provided the single stream total temperature ratio TTR was matched to the theoretical mixed flow TTR_{mix} of the HFJER jet. Comparison of measurements made in the HFJER facility operating in single-flow and dual-flow ($BPR = 0.3$) modes demonstrated that more accurate data were obtained when the single stream TTR was matched to the TTR_{core} of the dual stream jet. This discrepancy in the acoustic data of the two kinds of jets is being investigated further with additional experiments and examination the effect of the annular bypass stream and of a possible Reynolds number effect.

The unresolved issue of nonlinear propagation, which is just now being recognized in supersonic jet data, was demonstrated in rigs of both small and medium scale, particularly at polar angles of maximum acoustic output. The unresolved part is how to properly scale and correct for this effect, as demonstrated in the data presented here, without a major computational effort as reported by Saxena *et al.*. This becomes more of a problem as measurement locations are moved further away from the jet to be truly in the geometric far field.

Finally, data are presented that examine the accuracy of scaling measurements that are made in the outer regions of the near field to far field distances. These data demonstrate that measurements in supersonic jets must be made much further away from the jet to be in the geometric far-field. Presumably this is caused by the position of the dominant noise sources moving significantly downstream of the nozzle exit along with an increase in the *lengthwise extent* of the dominant source region.

Task 6.2 Assessment of Scaling Methodology for Chevron Nozzles

With the emergence of more powerful fighter aircraft, supersonic jet noise reduction devices are being intensively researched. Small scale measurements are a crucial step in evaluating the potential of noise reduction concepts at an early stage in the design process. With this in mind, the present study provides an acoustic assessment of small-scale military-style nozzles with chevrons. Comparisons are made between the present measurements and those made by NASA at moderate scale. Measurements made with baseline nozzles (without chevrons) show excellent agreement with NASA data (as described in the previous section) establishing the accuracy of the scaling methodology. The effect of chevrons on supersonic jets is then investigated for cold jets, highlighting the crucial role of the jet operating conditions on the effects of chevrons on the jet flow and subsequent acoustic benefits. At low Reynolds numbers (small scale) the penetration of the chevrons in the jet flow is the most important chevron parameter in reducing the generated noise. A small scale heat simulated jet is investigated in the over-expanded condition and shows no substantial noise reduction from the chevrons. This is contradictory to moderate scale measurements. The discrepancy is attributed to a Reynolds number low enough to sustain an annular laminar boundary layer in the nozzle that separates in the over-expanded flow condition. Transition of the boundary layer to turbulent flow is induced with inner roughness of the nozzle and results in more noise reduction with the chevrons. The resulting effect is comparable to

results from NASA, validating the hypothesis made that jets of too low Reynolds number cannot be used directly to observe and measure chevron noise reduction. These results are important in assessing the limitations of small scale measurements in this particular jet noise reduction method.

As communities pay more attention to the noise levels around airports, there is a strong need to reduce noise generated by military aircraft. Therefore, noise suppression mechanisms are being widely investigated and lead to the recent emergence of new nozzle design concepts such as chevron nozzles, and non-axisymmetric geometries. As new military aircraft are being developed, their enhanced capabilities are usually closely linked to larger noise signatures, rendering them dangerous for ground crews and failing to meet the noise regulations of some countries.

The high-speed jet noise laboratory at The Pennsylvania State University (PSU) has contributed to the studies of jet noise source generation and suppression mechanisms for several decades. Recently, studies have concentrated on noise reduction concepts and more accurate representations of military aircraft jets, such as the investigation of the potential benefits of a beveled nozzle or measurements conducted with a rectangular nozzle with thrust vectoring. The current paper focuses on another noise reduction application, the addition of chevrons to the nozzle. The testing candidate is a replica of the nozzle installed on F-18 fighter aircraft. This military-style nozzle is composed of multi-faceted straight sections in both the convergent and divergent parts of the nozzle. The metallic plates forming this inner geometry can slide between each other and allow for control of the area ratio between the throat and the exit plane. Chevrons with different degrees of penetration into the flow attached at the lip of the nozzle are being designed to reduce the noise production. This task was conducted within at The Pennsylvania State University, in partnership with GE and the NASA Glenn Research Center. One of the main objectives of this task is to investigate the validity of a scaling methodology that facilitates using small scale experiments to predict aeroacoustic performance of moderate scale supersonic jets. The jets being investigated are issuing from traditional converging-diverging axisymmetric nozzles as well as ones more representative of military-style nozzles, their design being provided by GE. Baseline nozzle measurements were performed earlier and the experimental results have been reported^{5,7}, demonstrating very good agreement between the small scale experiments performed at Penn State and moderate scale data acquired at NASA Glenn Research Center. The present study extends this first round of measurements by providing advanced acoustic assessment on small-scale military-style nozzle with chevrons.

The first step is to understand the characteristics of the flow field inside a jet before studying the acoustic far-field noise radiated from the turbulence in the noise generation regions of a jet issued from a nozzle. Some efforts^{100,101,102} have been made showing the characteristics of turbulence existing in the noise production regions of a jet. The characteristics of the turbulence distinguish the noise generation regions of a jet and helps in the methodology of noise source prediction. During a study on the effect of boundary layer thickness on jet spreading, Bradbury and Khadem¹⁰³ surprisingly found that inserting a small rectangular tab in the nozzle exit plane can induce a profound effect on jet spreading. This circumferential asymmetry on nozzle exit plane causes faster decay on jet centerline velocity, higher turbulent intensity level and entrainment, and gross distortion on radial jet cross-stream plane. Though the initial flow

structure is distorted, the flow development ultimately returns to the axisymmetric self-preserving jets in farther downstream locations. In addition to the jet distortion induced by tab, a pioneering study¹⁰⁴, stemming from the Concorde project, discussed the jet plumes issued from a notched nozzle obtained by cutting V-shaped notches from the nozzle exit edge. The most prominent flow-field modification was the counter-rotating streamwise vorticity shed from the notch edge of the nozzle and gradually growing in the downstream direction - similar to the flow field on the leading edges of delta wings. The jet plume cross-stream section is greatly modified by the lateral jet development on the notch plane until 20 nozzle diameters downstream and this induces lateral momentum transport related to a faster decay of the jet centerline velocity. It was also demonstrated that there is a tendency to modify the shock cell structure due to the presence of the notch. Wlezien and Kibens¹⁰⁵ demonstrated the effect of nozzle asymmetry on the acoustic far-field measurements and found that the nozzle asymmetry can lead to asymmetric shock structures, which can also suppress screech. The overall sound pressure level noise reduction is dependent significantly on the azimuthal angle due to nozzle asymmetry.

For higher speed (and Mach number) jets, compressibility effects emerge and significantly reduce the growth of the free shear layer causing slower jet spreading¹⁰⁶. Meanwhile, the decay of jet centerline velocity is a good indicator of the jet spreading. The additionally induced streamwise vortices from the nozzle exit were found to cause a faster decay of the jet centerline velocity and higher jet spreading and mixing enhancement^{107,108,109,110}. For round nozzles, the jet mixing process and jet momentum transfer are gradually reached through the activities of the viscous shear stresses in the jet free shear layer. Knowles and Saddington¹¹¹ provided a review categorizing nozzle varieties for jet mixing enhancement applications for aircraft propulsion.

Since the induced streamwise vortices generated by a chevron nozzle can effectively improve the jet spreading and distort the radial jet cross-stream development^{112,113}, it is necessary to understand the modified flow field and corresponding acoustic benefits. Callender *et al.*¹¹⁴ described the observed acoustic far-field trends from the measurements conducted with chevron nozzle: effective low frequency noise reduction and excess high frequency noise penalty. An investigation^{115,116} on flow turbulence intensity shows that chevrons modify the flow turbulence distribution and shift the peak of turbulent kinetic energy upstream. A parametric study on chevron and corresponding performance characterization¹¹⁷ provides more detailed information on the effect of chevrons. The amount of penetration of the chevrons in the flow has the greatest impact on the flow structure and acoustic far-field by altering the intensity of the streamwise vortices. A direct relation was found between the peak streamwise vorticity intensity and the penetration of the chevrons¹¹⁸. Other parameters have some influence too, including the number of chevrons.

The current task focuses on the effects of chevrons of various geometries on the noise produced by military style nozzles under different flow configurations. Measurements performed in the Pennsylvania State University small scale jet noise facility allow for reliable and inexpensive measurements that, early in the design process, can help in the selection of the most promising designs before full-scale production and testing. The study involves comparisons of chevron nozzle experiments with similar experiments conducted at NASA Glenn Research Center with nozzles approximately 7 times larger in size. In doing so it is necessary to adopt the convention developed by Henderson and Bridges, of characterizing the chevrons by three parameters: width,

length, and penetration. That paper summarizes the results of a series of measurements that demonstrate the effects of chevrons on supersonic jets operating at various conditions of under-expanded, perfectly expanded, and over-expanded pressure ratios. A specific goal of the present task is to investigate the conditions, and the chevron designs, at which scaling the results of the experiments to moderate scale (NASA size jets) works well. The task also identifies the conditions for which the scaling to large size does not work well and investigate the causes of the discrepancies.

Experimental results

The experimental facilities and data processing methodology were described under Tasks 3 and 6.1. The same approach is used for the experiments described in this section.

Model geometry of military style supersonic nozzle

This task presents the experimental results conducted predominantly with the military style nozzles representative of the exhaust of aircraft engines of the F404 family. (One experiment included here was performed with a contoured, purely converging nozzle with and without chevrons.) The exact inner contours of the military style nozzles were provided by General Electric Aviation under Task 1. While such military engines possess nozzles with variable geometry, adapting to different flight regimes, for this specific research, three nozzles with different exit-to-throat area ratios were used, as specified by GE Aviation. These nozzles were designed with a multi-faceted (12 segments) inside conical contour. At Penn State, the nozzles were fabricated via rapid prototyping techniques (stereolithography with Accura 50 giving 0.004" (0.102 mm) layer thickness and fused deposition modeling with ABS plastic giving 0.01" (0.254 mm) standard layer thickness). Nozzles of identical inner geometry but seven times larger were built by GE Aviation and tested at NASA GRC for moderate scale experiments. These military style supersonic nozzles (GE nozzles) were built with the identical inner geometry at small and moderate scale to demonstrate the scaling of small heat simulated jets to moderate and full size jets. In general, the expansion portion of the flow contour consists of 12 flat segments that are interleaved to facilitate area adjustment of the operational nozzles. Unlike well designed contoured CD nozzles, imperfections at the nozzle exit plane result in a plume with weak shock cells, even at perfectly balanced pressure conditions.

The chevron configurations were designed and provided partly by General Electric Aviation and partly by NASA Glenn Research Center. From a large pool of possible chevron choices three designs were chosen, for three different Mach number nozzles. These are summarized in Table 15 in terms of the non-dimensional chevron parameters: penetration, length and width. The chevrons extend from the nozzle exit plane of the baseline nozzles with one chevron per facet (totaling 12). These are shown schematically in Figure 119. In the study of supersonic jets, the nozzle exit diameter is commonly used to normalize the length of shock cells and jets' downstream locations. As noted earlier and in Table 15, the nozzle referred to as $M_d = 1$ was a purely contoured converging, axisymmetric nozzle whose 8 chevrons had no penetration at all. Table 15 also includes the corresponding properties of the NASA nozzles used in their chevron experiments, the results of which are used in our general comparisons.

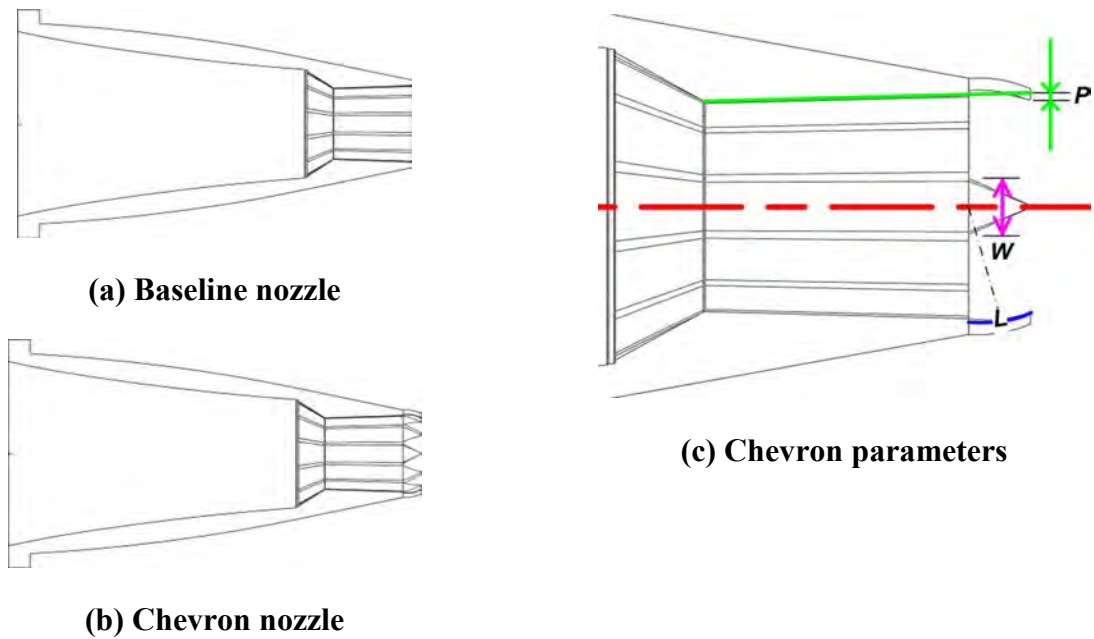


Figure 119. Schematic of military-style nozzle. a) Baseline nozzle. b) Chevron nozzle. c) Definition of chevron parameters⁴⁰

Table 15. Nozzle parameters and jet operation conditions for data shown in figures.

	Nozzle Parameters						Jet Operation Conditions		Fig. No.
	M_d	D (inch)	Chevron Counts	Penetration	Length	Width	M_j / TTR	$Re \times 10^{-6}$	
Penn State	1.0	1	8	0	0.25 D	0.4 D	1.5 / 1	1.5	4
	1.5	0.676	12	0.05 D	0.23 D	0.2 D	1.64 / 1	1.2	9
							1.64 / 3	0.7	11
	1.65	0.708	12	0.12 D	0.35 D	0.2 D	1.47 / 1	0.9	12
NASA GRC							1.47 / 3	0.5	13
	1.5	4.84					1.64 / 1	8.5	8
							1.64 / 3	2.1	10
	1.65	5.07		Baseline nozzle			1.47 / 1	6.6	17 a)
							1.47 / 3	1.7	17 b)
	1.65	5.07	12	0.12 D	0.35 D	0.2 D	1.47 / 3	1.7	14
Parameter range of chevrons used at NASA GRC				0.06 D	0.15 D	0.12 D			
				0.12 D	0.35 D	0.2 D			

Experimental results

Converging chevron nozzle with chevrons possessing no penetration

The major effect of chevrons on a jet flow is the generation of counter-rotating pairs of streamwise vortices. For a chevron nozzle to induce these streamwise vortices effectively there needs to be a favorable pressure gradient between the core of the jet and the ambient flow. More precisely, it has been shown experimentally that a significant pressure gradient must exist between the outer and inner side of the chevron to effectively produce these streamwise vortices. A series of measurements have been performed at NASA Glenn^{43,117} with a converging nozzle with chevrons designed for various penetration angles. These experimental data show that nozzles with chevrons at no penetration angle fail to generate the desired vortices in subsonic jets, resulting in no substantial difference in the acoustic measurements when compared to the baseline nozzle, with no chevrons. Similar acoustic measurements were conducted at Penn State in the scope of this study with two nozzles: one purely converging 2.54 cm (1") in diameter, and another with the same inner contours and 8 chevrons shaped in the nozzle exit, resulting in chevrons with no penetration. Acoustic measurements (not shown) performed with cold sonic ($M_j = 1.0$) jets exhausting from both these nozzles showed no acoustic difference, in line with the NASA results. Under-expanded jets, however, are bound to exhibit a significant pressure gradient at the nozzle exit, which should result in significant production of streamwise vortices, and therefore in noise reduction. Acoustic spectra were therefore measured at a range of polar angles for this nozzle operated in an under-expanded cold jet condition (with $M_j = 1.5$), with and without zero penetration chevrons. The resulting comparison is shown in Figure 120 for a representative number of polar angles. Focusing first on the large scale turbulence mixing noise, there is a very clear noise reduction measured with the chevrons, when compared to the baseline nozzle. As much as 2 dB reduction can be observed in the peak noise direction (around 30°) across the entire frequency range. This is in accordance with an enhanced mixing of the jet, resulting in a break-up of the largest structures. This mixing noise reduction corresponds to an enhanced mixing with the surrounding air, as can also be observed from the Schlieren images in Figure 121. Indeed, the jet spreading angle is clearly enhanced with the chevron nozzle, with obviously some differences between the tip and the valley plane of the chevrons which coincides with the larger overall noise reduction along that plane. Since the jets are strongly under-expanded, shock associated noise is also present in the spectra (and the shock cells are clearly visible in the schlieren images).

Screech tones appear in the acoustic measurements from both nozzles. The second mode of screech, dominates the sideline direction, and first mode of screech, dominates the upstream direction, with a similar trend in the measurements from both nozzles. The peak screech frequency is slightly higher for the measurements with the chevron nozzle, suggesting a slight shrinking of the shock cells. This can be confirmed by the schlieren visualization, which shows that the shock length is reduced from 1.66 D to 1.34 D between the baseline nozzle and the chevron configuration. A similar trend can be observed for the peak frequency of broadband shock-associated noise (BBSAN): it shifts to higher values for the chevron nozzle. The magnitude of BBSAN is also reduced substantially for the measurements with the chevron nozzle, suggesting that the shock strength has been reduced (which correspond to shallower angles of the oblique shocks and therefore smaller shock cells). Overall, when examining the

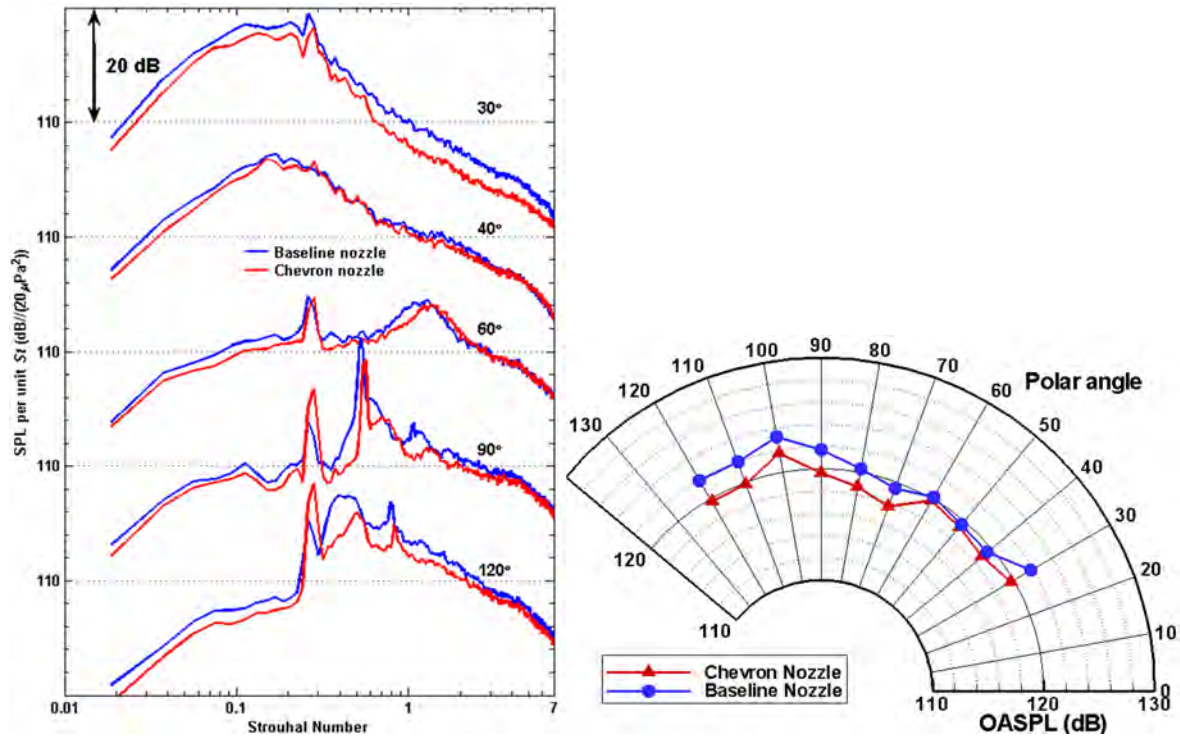


Figure 120. Acoustic spectra for a $M_d = 1.0$ nozzle and chevron nozzle, operating at $M_j = 1.5$, cold, scaled to R/D 100.

OASPL values from both of these nozzles, shown in Figure 120, the 2 dB noise reduction already observed at the peak noise emission on the sound pressure level can be generalized to the OASPL reduction across all polar angles.

These simple measurements demonstrate that while the penetration angle of the chevrons is indeed important to ensure they result in a reduced emitted noise, the nozzle operating condition is equally important. The outflow from the nozzle lip can have an outward orientation (for under-expanded jets), resulting in an increased effective penetration of the chevron, and therefore enhanced mixing and noise reduction.

Military-style CD chevron nozzle with chevrons possessing low penetration

Most nozzles are operated off-design, with a Nozzle Pressure Ratio that leads to a free-jet Mach number M_j different from the nozzle design Mach number M_d . Depending on the off-balance condition, three classes of jets are possible: over-expanded, under-expanded, and highly under-expanded jets. In practical applications, jets are never fully expanded, even though this condition is achievable in laboratories with careful design of the nozzles and control of the NPR. Unbalanced jets typically exhibit strong pressure gradients at the exit plane of the nozzle, that lead to flow field structures different from a simple conical jet. The appearance of shock cells has a strong influence, not only on the acoustic signature of the jet, but also on the physical shape of the jet flow. Even with a simplified convergent-divergent (CD) nozzle, the shape of the jet

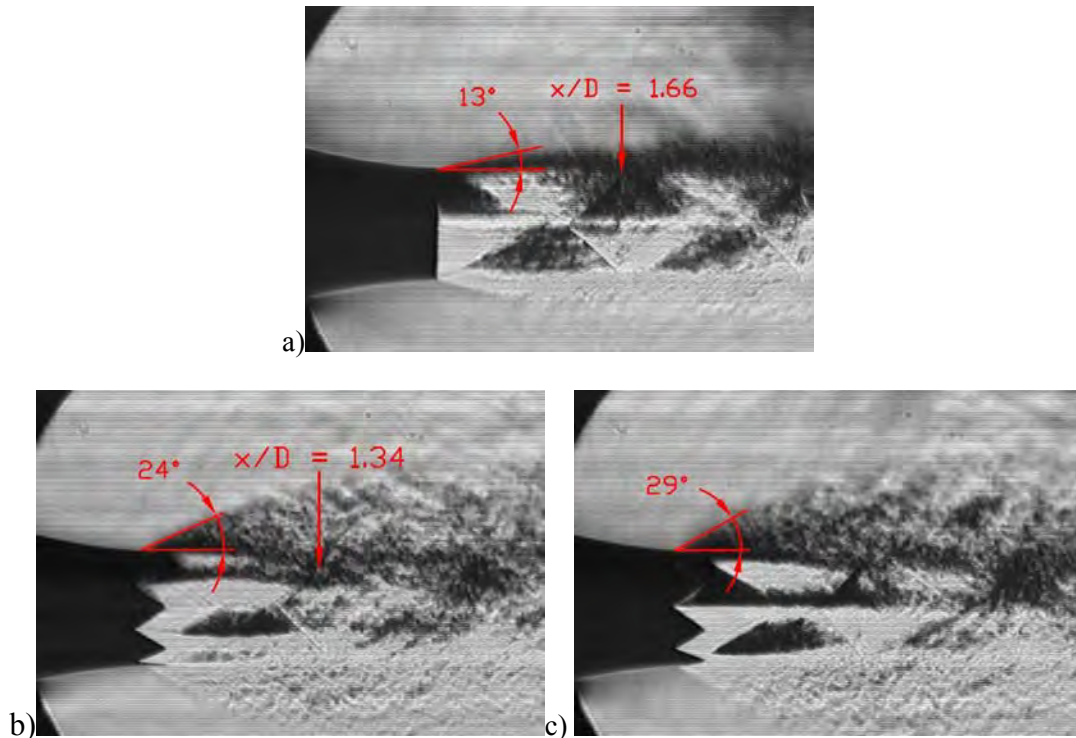


Figure 121. Schlieren visualization from the measurements operated at $M_j = 1.5$, cold jets respectively conducted with $M_d = 1.0$ nozzle. a) Baseline nozzle. b) Chevron nozzle measured at tip plane. c) Chevron nozzle measured at notch plane.

mixing layer is altered significantly with varying operating conditions, and this can in turn affect the performance of chevrons on the flow. To illustrate this, Figure 122 presents schlieren images visualized with the military-style nozzle possessing a design Mach number of 1.5 operated at $M_j = 1.3, 1.5, 1.7$, and 1.9 , respectively. As one can see the supersonic jet mixing layer at the nozzle exit is slightly altered from inward at $M_j = 1.3$ to parallel to the jet centerline at $M_j = 1.5$. The mixing layer exhibits a clear barrel shape as the jet operating condition is raised above the designed nozzle condition. Therefore, for a nozzle with chevrons, of a specific penetration angle, the effective penetration of the chevrons in the flow will depend on the jet operating condition. A specific chevron design may therefore be more or less efficient at producing the best acoustic benefit during various flight regimes. For a representative visualization of the **over-expanded jets**, Figure 123 shows schlieren visualizations obtained with the military-style baseline nozzle and the chevron nozzle operated at $M_j = 1.3$ (an over-expanded jet condition). The expected effect of excess jet spreading, described in the previous section, is not visible: the chevrons do not provide the enhanced mixing they were designed to. The chevrons on this nozzle are of low penetration in comparison with the range of penetrations defined by Henderson and Bridges. A higher penetration would undoubtedly affect the jet flow and subsequently have a measurable effect on the jet noise. However, this highlights the fact that not one chevron design will provide an optimal noise benefit at all operating conditions. This should be kept in mind before recommending one specific design.

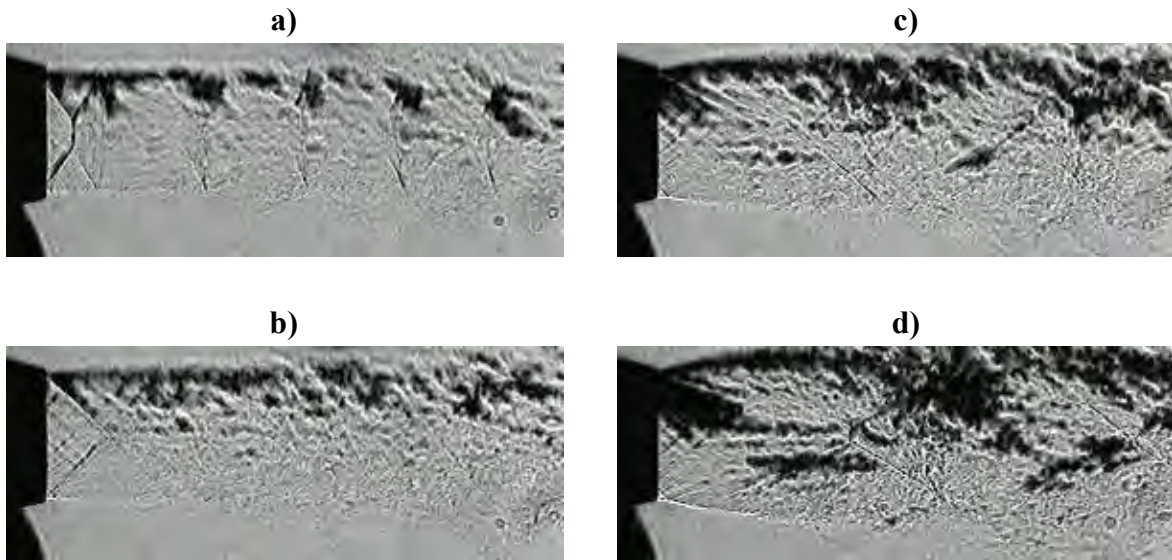


Figure 122. Schlieren images obtained with GE M_d 1.5 baseline nozzles respectively operated unheated with M_j at a) 1.3. b) 1.5. c) 1.7. d) 1.9.

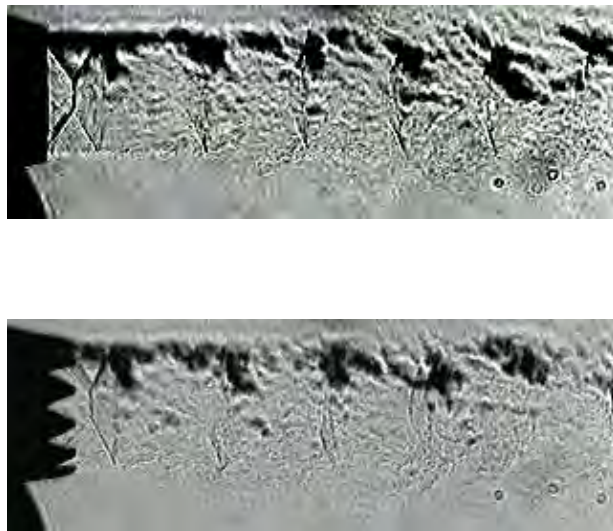


Figure 123. Schlieren images obtained with GE M_d 1.5 baseline nozzle and chevron nozzle operated at $M_j = 1.3$, cold.

Under-expanded supersonic jets

Reasonable success with the chevrons was achieved with the same $M_d = 1.5$ GE nozzle with the chevrons with low penetration angle, this time operating at the **under-expanded** jet Mach number of $M_j = 1.64$. **Figure 124** first shows the spectral comparison from the measurements conducted with small scale baseline nozzle ($D = 0.7''$) at Penn State and moderate scale baseline nozzle ($D = 4.8''$) at NASA GRC (both with no chevrons). This comparison demonstrates the capability of the acoustic measurements conducted in small scale supersonic jets at Penn State to replicate similar measurements at moderate (NASA) scale. How well the small scale jets replicate the moderate scale jets with chevrons is yet to be demonstrated. Spectra recorded at a range of polar angles are shown in Figure 125, with direct comparison between the small scale chevron nozzle jet and the baseline identical nozzle jet (without chevrons). Figure 125 presents spectra recorded with pure air cold $M_j = 1.64$ jet and they show substantial levels of noise reduction. Most of the noise reduction is experienced in the downstream arc, in the maximum noise emission direction. That is consistent with the observations from the last section, with noise reductions being dominant for the large scale turbulence noise part of the generated sound. The BBSAN also follows the same trend as previously observed: there is a shift in the peak BBSAN frequency to higher frequencies with the chevron configuration, as well as a decrease in amplitude. This suggests smaller shock cells and weaker shocks, and results in a noise reduction on the sideline. Overall, the OASPL noise reduction varies from 2 to 4 dB across the polar angle range measured. At this point it appears that the small scale chevron nozzle experiments produce noise reductions that are comparable to those measured by Henderson and Bridges at NASA. These comparisons were made with cold jets; we now turn to the more important hot jet cases.

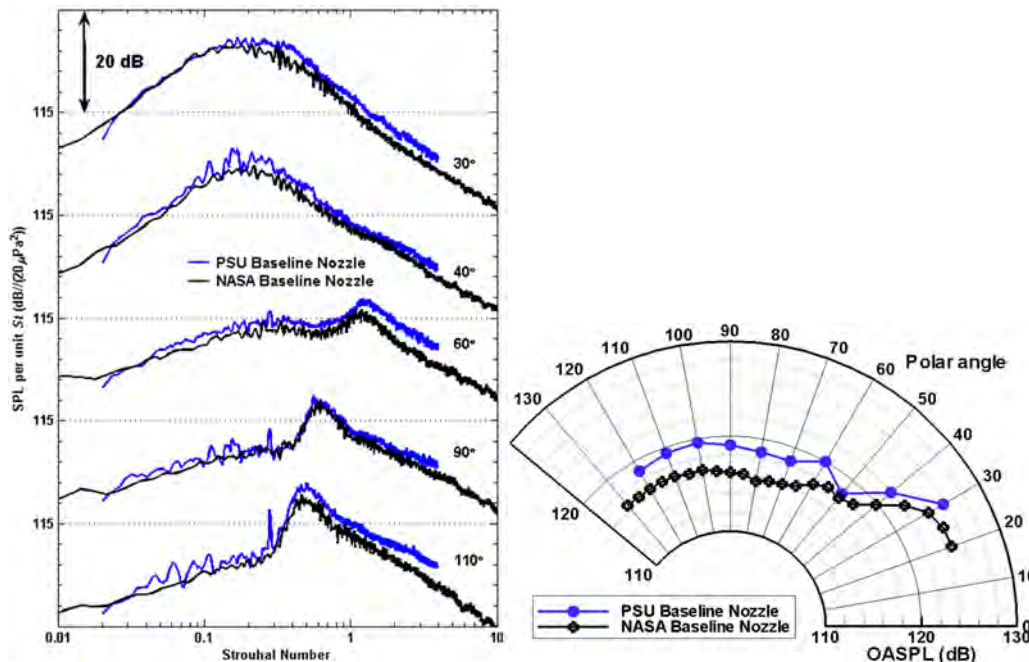


Figure 124. Spectra comparison from the measurements conducted with GE M_d 1.5 baseline nozzle at Penn State and NASA GRC⁴⁰ both operated under-expanded at M_j 1.64, TTR = 1.

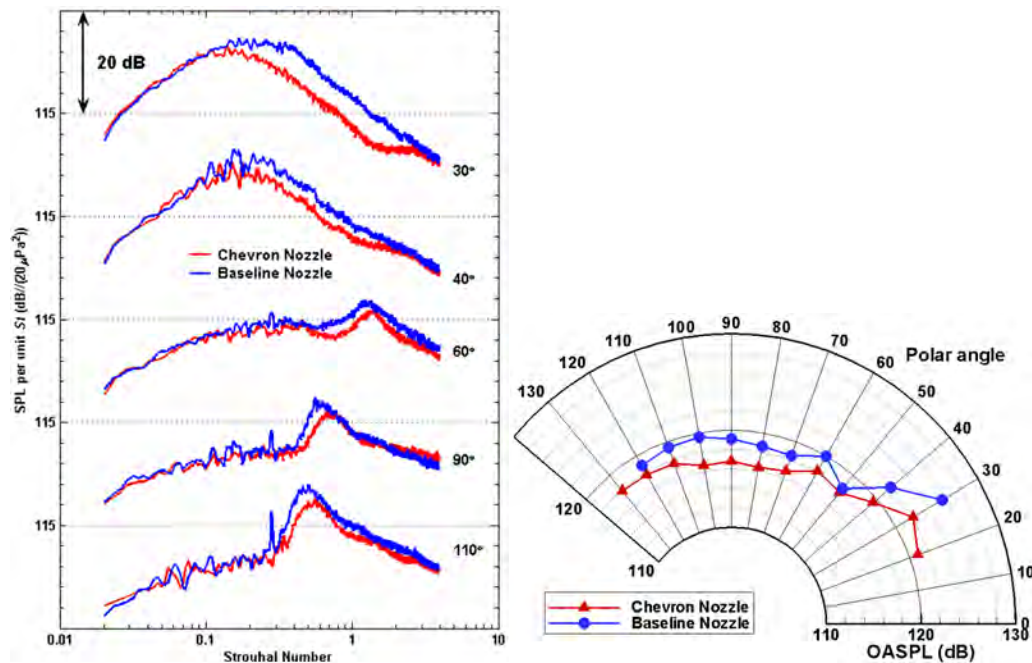


Figure 125. Acoustic spectra and OASPL from the measurements conducted with GE M_d 1.5 baseline and chevron nozzles operated under-expanded at M_j 1.64, $TTR = 1$.

Figure 126 shows a similar spectral comparison of data recorded at the same conditions as the data of Figure 124 except the jet is operated with a total temperature ratio of $TTR = 3.0$, where a helium-air mixture was used at Penn State and actual heated air was used at NASA GRC. Reasonable agreement is reached between the acoustic measurements obtained from both facilities. A systematic discrepancy in which the small scale jets are typically a couple of dB louder in the low frequency range has been previously identified, with a suspected cause attributed to low Reynolds number operation. Figure 127 then shows the spectral comparison of the measurements conducted with the baseline and chevron nozzle in small scale jets. Under this condition, the noise reduction associated with the low penetration chevrons is noticeably less, with maximum levels of about 1.5 dB in the maximum noise emission direction. No perceivable benefit is observed in the sideline direction. Since heat (and helium) affects the jet mixing layer by making it thicker, it is understandable that the increased mixing provided by the chevrons has less effect. Similarly, the BBSAN component is much less dominant in a heated jet on the sideline, due to 1) the increased level of the turbulence mixing noise (caused by a higher jet acoustic Mach number), and 2) the increased mixing layer thickness that weakens the shock cell strength. Therefore, the previously observed shift of the BBSAN frequency and decrease in amplitude is much less apparent and has no effect on the OASPL.

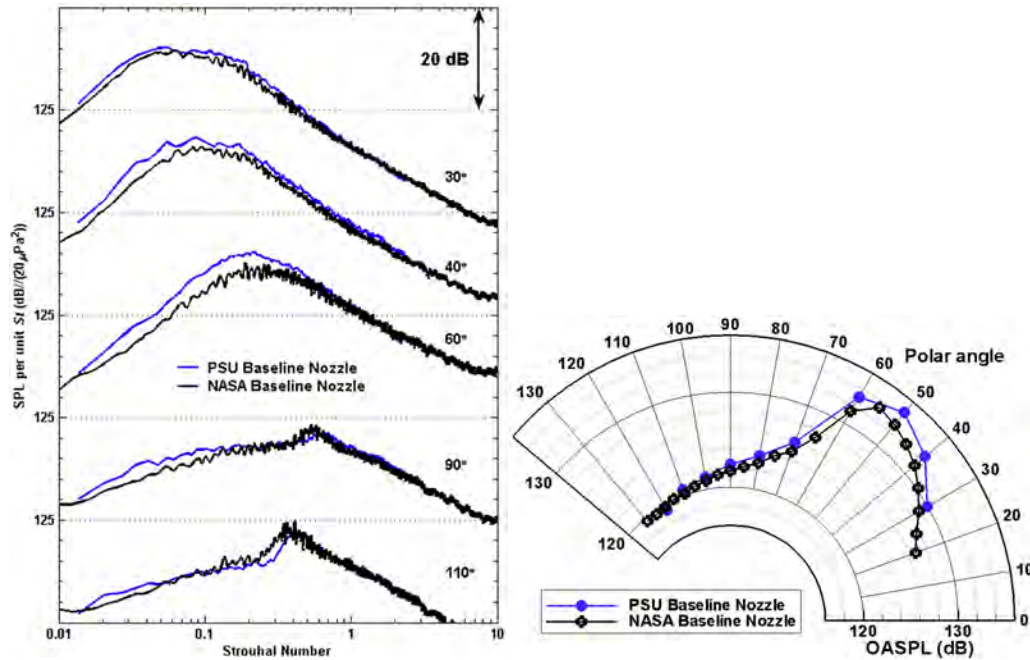


Figure 126. Spectra comparison from the measurements conducted with GE M_d 1.5 baseline nozzle at Penn State and NASA GRC⁴⁰ both operated under-expanded at M_j 1.64, TTR = 3.

Military-style CD chevron nozzle with chevrons possessing high penetration

Following the experience obtained with the two chevron jet experiments described in the previous sections, a new nozzle was designed and fabricated with chevrons whose parameters matched the highest values used in the NASA GRC experiments. The intention was to operate this $M_d = 1.65$ nozzle in an over-expanded condition, with a jet exit Mach number $M_j = 1.47$ and an effective jet diameter smaller than the nozzle exit diameter. This operating condition is of particular interest since it is representative of take-off conditions (at sea level pressures), during which the jet flow experiences its highest back pressure. Hence in order to affect the flow, long high penetration chevrons are required. The goal of this measurement is to demonstrate the capability of chevrons to provide noise reduction in small scale heat simulated supersonic jets operating in **over-expanded conditions**. As a first step, spectra measured from cold jets issuing from this chevron nozzle and the baseline nozzle are shown in Figure 128. As seen from this figure, there is a noise reduction of approximately 2 dB in the maximum noise emission direction, confirming the ability of the chevrons to affect the jet flow. These values are *approximately* comparable to levels obtained in moderate (NASA) size jet facility experiments. While there is noise reduction of large scale mixing noise, no reduction in the sideline direction is visible. However, the BBSAN component of the spectra shifts to higher frequency values, suggesting a similar shortening of the shock cell structures as previously observed.

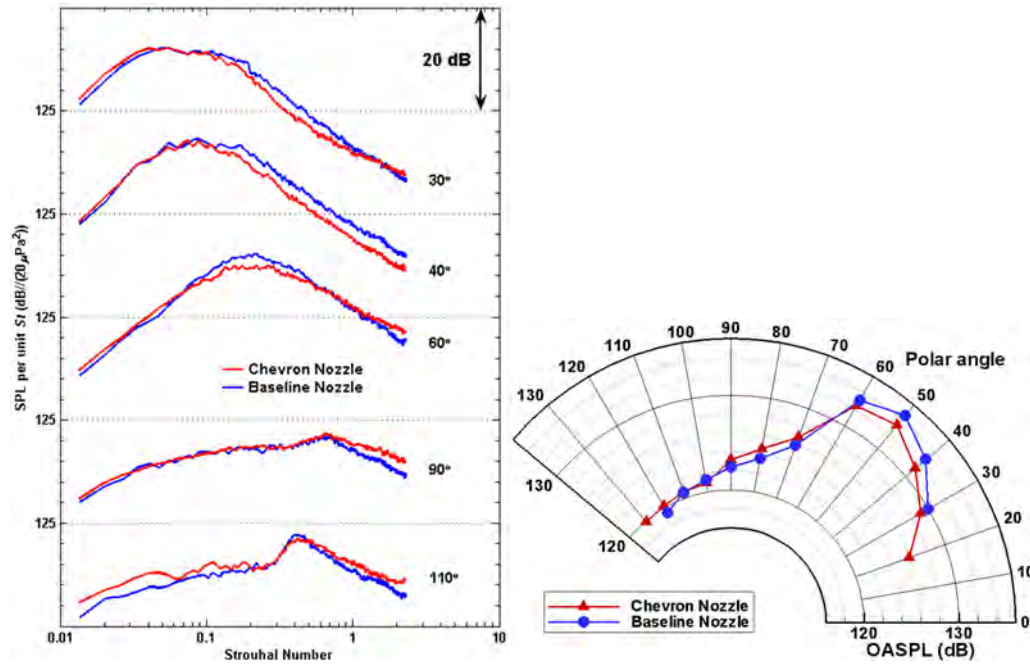


Figure 127. Acoustic spectra and OASPL from the measurements conducted with GE M_d 1.5 baseline and chevron nozzles operated under-expanded at M_j 1.64, $TTR = 3$.

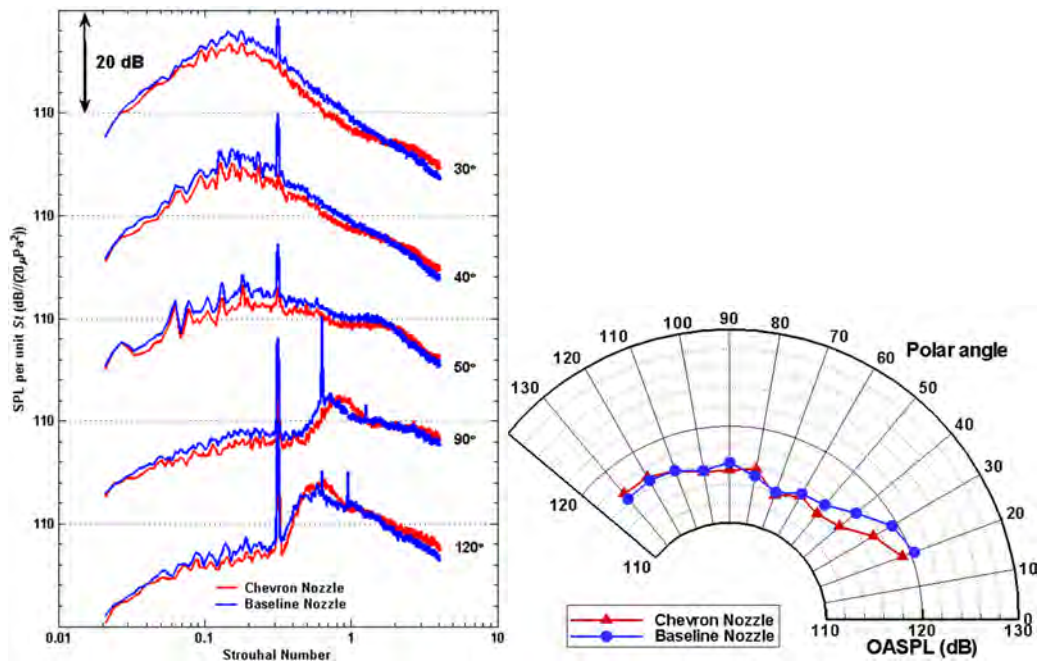


Figure 128. Acoustic spectra and OASPL from the measurements conducted with GE M_d 1.65 baseline and chevron nozzles operated at M_j 1.47, $TTR = 1$.

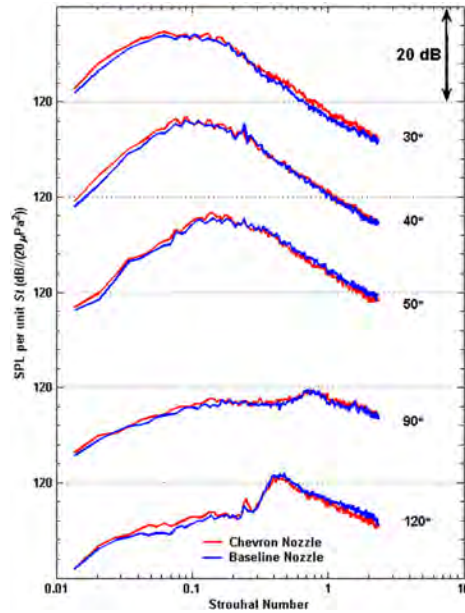


Figure 129. Acoustic measurements conducted with GE Md 1.65 baseline and chevron nozzles operated at $M_j = 1.47$, $TTR = 3$.

Turning to the simulated hot jet experiments, Figure 129 presents a group of spectral data recorded with the helium-air jets at the otherwise same conditions as the data in Figure 128. This time the effects of the chevrons on the noise spectra are **imperceptible**, and this is the most important operating condition in this study. For comparison, data measured by NASA GRC with an “identical” $M_d = 1.65$ chevron nozzle (with an exit diameter of $D_e = 12.88$ cm, 5.07 in) are presented in Figure 130. These larger scale data show a very large effect of the chevrons, with reduction of the peak noise amplitude by about 5dB, a shift of the BBSAN peak to higher frequencies. Even though these moderate scale data were obtained with a surrounding flow simulating the plane forward flight, similar effects of the chevrons are expected without the forward flight. This result is contradictory to the observations from the small scale experiments. The cause cannot be attributed to the heat simulation with helium-air, which has previously been validated; therefore more attention needs to be paid at the details of the experimental conditions.

The Reynolds number of the jet operating at the simulated heated jet condition of the data of Figure 129 is approximately 539,000 which compares to the value $Re = 1,677,000$ for the NASA experiment and to $Re = 922,000$ of the cold jet experiment (Figure 128). It is hypothesized that the first lowest value is low enough to sustain an annular laminar boundary layer in the nozzle that is more sensitive to separation than is a turbulent boundary layer. In the over-expanded condition it is likely that the adverse pressure gradient at the exit is separating the boundary layer to the point that the chevrons have an imperceptible effect on the flow, and the subsequent noise reduction. Papamoschou & Zill¹¹⁹ have clarified the shock formation inside the nozzle when the boundary layer separates from the nozzle surface when the supersonic nozzle operating in the over-expanded condition. While there is an issue of the Reynolds number, the location of the flow separation inside the nozzle therefore affects the efficiency of the chevrons.

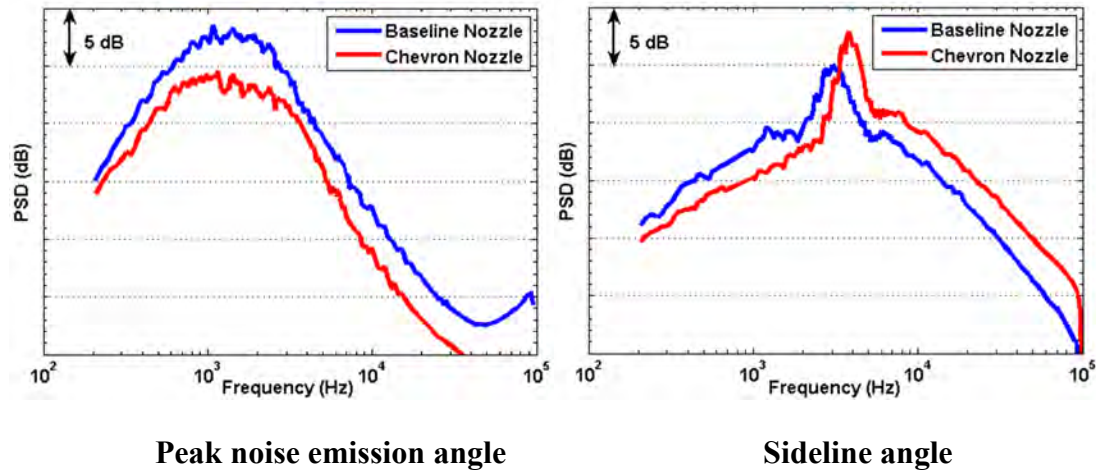


Figure 130. Acoustic measurements conducted with GE M_d 1.65 baseline and chevron nozzles under forward flight simulation with $M_f = 0.3$ operated at same conditions as Fig. 13 by NASA GRC⁴⁰ with a jet of exit diameter 5.07”.

Fortunately there is a quite easy test of the hypothesis discussed above. An alternate method of rapid prototyping uses fused deposition modeling with ABS plastic. This method produces a nozzle that meets the geometric requirements but has a noticeably rougher surface. The disturbances introduced into the boundary layer flow have the potential to trip the flow to transition to turbulence, or at least introduce enough disturbances to delay separation. In the case of the chevron nozzle this would permit the chevrons to penetrate enough of the high speed flow to alter the downstream flow and provide some noise reduction. A schematic of the flow separation with the laminar and turbulent boundary layers respectively is shown in Figure 131 to help visualize the situation occurring in the small scale jets. Figure 132 first presents acoustic data measured with both the ABS rough baseline nozzle and the SLA smooth baseline nozzle. The nozzle designs were both the GE $M_d = 1.65$ type, and the operating condition for both was $M_j = 1.47$, $TTR = 1.0$ and 3.0 . It is clearly seen that the roughness effect does not significantly alter the measurements in the cold and heated jets with no chevrons. This is in line with results from Bradbury and Khadem who have demonstrated that there is no significant effect in the round jet acoustic measurements due to the boundary layer thickness variation. The variation of the turbulence intensity level at the nozzle exit needs to be at least 20 % of the amount at the end of the potential core to significantly affect the experimental results.

Figure 133 presents the spectral comparison between the **small scale and moderate scale jets** at the same operating condition shown in Figure 132. Good matching is shown in the cold jet case and reasonable agreement is reached in heated jet case. This again validates the capability and accuracy of the acoustic measurements operated in the small scale supersonic jets at Penn State. Figure 134 then presents acoustic data measured with both the ABS rough nozzle and the SLA smooth nozzle both with the high penetration chevrons. In the cold jet case, where the Reynolds number is around 922,000, it can be seen that both nozzles result in the same amount of noise reduction. However, in the heated jet case, where the Reynolds number is reduced to around 539,000, discrepancies emerge in the noise benefits of the chevrons.

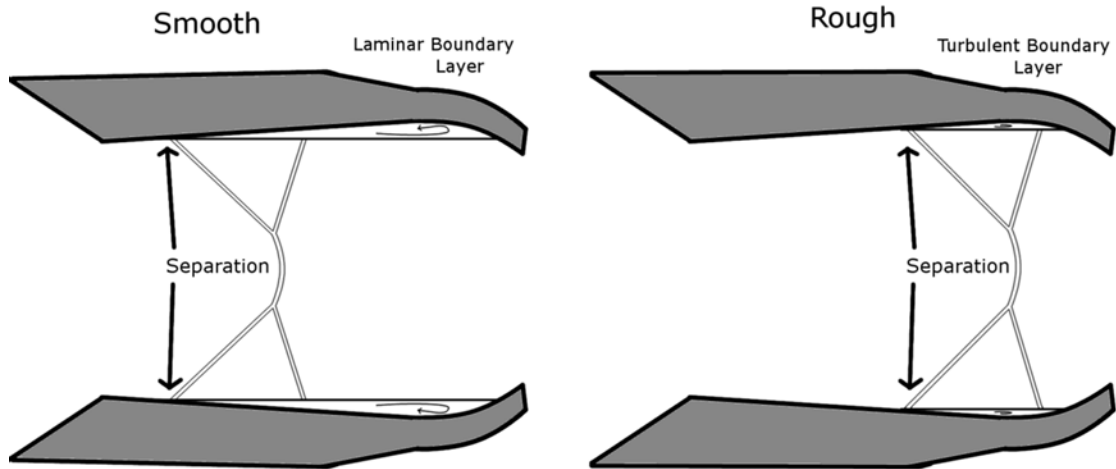


Figure 131. Schematic of the hypothesized flow separation respectively in the laminar boundary layer given by the smooth nozzle and turbulent boundary layer given by the rough nozzle in the small scale jets.

Figure 135 shows the noise reduction level from the measurements conducted with rough baseline nozzle and rough chevron nozzle both operated at $M_j = 1.47$, $TTR = 3.0$. The observed noise reduction level is somewhat less than the one observed in the moderate scale jets but it is definitely present. More detailed examination is necessary to exactly evaluate the noise reduction level from the measurements conducted with small scale jets and moderate scale jets, including some direct comparisons with moderate scale chevron nozzles. However, a preliminary conclusion is that small scale chevron nozzle experiments with high temperature ratio jets may fail to accurately represent the noise reduction potential of jets of practical size.

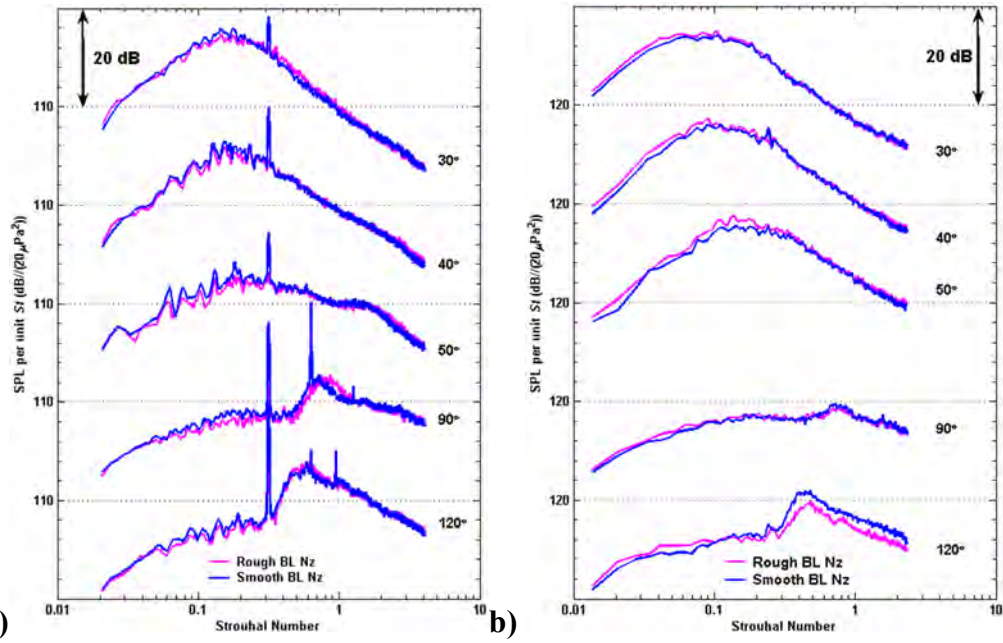


Figure 132. Acoustic spectra from the measurements conducted with GE M_d 1.65 baseline nozzles (rough and smooth) operated at $M_j = 1.47$ with a) TTR = 1. b) TTR = 3.

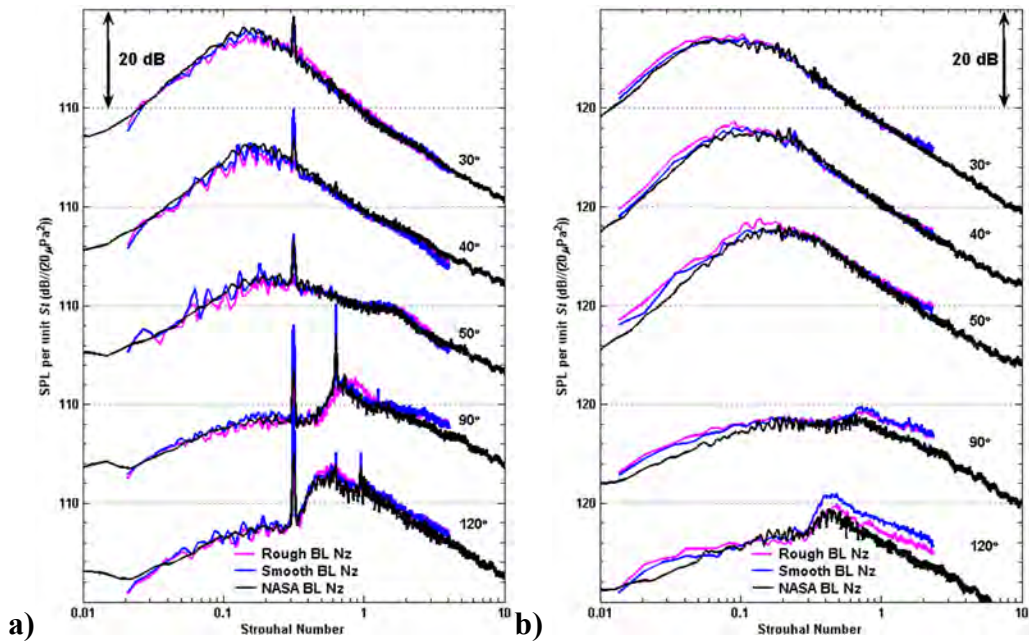


Figure 133. Acoustic spectra from the measurements conducted with GE M_d 1.65 baseline nozzles at NASA GRC⁴³ and PSU with rough and smooth baseline nozzles operated at $M_j = 1.47$ with a) TTR = 1. b) TTR = 3.

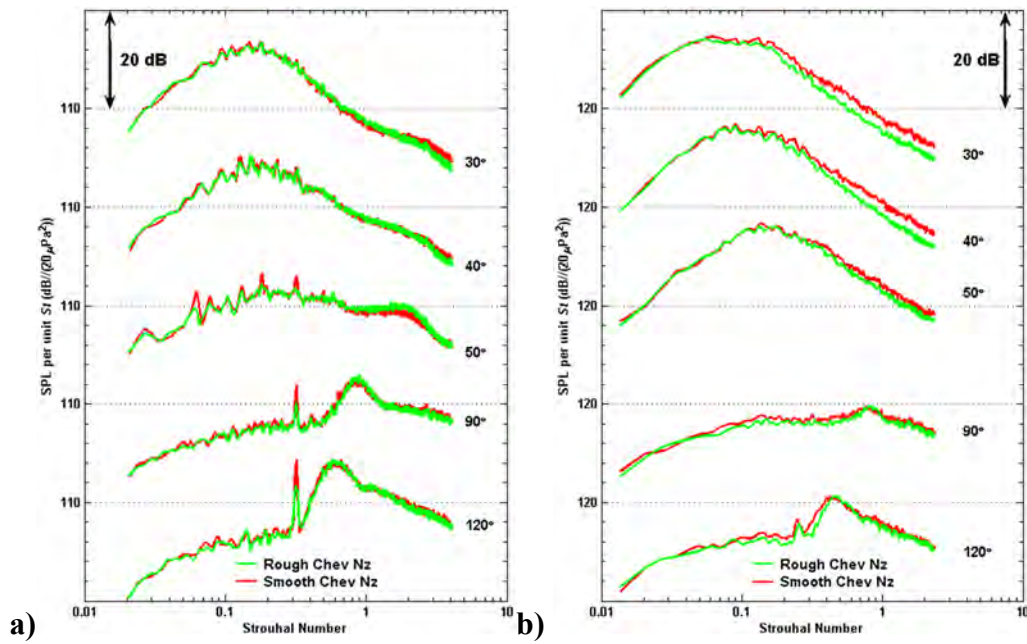


Figure 135. Acoustic spectra from the measurements conducted with GE M_d 1.65 chevron nozzles (rough and smooth) operated at $M_j = 1.47$ with a) TTR = 1. b) TTR = 3.

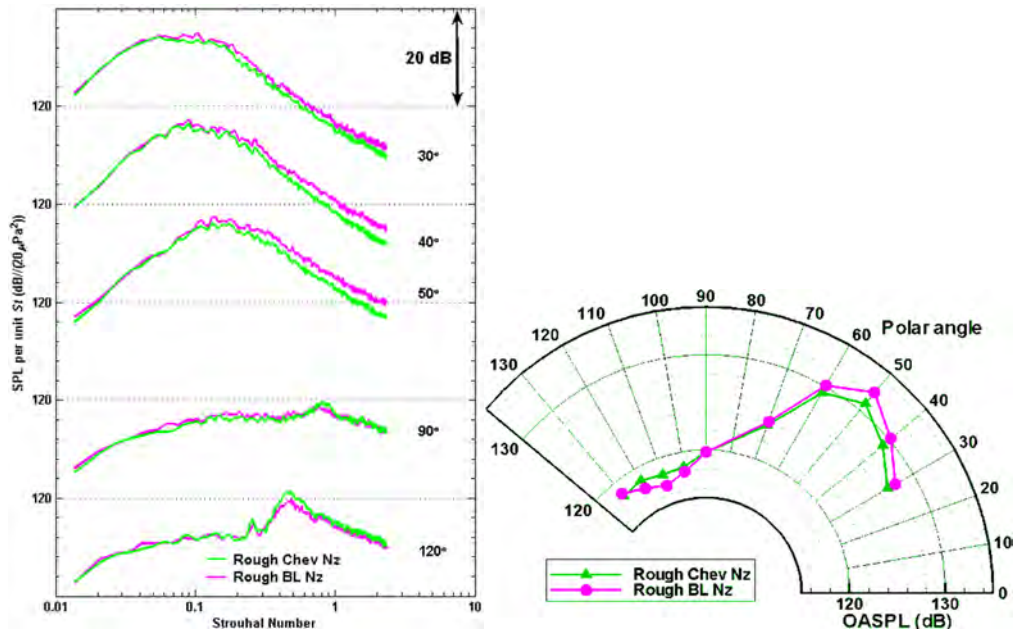


Figure 134. Acoustic spectra and OASPL from the measurements conducted with GE M_d 1.65 baseline and chevron nozzles (both rough) operated at $M_j = 1.47$ with TTR = 3.

11. Summary and Conclusions

a) Background

The intense noise generated by high performance military fighter aircraft has a significant impact on communities near airbases as well as ground crews. This can impact basing decisions in addition to operations and training requirements. Prior to the initiation of this project relatively little attention had been paid to the fundamental noise generation mechanisms of high performance supersonic military aircraft, or to methods for source noise reduction. This project has addressed this need.

b) Initial Project Objectives

- To identify and test promising noise reduction concepts for military aircraft engines, in low cost, scale-model experiments.
- To develop methodology for using data obtained from testing at small and moderate-scale, supported by computations, to reliably predict full scale engine noise.
- To develop a constrained optimization design methods that minimizes shock-associated noise through nozzle internal shaping.
- To assess installation effects on high performance military aircraft engine noise.
- To gain a fundamental understanding of the source mechanisms in military aircraft engines.
- To enhance an existing community noise prediction model.

c) Technical Approach and Results

This collaborative program conducted an ambitious array of experiments of military style moderate ($1/5$) and small ($1/25$) scale model exhaust jets, supplemented with advanced numerical simulations. Aeroacoustic experiments and computations were conducted for a wide range of flow conditions and nozzle geometries directly relevant to high performance supersonic aircraft. The initial outcome of these studies has been the development of an improved fundamental understanding of the noise radiation mechanisms that have provided directions for future noise reduction methods.

A second major focus was the development of a scaling methodology to assist in the prediction of noise radiated by larger scale nozzle exhaust jets, including full-scale engines. The approach was to perform experiments at two scale sizes ($1/5$ and $1/25$) and compare non-dimensional results for comparable geometries and flow conditions. The major result was to establish conditions under which the developed scaling methods work exceptionally well. In particular, the components of noise classified as large-scale structure noise, and broadband shock associated noise (BBSAN) were replicated very well at the two experimental scales.

Two promising noise reduction techniques were explored at the two experimental scales (small scale at Penn State and moderate scale at NASA). Chevrons with several geometric parameter variations and flow-field conditions were evaluated both experimentally and computationally. Since the flow in the vicinity of the chevrons is strongly Reynolds number dependent, the small scale experiments were not always capable of replicating the phenomena observed in the larger scale experiments. The reasons for these discrepancies were identified and this establishes a range under which small scale experiments should be interpreted with caution.

The small scale experiments were very successful in replicating the results and noise benefit of jet nozzles with beveled exit planes. The experiments demonstrated significant noise reduction with very little estimated thrust penalty. Further exploration of these nozzle concepts has formed a major position in future NASA experiments.

As a complement to the experimental studies, a numerical simulation methodology was developed. These large scale numerical computations were based on a solution of the short time-averaged equations of motion. The same nozzle geometries used in the experiments were replicated in the simulations. Comparisons between predictions for the baseline nozzles and experiment showed good agreement. In addition, a methodology to predict the effect of noise reduction devices – in particular chevrons – was developed. It is based on the Immersed Boundary Method. The results showed that this approach is capable of the efficient simulation of both the flow and noise from nozzles fitted with noise reduction devices.

An adjoint design method was also developed to automatically determine the optimum nozzle shape needed to achieve a desired pressure distribution inside the nozzle. Flow both with and without shocks were considered. This optimization approach has considerable potential for future use in aeroacoustic applications.

The major results of the laboratory experiments on the baseline nozzles and the chevron nozzles were compiled into file formats convenient for incorporation into the community noise model being upgraded by Wyle laboratories. The upgraded version of this model, now called the Advanced Acoustic Model (AAM), has more realistic non-round nozzle capability as well as the capability to include twin jets and nozzles with chevrons in its predictions. This new capability will play an important role in most environmental impact studies associated with new air bases and/or deployment of new aircraft types into existing bases.

d) Future Directions

The understanding of the fundamental physical processes responsible for noise generation in high performance military aircraft, as well as the experimental and computational techniques developed in the research program, have provided directions for ongoing activities in jet noise reduction. In addition, the limitations observed in the noise predictions have resulted in the development of additional numerical techniques for their improvement.

An examination of existing noise reduction methods, some of which were examined as part of the research study, indicated that they had limited potential. In addition, other noise reduction methods, such as the use of mechanical inserts into the diverging section of the nozzle, gave considerable performance penalties. This knowledge has shown a direction forward in jet noise reduction that is currently being pursued by the Principal Investigators under sponsorship from the US Navy and the Office of Naval Research. This work is also being pursued in cooperation with Lockheed-Martin Aeronautics Company and United Technologies Pratt & Whitney Division.

The basic idea is to use blowing in the divergent nozzle section to have an effect similar to the mechanical seal inserts but with the ability to change the effective nozzle area ratio and shape fluidically. It is anticipated that this concept will reduce both broadband shock-associated noise as well as the large-scale structure noise. The tools and methods developed in the present research program are being brought to be art to design, optimize, and

demonstrate this noise reduction concept. Experiments are being conducted at small scale in the Penn State High Speed Jet Acoustic Facility. Numerical simulations are also being conducted to provide insight into the experimental observations. Finally, adjoint design methods for boundary control are being used to optimize the nozzle and blowing design. Preliminary results are promising with some noise reductions already achieved and flow simulations of the internal nozzle flow with blowing helping to interpret the experimental observations.

12. References

1. Seiner, J.M., B.J. Jansen, B.J., and Ukeiley, L.S., “Acoustic Fly-Over Studies of F/A-18E/F Aircraft During FCLP Mission,” AIAA 2003-3330, 2003.
2. Bridges, J., and Brown, C., “Validation of the small hot jet acoustic rig for aeroacoustic research,” AIAA Paper No. 2005-2846, 2005.
3. Doty, M. J., and McLaughlin, D. K., “Acoustic and mean flow measurements of high-speed, helium-air mixture jets,” *International Journal of Aeroacoustics*, **2**(2), 2003, pp. 293–334.
4. Papamoschou, D., “Acoustic simulation of coaxial hot air jets using cold helium–air mixture jets,” *Journal of Propulsion and Power*, **23**(2), 2007, pp. 375-181.
5. Kuo, C.-W., Veltin, J., and McLaughlin, D. K., “Acoustic measurements of models of military style supersonic nozzle jets,” AIAA Paper No. 2009-18, 2009.
6. Kuo, C.-W., Veltin, J., and McLaughlin, D. K., “Methods to improve the accuracy of acoustic measurements in small scale high speed jets,” AIAA Paper No. 2009-3251, 2009.
7. McLaughlin, D. K., Bridges, J., and Kuo, C.-W., “On the scaling of small, heat simulated jet noise measurements to moderate size exhaust jets,” *International Journal of Aeroacoustics*, **9**(4&5), 2010, pp. 627-654.
8. Lee, S. S., and Bridges, J., “Phased-array measurements of single flow hot jets,” AIAA Paper No. 2005-2842, 2005.
9. McLaughlin, D. K., Kuo, C.-W., and Papamoschou, D., “Experiments on the effect of ground reflections on supersonic jet noise,” AIAA Paper No. 2008-0022, 2008.
10. Papamoschou, D., and Debiase, M., “Noise measurements in supersonic jets treated with the Mach wave elimination method,” *AIAA Journal*, **37**(2), 1999, pp. 154-160.
11. Koch, L. D., Bridges, J., Brown, C., and Kavarano, A., “Experimental and analytical determination of the geometric far field for round jets,” *Noise Control Engineering Journal*, **53**(1), 2005, pp.20–28.
12. Viswanathan, K., “Instrumentation considerations for accurate jet noise measurements,” *AIAA Journal*, **44**(6), 2006, pp. 1137-1149.
13. Tanna, H. K., “An experimental study of jet noise Part I: Turbulent mixing noise,” *Journal of Sound and Vibration*, Vol. 50, No. 3, 1977, pp. 405–428.

14. Seiner, J. M. and Ponton, M. K., "Aeroacoustic data for high Reynolds number supersonic axisymmetric jets," NASA TM 86296, 1985.
15. Bridges, J., "Measurements of turbulent flow field in separate flow nozzles with enhanced mixing devices-Test report," NASA TM-2002-211366, 2002.
16. Nagamatsu, H. T., Sheer, R. E., and Horvay, G., "Supersonic jet noise theory and experiments," Basic aerodynamic noise research NASA SP-207, Washington, D. C., July 14-15, 1969.
17. Chu, W. T., Laufer, J., and Kao, K., "Noise source distribution in subsonic jets," International Conference on Noise Control Engineering, Washington D.C., Oct 4-6, 1972.
18. Grosche, F. -R., "Distributions of sound source intensities in subsonic and supersonic jets," AGARD-CP-131, 1974, pp. 4.1-4.10.
19. Laufer, J., Schlinker, R., and Kaplan, R. E. "Experiments on Supersonic Jet Noise," *AIAA Journal*, 4(4), 1976, pp. 489-497.
20. Papamoschou, D., and Dadvar, A., "Localization of multiple types of jet noise sources," AIAA Paper No. 2006-2644, 2006.
21. Dougherty, R. P., and Podboy, G. G., "Improved phased array imaging of a model jet," AIAA Paper No. 2009-3186, 2009.
22. Tester, B. J., Morris, P. J., Lau, J. C., and Tanna, H. K., "The generation, radiation, and prediction of supersonic jets noise," AFAPL-TR-78-85, Vol. 1, 1978.
23. Potter, R. C., "Jet-orifice-surface interaction noise," Basic aerodynamic noise research NASA SP-207, Washington, D. C., July 14-15, 1969.
24. Bishop, K. A., Ffowcs Williams, J. E., and Smith, W., "On the noise source of the unsuppressed high-speed jet," *J. Fluid Mech.*, **50**, 1971, pp. 21-31.
25. MacGregor, G. R., and Simcox, C. D., "The location of acoustic sources in jet flows by means of the 'wall isolation' technique," AIAA Paper No. 73-1041, 1973.
26. Harper-Bourne, M., "Jet noise turbulence measurements," AIAA Paper No. 2003-3214, 2003.
27. Kerhervé, F., Fitzpatrick, J., and Jordan, P., "The frequency dependence of jet turbulence for noise source modeling," *J. Sound Vib.*, **296**, 2006, pp. 209-225.

28. Morris P. J., and Zaman, K. B. M. Q., “Velocity measurements in jets with application to noise source modeling,” *J. Sound Vib.*, **329**, 2010, pp. 394-414.
29. Veltin J., McLaughlin, D.K., “Noise mechanisms investigation in shock containing screeching jets using optical deflectometry,” AIAA paper 2008-288, 2008.
30. Lau, J. C., Morris, P. J., and Fisher, M. J., “Measurements in subsonic and supersonic free jets using a laser velocimeter,” *J. Fluid Mech.*, **93**, 1979, pp. 1–27.
31. Petitjean, B. P., and McLaughlin, D. K., “Experiments on the nonlinear propagation of noise from supersonic jets,” AIAA Paper No. 2003-3127, 2003.
32. Howell, G. P., and Morfey, C. L., “Nonlinear propagation of broadband noise signals,” *J. Sound Vib.*, **114**(2), 1987, pp. 189–201.
33. Papamoschou, D., “Prediction of Jet Noise Shielding,” AIAA Paper 2010-0653, Jan. 2010.
34. Petitjean, B. P., Viswanathan, K., McLaughlin, D. K., and Morris, P. J., “Space-time correlation measurements in subsonic and supersonic jets using optical deflectometry,” AIAA Paper No. 2007-3613, 2007.
35. Goss, A. E., Veltin, J., Jaehyung, L., and McLaughlin, D. K., “Acoustic measurements of high-speed jets from rectangular nozzle with thrust vectoring,” *AIAA Journal*, **47**(9), 2009, pp. 1482-1490.
36. Kuo, C.-W., Veltin, J., and McLaughlin, D. K., “Advanced acoustic assessment of small-scale military-style nozzles with chevrons,” AIAA Paper No. 2010-3923, 2010.
37. Viswanathan, K. and Czech, M. J., “Adaptation of the beveled nozzle for high speed jet noise reduction,” *AIAA Journal*, **49**(5), 2011, pp. 932-944.
38. Settles, G.S., *Schlieren and Shadowgraph Techniques*, Springer-Verlag, New York, 2001.
39. Soeder, R. H., Wnuk, S. P., and Loew, R. “Aero-Acoustic Propulsion Laboratory Nozzle Acoustic Test Rig User Manual,” NASA/TM – 2006-212939, 2006.
40. Henderson, B. and Bridges, J. “An MDOE investigation of chevrons for supersonic jet noise reduction,” AIAA-2010-3926, 2010.
41. Ffowcs Williams, J. E. and Hawkings, D. L., “Sound generated by turbulence and surfaces in arbitrary motion,” *Philosophical Transactions of the Royal Society of London (A)*, **264**, 1969, pp. 321-342.

42. Callender, B., Gutmark, E., and Martens, S., "Far-field acoustic investigation into chevron nozzle mechanisms and trends," *AIAA Journal*, **43**(1), 2005, pp. 87-95.
43. Bridges, J. and Brown, C. A., "Parametric testing of chevrons on single flow hot jets," AIAA Paper 2004-2824, 2004.
44. Shur, M. L., Spalart, P. R., Strelets, M. K., and Garbaruk, A. V., "Further step in LES-based noise prediction for complex jets," AIAA Paper 2006-485, 2006.
45. Liu, J., Kailasanath, K., Ramamurti, R., Munday, D., Gutmark, E., and Lohner, R., "Large-eddy simulations of a supersonic jet and its near-field acoustics properties," *AIAA Journal*, **47**(8), 2009, pp. 1849-1864.
46. Uzun, A. and Hussaini, M. Y., "Simulation of Noise generation in near-nozzle region of a chevron nozzle jet," *AIAA Journal*, **47**(8), 2009, pp. 1793-1810.
47. Xia, H., Tucker, P. G., and Eastwood, S., "Large-eddy simulations of chevron jet flows with noise predictions," *International Journal of Heat and Fluid Flow*, **30**(6), 2009, pp. 1067-1079.
48. Kuo, C., "Extending acoustic data measured with small scale supersonic model jets to practical aircraft exhaust jets," Ph.D. thesis, The Pennsylvania State University, 2010.
49. Bridges, J., "PIV measurements of chevrons on F400-series tactical aircraft nozzle model," AIAA Paper 2011-1157, 2011.
50. Grinstein, F., "Recent progress on monotone integrated large eddy simulation of free jets," *JSME International Journal*, **49**(4), 2006, pp. 890-898.
51. Tam, C. K. W. and Webb, J. C., "Dispersion-relation-preserving finite difference schemes for computational aeroacoustics," *Journal of Computational Physics*, **107**(1), 1993, pp. 262-281.
52. Brentner, K. S. and Farassat, F., "Analytical comparison of the acoustic analogy and Kirchhoff formulation for moving surfaces," *AIAA Journal*, **36**(8), 1998, pp. 477-491.
53. Mittal, R. and Jaccarino, G., "Immersed boundary methods," *Annual Review of Fluid Mechanics*, **37**, 2005, pp. 239-261.
54. Mohd-Yusof, J., "Combined immersed-boundary/B-spline methods for simulations of flow in complex geometries," NASA TM-2007-214853, 2007.

55. Shur, M. L., Spalart, P. R., and Strelets, M. K., "LES-based evaluation of a microjet noise reduction concept in static and flight conditions," IUTAM Symposium on Computational Aeroacoustics for Aircraft Noise Prediction, 2010.
56. LaBozzetta, W. F., Gatzke, T. D., Ellison, S., Finfrock, G. P., and Fisher, M. S., "MACGS-towards the complete grid generation system." AIAA Paper 94-1923, 1994.
57. Dong, T. Z., "On boundary conditions for acoustic computations in non-uniform mean flows," *Journal of Computational Acoustics*, **5**(3), 1997, pp. 297-315.
58. Kim, J. W. and Lee, D. J., "Characteristic interface conditions for multiblock high-order computations on singular structured grid," *AIAA Journal*, **41**(12), 2003, pp. 104-129.
59. Veltin, J., "On the characterization of noise sources in supersonic shock-containing jets," Ph.D. thesis, The Pennsylvania State University, 2008.
60. Khalighi, Y., Ham, F., Moin, P., Lele, S. K., Colonius, T., Schlinker, R. H., Reba, R. A., and Simonich, J., "Unstructured large eddy simulation technology for prediction and control of jet noise," Proceedings of the ASME Turbo Expo 2010, Vol. 1, 2010, pp. 57-70, 2010.
61. Viswanathan, K., Shur, M., Spalart, P. R., and Strelets, M., "Comparisons between experiment and large-eddy simulation for jet noise," *AIAA Journal*, **45**(8), 2007, pp. 1952-1966.
62. Bogey, C., Marsden, O., and Bailly, C., "Large-eddy simulation of the flow and acoustic fields of a Reynolds number 10^5 subsonic jet with tripped exit boundary layers," *Physics of Fluids*, **23**(3), 2011, 035104.
63. Lui, C. and Lele, S. K., "A numerical investigation of broadband shock noise," AIAA Paper 2002-0074, 2002.
64. Lui, C. and Lele, S. K., "Sound generation mechanism of shock-associated noise," AIAA Paper 2003-3315, 2003.
65. Kerherve, F., Jordan, P., Gervais, Y., Valiere, J.-C., and Braud, P., "Two-point laser Doppler velocimetry measurements in a Mach 1.2 cold supersonic jet for statistical aeroacoustic source model," *Experiments in Fluids*, **37**, 2004, pp. 419-437.
66. Morris, P. J. and Zaman, K., "Velocity measurements in jets with application to noise source modeling," *Journal of Sound and Vibration*, **329**, 2010, pp. 394-414.
67. Morris, P. J., Boluriaan, S., Lilley, G. M., and Long, L. N., "Two-point cross correlations of turbulence and noise predictions: analysis and simulation," AIAA Paper 2002-0071, 2002.

68. Morris, P. J. and Miller, S. A. E., "Prediction of broadband shock-associated noise using Reynolds-averaged Navier-Stokes computational fluid dynamics," *AIAA Journal*, **48**(12), 2010, pp. 2931-2961.
69. Crow, S. C. and Champagne, F. H., "Orderly structure in jet turbulence," *Journal of Fluid Mechanics*, **48**, 1971, pp. 547-591.
70. Ahuja, K. K., Lepicovsky, J., Tam, C. K. W., Morris, P. J., and Burrin, R. H., "Tone excited jet: theory and experiments," NASA CR-3538, NASA, 1982.
71. Bodony, D. J. and Lele, S. K., "Current status of jet noise predictions using large-eddy simulation," *AIAA Journal*, **46**(2), 2008, pp. 364-380.
72. Jameson, A., "Aerodynamic design via control theory," *Journal of Scientific Computing*, **3**, 1988, pp. 233-260.
73. Jameson, A., "Optimum aerodynamic design using CFD and control theory," AIAA Paper 95-1729, 1995.
74. Jameson, A., "Optimum aerodynamic design using control theory," in: Hafez, M. and Oshima, K. (eds.), *Computational Fluid Dynamics Review, Annual Book Series*. John Wiley & Sons, New York, 1995, pp. 495-528.
75. Jameson, A., Pierce, N.A. and Martinelli, L., "Optimum aerodynamic design using Navier-Stokes equations," AIAA Paper No. 97-0101, 1997.
76. Reuther, J. and Jameson, A., "Control based airfoil design using the Euler equations," AIAA Paper No. 94-4272, 1994.
77. Reuther, J., Jameson, A., Farmer, J., Martinelli, L., and Saunders, D., "Aerodynamic shape optimization of complex aircraft configurations via an adjoint formulation," AIAA Paper No. 96-0094, 1996.
78. Giles, M. B. and Pierce, N. A., "An introduction to the adjoint approach to design", *Flow, Turbulence and Combustion*, **65**, 2000, pp. 393-415.
79. Giles, M. B. and Pierce, N. A., "Analytic adjoint solutions for the quasi-one-dimensional Euler equations," *Journal of Fluid Mechanics*, **426**, 2001, pp. 327-345.
80. Lions, J. L., "Optimal Control of Systems Governed by Partial Differential Equations," translated by S.K. Mitter. Springer-Verlag, Berlin, 1971.

81. Pironneau O., “On optimum design in fluid mechanics” *Journal of Fluid Mechanics*, **64**, 1974, pp. 97–110.
82. Elliott, J., “Aerodynamic optimization based on the Euler and Navier–Stokes equations using unstructured grids” Ph.D. thesis, MIT, Department of Aeronautics and Astronautics, (1998).
83. Nielsen, E. and Anderson, W. K., “Aerodynamic design optimization on unstructured meshes using the Navier–Stokes equations” AIAA Paper 98-4809 (1998).
84. Anderson, W. K. and Bonhaus, D. L., “Airfoil design on unstructured grids for turbulent flows”, *AIAA Journal*, **37**(2), 1999, pp. 185–191.
85. Mohammadi, B., “Optimal shape design, reverse mode of automatic differentiation and turbulence” AIAA Paper No. 97-0099, 1997.
86. Anderson J. D., *Computational Fluid Dynamics: The Basics with Applications* McGraw Hill, 1995.
87. Veltin, J., McLaughlin, D. K., and Morris, P. J., “Improvement of acoustic models for community noise exposure prediction,” AIAA Paper 2008-0012, 2008.
88. Plotkin, K.J. et al, “Advanced Acoustic Models for Military Aircraft Noise Propagation and Impact Assessment,” SERDP Project WP-1304, Wyle Report WR 10-17, September 2010.
89. Viswanathan, K., “Does a model scale nozzle emit the same jet noise as a jet engine,” *AIAA Journal*, **46**(2), 2008, pp. 336-355.
90. Bridges, J. and Brown, C. A., “Parametric testing of chevrons on single flow hot jets,” AIAA Paper No. 2004-2824, 2004.
91. Ahuja, K. K., “Designing clean jet-noise facilities and making accurate jet-noise measurements,” *International Journal of Aeroacoustics*, **2**(3&4), 2003, pp. 371–412.
92. Koch, L. D., Bridges, J., Brown, C., and Khavaran, A., “Experimental and analytical determination of the geometric far field for round jets,” *Noise Control Engineering Journal*, **53**(1), 2005, pp.20–28.
93. Seiner, J. M. and Norum, T. D., Jet noise data provided by private communication, 2001.
94. Petitjean, B. P., Morris, P. J., and McLaughlin, D. K., “On the nonlinear propagation of shock-associated jet noise,” AIAA Paper No. 2005-2930, 2005.

95. Saxena, S., Morris, P.J. and Viswanathan, K., "Algorithm for the nonlinear propagation of broadband jet noise," *AIAA Journal*, **47**(1) pp. 186-194, 2009
96. Papamoschou, D., "Mach wave elimination in supersonic jets," *AIAA Journal*, **35**(10), 1997, pp. 1604-1611.
97. Viswanathan, K., "Aeroacoustics of hot jets," *J. Fluid Mech.*, **516**, 2004, pp. 39–82.
98. Lee, S. S. and Bridges, J., "Phased-array measurements of single flow hot jets," AIAA Paper No. 2005-2842, 2005.
99. Norum, T.D., Garber, D.P., Golub, R.A., and Santa Maria, O.L., "Supersonic Jet Exhaust Noise at High Subsonic Flight Speed," NASA/TP-2004-212686, 2004.
100. Davies, P. O. A. L., Fisher, M. J., and Barratt, M. J., "The characteristics of the turbulence in the mixing region of a round jet," *Journal of Fluid Mechanics*, **15**, 1963, pp. 337–367.
101. Bradshaw, P., Ferris, D. H., and Johnson, R. F., "Turbulence in the noise-producing region of a circular jet," *Journal of Fluid Mechanics*, **19**, 1964, pp. 591–624.
102. Wygnanski, I. and Fiedler, H., "Some measurements in the self-preserving jet," *Journal of Fluid Mechanics*, **38**, 1969, pp. 577–612.
103. Bradbury, L. J. S. and Khadem, A. H., "The distortion of a jet by tabs," *Journal of Fluid Mechanics*, **70**, 1975, pp. 801–813.
104. Pannu, S. S. and Johannesen, N. H., "The structure of jets from notched nozzles," *Journal of Fluid Mechanics*, **74**, 1976, pp. 515–528.
105. Wlezien, R. W. and Kibens, V., "Influence of nozzle asymmetry on supersonic jets," *AIAA Journal*, **26**(1), 1988, pp. 27-33.
106. Elliott, G. S. and Samimy M., "Compressibility effects in free shear layers," *Physics of Fluids A*, **2**(7), 1990, pp. 1231-1240.
107. Tillman, T. G., Patrick, W. P., and Paterson, R. W., "Enhanced mixing of supersonic jets," *Journal of Propulsion and Power*, **7**(6), 1991, pp. 1006–1014.
108. Samimy, M., Zaman, K. B. M. Q., and Reeder, M. F., "Effect of tabs on the flow and noise field of an axisymmetric jet," *AIAA Journal*, **31**(4), 1993, pp. 609-619.
109. Krothapalli, A., King, C. J., and Strykowski, P. J., "The role of streamwise vortices on the sound generation of supersonic jets," AIAA Paper No. 93-4320, 1993.

110. Carletti, M. J., Rogers, C. B., and Parekh, D. E., "Use of streamwise vorticity to increase mass entrainment in a cylindrical ejector," *AIAA Journal*, **33**(9), 1995, pp. 1641-1645.
111. Knowles, K. and Saddington, A. J., "A review of jet mixing enhancement for aircraft propulsion applications," *Proc. I.Mech.E Part G: J. Aerospace Engineering*, **220**, 2006, pp. 103–127.
112. Longmire, E. K., Eaton, J. K., and Elkins, C. J., "Control of jet structure by crown-shaped nozzles," *AIAA Journal*, **30**(2), 1992, pp. 505-512.
113. Alkislar, M. B., Krothapalli, A., and Butler, G. W., "The effect of streamwise vortices on the aeroacoustics of a Mach 0.9 jet," *Journal of Fluid Mechanics*, **578**, 2007, pp. 139–169.
114. Callender, B., Gutmark, E., and Martens, S., "Far-field acoustic investigation into chevron nozzle mechanisms and trends," *AIAA Journal*, **43**(1), 2005, pp. 87-95.
115. Bridges, J. and Wernet, M. P., "Turbulence measurements of separate flow nozzle with mixing enhancement features," AIAA Paper No. 2002-2484, 2002.
116. Gutmark, E., Callender, B. W., and Martens, S., "Aeroacoustics of turbulent jets: flow structure, noise sources, and control," *JSME International Journal Series B*, **49**(4), 2006, pp. 1078-1085.
117. Opalski, A. B., Wernet, M. P., and Bridges, J., "Chevron nozzle performance characterization using stereoscopic DPIV," AIAA Paper No. 2005-444, 2005.
118. Foss, J. K. and Zaman, K. B. M. Q., "Large- and small-scale vortical motions in a shear layer perturbed by tabs," *Journal of Fluid Mechanics*, **382**, 1999, pp. 307-329.
119. Papamoschou, D. and Zill, A., "Fundamental investigation of supersonic nozzle flow separation," AIAA Paper No. 2004-1111, 2004.
120. Zapryagaev, V. I., Solotchin, A. V., "An experimental investigation of the nozzle roughness effect on streamwise vortices in a supersonic jet," *Journal of Applied Mechanics and Technical Physics*, **38**(1), 1997, pp. 78-86.